

Ministry of Science and Higher Education of the Russian Federation  
ITMO University

ISSN 2220-8054

***NANOSYSTEMS:***  
***PHYSICS, CHEMISTRY, MATHEMATICS***

**2024, volume 15(4)**

**Наносистемы: физика, химия, математика**

**2024, том 15, № 4**



# **NANOSYSTEMS:**

## **PHYSICS, CHEMISTRY, MATHEMATICS**

### **ADVISORY BOARD MEMBERS**

**Chairman:** V.N. Vasiliev (*St. Petersburg, Russia*),  
V.M. Buznik (*Moscow, Russia*); V.M. Ievlev (*Voronezh, Russia*), P.S. Kop'ev (*St. Petersburg, Russia*), V.N. Parmon (*Novosibirsk, Russia*), A.I. Rusanov (*St. Petersburg, Russia*),

### **EDITORIAL BOARD**

**Editor-in-Chief:** I.Yu. Popov (*St. Petersburg, Russia*)

#### **Section Co-Editors:**

Physics – V.M. Uzdin (*St. Petersburg, Russia*),

Material science – V.V. Gusarov (*St. Petersburg, Russia*); O.V. Al'myasheva (*St. Petersburg, Russia*);

Chemistry – V.K. Ivanov (*Moscow, Russia*),

Mathematics – I.Yu. Popov (*St. Petersburg, Russia*).

#### **Editorial Board Members:**

V.M. Adamyan (*Odessa, Ukraine*); A.P. Alodjants (*St. Petersburg, Russia*); S. Bechta (*Stockholm, Sweden*); J. Behrndt (*Graz, Austria*); A. Chatterjee (*Hyderabad, India*); A.V. Chizhov (*Dubna, Russia*); A.N. Enyashin (*Ekaterinburg, Russia*), P.P. Fedorov (*Moscow, Russia*); E.A. Gudilin (*Moscow, Russia*); H. Jónsson (*Reykjavik, Iceland*); A.A. Kiselev (*Durham, USA*); Yu.S. Kivshar (*Canberra, Australia*); S.A. Kozlov (*St. Petersburg, Russia*); P.A. Kurasov (*Stockholm, Sweden*); A.V. Lukashin (*Moscow, Russia*); I.V. Melikhov (*Moscow, Russia*); G.P. Miroshnichenko (*St. Petersburg, Russia*); I.Ya. Mittova (*Voronezh, Russia*); H. Najjar (*Monastir, Tunisia*), Nguyen Anh Tien (*Ho Chi Minh, Vietnam*); V.V. Pankov (*Minsk, Belarus*); K. Pankrashkin (*Orsay, France*); A.V. Ragulya (*Kiev, Ukraine*); V. Rajendran (*Tamil Nadu, India*); A.A. Rempel (*Ekaterinburg, Russia*); A.A. Rogachev (*Minsk, Belarus*); V.Ya. Rudyak (*Novosibirsk, Russia*); H.M. Sedighi (*Ahvaz, Iran*); D Shoikhet (*Karmiel, Israel*); M.N. Smirnova (*Moscow, Russia*); P. Stovicek (*Prague, Czech Republic*); V.M. Talanov (*Novocherkassk, Russia*); A.Ya. Vul' (*St. Petersburg, Russia*); A.V. Yakimansky (*St. Petersburg, Russia*), V.A. Zagrebnoy (*Marseille, France*).

#### **Editors:**

I.V. Blinova; A.I. Popov; A.I. Trifanov; E.S. Trifanova (*St. Petersburg, Russia*),

R. Simoneaux (*Philadelphia, Pennsylvania, USA*).

**Address:** ITMO University, Kronverkskiy pr., 49, St. Petersburg 197101, Russia.

**Phone:** +7(812)607-02-54, **Journal site:** <http://nanojournal.ifmo.ru/>,

**E-mail:** [nanojournal.ifmo@gmail.com](mailto:nanojournal.ifmo@gmail.com)

### **AIM AND SCOPE**

The scope of the journal includes all areas of nano-sciences. Papers devoted to basic problems of physics, chemistry, material science and mathematics inspired by nanosystems investigations are welcomed. Both theoretical and experimental works concerning the properties and behavior of nanosystems, problems of its creation and application, mathematical methods of nanosystem studies are considered.

The journal publishes scientific reviews (up to 30 journal pages), research papers (up to 15 pages) and letters (up to 5 pages). All manuscripts are peer-reviewed. Authors are informed about the referee opinion and the Editorial decision.

# CONTENT

## MATHEMATICS

Z.I. Muminov, V.U. Aktamova

**The point spectrum of the three-particle Schrödinger operator for a system comprising two identical bosons and one fermion on  $\mathbb{Z}$**  438

P. Agarwal, U. Baltaeva, U. Madrakhimov, J.I. Baltaev

**The Cauchy problem for a high-order wave equation with a loaded convolution type** 448

## PHYSICS

J.D. Matrasulov, J.R. Yusupov, Kh.Sh. Matyokubov

**Fast forward problem for adiabatic quantum dynamics: estimation of the energy cost** 457

A.N. Perevalova, B.M. Fominykh, V.V. Chistyakov, V.V. Marchenkov  
**Role of bulk and surface current carriers in resistivity of thin films of the topological insulator  $\text{Bi}_2\text{Se}_3$**  465

I.Y. Popov, A.I. Popov, P.A. Gilev, A. Chatterjee

**Quantum graph as a benchmark for persistent current** 469

Monoj Das

**Diameter dependent geometrical and electrical properties of zigzag HgSe nanotubes: a density functional study** 473

A.L. Dymova, V.A. Prikazchikov, A.V. Astrakhantseva, T.M. Minnebaev, M.R. Zaitov, M.S. Pudovkin, A.S. Nizamutdinov

**Crystalline  $\text{LiYF}_4:\text{Nd}^{3+}$  nanoparticles synthesized via laser ablation method in water solutions of ethanol** 481

## CHEMISTRY AND MATERIAL SCIENCE

Hein Myat Lwin, O.V. Yarovaya

**Colloidal chemical properties of the sol  $\text{V}_2\text{O}_5 \cdot n\text{H}_2\text{O}$**  487

M.A. Maksimova, E.V. Polyakov, I.V. Volkov, A.P. Tyutyunnik, A.A. Ioshin

**Kinetic of colloidal-chemical transformations during the decomposition of ammonia complexes of Zn(II) in alkaline solutions** 498

D.P. Ordinartsev, N.V. Pechishcheva, S.Kh. Estemirova, A.V. Kim, E.V. Sterkhov, S.A. Petrova, G.A. Shilenko

**Composite sorbent based on  $\text{Fe}_3\text{O}_4$  with  $\text{Fe}(\text{N}_2\text{H}_4)_x\text{Cl}_y$  for the removal of Chromium (VI) from wastewater** 510

G.M. Zirnik, A.S. Chernukha, D.A. Uchaev, I.A. Solizoda, S.A. Gudkova, N.S. Nekorysnova, D.A. Vinnik <b>Phase formation of nanosized InGaZnO<sub>4</sub> obtained by the sol-gel method with different chelating agents</b>	<b>520</b>
Yu.A. Avdeeva, I.V. Luzhkova, A.M. Murzakaev, A.N. Ermakov <b>Formation of ultra- and nanodispersed “core-shell” structures Ti<sub>0.8</sub>Mo<sub>0.2</sub>C<sub>0.5</sub>N<sub>0.5</sub> – Ni – Mo in the process of plasma-chemical synthesis of a mechanical mixture of titanium carbonitride with metallic nickel and molybdenum</b>	<b>530</b>
T.I. Chupakhina, O.I. Gyrdasova, A.M. Uporova, L.Y. Buldakova, M.Y. Yanchenko, D.V. Mamedov, Y.A. Deeva, I.V. Baklanova <b>Study of photocatalytic activity in two light ranges of Sr<sub>2</sub>Mn<sub>0.4</sub>Ti<sub>0.6</sub>O<sub>4</sub> oxide with the K<sub>2</sub>NiF<sub>4</sub>-type structure</b>	<b>540</b>
K.O. Potapenko, E.E. Aydakov, E.Y. Gerasimov, E.A. Kozlova <b>The control of by-product formation rates in photocatalytic hydrogen evolution reaction from organic substances over Pt/g-C<sub>3</sub>N<sub>4</sub></b>	<b>548</b>
<b>Information for authors</b>	<b>558</b>

# Obituary



**28.07.1932 – 25.07.2024**

Nikita Fedorovich Morozov, a member of the Advisory Board of our journal, Academician of the Russian Academy of Sciences, an outstanding scientist, mathematician, Doctor of Physical and Mathematical Sciences, Head of the Department of Elasticity Theory of the Faculty of Mathematics and Mechanics of St. Petersburg State University, Laureate of the State Prize of the Russian Federation in Science and Technology, has passed away.

Being the world's leading specialist in nonlinear mechanics, strength and fracture theory, nanostructures and related critical technologies, Nikita Fedorovich headed the famous school of mechanics of St. Petersburg State University for many years, and in recent years, he actively supported and directed research in various fields of mechanics conducted in St. Petersburg and other regions of Russia.

Along with the qualities of a great scientist, Nikita Fedorovich also possessed high human qualities that united people from a wide variety of fields, not only scientific ones, around him, many of whom could call him their teacher and saw in him a life support and guide. We express our deep condolences to his family and all close people. The memory of Nikita Fedorovich Morozov, as well as his enormous contribution to world science, will remain with us forever.

## The point spectrum of the three-particle Schrödinger operator for a system comprising two identical bosons and one fermion on $\mathbb{Z}$

Zahriddin I. Muminov<sup>1,2,a</sup>, Vasila U. Aktamova<sup>3,b</sup><sup>1</sup>Tashkent State University of Economics, 100066, Tashkent, Uzbekistan<sup>2</sup>Institute of Mathematics named after V.I.Romanovsky, 100174, Tashkent, Uzbekistan<sup>3</sup>Samarkand Institute of Veterinary Medicine, 140103, Samarkand, Uzbekistan<sup>a</sup>zimuminov@gmail.com, <sup>b</sup>vaktamova@mail.ru

Corresponding author: Z. I. Muminov, zimuminov@gmail.com

PACS 02.70.Hm, 02.30.-f

**ABSTRACT** We consider the Hamiltonian of a system of three quantum particles (two identical bosons and a fermion) on the one-dimensional lattice interacting by means of zero-range attractive or repulsive potentials. We investigate the point spectrum of the three-particle discrete Schrödinger operator  $H(K)$ ,  $K \in \mathbb{T}$  which possesses infinitely many eigenvalues depending on repulsive or attractive interactions, under the assumption that the bosons in the system have infinite mass.

**KEYWORDS** Schrödinger operator, dispersion functions, zero-range pair potentials, discrete spectrum, essential spectrum.

**ACKNOWLEDGEMENTS** The authors acknowledge support from the Innovative Development Agency of the Republic of Uzbekistan (Grant No. FZ–20200929224), and they thank the anonymous referee for reading the manuscript carefully and for making valuable suggestions.

**FOR CITATION** Muminov Z.I., Aktamova V.U. The point spectrum of the three-particle Schrödinger operator for a system comprising two identical bosons and one fermion on  $\mathbb{Z}$ . *Nanosystems: Phys. Chem. Math.*, 2024, **15** (4), 438–447.

### 1. Introduction

In physics, stable composite objects often result from attractive forces, enabling the constituents to lower their energy by binding together. In contrast, repulsive forces tend to scatter particles when they are in free space. However, within structured environments such as a periodic potential, and in the absence of dissipation, stable composite objects can exist even with repulsive interactions arising from the lattice band structure [1].

The Bose-Hubbard model, which describes repulsive pairs, serves as the theoretical basis for various applications.

The work referenced by [1] exemplifies the crucial link between the Bose-Hubbard model [2, 3] and atoms in optical lattices, and helps pave the way for many more interesting developments and applications, as discussed in [4]. In cold atom lattice physics, stable repulsively bound objects are expected to be common, which leading to potential composites with fermions [5] or Bose-Fermi mixtures [6], and can even be formed with more than two particles in a similar manner.

The Efimov effect, first discovered by V. Efimov in 1970 [7], is one of the most intriguing phenomena in physics. It occurs in three-body systems in three-dimensional space that interact through short-range pairwise potentials. It is always possible to ensure the couplings of the interactions in such a way that none of the particle pairs has a negative energy bound state, but at least two pairs exhibit a resonance at zero energy. The existence of this effect of a three-particle Schrödinger operator was discovered by Yafaev [8] and in the discrete case by others [9–14].

Recently, the authors [15–17] considered perturbations of the system of three arbitrary quantum particles on lattices  $\mathbb{Z}^d$ ,  $d = 1, 2$ , interacting through attractive zero-range pairwise potentials. They established that the three-particle Schrödinger operators possess infinitely many negative eigenvalues for all positive non-zero point interactions, under the assumption that two particles in the system have infinite mass. Also, note that the author of [17] obtained asymptotics for these eigenvalues.

The main goal of the paper is to investigate the existence of infinite number of bound states of the three-particle discrete Schrödinger operator associated with a system of two identical bosons and a fermion, where the bosons have infinite mass and the fermion has a finite mass. This investigation is performed on the one-dimensional lattice  $\mathbb{Z}$  and involves repulsive or attractive zero-range pairwise interactions. The problem is reduced to the study the Fredholm determinant of a diagonal operator.

It should be noted that, unlike the last three articles [15–17], we study eigenvalues below and above the essential spectrum of the unperturbed operator for all repulsive or attractive zero-range pairwise interactions.

It is worth mentioning that in the continuous case, the authors of [18] studied a very similar system, specifically a system consisting of two infinitely heavy quantum particles and one light particle in three-dimensional space  $\mathbb{R}^3$ , interacting via long-range Coulomb pair potentials. Although the authors of this book are not interested in the number of eigenvalues, they briefly explained the scheme for solving problems of this type using the Coulomb spheroidal function decomposition. In the present paper, the problem is reduced to the study of eigenvalues of convolution type compact integral operators.

The paper is organized as follows. In Section 2, we introduce the three-particle discrete Schrödinger operator  $H(K)$  and the two-particle discrete Schrödinger operators associated with subsystems of the system of two identical bosons and a fermion. In Section 3, we study the essential spectrum of the three-particle discrete Schrödinger operator  $H(K)$ . The eigenvalues of  $H(K)$  below and above the spectrum of the non-perturbed operator  $H_0(K)$  are investigated in Section 4. Section 5 is devoted to showing main result, Theorem 5.1.

**2. Three-particle discrete Schrödinger operator on the lattice  $\mathbb{Z}$**

Let  $L_s^2(\mathbb{T}^2)$  be the linear subspace of the symmetric functions of the Hilbert space  $L^2((\mathbb{T})^2)$ .

Let us consider the discrete Schrödinger operator  $H(K)$ , where  $K \in \mathbb{T}$ , associated with a system consisting of two identical bosons and a fermion moving on the one-dimensional lattice  $\mathbb{Z}$  (see [15, 17]).

$$H(K) = H_0(K) - V$$

with zero-range attractive potentials

$$V = V_1 + V_2 + V_3,$$

where

$$\begin{aligned} (V_1 f)(p, q) &= \frac{\lambda}{2\pi} \int_{\mathbb{T}} f(p, t) dt, & (V_2 f)(p, q) &= \frac{\lambda}{2\pi} \int_{\mathbb{T}} f(t, q) dt \\ (V_3 f)(p, q) &= \frac{\mu}{2\pi} \int_{\mathbb{T}} f(t, p + q - t) dt, & f &\in L_s^2(\mathbb{T}^2), p, q \in \mathbb{T}, \end{aligned}$$

and numbers  $\lambda$  and  $\mu$  serve as the parameters of boson-fermion interaction and boson-boson interaction, respectively.

Here the numbers  $\lambda$  and  $\mu$  indicate repulsive pair-wise interaction when  $\lambda < 0$  and  $\mu < 0$ , and attractive pair-wise interaction when  $\lambda > 0$  and  $\mu > 0$ . The operator  $H_0(K)$  is defined on the Hilbert space  $L_s^2(\mathbb{T}^2)$  by

$$(H_0(K)f)(p, q) = E(K; p, q)f(p, q), \quad f \in L_s^2(\mathbb{T}^2),$$

and

$$E(K; p, q) = \varepsilon_b(p) + \varepsilon_b(q) + \varepsilon_f(K - p - q), \quad p, q \in \mathbb{T}.$$

Here, the real-valued continuous function  $\varepsilon_b(\cdot)$  and  $\varepsilon_f(\cdot)$ , referred to as *the dispersion relation* associated with the free boson and fermion, is defined as

$$\varepsilon_b(p) = \frac{1}{m} \varepsilon(p), \quad \varepsilon_f(p) = \frac{1}{\mathfrak{m}} \varepsilon(p), \quad \varepsilon(p) = 1 - \cos(p), \quad p \in \mathbb{T}, \tag{1}$$

respectively, and  $m$  and  $\mathfrak{m}$  represents the mass of the boson and fermion, respectively.

Let  $k \in \mathbb{T}$  and  $L_k^2(\mathbb{T})$  be a linear subspace of the Hilbert space  $L^2(\mathbb{T})$  defined by

$$L_k^2(\mathbb{T}) = \{f \in L^2(\mathbb{T}) | f(p) = f(k - p)\}.$$

A two-particle discrete Schrödinger operator corresponding to the subsystem {bozon,fermion} and {bozon,bozon}, of the three-particle system acts on the Hilbert space  $L^2(\mathbb{T})$  and  $L_k^2(\mathbb{T})$  as

$$h_1(k) = h_1^0(k) - v_1, \quad \text{and} \quad h_2(k) = h_2^0(k) - v_2, \quad k \in \mathbb{T}, \tag{2}$$

respectively.

Here, the operators  $h_\alpha^0(k)$

$$(h_1^0(k)f)(p) = E_k^{(1)}(p)f(p), \quad f \in L^2(\mathbb{T}),$$

and

$$(h_2^0(k)f)(p) = E_k^{(2)}(p)f(p), \quad f \in L_k^2(\mathbb{T}),$$

where

$$E_k^{(1)}(p) = \varepsilon_b(p) + \varepsilon_f(k - p), \quad E_k^{(2)}(p) = \varepsilon_b(p) + \varepsilon_b(k - p), \quad p \in \mathbb{T}. \tag{3}$$

The operators  $v_1$  and  $v_2$  are defined as

$$(v_1 f)(p) = \frac{\mu}{2\pi} \int_{\mathbb{T}} f(q) dq, \quad f \in L^2(\mathbb{T}), p \in \mathbb{T}.$$

and

$$(v_2 f)(p) = \frac{\lambda}{2\pi} \int_{\mathbb{T}} f(q) dq, \quad f \in L_k^2(\mathbb{T}), p \in \mathbb{T},$$

respectively.

**2.1. Spectral properties of the two-particle discrete Schrödinger operators when  $m = \infty$  and  $0 < m < \infty$**

With  $m = \infty$  and  $0 < m < \infty$  and the equality (1), the functions (3) can be written as

$$E_k^{(1)}(p) = \varepsilon_f(k - p) = \varepsilon(k - p)/m, \quad E_k^{(2)}(p) = 0, \quad p \in \mathbb{T}.$$

Consequently, since the potentials  $v_\alpha, \alpha = 1, 2$  have a convolution-type property, all two-particle Schrödinger operators do not depend on the quasi-momentum  $k \in \mathbb{T}$ ,

$$h_1 := h_1(k) \quad \text{and} \quad h_2 := h_2(k).$$

Then, the operators  $h_1(k)$  and  $h_2(k)$  act as

$$h_1(k)f(p) = \varepsilon_f(p)f(p) - (v_1f)(p), \quad f \in L^2(\mathbb{T}) \quad \text{and} \quad h_2(k)f(p) = -(v_2f)(p), \quad f \in L^2_k(\mathbb{T}).$$

As  $v_1$  is a finite rank operator, according to the Weyl theorem, the essential spectrum  $\sigma_{ess}(h_1(k))$  of the operator  $h_1(k)$  in (2) coincides with the spectrum  $\sigma(h_1^0(k))$  of the non-perturbed operator  $h_1^0(k)$ . More specifically,

$$\sigma_{ess}(h_1(k)) = [E_{\min}^{(1)}(k), E_{\max}^{(1)}(k)],$$

where

$$E_{\min}^{(1)}(k) \equiv \min_{p \in \mathbb{T}} E_k^{(1)}(p), \quad E_{\max}^{(1)}(k) \equiv \max_{p \in \mathbb{T}} E_k^{(1)}(p).$$

Therefore, in our case, we have

$$\sigma_{ess}(h_1(k)) = [0, 2/m] \quad \text{and} \quad \sigma_{ess}(h_2(k)) = \{0\}.$$

The Fredholm determinants associated with the operators  $h_1(k)$  are defined as

$$\Delta(\lambda; z) = 1 - \lambda d_0(z), \quad d_0(z) = \frac{1}{2\pi} \int_{\mathbb{T}} \frac{ds}{\varepsilon_f(s) - z}, \quad z \in \mathbb{C} \setminus [0, 2/m].$$

**Lemma 2.1.** (a) The number  $z \in \mathbb{C} \setminus [0, 2/m]$  is an eigenvalue of  $h_1(k)$  if and only if  $\Delta(\lambda; z) = 0$ .

(b) If  $\lambda < 0$  and  $\lambda > 0$ , then there exists a unique simple eigenvalue  $z = z_1^0$  of  $h_1(k)$  in the interval  $(-2/m - \mu, \infty)$  and  $(-\infty, 0)$ , respectively. Moreover,  $z_1^0$  does not depend on  $k \in \mathbb{T}$ .

*Proof.* (a) The equation

$$h_1(k)f = zf \quad \text{i.e.,} \quad f = (h_1^0(k) - z)^{-1}v_1f$$

has a non-trivial solution if and only if

$$\Delta(\lambda; z)C = 0, \quad C \in \mathbb{C},$$

has a non-trivial solution.

Therein, the solutions  $C \in \mathbb{C}$  and  $f \in L^2(\mathbb{T})$  are related as follows

$$C = v_1f \quad \text{and} \quad f = (h_1^0(k) - z)^{-1}C.$$

(b) Let  $\lambda > 0$ . The function  $\Delta(\lambda; z)$  is monotonic decreasing in  $(-\infty, 0)$  and  $\Delta(\lambda; z) > 1$  in  $(-2/m - \mu, \infty)$ . Since

$$\lim_{z \rightarrow -\infty} \Delta(\lambda; z) = 1 \quad \text{and} \quad \lim_{z \rightarrow 0^-} \Delta(\lambda; z) = -\infty,$$

the intermediate-value theorem implies the existence of a unique simple zero  $z = z_1^0, z_1^0 \in (-\infty, 0) \cup (-2/m - \mu, \infty)$  of the function  $\Delta(\lambda; \cdot)$ , and furthermore  $z_1^0 \in (-\infty, 0)$ .

The lemma can be proven in a similar way when  $\lambda < 0$ . □

Now, we can summarize the results of this section in the following lemma.

**Lemma 2.2.** We have

$$\begin{aligned} \sigma_{\text{disc}}(h_1(k)) &= \{z_1^0\}, \quad \text{if } \lambda \neq 0, \\ \sigma(h_1(k)) &= \{z_1^0\} \cup [0, 2/m], \quad \text{if } \lambda \neq 0 \end{aligned}$$

and

$$\sigma_{\text{disc}}(h_2(k)) = \{-\mu\}, \quad \sigma(h_2(k)) = \{-\mu\} \cup \{0\}.$$

### 3. Essential spectrum of $H(K)$

One of the notable outcomes in the spectral theory of multi-particle continuous Schrödinger operators involves characterizing the essential spectrum of the Schrödinger operators in terms of cluster operators (the HVZ-theorem. See Refs. [19–23] for the discrete case and [24] for a pseudo-relativistic operator).

**Lemma 3.1.** *The essential spectrum of  $H(K)$  satisfies the relation*

$$\sigma_{ess}(H(K)) = \bigcup_{k \in \mathbb{T}} \left\{ \sigma(h_1(K - k)) + \varepsilon_b(k) \right\} \cup \bigcup_{k \in \mathbb{T}} \left\{ \sigma(h_2(K - k)) + \varepsilon_f(k) \right\}.$$

*Proof.* The proof can be found in [17, 21]. □

#### 3.1. The essential spectrum of $H(K)$ with $m = \infty$ , and $m < \infty$

Due to Lemma 2.2 and the relations  $\varepsilon_b(p) = 0$  and  $\varepsilon_f(p) = \varepsilon(p)/m$ , we obtain

$$\begin{aligned} \bigcup_{k \in \mathbb{T}} \left\{ \sigma(h_1(K - k)) + \varepsilon_b(k) \right\} &= \sigma(h_1(k)) = \{z_1^0\} \cup [0, 2/m], \\ \bigcup_{k \in \mathbb{T}} \left\{ \sigma(h_2(K - k)) + \varepsilon_f(k) \right\} &= \bigcup_{k \in \mathbb{T}} \left\{ \{-\mu\} \cup \{0\} + \varepsilon_f(k) \right\} = [-\mu, 2/m - \mu] \cup [0, 2/m]. \end{aligned}$$

According to the last two relations and Lemma 3.1, we have

**Lemma 3.2.**

$$\sigma_{ess}(H(K)) = \{z_1^0\} \cup ([-\mu, 2/m - \mu] \cup [0, 2/m]).$$

### 4. The point spectrum of $H(K)$ for $m = \infty$ and $m < \infty$

One can show easily that the subspace

$$\mathcal{A}_0 = \{f \in L_s^2(\mathbb{T} \times \mathbb{T}) \mid f(p, q) = g(p + q), g \in L^2(\mathbb{T})\}$$

is invariant under the operator  $H(K)$ , and so it is  $\mathcal{A}_0^\perp = L_s^2(\mathbb{T} \times \mathbb{T}) \ominus \mathcal{A}_0$ .

Therefore, we have

$$\sigma_{pp}(H(K)) = \sigma_{pp}(A_0(K)) \cup \sigma_{pp}(A_1(K)),$$

where  $A_0(K)$  and  $A_1(K)$  are restrictions of  $H(K)$  on the linear subspaces  $\mathcal{A}_0$  and  $\mathcal{A}_0^\perp$ , respectively.

Since  $\mathcal{A}_0$  and  $L^2(\mathbb{T})$  are isomorphic, the operator  $A_0(K)$  is unitarily equivalent to the operator  $B_0$  on  $L^2(\mathbb{T})$ , where

$$B_0 = E_0(K) - \mu I - 2\lambda v, \tag{4}$$

$E_0(K)$  denotes the multiplication by the function  $\varepsilon_f(K - p)$ ,  $I$  is the identity operator, and  $v$  is an integral operator defined by

$$(vf)(p) = \frac{1}{2\pi} \int_{\mathbb{T}} f(q) dq, \quad f \in L^2(\mathbb{T}), p \in \mathbb{T}.$$

The operator  $A_1(K)$  takes the form

$$A_1(K) = H_0(K) - \lambda V_1 - \lambda V_2.$$

Let  $U_K : L_s^2(\mathbb{T} \times \mathbb{T}) \rightarrow L_s^2(\mathbb{T} \times \mathbb{T})$  be a unitary operator defined as

$$(U_K f)(p, q) = f(-K/2 + p, -K/2 + q). \tag{5}$$

It establishes a unitary equivalence between  $H(K)$  and  $H(0)$ , and so we can prove the coming statements for  $H(0)$ .

#### 4.1. Spectrum of $A_0(K)$

The equivalence (4) and the Weyl theorem imply that

$$\sigma_{ess}(A_0(K)) = [-\mu, 2/m - \mu].$$

The following lemma describes the behaviour of the eigenvector of  $H(K)$  in the linear space  $\mathcal{A}_0$ .

**Lemma 4.1.** (a) *If  $\lambda < 0$ , then  $A_0(K)$  has an unique eigenfunction with the corresponding eigenvalue  $\eta$ ,  $\eta \in (2/m - \mu, \infty)$  for any  $\mu \in \mathbb{R}$ .*

(b) *If  $\lambda = 0$ , then  $A_0(K)$  has no eigenvalues for any  $\mu \in \mathbb{R}$ .*

(c) *If  $\lambda > 0$ , then  $A_0(K)$  has an unique eigenfunction with the corresponding eigenvalue  $\eta$ ,  $\eta \in (-\infty, -\mu)$  for any  $\mu \in \mathbb{R}$ .*

*Proof.* The equation

$$H(0)f = zf, \quad f \in A_0,$$

has a solution if and only if the equation

$$C(1 - 2\lambda d_0(\mu + z)) = 0, \tag{6}$$

has one, and their solutions are related by

$$f(p, q) := g(p + q) = \frac{2\lambda}{\varepsilon_f(-p - q) - \mu - z} C,$$

where

$$C = \frac{1}{2\pi} \int_{\mathbb{T}} g(t) dt.$$

Equation (6) has a nontrivial solution  $C$  if and only if the equation

$$\Delta(2\lambda; z) = 1 - 2\lambda d_0(\mu + z) = 0$$

has a root. The function  $\Delta(2\lambda; z)$  is defined on  $(-\infty, -\mu) \cap (2/m - \mu, \infty)$  and according to Lemma 2.1: (a) If  $\lambda > 0$ , then  $\Delta(2\lambda; z) = 1 - 2\lambda d_0(\mu + z)$  has a unique zero in  $(-\infty, -\mu)$ , but does not have one in  $(2/m - \mu, \infty)$ ; (c) If  $\lambda < 0$ , then  $\Delta(2\lambda; z)$  has a unique zero in  $(2/m - \mu, \infty)$ , but does not have one in  $(-\infty, -\mu)$ .

(b) If  $\lambda = 0$ , then  $B_0 = E_0(K) - \mu I$  is a multiplication operator, and so  $A_0(K)$  has no eigenvalues for any  $\mu \in \mathbb{R}$ .  $\square$

### 4.2. Spectrum of $A_1(K)$

As the operator  $A_1(K)$  does not contain the parameter  $\mu$ , Lemma 3.2 implies that

$$\sigma_{ess}(A_1(K)) = \{z_1^0\} \cup [0, 2/m].$$

In order to study need, we define the following integral depending on  $n \in \mathbb{Z}$ :

$$d_n(z) = \frac{1}{2\pi} \int_{\mathbb{T}} \frac{e^{int}}{\varepsilon_f(t) - z} dt, \quad z \in \mathbb{C} \setminus [0, 2/m].$$

**Lemma 4.2.** *For any fixed  $n \in \mathbb{Z}$ , the function  $d_n(z)$  satisfies the equality*

$$d_n(z) = m \frac{(1 - mz - \sqrt{m^2 z^2 - 2z/m})^{|n|}}{\sqrt{m^2 z^2 - 2z/m}} \quad z \in \mathbb{C} \setminus [0, 2/m].$$

*Proof.* The theory of residues provides the proof (see [17, Lemma 6]).  $\square$

The operators  $V_1$  and  $V_2$  are represented as  $V_1 = \lambda \varphi_1^* \varphi_1$  and  $V_2 = \lambda \varphi_2^* \varphi_2$ , respectively, where the operators  $\varphi_1, \varphi_2 : L_s^2(\mathbb{T} \times \mathbb{T}) \rightarrow L^2(\mathbb{T})$  are of the form

$$(\varphi_1 f)(p) = \frac{1}{(2\pi)^{\frac{1}{2}}} \int_{\mathbb{T}} f(p, t) dt \quad \text{and} \quad (\varphi_2 f)(q) = \frac{1}{(2\pi)^{\frac{1}{2}}} \int_{\mathbb{T}} f(t, q) dt.$$

**Lemma 4.3.** *The number  $z \in \mathbb{C} \setminus \sigma_{ess}(A_1(K))$  is an eigenvalue of the operator  $A_1(K)$  if and only if  $D(z) = 0$ , where*

$$D(z) = \frac{1}{\Delta^2(\lambda; z)} \prod_{n \in \mathbb{Z}} \Delta_n^+(\lambda; z), \tag{7}$$

with

$$\Delta_n^+(\lambda; z) = 1 - \lambda(d_0(z) + d_n(z)).$$

If  $z_n \in \mathbb{C} \setminus \sigma_{ess}(A_1(K))$  is an eigenvalue of  $A_1(K)$ , then  $D_n(z_n) = 0$ ,  $n \in \mathbb{Z}$  and the corresponding eigenfunction is of the form

$$f_n(p, q) = \frac{\lambda}{\varepsilon_f(K - p - q) - z_n} \left( \cos(n(-K/2 + p)) + \cos(n(-K/2 + q)) \right) \tag{8}$$

*Proof.* Given the unitary equivalence of  $H(K)$  and  $A_1(K)$  to  $H(0)$  and  $A_1(0)$ , respectively, we first establish the claim for the latter operators.

Let  $z \in \mathbb{C} \setminus \sigma_{ess}(A_1(0))$  be an eigenvalue of  $A_1(0)$ , and let  $f$  be the corresponding eigenfunction, then

$$f = R_0(z) [\lambda V_1 + \lambda V_2] f, \tag{9}$$

where  $R_0(z) = (H_0(0) - zI)^{-1}$  is a resolvent of  $H_0(0)$ .

This equation has a non-trivial solution if and only if the system of two linear equations

$$\tilde{\varphi}_\alpha = \varphi_\alpha(R_0(z) [\lambda \varphi_1^* \tilde{\varphi}_1 + \lambda \varphi_2^* \tilde{\varphi}_2]), \quad \alpha = 1, 2, \quad \tilde{\varphi}_1, \tilde{\varphi}_2 \in L^2(\mathbb{T}) \tag{10}$$

on the space  $L^2(\mathbb{T}) \oplus L^2(\mathbb{T})$  has a non-zero solution.

Solutions of equations (9) and (10) are linked by

$$f(p, q) = R_0(z)[\lambda\varphi_1^*\tilde{\varphi}_1 + \lambda\varphi_2^*\tilde{\varphi}_2], \tag{11}$$

and

$$\tilde{\varphi}_\alpha = \varphi_\alpha f, \quad \alpha = 1, 2.$$

Since  $f$  is a symmetric function,  $\tilde{\varphi}_1$  and  $\tilde{\varphi}_2$  are the same function, and only their arguments are different, that is, the argument of  $\tilde{\varphi}_1$  is the variable  $p$ , while  $q$  is an independent variable of  $\tilde{\varphi}_1$ :

$$\tilde{\varphi}_2(p) = \tilde{\varphi}_1(p). \tag{12}$$

We note that the functions

$$\Delta_\alpha := I - \lambda\varphi_\alpha R_0(z)\varphi_\alpha^*, \quad z \in \mathbb{C} \setminus \sigma_{ess}(H_0(0)), \quad \alpha = 1, 2,$$

are nonzero for any  $z \in \mathbb{C} \setminus \sigma_{ess}(A_1(0))$ , therefore, their inverses exist,

$$\Delta_\alpha^{-1} = (I - \lambda\varphi_\alpha R_0(z)\varphi_\alpha^*)^{-1}.$$

Then, the solutions  $\tilde{\varphi}_\alpha, \alpha = 1, 2$ , of the equation (10) satisfy the following system of integral equations

$$\begin{cases} \tilde{\varphi}_1 = \lambda\Delta_1^{-1}Q\tilde{\varphi}_2, \\ \tilde{\varphi}_2 = \lambda\Delta_2^{-1}Q^*\tilde{\varphi}_1, \end{cases} \tag{13}$$

where

$$Q = \varphi_1 R_0(z)\varphi_2^*$$

is the integral operator on  $L^2(\mathbb{T})$  defined as

$$(Q\varphi)(p) = \frac{1}{2\pi} \int_{\mathbb{T}} \frac{\varphi(t)dt}{\varepsilon_f(-p-t) - z}$$

and  $Q^*$  is the adjoint of  $Q$ .

Using the substitution method, system (13) can be reduced into the form

$$\tilde{\varphi}_1 = Q(z)\tilde{\varphi}_1, \quad \text{i.e.,} \quad Q(z) = \lambda^2\Delta_1^{-1}\Delta_2^{-1}QQ^*. \tag{14}$$

Moreover, if  $\Phi = (\tilde{\varphi}_1, \tilde{\varphi}_2)$  is a solution to (13), then  $\tilde{\varphi}_1$  is an eigenfunction of  $Q(z)$  corresponding to the eigenvalue 1. Conversely, suppose that  $\tilde{\varphi}_1$  is an eigenfunction corresponding to the eigenvalue 1 of the operator  $Q(z)$ . Then  $\Phi = (\tilde{\varphi}_1, \tilde{\varphi}_2)$ , with  $\tilde{\varphi}_2 = \frac{\lambda}{\Delta(\lambda; z)}Q\tilde{\varphi}_1$  is a solution to (13) (i.e. (10)). Notice that the multiplicities of the linearly independent eigenvectors  $\tilde{\varphi}_1$  and  $\Phi$  coincide.

We also note that the function  $f$  defined in (11) is an eigenfunction of  $A_1(0)$  corresponding to an eigenvalue  $z \in \mathbb{C} \setminus \sigma_{ess}(A_1(0))$ . Moreover, the multiplicity of the eigenvalues  $z$  of  $A_1(0)$  is the same as the multiplicity of the eigenvalue  $\mu = 1$  of  $Q(z)$ .

The operator  $Q(z)$  is a convolution-type trace-class integral operator. The standard Fourier transform  $\mathcal{F}_1 : L^2(\mathbb{T}) \rightarrow \ell^2(\mathbb{Z})$ ,

$$(\mathcal{F}_1g)(n) = \frac{1}{(2\pi)^{\frac{1}{2}}} \int_{\mathbb{T}} e^{inp}g(p)dp, \quad g \in L^2(\mathbb{T}), \quad n \in \mathbb{Z},$$

establishes that  $\widehat{Q}(z) := \mathcal{F}_1Q(z)\mathcal{F}_1^*$  acts as a multiplication operator on the space  $\ell^2(\mathbb{Z})$  by the function

$$\kappa_n(z) = \frac{\lambda^2}{(\Delta(\lambda; z))^2}d_n(z)d_{-n}(z), \quad n \in \mathbb{Z}. \tag{15}$$

Thus, the spectrum of  $\widehat{Q}(z)$  consists of the following union

$$\sigma(\widehat{Q}(z)) = \{0\} \cup \bigcup_{n \in \mathbb{Z}} \{\kappa_n(z)\},$$

with the space of eigenfunctions

$$\hat{\varphi}_n(m) = \delta_{n,m}, \quad n, m \in \mathbb{Z},$$

where  $\delta_{\cdot, \cdot}$  is the Kronecker delta function on  $\mathbb{Z}$ .

Note that the compact operator  $Q(z)$  has eigenvalues  $\kappa_n(z), n \in \mathbb{Z}$  with the corresponding eigenfunctions

$$\psi_n(p) = e^{inp}, \quad n \in \mathbb{Z}, \quad p \in \mathbb{T}.$$

Therefore, the determinant of the operator  $I - Q(z)$  can be written as the following product

$$\det(I - Q(z)) = \prod_{n \in \mathbb{Z}} (1 - \kappa_n(z)), \tag{16}$$

which takes the form (7), since  $d_{-n}(z) = d_n(z)$  and (15).

Let  $\kappa_n(z_n) = 1$  be an eigenvalue of  $Q(z_n)$ , then  $\psi_n$  is the first component of the solution  $\varphi_n = (\psi_n, \tilde{\psi}_n)$  of equation (10), and the second component is defined as

$$\tilde{\psi}_n(q) := \tilde{\varphi}_2(q) = \lambda \Delta_2^{-1} Q^* \psi_n(q) = \frac{\lambda d_n(z_n)}{\Delta(\lambda; z_n)} \tilde{\psi}_{-n}(q). \tag{17}$$

Using the equality (12) in the last relation, we get

$$e^{i(n,q)} = \lambda \Delta_2^{-1} Q^* \psi_n(q) = \frac{\lambda d_n(z_n)}{\Delta(\lambda; z_n)} e^{-i(n,q)},$$

which is a contradiction.

However, if  $\vartheta_n(p) = (e^{i(n,p)} + e^{-i(n,p)})/2 = \cos((n, p))$ , it satisfies (12) and (17) if and only if

$$\frac{\lambda d_n(z_n)}{\Delta(\lambda; z_n)} = 1, \quad \text{i.e.} \quad \Delta_n^+(\lambda; z) = 1 - \lambda(d_0(z_n) + d_n(z_n)) = 0.$$

However, for the functions  $\theta_n(p) = (e^{i(n,p)} - e^{-i(n,p)})/2i = \sin((n, p))$  the relation

$$\theta_n = \lambda \Delta_2^{-1} Q^* \theta_n = -\frac{\lambda d_n(z_n)}{\Delta(\lambda; z_n)} \theta_n,$$

holds, which contradicts with (12). It implies

$$-\frac{\lambda d_n(z_n)}{\Delta(\lambda; z_n)} = 1, \quad \text{i.e.} \quad \Delta_n^-(\lambda; z) = 1 - \lambda(d_0(z_n) - d_n(z_n)) = 0.$$

Since the system  $\{\vartheta_n, \theta_n\}$ ,  $n \in \mathbb{Z}$  is complete in  $\ell^2(\mathbb{Z})$ , the last three relations and (15) allow us to use the Fredholm determinant (7) instead of (16).

Subsequently, the number  $z_n$  is an eigenvalue of  $A_1(0)$  and the corresponding eigenfunction can be found by (11) as

$$f_n^0 = R_0(z_n) [\lambda \varphi_1^* \psi_n + \lambda \varphi_2^* \tilde{\psi}_n],$$

i.e.,

$$f_n^0(p, q) = \frac{\lambda}{\varepsilon_f(-p - q) - z} (\cos(np) + \cos(nq)).$$

According to the relation  $H(0) = U_K^* H(K) U_K$ , the number  $z_n$  is also an eigenvalue of  $H(K)$  with the eigenfunction  $f_n = U_K f_n^0$  in (8), where the unitary operator  $U_K$  is defined in (5). □

**Remark 4.4.** Since  $\Delta_n^+(\lambda; z)$  is even with respect to  $n \in \mathbb{Z}$ , then  $z_n = z_{-n}$ , where  $z_n$  is a zero of  $\Delta_n^+(\lambda; z)$ , and eigenfunctions (8) are same.

**Lemma 4.5.** For any fixed  $n \in \mathbb{Z}$ , the function  $d_0(z) + d_n(z)$  is positive and monotonically increasing in the interval  $(-\infty, 0)$  as a function of  $z$ .

Additionally,

$$\lim_{z \rightarrow 0^-} (d_0(z) + d_n(z)) = \infty, \tag{18}$$

$$\lim_{z \rightarrow -\infty} (d_0(z) + d_n(z)) = 0. \tag{19}$$

and for any  $z \in (-\infty, 0)$

$$\lim_{n \rightarrow \infty} d_n(z) = 0 \tag{20}$$

hold.

*Proof.* The equalities

$$d_n(z) = \frac{1}{2\pi} \int_{\mathbb{T}} \frac{\cos nt}{\varepsilon_f(t) - z} dt$$

and

$$d_0(z) + d_n(z) = \frac{1}{2\pi} \int_{\mathbb{T}} \frac{1 + \cos nt}{\varepsilon_f(t) - z} dt$$

imply the positivity and monotonicity of  $d_0(z) + d_n(z)$  in  $(-\infty, 0)$ .

The limits (18), (19) and (20) follow from Lemma 4.2. □

**4.3. Eigenvalues of  $H(K)$  below  $[0, 2/m]$**

Let  $z_1^0$  be a zero of  $\Delta_\alpha(\cdot) = 0$ , i.e. an eigenvalues of  $h_1(k)$  in the interval  $\mathbb{R} \setminus [0, 6/m]$  (see Lemma 2.1).

**Lemma 4.6.** (a) Let  $\lambda > 0$ . Then  $\Delta_n^+(\lambda; z)$  has a unique zero  $z_n$  in  $(-\infty, 0)$  such that  $z_n < z_1^0 < 0$ . Moreover,  $z_n < z_m$  if  $|m| > |n|$ .

(b) The following limit

$$\lim_{n \rightarrow \infty} z_n = z_1^0 \tag{21}$$

holds.

*Proof.* (a) Since  $\Delta_n^+(\lambda; z)$  is symmetric about the interval  $[0, 2/m]$ , we prove part (a). According to Lemma 4.5, the function  $\Delta_n^+(\lambda; z)$  is monotonically increasing in  $(-\infty, 0)$  and

$$\begin{aligned} \lim_{z \rightarrow -\infty} \Delta_n^+(\lambda; z) &= 1, \\ \Delta_n^+(\lambda; z_1^0) &< \Delta(\lambda; z_1^0) = 0, \end{aligned}$$

holds.

Consequently, the function  $\Delta_n^+(\lambda; z)$  has a unique zero  $z_n$  in the interval  $(-\infty, z_1^0)$  if  $\lambda > 0$ .

If  $|n| < |m|$ , then Lemma 4.2 implies that  $\Delta_n^+(\lambda; z) < \Delta_m^+(z)$  and hence  $\Delta_n^+(\lambda; z_m) < \Delta_m^+(z_m) = 0$ . The last equality provides the inequality  $z_n < z_m$ .

(b) The equalities

$$\begin{aligned} \Delta_n^+(\lambda; z_1^0) &= (\Delta_n^+(\lambda; \xi_n))'(z_1^0 - z_n), \\ \Delta_n^+(\lambda; z_1^0) &= -\lambda d_n(z_1^0), \\ (\Delta_n^+(\lambda; z))' &= -\lambda(d_0'(z) + d_n'(z)), \end{aligned}$$

where  $z_n < \xi_n < z_1^0$  is a number obtained due to the intermediate value theorem, imply

$$z_n - z_1^0 = -\frac{d_n(z_1^0)}{d_0'(\xi_n) + d_n'(\xi_n)}.$$

By Lemma 4.6, the inequality  $z_0 \leq z_n < \xi_n < z_1^0$  and the monotonicity of the derivative of  $(\Delta_n^+(\lambda; z))'$ ,

$$(\Delta_n^+(\lambda; z_0))' \geq (\Delta_n^+(\lambda; \xi_n))' \geq (\Delta_n^+(\lambda; z_1^0))'$$

Applying the limit (20) in the last inequality, we get the proof of the limit in (21). □

**4.4. Eigenvalues of  $H(K)$  above  $[0, 2/m]$**

The unitary operator  $U_{\pi/2}$  in (5) is used to establish the equalities

$$U_{\pi/2}H_0(K)U_{\pi/2} = \frac{2}{m} - H_0(K) \quad \text{and} \quad U_{\pi/2}VU_{\pi/2} = V$$

which implies the relation

$$U_{\pi/2}(H_0(K) - V)U_{\pi/2} = \frac{2}{m} - (H_0(K) + V). \tag{22}$$

The final relationship enables us to shift the investigation of the eigenvalues of  $H(K)$  from above the interval  $[0, 2/m]$  to below it.

Note that  $z_n$  is a zero of  $\Delta_n^+(\lambda; z)$ ,  $n \in \mathbb{Z}$ , if it exists.

**Lemma 4.7.** Assume  $\lambda < 0$ .

(a) The function  $\Delta_n^+(\lambda; z)$  has a unique zero  $z_n$  in  $(2/m, \infty)$  such that  $2/m < z_1^0 < z_n$ . Moreover,  $z_n > z_m$  if  $|m| > |n|$ .

(b) The following limit

$$\lim_{n \rightarrow \infty} z_n = z_1^0$$

holds.

*Proof.* The proof is a consequence of Lemma 4.6 and the identity (22). □

## 5. Main theorem

Recall that  $z_1^0$  be a zero of  $\Delta(\lambda; \cdot) = 0$ , i.e. an eigenvalues of  $h_1(k)$ , and  $z_1^0 < 0$  if  $\lambda > 0$  and  $2/m < z_1^0$  if  $\lambda < 0$ . Let  $\eta$  be an eigenvalue of  $H(K)$  mentioned in Lemma 4.1.

Now, we are ready to formulate the main result of the paper.

**Theorem 5.1.** Assume  $\mu \in \mathbb{R}$  and  $\lambda \in \mathbb{R}$ . (a) Let  $\lambda < 0$ . Then

$$\sigma_{pp}(H(K)) = \bigcup_{n \in \mathbb{Z}} \{z_n\} \cup \{\eta\},$$

where  $2/m < z_1^0 < z_n$  and  $2/m - \mu < \eta$ .

(b) Let  $\lambda = 0$ . Then

$$\sigma_{pp}(H(K)) = \emptyset.$$

(c) Let  $0 < \lambda$ . Then

$$\sigma_{pp}(H(K)) = \bigcup_{n \in \mathbb{Z}} \{z_n\} \cup \{\eta\},$$

and  $z_n < z_1^0 < 0$  and  $\eta < -\mu$ .

*Proof.* Lemmas 4.1, 4.6 and 4.7 provide the proof. For example, by combining the assertions (a) in Lemma 4.1 and (a) in Lemma 4.7, we get the proof of the part (a) of the theorem.  $\square$

**Remark 5.2.** According to Lemma 3.2

$$\sigma_{ess}(H(K)) = \{z_1^0\} \cup \left( [-\mu, 2/m - \mu] \cup [0, 2/m] \right).$$

Theorem 5.1 demonstrates that  $z_n$  or  $\eta$  could be within  $\sigma_{ess}(H(K))$  or within a gap of the essential spectrum.

## 6. Conclusion

The discrete Schrödinger operator corresponding to the Hamiltonian of a system of three quantum particles (two identical bosons and a fermion) with masses  $m = \infty$  and  $m < \infty$ , respectively, is considered on the one-dimensional lattice for all non-zero point interactions. The point spectrum of the three-particle discrete Schrödinger operator, which possesses infinitely many eigenvalues, has been studied for all non-zero point interactions.

## References

- [1] Winkler K. et al. Repulsively bound atom pairs in an optical lattice. *Nature*, 2006, **441**, P. 853–56.
- [2] Bloch I. Ultracold quantum gases in optical lattices. *Nat. Phys.*, 2005, **1**, P. 23–30.
- [3] Jaksch D. and Zoller P. The cold atom Hubbard toolbox. *Ann. of Phys.*, 2005, **315**(1), P. 52–79.
- [4] Thalhammer G. et al. Inducing an optical Feshbach resonance via stimulated Raman coupling. *Phys. Rev. A.*, 2005, **71**, P. 033403.
- [5] Hofstetter W., et al. High-temperature superfluidity of fermionic atoms in optical lattices. *Phys. Rev. Lett.*, 2002, **89**, P. 220407.
- [6] Lewenstein M. et al. Atomic Bose-Fermi mixtures in an optical lattice. *Phys. Rev. Lett.*, 2004, **92**, P. 050401.
- [7] Efimov V.N. Energy levels arising from resonant two-body forces in a three-body system. *Physics Letters.*, 1970, **33**(8), P. 563–564.
- [8] Yafaev D. On the theory of the discrete spectrum of the three-particle Schrödinger operator. *Math. USSR-Sb.*, 1974, **23**, P. 535–559.
- [9] Lakaev S.N. The Efimov's effect of a system of three identical quantum lattice particles. *Funct. Anal. Its Appl.*, 1993, **27**, P. 15–28.
- [10] Lakaev S.N. and Muminov Z.I. The Asymptotics of the Number of Eigenvalues of a Three-Particle Lattice Schrödinger Operator. *Funct. Anal. Appl.*, 2003, **37**, P. 228–231.
- [11] Abdullaev Zh.I. and Lakaev S.N. Asymptotics of the Discrete Spectrum of the Three-Particle Schrödinger Difference Operator on a Lattice. *Theor. Math. Phys.*, **136**, P. 1096–1109.
- [12] Albeverio S., Lakaev S.N., Muminov Z.I. "Schrödinger operators on lattices. The Efimov effect and discrete spectrum asymptotics. *Ann. Inst. H. Poincaré Phys. Theor.*, 2004, **5**, P. 743–772.
- [13] Dell'Antonio G., Muminov Z.I., Shermatova Y.M. On the number of eigenvalues of a model operator related to a system of three-particles on lattices. *J. Phys. A: Math. Theor.*, 2011, **44**, P. 315302.
- [14] Khalkhuzhaev A.M., Abdullaev J.I., Boymurodov J.K. The Number of Eigenvalues of the Three-Particle Schrödinger Operator on Three Dimensional Lattice. *Lob. J. Math.*, 2022, **43**(12), P. 3486–3495.
- [15] Muminov M., Aliev N. Discrete spectrum of a noncompact perturbation of a three-particle Schrödinger operator on a lattice. *Theor. Math. Phys.*, 2015, **182**(3), P. 381–396.
- [16] Muminov Z.I., Aliev N.M., Radjabov T. On the discrete spectrum of the three-particle Schrödinger operator on a two-dimensional lattice. *Lob. J. Math.*, 2022, **43**(11), P. 3239–3251.
- [17] Aliev N.M. Asymptotic of the Discrete Spectrum of the Three-Particle Schrödinger Operator on a One-Dimensional Lattice. *Lob. J. Math.*, 2023, **44**(2), P. 491–501.
- [18] Komarov I.V., Ponomarev L.I., and Slavnyanov S.Yu. Spheroidal and Coulomb Spheroidal Functions [in Russian]. Nauka, Moscow, 1976.
- [19] Rabinovich V.S., Roch S. The essential spectrum of Schrödinger operators on lattice. *J. Phys. A: Math. Gen.*, 2006, **39**, P. 8377.
- [20] Albeverio S., Lakaev S., Muminov Z. On the structure of the essential spectrum for the three-particle Schrödinger operators on lattices. *Math. Nachr.*, 2007, **280**, P. 699–716.
- [21] Kholmatov Sh.Yu., Muminov Z.I. The essential spectrum and bound states of  $N$ -body problem in an optical lattice. *J. Phys. A: Math. Theor.*, 2018, **51**, P. 265202.
- [22] Muminov Z., Lakaev Sh. Aliev N. On the Essential Spectrum of Three-Particle Discrete Schrödinger Operators with Short-Range Potentials. *Lob. J. Math.*, 2021, **42**(6), P. 1304–1316.

- [23] Lakaev S.N., Boltaev A.T. The Essential Spectrum of a Three Particle Schrödinger Operator on Lattices. *Lob. J. Math.*, 2023, **44**(3), P. 1176–1187.  
[24] Jakubaba-Amundsen D.H. The HVZ Theorem for a Pseudo-Relativistic Operator. *Ann. Henri Poincaré*, 2007, **8**, P. 337–360.
- 

*Submitted 18 April 2024; revised 21 June 2024; accepted 26 June 2024*

*Information about the authors:*

*Zahridin I. Muminov* – Tashkent State University of Economics, 100066, Tashkent, Uzbekistan; Institute of Mathematics named after V.I.Romanovsky, 100174, Tashkent, Uzbekistan; ORCID 0000-0002-7201-6330; zimuminov@gmail.com

*Vasila U. Aktamova* – Samarkand Institute of Veterinary Medicine, 140103, Samarkand, Uzbekistan; ORCID 0009-0000-6587-0021; vaktamova@mail.ru

*Conflict of interest:* the authors declare no conflict of interest.

## The Cauchy problem for a high-order wave equation with a loaded convolution type

Praveen Agarwal<sup>1,2,a</sup>, Umida Baltaeva<sup>3,4,b</sup>, Umrbek Madrakhimov<sup>4,c</sup>, Jamol I. Baltaev<sup>5,d</sup>

<sup>1</sup>Department of Mathematics, Anand International College of Engineering, Jaipur, India

<sup>2</sup>Nonlinear Dynamics Research Center (NDRC), Ajman University, Ajman, UAE

<sup>3</sup>Department of Exact sciences, Khorezm Mamun Academy, Khiva, Uzbekistan

<sup>4</sup>Department of Applied Mathematics and Mathematical Physics, Urgench State University, Urgench, Uzbekistan

<sup>5</sup>Department of Technology, RANCH University of Technology, Urgench, Uzbekistan

<sup>a</sup>[goyal.praveen2011@gmail.com](mailto:goyal.praveen2011@gmail.com), <sup>b</sup>[umida.baltayeva@mail.ru](mailto:umida.baltayeva@mail.ru), <sup>c</sup>[us.madrakhimov@gmail.com](mailto:us.madrakhimov@gmail.com),

<sup>d</sup>[jamol.06@yahoo.com](mailto:jamol.06@yahoo.com)

Corresponding author: Umida Baltaeva, [umida.baltayeva@mail.ru](mailto:umida.baltayeva@mail.ru)

**ABSTRACT** The present paper is devoted to the problem for one of the loaded wave integro-differential equations, which is equivalent to the nonlocal problem for a higher-order wave equation. The study aims at nonlocal problems and constructs a representation of the solution to the problem for an equation of hyperbolic type. Also, the paper provides examples of some cases where it will be possible to construct solutions to the problem explicitly and in the graphs.

**KEYWORDS** Integro-differential equation, Cauchy problem, loaded equation, nonlocal problem.

**FOR CITATION** Praveen Agarwal, Umida Baltaeva, Umrbek Madrakhimov, Jamol I. Baltaev The Cauchy problem for a high-order wave equation with a loaded convolution type. *Nanosystems: Phys. Chem. Math.*, 2024, **15** (4), 448–456.

### 1. Introduction

In recent years, differential equations with an integral term and high-order integro-differential equations have been of great interest from the point of view of mathematical engineering, mathematical physics, and chemical reaction-diffusion models. For example, various problems of mathematical engineering, chemical reaction-diffusion models, fundamental and applied physics such as fluid dynamics, beam theory, gas dynamics [1–4], nanoscience [5–7], and various problems of the theory of elasticity, plates, and shells are reduced to such equations (see [8–15] and the references therein).

Equations of the convolution type with the integro-differential operators arise in mathematical models of physical and technical systems where it is necessary to take into account the history of the processes. Constitutive relations in a linear processes of inhomogeneous diffusion and propagation of waves with memory contain a time- and space-dependent memory kernel. Problems of memory kernels [16, 17] identification in parabolic and hyperbolic integro-differential equations have been intensively studied.

In many cases, the equations describing the propagation of electrodynamic and elastic waves are reduced to hyperbolic equations with integral convolution [18–23]. Determination of time- and space-dependent kernels in parabolic integro-differential equations were investigated [24] (see, for example, [25] and references therein).

Various initial, boundary, and non-classical problems for loaded partial differential equations [26] have been studied in many works. We note recent research works [27–35], where there were studies of actual problems for the loaded partial differential and integro-differential equations of classical and mixed types. But we must note that problems for loaded differential and partial differential equations involving convolution types have not been investigated yet.

Proceeding from this, we study an analog of the Cauchy problem for a high-order loaded-wave equation with convolution-type operators in the multidimensional domain. The study is targeted on construction of optimal representations for the solution of the hyperbolic type equation and investigation of the existence and uniqueness of the solution to the Cauchy problem for the loaded differential equation. Representation of a higher-order partial differential operator in the form of a convolution type operator makes it possible, in particular, to reduce the problem of the propagation of electrodynamic and elastic waves and apply the methods of the theory of loaded differential equations.

**2. Statement of the problem and its nonlocality**

We consider the following loaded integro-differential equation of high order

$$L^m(u) \equiv \left( \frac{\partial^2}{\partial t^2} - A \right)^m u(x, t) = f(x, t) + \mu \int_0^t k(x, \tau) u(0, t - \tau) d\tau, \quad (x, t) \in \Omega, \tag{2.1}$$

where  $k(x, t), f(x, t)$  are given real-valued sufficiently smooth functions,  $A$  is a linear differential operator acting on variables  $x(x_1, x_2, \dots, x_n), L^m = L^1(L^{m-1}), m \in N, \mu$  is given real parameter.

$\Omega$  is the domain of the solutions of problem, depending on the form of the operator  $A$ .

$$\Omega = \{(x, t) : x \in R^n, 0 < t < +\infty\}.$$

In the domain  $\Omega$ , we study the following problem.

**Cauchy problem.** Find a solution  $u(x, t)$  of equation (2.1) from the class of functions:

$$W = \{u(x, t) : u(x, t) \in C^{2m-1}(\overline{\Omega}) \cap C^{2m}(\Omega)\},$$

that satisfies the initial conditions

$$\frac{\partial^k u}{\partial t^k} \Big|_{t=0} = 0, \quad k = \overline{0, 2m-1}. \tag{2.2}$$

The inhomogeneous problem (2.1) - (2.2) for  $\mu = 0$  was studied in [11], [36] but has not yet been studied for  $\mu \neq 0$ . The following theorem is true.

**Theorem 2.1.** Let function  $\tilde{u}(x, t, t_1)$  depending on parameter  $t_1$ , be a solution of the equation

$$L^m(\tilde{u}) \equiv \left( \frac{\partial^2}{\partial t^2} - A \right)^m \tilde{u}(x, t, t_1) = 0, \quad t > t_1, \tag{2.3}$$

satisfying the initial and nonlocal conditions

$$\frac{\partial^k \tilde{u}}{\partial t^k} \Big|_{t=t_1} = 0, \quad \frac{\partial^{2m-1} \tilde{u}}{\partial t^{2m-1}} \Big|_{t=t_1} = f(x, t_1) + \mu \int_0^{t_1} ds \int_0^{t_1-s} k(x, z) \tilde{u}(0, t_1 - z, s) dz, \tag{2.4}$$

for  $k = \overline{0, 2m-2}$ , then function

$$u(x, t) = \int_0^t \tilde{u}(x, t, t_1) dt_1, \quad (x, t) \in \Omega, \quad t > t_1, \tag{2.5}$$

is a solution of the problem (2.1) and (2.2).

Proof of Theorem 2.1. Initially, let us differentiate expressions (2.5) twice in respect to  $t$  and, taking into account (2.4), we obtain

$$\frac{\partial^2 u}{\partial t^2} = \tilde{u}_t(x, t, t_1) \Big|_{t_1=t} + \int_0^t \tilde{u}_{tt}(x, t, t_1) dt_1 = \int_0^t \tilde{u}_{tt}(x, t, t_1) dt_1, \tag{2.6}$$

On the other hand, applying the operator  $A$  to this equality (2.5), we obtain

$$A(u(x, t)) = \int_0^t A(\tilde{u}(x, t, t_1)) dt_1, \quad (x, t) \in \Omega. \tag{2.7}$$

Therefore, subtracting the resulting equality (2.7) from (2.6), we can easily obtain the first operator function

$$L^1(u) \equiv \left( \frac{\partial^2}{\partial t^2} - A \right) u(x, t) = \int_0^t L^1(\tilde{u}(x, t, t_1)) dt_1. \tag{2.8}$$

Continuing to repeat this process up to  $m - 1$  and taking into account conditions (2.4), we come to the expression

$$L^{m-1}(u) = \int_0^t L^{m-1}(\tilde{u}(x, t, t_1)) dt_1. \tag{2.9}$$

Hence, differentiating the last expression in respect to  $t$  up to the second order and taking (2.2) into account, we have

$$\frac{\partial^2}{\partial t^2} L^{m-1}(u) = \frac{\partial}{\partial t} \left( \frac{\partial^2}{\partial t^2} - A \right)^{m-1} \tilde{u}(x, t, t_1) \Big|_{t_1=t} + \int_0^t \frac{\partial^2}{\partial t^2} L^{m-1}(\tilde{u}(x, t, t_1)) dt_1 =$$

$$= f(x, t) + \mu \int_0^t ds \int_0^{t-s} k(x, z) \tilde{u}(0, t-z, s) dz + \int_0^t \frac{\partial^2}{\partial t^2} L^{m-1}(\tilde{u}(x, t, t_1)) dt_1. \tag{2.10}$$

Applying the operator  $A$  to the function  $L^{m-1}(u)$  and then subtracting the result obtained from (2.10), due to (2.9), (2.3) and  $L^m(\tilde{u}) = 0$ , we have

$$(\partial^2/\partial t^2 - A) L^{m-1}(u) = \mu \int_0^t k(x, t_1) u(0, t-t_1) dt_1 + f(x, t).$$

Also, one can easily make sure that the function  $u(x, t)$ , defined by equality (2.5), satisfies the initial condition (2.2) which was to be proved. Thus, the theorem 2.1 is proved.

By introducing a new variable,  $\tau = t - t_1$ , the equations (2.3) - (2.4) can be reduced to the problem:

$$L^m(\tilde{u}) \equiv \left( \frac{\partial^2}{\partial t^2} - A \right)^m \tilde{u} = 0, \quad \tau > 0, \tag{2.11}$$

$$\frac{\partial^k \tilde{u}}{\partial \tau^k} \Big|_{\tau=0} = 0, \quad \frac{\partial^{2m-1} \tilde{u}}{\partial \tau^{2m-1}} \Big|_{\tau=0} = f(x, t_1) + \mu \int_0^{t_1} ds \int_s^{t_1} k(x, t_1 - z) \tilde{u}(0, z, s) dz, \tag{2.12}$$

for  $k = \overline{0, 2m-2}$ ,  $\tau > 0$ . Consequently, by solving the problem (2.11) - (2.12) and again passing to the variables introduced at the beginning of the section, we can find the required function  $\tilde{u}(x, t, t_1)$ . Thus, from formula (2.5), we restore the solution of the problem (2.1) - (2.2).

In studying equation (2.11) concerning nonlocal terms, it becomes necessary to use the spherical means wave equation. The problem under consideration refers to a loaded wave equation involving convolution-type operators, for which the spherical mean method has not yet been studied.

**3. Solutions of the problem on  $R^1$**

Let  $n = 1$ ,  $A = \partial^2/\partial x^2$ . Find a solution  $u(x, t)$  of equation

$$\left( \frac{\partial^2}{\partial t^2} - \frac{\partial^2}{\partial x^2} \right)^m u(x, t) = f(x, t) + \mu \int_0^t k(x, \tau) u(0, t-\tau) d\tau, \quad (x, t) \in \Omega, \tag{3.1}$$

from the class of functions  $W$  that satisfies the initial conditions

$$u(x, t)|_{t=0} = \frac{\partial u(x, t)}{\partial t} \Big|_{t=0} = \frac{\partial^2 u(x, t)}{\partial t^2} \Big|_{t=0} = \dots = \frac{\partial^{2m-1} u(x, t)}{\partial t^{2m-1}} \Big|_{t=0} = 0, \tag{3.2}$$

where  $k(x, t)$ ,  $f(x, t)$  are given real-valued functions.

We introduce the following notations

$$v_0(x, t, \tau) = \tilde{u}(x, t, \tau), \quad v_1(x, t, \tau) = L_1 v_0(x, t, \tau), \dots, v_{m-1}(x, t, \tau) = L_{m-1} v_0(x, t, \tau). \tag{3.3}$$

Thus, considering the loaded part analogously to [28], one reduces problem (2.11) - (2.12) to the following system for the functions  $v_k(x, t, t_1)$

$$\begin{cases} \frac{\partial^2 v_0}{\partial t^2} - \frac{\partial^2 v_0}{\partial x^2} = v_1, \\ \frac{\partial^2 v_1}{\partial t^2} - \frac{\partial^2 v_1}{\partial x^2} = v_2, \\ \dots\dots\dots \\ \frac{\partial^2 v_{m-2}}{\partial t^2} - \frac{\partial^2 v_{m-2}}{\partial x^2} = v_{m-1}, \\ \frac{\partial^2 v_{m-1}}{\partial t^2} - \frac{\partial^2 v_{m-1}}{\partial x^2} = 0, \end{cases} \tag{3.4}$$

and initial conditions

$$v(x, t, t_1)|_{t=0} = \frac{\partial v_k(x, t, t_1)}{\partial t} \Big|_{t=0} = 0, \dots, \frac{\partial v_{m-1}}{\partial t} \Big|_{t=0} = g_{m-1}(x, t_1), \tag{3.5}$$

where

$$g_{m-1} = \sum_{j=0}^{m-1} (-1)^j c_k^j (f^{(j)}(x, t_1) + \mu \int_0^{t_1} ds \int_s^{t_1} k(x, t_1 - z) v_0^{(j)}(0, z, s) dz), \quad c_k^j = k!/[j!(k-j)!]$$

is the binomial coefficient. Hence, by applying the classical method of spherical means [37] analogously to work [11], we can find the solution to the problem (2.1)-(2.2).

Consequently, after determining the solution to the problem (3.4) - (3.5) by (3.11) from [36] and using the introduced notation (3.3), the solution to the problem (2.11) - (2.12) can be written as:

$$\begin{aligned} \tilde{u}(x, t, t_1) = & 2^{-2m+1} \int_{x-(t-t_1)}^{x+(t-t_1)} k_1(x, s, t-t_1) f(s, t_1) ds + \\ & + 2^{-2m+1} \mu \int_{x-(t-t_1)}^{x+(t-t_1)} k_1(x, s, t-t_1) \int_0^{t_1} dz \int_z^{\tau} k(x, t_1-\eta) \tilde{u}(0, \eta, z) d\eta ds, \end{aligned} \tag{3.6}$$

where  $k_1(x, s, t) = [(t^2 - (s-x)^2)]^{m-1} / [(m-1)!]^2$ .

Substituting the obtained function into (2.5), we find the solution to the problem (2.1), and (2.2) in the following form:

$$\begin{aligned} u(x, t) = & 2^{-2m+1} \mu \int_0^t dt_1 \int_{x-(t-t_1)}^{x+(t-t_1)} k_1(x, s, t-t_1) ds \int_0^{t_1} k(s, t_1-z) u(0, z) dz + \\ & + 2^{-2m+1} \int_0^t dt_1 \int_{x-(t-t_1)}^{x+(t-t_1)} k_1(x, s, t-t_1) f(s, t_1) ds. \end{aligned} \tag{3.7}$$

The resulting expressions (3.6) and (3.7) are represented as loaded integral equations concerning the unknown functions  $\tilde{u}(x, t, t_1)$  and  $u(x, t)$ , respectively. Therefore, to solve the integral equation (3.7), we put  $x = 0$ :

$$u(0, t) - \mu \int_0^t K(0, t, \tau) u(0, \tau) d\tau = \tilde{f}(0, t), \tag{3.8}$$

where

$$\begin{aligned} K(0, t, \tau) = & \frac{\mu}{2^{2m-1}} \int_{\tau}^t dz \int_{-(t-z)}^{(t-z)} k(s, z-\tau) k_1(0, s, t-\tau) ds, \\ \tilde{f}(x, t) = & \frac{1}{2^{2m-1}} \int_0^t dz \int_{x-(t-z)}^{x+(t-z)} k_1(x, s, t-z) f(s, z) ds. \end{aligned}$$

Hence, taking into account the notation  $k_1(x, s, t-\tau)$  and some changes of variables, it is easy to verify that:

$$\begin{aligned} \left| \tilde{f}(x, t) \Big|_{x=0} \right| &= \left| \frac{1}{2^{2m-1}} \int_0^t dz \int_{-(t-z)}^{(t-z)} k_1(0, s, t-z) f(s, z) ds \right| \leq \\ &\leq \left| \frac{C}{2^{2m-1} [(m-1)!]^2} \int_0^t (t-z)^{2m-1} dz \int_{-1}^1 (1-s^2)^{m-1} ds \right| \leq \\ &\leq \left| \frac{C}{(2m-1)!} \int_0^t (t-z)^{2m-1} dz \right| \leq \left| C \frac{t^{2m}}{(2m)!} \right|. \end{aligned} \tag{3.9}$$

Considering  $k(x, t) \in H^{l, l/2}(\Omega)$  analogously, we obtain  $|K(0, t, \tau)| \leq C |(t-\tau)^{2m}|$ , at  $m \geq 1$ .

Thus, we can write the solutions of equation (3.8) in the form:

$$u(0, t) = \tilde{f}(0, t) + \mu \int_0^t R(0, t, \tau) \tilde{f}(0, \tau) d\tau, \tag{3.10}$$

where  $R(0, t, \tau)$  is the resolvent of the kernel  $K(0, t, \tau)$ . The solution (3.8), according to the theory of integral equations, can be easily verified that it is unique in a class of functions that can have a weak singularity.

Thus, from formula (3.7), taking into account (3.10), we can write an explicit form of the solution to the problem (2.1) - (2.2).

**4. Examples**

This section of the work is devoted to the study of the obtained results, giving several examples confirming the validity of the conclusions, from a numerical perspective. Note that the problems under consideration are illustrated by figures with limited solution parameters, which can be continued further.

Example 4.1. Find the solution  $u(x, t)$  of the Cauchy problem in the class of functions

$$W = \{u(x, t) : u(x, t) \in C^1(\bar{\Omega}) \cap C^2(\Omega)\},$$

for the equation

$$u_{tt}(x, t) - u_{xx}(x, t) = t - x + \int_0^t u(0, t - s) ds, \quad (x, t) \in \Omega, \tag{4.1}$$

with the initial conditions

$$u(x, t)|_{t=0} = u_t(x, t)|_{t=0} = 0, \tag{4.2}$$

where  $\Omega = \{(x, t) : x \in R, t > 0\}$ .

In this case, for  $k(x, t) \equiv 1$ , taking into account the following replacement,  $s = x + (t - \tau)s'$ , and some properties of special functions, we have

$$\begin{aligned} K(0, t, \tau) &= \frac{\mu}{2^{2m-1}[(m-1)!]^2} \int_{\tau}^t (t-z)^{2m-1} dz \int_{-1}^1 (1-s^2)^{m-1} ds = \\ &= \frac{\mu}{2^{2m-1}[(m-1)!]^2} \int_{\tau}^t (t-z)^{2m-1} dz \int_0^1 (1-s)^{-\frac{1}{2}} s^{m-1} ds = \\ &= \frac{\mu}{2^{2m-1}[(m-1)!]^2} B(m, 1/2) \int_{\tau}^t (t-z)^{2m-1} dz = \frac{\mu(t-\tau)^{2m}}{2m!}. \end{aligned} \tag{4.3}$$

Hence, taking into account the method of successive approximations, we can conclude that for  $k(x, t) \equiv 1$  and for any  $\mu$  there exists a resolvent of the kernel  $K(0, t, \tau)$  in the form

$$R(0, t, \tau) = \sum_{i=1}^{\infty} \left[ (t-\tau)^{(2m+1)i-1} \right] / [((2m+1)i-1)!]. \tag{4.4}$$

By the same method, it will be possible to find the explicit form of the resolvent in other cases from the kernel function  $k(x, t) \neq 1$ .

Thus, from (3.10), taking into account (4.4) at  $f(x, t) = -x + t$ , we have

$$u(0, t) = \sum_{i=0}^{\infty} \frac{t^{3i+3}}{(3i+3)!}.$$

Therefore, setting  $\mu = 1$ , we find the final solution of problem (4.1) and (4.2) in the form:

$$u(x, t) = \frac{t^3}{6} - \frac{xt^2}{2} + \sum_{i=0}^{\infty} \frac{t^{3i+6}}{(3i+6)!},$$

which is represented in Fig. 1.

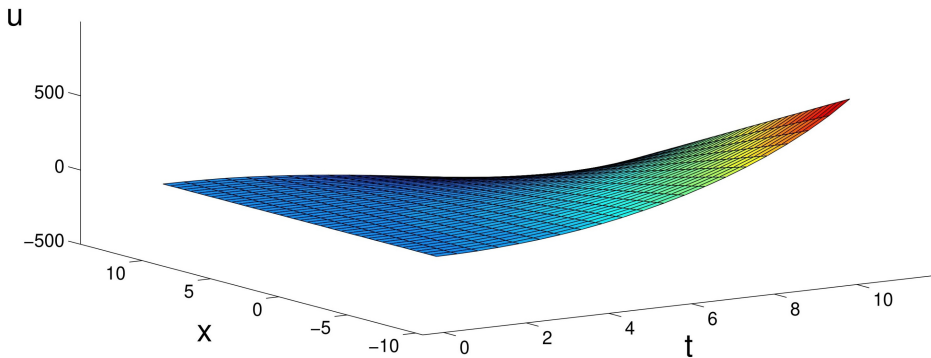


FIG. 1. The solution to the Example 4.1

Example 4.2. Find a solution  $u(x, t)$  of the Cauchy problem in the class of functions  $W$  for the equation

$$u_{tt}(x, t) - u_{xx}(x, t) = xt + \int_0^t su(0, t - s)ds, \tag{4.5}$$

with initial conditions (4.2).

If we substitute  $k(x, t) = t$ , first, we should find the solution of the integral equation (3.8). To find the solution, we should determine the kernel  $K(0, t, \tau)$  and its resolvent  $R(0, t, \tau)$ . Thus, the function  $K$  from the definition in equation (3.8) has the form

$$K(0, t, \tau) = \frac{\mu}{2^{2m-1}} \int_{\tau}^t (z - \tau) dz \int_{-(t-z)}^{(t-z)} k_1(0, s, t - \tau) ds,$$

Hence, similarly to (4.3), we obtain

$$K(0, t, \tau) = \frac{(t - \tau)^{2m+1}}{[(m + 1)!]}, \text{ if } k(x, t) = t. \tag{4.6}$$

From here, we can easily find the resolvent of the kernel (4.6) which has the form

$$R(0, t, \tau) = \sum_{i=1}^{\infty} (t - \tau)^{2i(m+1)-1} / (2i(m + 1) - 1)!. \tag{4.7}$$

Thus, similarly to example 4.1, we can find a solution to the problem (4.5) and (4.2), for  $m = 1, 2, \dots$ . If  $m=1$ , we can illustrate the explicit solution as

$$u(x, t) = \frac{xt^3}{3!} + \sum_{i=0}^{\infty} \frac{t^{4i+8}}{(4i + 8)!},$$

which is represented in Fig. 2.

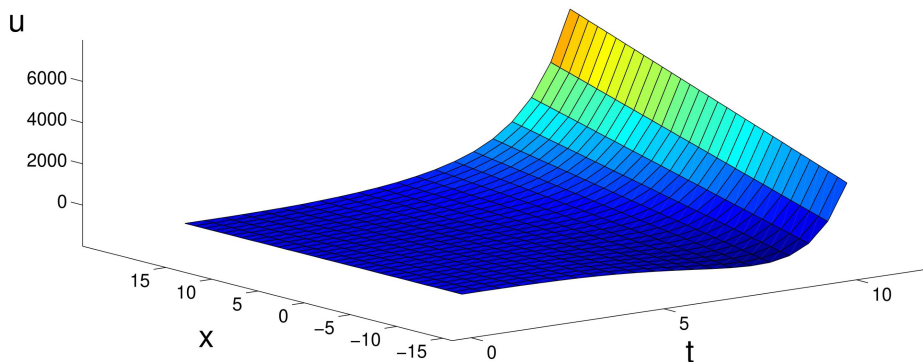


FIG. 2. The solution to the Example 4.2

The solution to the problem is found similarly, respectively, for the cases  $m = 2, 3, \dots$

Example 4.3. Find a solution  $u(x, t) \in C^3(\bar{\Omega}) \cap C^6(\Omega)$  of the Cauchy problem in  $\Omega \in R^2$ , for the equation

$$\left( \frac{\partial^2}{\partial t^2} - \frac{\partial^2}{\partial x^2} \right)^2 u(x, t) = xt + \int_0^t su(0, t - s)ds, \tag{4.8}$$

with initial conditions

$$u(x, t)|_{t=0} = u_t(x, t)|_{t=0} = u_{tt}(x, t)|_{t=0} = u_{ttt}(x, t)|_{t=0} = 0. \tag{4.9}$$

Similarly to examples 4.1 and 4.2, we can find solutions to the problem (4.8) - (4.9), for  $m = 1, 2, \dots$ . If  $m=1$  (for  $m = 2, 3, \dots$ , appropriately), we can illustrate the solution as

$$u(x, t) = \frac{xt^5}{5!} + \frac{3}{2} \sum_{i=0}^{\infty} \frac{t^{6i+12}}{(6i + 12)!},$$

which is represented in Fig. 3.

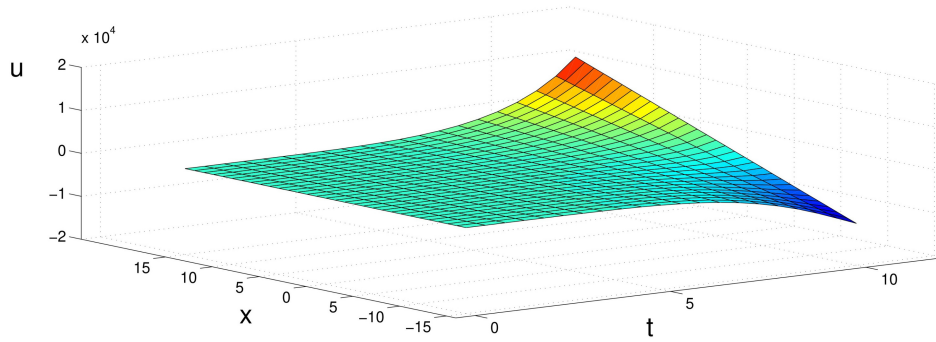


FIG. 3. The solution to the Example 4.3

**5. Solutions of the problem in  $R^3$**

Let  $n = 3$ ,  $A \equiv \sum_{i=1}^3 \partial^2 / \partial x_i^2$ . Find a solution  $u(x, t) = u(x_1, x_2, x_3, t)$  of equation

$$\left( \frac{\partial^2}{\partial t^2} - \left( \frac{\partial^2}{\partial x_1^2} - \frac{\partial^2}{\partial x_2^2} - \frac{\partial^2}{\partial x_3^2} \right) \right)^m u(x, t) = f(x, t) + \mu \int_0^t k(x, s)u(0, t - s)ds, \tag{5.1}$$

from the class  $W$  of functions that satisfies the initial conditions (2.2), where  $k(x, t)$ ,  $f(x, t)$  are given smooth functions.

When considering problem (5.1) - (2.2), which equivalently reduces to problem (2.11) - (2.12) as  $A \equiv \sum_{i=1}^3 \partial^2 / \partial x_i^2$  [34], using the methods of spherical means [37], we have

$$\begin{aligned} \tilde{u}(x, t, t_1) &= \frac{1}{2^{2m-1}\pi} \int_{|\xi-x| \leq t-t_1} K_1(x, \xi, t-t_1) f(\xi, t_1) d\xi + \\ &+ \frac{\mu}{2^{2m-1}\pi} \int_{|\xi-x| \leq t-t_1} K_1(x, \xi, t-t_1) d\xi \int_0^{t_1} ds \int_s^{t_1} k(\xi, t_1-z) \tilde{u}(0, z, s) dz, \end{aligned} \tag{5.2}$$

$K_1(x, \xi, t) = [t^2 - |\xi - x|^2]^{m-2} / [(m-2)!(m-1)!]$ ,  $|\xi - x|^2 = \sum_{k=1}^3 (\xi_k - x_k)^2$ . Therefore, substituting  $x = 0$ , we obtain the following integral equation

$$\tilde{u}(0, t, t_1) - \int_0^{t_1} ds \int_s^{t_1} \tilde{K}(0, t; z, t_1) \tilde{u}(0, z, s) dz = \tilde{f}(0, t, t_1), \tag{5.3}$$

where

$$\tilde{K}(x, t; z, t_1) = \frac{\mu}{2^{2m-1}\pi} \int_{|\xi-x| \leq t-t_1} k(\xi, t_1-z) K_1(x, \xi, t-t_1) d\xi, \tag{5.4}$$

$$\tilde{f}(x, t, t_1) = \frac{1}{2^{2m-1}\pi} \int_{|\xi-x| \leq t-t_1} K_1(x, \xi, t-t_1) f(\xi, t_1) d\xi. \tag{5.5}$$

Similarly, taking into account  $k(x, t) \in H^{l, l/2}(\Omega)$  at  $m > 1$ , and solution (5.3) by writing via the resolvent  $R(0, t; z, t_1)$  of the kernel equation, we obtain

$$\tilde{u}(0, t, t_1) = \tilde{f}(0, t, t_1) + \int_0^{t_1} ds \int_s^{t_1} R(0, t; z, t_1) \tilde{f}(0, z, s) dz, \tag{5.6}$$

Thus, from formula (2.5), the solution of problem (5.1) - (2.2) has the form:

$$u(x, t) = \frac{1}{2^{2m-1}\pi} \int_0^t \int_{|\xi-x| \leq t-\tau} K_1(x, \xi, t-\tau) f(\xi, \tau) d\xi d\tau +$$

$$+ \frac{1}{2^{2m-1}\pi} \int_0^t \int_{|\xi-x| \leq t-\tau} K_1(x, \xi, t-\tau) \tilde{F}(0, \tau) d\xi d\tau, \quad (5.7)$$

here  $\tilde{F}(0, \tau) = \int_0^\tau ds \int_s^\tau k(\xi, \tau-z) \tilde{u}(0, z, s) dz$ ,  $\tilde{u}(0, t, \tau)$  is a known function according to the formula (5.6).

Note that solutions to problem (2.1)-(2.2) can also be written in other cases  $n$  since  $n = 4, 5, \dots$

## References

- [1] Bitsadze A.V. *Some classes of partial differential equations*. M., Nauka, 1981, 448 p. [in Russian].
- [2] Agarwal R.P. *Boundary value problems for higher order differential equations*, World Scientific, Singapore, 1986.
- [3] Obolashvili E. Higher Order Partial Differential Equations in Clifford Analysis. *Progress in Mathematical Physics*, eBook ISBN 978-1-4612-0015-4.
- [4] Weaver W., Timoshenko S.P., Young D.H. *Vibration Problems in Engineering*. New York, John Wiley and Sons, 1990.
- [5] Manolis G.D., Dineva P.S., Rangelov T., Sfyris D. Mechanical models and numerical simulations in nanomechanics: A review across the scales. *Engineering Analysis with Boundary Elements*, 2021, **128**, P. 149–170.
- [6] Perelmuter M.N. Interface cracks bridged by nanofibers. *Nanosystems: Phys. Chem. Math.*, 2022, **13**(4), P. 356–364.
- [7] Baltaeva U., Alikulov Y., Baltaeva I.I., Ashirova A. Analog of the Darboux problem for a loaded integro-differential equation involving the Caputo fractional derivative. *Nanosystems: Physics, Chemistry, Mathematics*, 2021, **12**(4), P. 418–424.
- [8] Syed Tauseef Mohyud-Din, Muhammad Aslam Noor, Solving higher-order Integro-differential equations using he's polynomials. *J. KSIAM*, 2009, **13**(2), P. 109–121.
- [9] Toaldo B. Convolution-type derivatives, hitting-times of subordinators and time-changed C 0-semigroups. *Potential Anal.*, 2015, **42**, P. 115–140.
- [10] Khan M. A new algorithm for higher order integro-differential equations. *Afr. Mat.*, 2015, **26**, P. 247–255.
- [11] Urinov A., Karimov S. Solution of the analogue of the Cauchy problem for the iterated multidimensional Klein-Gordon-Fock equation with the Bessel operator. *arXiv preprint arXiv:1711.00093*, 2017 - arxiv.org.
- [12] Karimov S.T. Method of solving the Cauchy problem for one-dimensional polywave equation with singular Bessel operator, *Russ Math.*, 2017, **61**, P. 22–35.
- [13] Dai Z., Li H. and Li Q. Inequalities for the fractional convolution operator on differential forms. *J Inequal Appl.*, 2018, **176**.
- [14] Yuldashev T.K., Shabadikov K.K. Initial-value problem for a higher-order quasilinear partial differential equation. *J. Math Sci.*, 2021, **254**, P. 811–822.
- [15] Marcello D'Abbicco. Asymptotics of higher order hyperbolic equations with one or two dissipative lower order terms *arXiv preprint arXiv:2109.14067*, 2021 - arxiv.org.
- [16] Lorenzi A., Sinestrari E. An inverse problem in theory of materials with memory. *Nonlinear Anal. TMA*, 1988, **12**, P. 411–423.
- [17] Yelmez H., Kehmayer M., Chia Wei Hsu, Rotter S., Hui Cao. Customizing the Angular Memory Effect for Scattering Media. *Phys. Rev. X*, 2021, **11**, P. 031010.
- [18] Durdiev D.K. An inverse problem for a three-dimensional wave equation in the medium with memory *Math. Anal. and Disc. math.*, Novosibirsk, NGU, 1989, P. 19–26.
- [19] Grasselli M. An identification problem for an abstract linear hyperbolic integro-differential equation with applications *Journal of Mathematical Analysis and Applications*, 1992, **171**(1), P. 27–60.
- [20] Durdiev D.K. Global solvability of an inverse problem for an integro-differential equation of electrodynamics *Diff. Equ.*, 2008, **44**(4), P. 893–899.
- [21] Kasemets K., Janno J. Inverse problems for a parabolic integro-differential equation in convolutional weak form. *Abstract and Applied Analysis*, 2013, Article ID 297104.
- [22] P.Podio-Guidugli. A virtual power format for hydromechanics, *Continuum Mech. Thermodyn.*, 2009, **20**, P. 479–487.
- [23] Safarov Zh.Sh., Durdiev D.K. Inverse problem for an integro-differential equation of acoustics, *Diff. Equ.*, 2018, **54**(1), P. 134–142.
- [24] Totieva Zh.D., Durdiev D.K. The problem of finding the one-dimensional kernel of the thermoviscoelasticity equation, *Math. Notes*, 2018, **103**(1–2), P. 118–132.
- [25] Durdiev D.K., Nuriddinov Zh.Z. Determination of a multidimensional kernel in some parabolic integro-differential equation *Journal of siberian federal uni versity. mathematics and physics* 2021, **14**(1), P. 117–127.
- [26] Nakhushiev A.M. *Equations of mathematical biology*, Vishaya shkola, Moscow, 1995, p. 302.
- [27] Dzhaneliev M.T., Ramazanov M.I. On the boundary value problem for the spectrally loaded heat conduction operator. *Sib. Math. J.*, 2006, **47**, P. 433–451.
- [28] Islomov B., Baltaeva U.I. Boundary value problems for a third-order loaded parabolic-hyperbolic equation with variable coefficients, *Electronic Journal of Differential Equations*, 2015, **221**, P. 1–10.
- [29] Sadarangani K.B., Abdullaev O.K. About a problem for loaded parabolic-hyperbolic type equation with fractional derivatives. *Int. J. Differential Equ.*, 2016, P. 1–6.
- [30] Assanova A.T., Kadirbayeva Z.M. Periodic problem for an impulsive system of the loaded hyperbolic equations. *Electronic Journal of Differential Equations*, 2018, **2018**(72), P. 1–8.
- [31] Beshtokov M.K. Boundary-value problems for loaded pseudo parabolic equations of fractional order and difference methods of their solving, *Russ Math.*, 2019, **63**, P. 1–10.
- [32] Agarwal P., Baltaeva U., Alikulov Y. Solvability of the boundary-value problem for a linear loaded integro-differential equation in an infinite three-dimensional domain. *Chaos Solitons Fractals*, 2020, **140**, P. 110108.
- [33] Kozhanov A.I. Shipina T.N. Loaded differential equations and linear inverse problems for elliptic equations. *Complex Variables and Elliptic Equations*, 2021, **66**, P. 910–928.
- [34] Baltaeva U., Baltaeva I., Agarwal P. Cauchy problem for a high-order loaded integro-differential equation. *Math Meth Appl Sci.*, 2022, P. 1-10.
- [35] Khubiev K.U. Boundary-value problem for a loaded hyperbolic-parabolic equation with degeneration of order. *J. Math. Sci.*, 2022, **260**, P. 387–391.

- [36] Karimov Sh. Erd'lyi-Kober operators and their application to partial differential equations. Dissertation Abstract of Doctoral Dissertation (Dsc) on physical and Mathematical Sciences. Tashkent, 2019.
- [37] Courant R. Partial Differential Equations [in Russian]. Mir, Moscow, 1964.

---

*Submitted 19 July 2024; revised 27 July 2024; accepted 28 July 2024*

*Information about the authors:*

*Praveen Agarwal* – Department of Mathematics, Anand International College of Engineering, Jaipur-303012, India; Non-linear Dynamics Research Center (NDRC), Ajman University, Ajman, UAE; ORCID 0000-0001-7556-8942; goyal.praveen2011@gmail.com

*Umida Baltaeva* – Department of Exact sciences, Khorezm Mamun Academy, Khiva, Uzbekistan; Department of Applied Mathematics and Mathematical Physics, Urgench State University, Urgench, Uzbekistan; ORCID 0000-0001-9687-5220; umida.baltayeva@mail.ru

*Umrbek Madrakhimov* – Department of Applied Mathematics and Mathematical Physics, Urgench State University, Urgench, Uzbekistan; ORCID 0000-0002-8387-6993; us.madrakhimov@gmail.com

*Jamol I. Baltaev* – Department of Technology, RANCH University of Technology, Urgench-220100, Uzbekistan; ORCID 0009-0000-7438-1246; jamol\_06@yahoo.com

*Conflict of interest:* the authors declare no conflict of interest.

## Fast forward problem for adiabatic quantum dynamics: Estimation of the energy cost

J. D. Matrasulov<sup>1,2,a</sup>, J. R. Yusupov<sup>3,1,b</sup>, Kh. Sh. Matyokubov<sup>4,5,c</sup>

<sup>1</sup>Faculty of Physics, National University of Uzbekistan, Vuzgorodok, Tashkent, Uzbekistan

<sup>2</sup>Institute of Fundamental and Applied Research, National Research University TIIAME, Tashkent, Uzbekistan

<sup>3</sup>Kimyo International University in Tashkent, Tashkent, Uzbekistan

<sup>4</sup>Urgench State Pedagogical Institute, Urgench, Uzbekistan

<sup>5</sup>Urgench State University, Urgench, Uzbekistan

<sup>a</sup>jasur1362@gmail.com, <sup>b</sup>j.yusupov@ytit.uz, <sup>c</sup>hikmat.shuhratovich@gmail.com

Corresponding author: J. D. Matrasulov, jasur1362@gmail.com

PACS 03.65.Ta, 32.80.Qk, 37.90.j, 05.30.d, 03.65.w

**ABSTRACT** We consider the problem of energy cost needed for acceleration (deceleration) of the evolution of a quantum system using the Masuda–Nakamura’s fast forward protocol. In particular, we focus on dynamics by considering models for a quantum box with a moving wall and harmonic oscillator with time-dependent frequency. For both models we computed the energy needed for acceleration (deceleration) as a function of time. The results obtained are compared with those of other acceleration (deceleration) protocols.

**KEYWORDS** energetic cost, shortcuts to adiabaticity, statistical physics and thermodynamics

**ACKNOWLEDGEMENTS** This work is supported by the grant of the Agency of Innovative Development of the Republic of Uzbekistan, World Bank Project “Modernizing Uzbekistan National Innovation System” (Ref. Nr. REP-05032022/235).

**FOR CITATION** Matrasulov J.D., Yusupov J.R., Matyokubov Kh.Sh. Fast forward problem for adiabatic quantum dynamics: Estimation of the energy cost. *Nanosystems: Phys. Chem. Math.*, 2024, **15** (4), 457–464.

### 1. Introduction

Controlling of evolution and manipulation of physical processes in quantum systems is of practical importance in emerging quantum technologies. Achieving such a goal allows one to improve device miniaturization and operational speed at nanoscale and quantum functional materials. Solving such a problem requires developing of cost-efficient methods for acceleration and deceleration of quantum processes. One of the methods allowing to accelerate (decelerate) the quantum evolution, including that in adiabatic regime has been proposed in [1], which was later modified for different cases and situations (see [2–10]). According to the protocol of this approach, evolution of a given quantum system can be accelerated (decelerated) by acting some external electromagnetic potential on it. The method was later called Masuda–Nakamura’s fast forward protocol in quantum mechanics [1]. It is important to note that there are different protocols for acceleration (deceleration) of quantum evolution. Therefore, an important problem that arises in the context of their practical applications is energy-efficiency of a fast-forward protocol. Such efficiency can be estimated in terms of so called fast forward energy cost which was introduced first in the [11] and applied later to different physical systems in [12, 13]. Here we estimate such a cost for Masuda–Nakamura’s fast forward protocol in case of dynamical quantum confinement by considering harmonic oscillator with time-dependent frequency and a quantum box with a moving wall.

Remarkable feature of the Masuda–Nakamura’s fast forward protocol developed in [1] is the fact that it allows one to accelerate the time evolution of a quantum system by tuning the external potential that can be reduced to regulation of an additional phase in the wave function. The improved version of the prescription was proposed later in [4] which is used for acceleration of the soliton dynamics described in terms of the nonlinear Schrödinger equation and tunneling in quantum regime [4]. Different modifications and application of the protocol have been presented later in [4–8]. One of the advantages of the Masuda–Nakamura protocol is its effective application to so-called adiabatic quantum processes. These processes are those occurring in very slowly evolving quantum systems. An interesting problem in this case is so-called quantum short cuts, implying the shortest path (in time) to the end of the (adiabatic) processes among others. In [2, 3] the Masuda–Nakamura protocol was adopted to the problem of short cuts. In the literature, the problem called “short cuts to adiabaticity” [14–18] (called also “transitionless quantum driving” by Berry [19]). One should also note successful application of the fast forward protocol to the problem of stochastic [8] and classical [20] heat engine.

This paper is organized as follows. In the next section, we present a brief description of the fast-forward protocol following [1]. Section 3 presents an application of the fast forward protocol to harmonic oscillator with time-dependent frequency and quantum box with moving wall. In Section 4, we calculate energetic cost of fast forward protocol for

the harmonic oscillator with time-dependent frequency and compare it with the cost of inverse engineering protocol. In addition, Section 4 presents the results for quantum box with moving boundary conditions. Finally, the section 5 presents some concluding remarks.

## 2. Fast forward protocol for adiabatic quantum dynamics

Here we briefly recall the fast forward prescription for adiabatic quantum dynamics and its application to the harmonic oscillator with time-dependent frequency [7]. Consider the dynamics of a wave function  $\psi_0$  under the dynamical confinement  $V_0 = V_0(x, R(t))$  which varies adiabatically (slowly). This adiabatic change is characterized by slowly-varying control parameter  $R = R(t)$  which is given by

$$R(t) = R_0 + \epsilon t, \quad (1)$$

with the growth rate  $\epsilon \ll 1$ . The time-dependent 1D Schrödinger equation (1D TDSE) for  $\psi_0$  is given as:

$$i\hbar \frac{\partial \psi_0}{\partial t} = -\frac{\hbar^2}{2m} \partial_x^2 \psi_0 + V_0(x, R(t)) \psi_0, \quad (2)$$

where the coupling with electromagnetic field is assumed to be absent. If  $R = \text{const}$  the problem reduces to an eigenvalue problem for stationary bound state  $\phi_0$  which satisfies the time-independent Schrödinger equation

$$E\phi_0 = \hat{H}_0\phi_0 \equiv \left[ -\frac{\hbar^2}{2m} \partial_x^2 + V_0(x, R) \right] \phi_0. \quad (3)$$

With use of the eigenstate  $\phi_0 = \phi_0(x, R)$ , one can conceive the corresponding time-dependent state to be a product of  $\phi_0$  and a dynamical factor as

$$\phi_0(x, R(t)) = \bar{\phi}_0(x, R(t)) e^{i\eta(x, R(t))}, \quad (4)$$

As it stands, however,  $\psi_0$  does not satisfy TDSE in Eq. (2). To overcome this difficulty, we introduce a regularized wave function

$$\begin{aligned} \psi_0^{reg} &\equiv \phi_0(x, R(t)) e^{i\epsilon\theta(x, R(t))} e^{-\frac{i}{\hbar} \int_0^t E(R(t')) dt'} \\ &\equiv \bar{\phi}_0^{reg}(x, R(t)) e^{-\frac{i}{\hbar} \int_0^t E(R(t')) dt'} \end{aligned} \quad (5)$$

and regularized potential

$$V_0^{reg} \equiv V_0(x, R(t)) + \epsilon \tilde{V}(x, R(t)). \quad (6)$$

Regularized wave function  $\psi_0^{reg}$  should satisfy the TDSE for regularized system,

$$i\hbar \frac{\partial \psi_0^{reg}}{\partial t} = -\frac{\hbar^2}{2m} \partial_x^2 \psi_0^{reg} + V_0^{reg} \psi_0^{reg}, \quad (7)$$

up to the order of  $\epsilon$ .

The potential  $\tilde{V}$  is determined as

$$\tilde{V} = -\hbar \cdot \text{Im} \left[ \frac{\partial \phi_0}{\partial R} / \phi_0 \right] - \frac{\hbar^2}{m} \cdot \text{Im} \left[ \frac{\nabla \phi_0}{\phi_0} \right] \cdot \nabla \theta. \quad (8)$$

Rewriting  $\phi_0(x, R(t))$  in terms of the real positive amplitude  $\bar{\phi}_0(x, R(t))$  and phase  $\eta(x, R(t))$  as

$$\phi_0(x, R(t)) = \bar{\phi}_0(x, R(t)) e^{i\eta(x, R(t))}, \quad (9)$$

we see  $\theta$  to satisfy

$$\partial_x(\bar{\phi}_0^2 \partial_x \theta) = -\frac{m}{\hbar} \partial_R \bar{\phi}_0^2. \quad (10)$$

Integrating Eq. (10) over  $x$ , we have

$$\partial_x \theta = -\frac{m}{\hbar} \frac{1}{\bar{\phi}_0^2} \int^x \partial_R \bar{\phi}_0^2 dx', \quad (11)$$

which is the core equation of the regularization procedure. We shall now accelerate the quasi-adiabatic dynamics of  $\psi_0^{reg}$  in Eq. (5) by applying the external driving potential (fast forward potential). For this purpose, we introduce the fast-forward version of  $\psi_0^{reg}$  as

$$\psi_{FF} = \bar{\phi}_0(x, R(\Lambda(t))) e^{i\eta(x, R(\Lambda(t)))} e^{iv(t)\theta(x, R(\Lambda(t)))} e^{-\frac{i}{\hbar} \int_0^t E(R(\Lambda(s))) ds}. \quad (12)$$

For accelerated system, control parameter  $R$  now can be rewritten as

$$R(\Lambda(t)) = R_0 + \epsilon \Lambda(t), \quad (13)$$

where  $\Lambda(t)$  is the future or advanced time

$$\Lambda(t) = \int_0^t \alpha(t') dt'. \quad (14)$$

The wave function of fast forward state given by Eq. (12) satisfies TDSE with a fast-forward Hamiltonian  $H_{FF}$ :

$$i\hbar \frac{\partial \psi_{FF}}{\partial t} = H_{FF} \psi_{FF} \equiv \left( -\frac{\hbar^2}{2m} \partial_x^2 + V_0 + V_{FF} \right) \psi_{FF}. \quad (15)$$

Here  $V_0 = V_0(x, R(\Lambda(t)))$  and  $V_{FF}$  is given by

$$V_{FF} = -\frac{\hbar^2}{m} v(t) \partial_x \theta \cdot \partial_x \eta - \frac{\hbar^2}{2m} (v(t))^2 (\partial_x \theta)^2 - \hbar v(t) \partial_R \eta - \hbar \dot{v}(t) \theta - \hbar (v(t))^2 \partial_R \theta. \quad (16)$$

### 3. Application to adiabatic dynamical confinement

Masuda–Nakamura's fast forward protocol presented in the previous section can be applied to the simplest time-dependent system such as one-dimensional quantum box with a moving wall and one-dimensional harmonic oscillator with time-dependent frequency, evolving in the adiabatic regime. The main result for such a task is analytically or numerically calculated wave function  $\Psi_{FF}$  of the fast forwarded system and fast forwarding (driving) potential,  $V_{FF}$ .

#### 3.1. Time-dependent harmonic oscillator

Consider first the harmonic oscillator with time-dependent frequency. The evolution of such system is described in terms of the following non stationary Schrödinger equation:

$$i\hbar \frac{\partial}{\partial t} \psi_0(x, R(t)) = -\frac{\hbar^2}{2m} \partial_x^2 \psi_0(x, R(t)) + \frac{1}{2} m \omega^2(R(t)) x^2 \psi_0(x, R(t)), \quad (17)$$

where time dependence of the frequency  $\omega(t)$  is caused by adiabatically changing parameter  $R(t)$  defined as  $R(t) = \sqrt{1/\omega(t)}$ . For adiabatic regime of evolution, the eigenvalue problem can be written in terms of the following Schrödinger equation:

$$H_0(x, R) \phi = E(R) \phi, \quad (18)$$

that gives one the eigenvalue and the eigenstate as

$$\begin{aligned} E_n &= \left( n + \frac{1}{2} \right) \hbar \omega(R), \\ \phi_n &= \left( \frac{m\omega(R)}{\pi\hbar} \right)^{1/4} \frac{1}{(2^n n!)^{1/2}} e^{-\frac{m\omega(R)}{2\hbar} x^2} H_n \left( \left( \frac{m\omega(R)}{\hbar} \right)^{1/2} x \right) \end{aligned}$$

with  $n = 0, 1, 2, \dots$ . Here  $H_n(\cdot)$  are the Hermite polynomials.

Fast forward state and fast forward potential for such system can be calculated analytically. It is given by (see [7] for details):

$$\psi_{FF} = \phi_n(x, R(\Lambda(t))) e^{i \frac{m\hbar}{2\hbar} \dot{R} x^2} e^{-(n+\frac{1}{2})i \int_0^t \omega(R(\Lambda(t'))) dt'} \equiv \langle x|n \rangle$$

and

$$V_{FF} = -\frac{m\ddot{R}}{2R} x^2. \quad (19)$$

#### 3.2. Time-dependent quantum box

Now, let us investigate 1D quantum box with a moving wall. The dynamics of a particle is governed by

$$i\hbar \frac{\partial \psi}{\partial t} = H_0 \psi = -\frac{\hbar^2}{2m} \partial_x^2 \psi \quad (20)$$

with the time-dependent box boundary conditions as  $\psi(x = 0, t) = 0$  and  $\psi(x = L(t), t) = 0$ .  $L(t)$  is assumed to change adiabatically as  $L(t) = L_0 + \epsilon t$ . Length of the wall  $L(t)$  is to be assumed as control parameter of the confinement.

The adiabatic eigenvalue problem related to Eq. (20) gives one eigenvalues and eigenstates as follows

$$\begin{aligned} E_n &= \frac{\hbar^2}{2m} \left( \frac{\pi n}{L(t)} \right)^2, \\ \phi_n &= \sqrt{\frac{2}{L(t)}} \sin \left( \frac{\pi n}{L(t)} x \right). \end{aligned} \quad (21)$$

The phase  $\theta$  which the regularized state acquires is given using the formula (11), as

$$\begin{aligned}\partial_x \theta &= -\frac{m}{\hbar} \frac{1}{\phi_n^2} \partial_L \int_0^x \phi_n^2 dx = \frac{m}{\hbar} \frac{x}{L(t)}, \\ \theta &= \frac{m}{2\hbar} \frac{x^2}{L(t)}.\end{aligned}\quad (22)$$

Due to the real nature of  $\phi_n$ , we find  $\eta = 0$  in Eq. (8) and see that  $\tilde{V}$  vanishes.

Now, we apply the fast forward scheme from Section 2. This will be done by changing time  $t$  by future time  $\Lambda(t)$  in control parameter  $L(t)$ . By taking the asymptotic limit ( $\epsilon \rightarrow 0, \bar{\alpha} \rightarrow \infty$  with  $\epsilon\bar{\alpha} = v(t)$ ), the fast forward state can be written as:

$$\psi_{FF} = \phi_n(x, L(\Lambda(t))) e^{i \frac{m \dot{L}(\Lambda(t))}{2\hbar L(\Lambda(t))} x^2} e^{-i \frac{\hbar}{2m} (\pi n)^2 \int_0^t \frac{dt'}{L^2(\Lambda(t'))}}, \quad (23)$$

where  $L(\Lambda(t)) = L_0 + \int_0^t v(t') dt'$  with the time scaling factor  $v(t)$ . In accordance with Eq. (16), the fast forward potential is given by

$$V_{FF} = -\frac{m}{2} \frac{\ddot{L}(\Lambda(t))}{L(\Lambda(t))} x^2. \quad (24)$$

In the next section, we compute energy cost needed for realization of the above models, i.e. for fast forwarding of the quantum evolution in time-dependent box and time-dependent harmonic oscillator.

#### 4. Energy cost needed for fast forwarding of the evolution of a quantum system

The practical application of the above (or any other) fast forward evolution prescription is closely related to the question: how much energy one needs to use to apply the prescription. In other words, the effectiveness of the fast forward protocol depends on the cost of energy to be spent: as smaller the energy cost as effective the protocol. Here we consider the problem for estimation of the energy cost needed for application of the Masuda–Nakamura's fast forward protocol. According to the Ref. [11] energy cost to be paid for a given fast forward protocol is determined as:

$$C = \frac{1}{T_{FF}} \int_0^{T_{FF}} \|H\| dt, \quad (25)$$

where  $\|\hat{A}\|$  denotes the Frobenius norm defined as follows:  $\|\hat{A}\| = \sqrt{\text{Tr}[\hat{A}^\dagger \hat{A}]}$  and  $H$  is the total Hamiltonian of the system, which is given by

$$H = H_0 + V_{FF},$$

where  $H_0$  is the Hamiltonian of the standard system (to be fast forwarded) and  $V_{FF}$  is the fast forward potential given by Eq. (16). Here we estimate the energy cost for two systems adiabatically evolving under the dynamical confinement. Namely, we consider the time-dependent harmonic oscillator and the quantum box with moving wall described above. Let us start with the time-dependent harmonic oscillator given by Eq. (17).

According to [12] the energy cost needed to fast forward a quantum system with an unbound (discrete) spectrum (which is the case for our system) can be rewritten as

$$C_{FF} = \frac{1}{T_{FF}} \int_0^{T_{FF}} \bar{U} dt, \quad (26)$$

where  $T_{FF}$  shortened or fast-forward time and  $U$  is the internal energy given by the following formula

$$\bar{U} = \text{Tr}(\rho \hat{H}_{FF}), \quad (27)$$

with density matrix  $\rho$  defined as follows:

$$\rho(t) = \sum_{n=0}^{\infty} |n\rangle f_n \langle n|, \quad (28)$$

where  $\{|n\rangle\}$  is the exact solution of TDSE (15) and  $f_n$  is the Fermi–Dirac distribution having the form

$$f_n = \frac{1}{e^{\beta(E_n(L(\Lambda(t))) - \mu)} + 1}.$$

For the time-dependent harmonic oscillator, the expression of  $U$  can be written as (see [7] for details):

$$\bar{U} = A \left( \frac{\hbar^2}{4mL^2} - \frac{m}{8} L \ddot{L} + \frac{m}{8} \dot{L}^2 \right) \quad (29)$$

with

$$A = N^2 \left[ 1 + \frac{4\pi^2}{3} L_0^2 \left( \frac{mkT}{\hbar^2} \right)^2 \left( \frac{N}{L_0} \right)^{-2} + \dots \right]$$

and

$$L = L_0 + \bar{v} \left( \frac{1}{2} \frac{t^2}{T_{FF}} - \frac{1}{3} \frac{t^3}{T_{FF}^2} \right), \quad (30)$$

$$\dot{L} = \bar{v} \left( \frac{t}{T_{FF}} - \frac{t^2}{T_{FF}^2} \right). \quad (31)$$

Thus, for the cost, we have the formula

$$\begin{aligned} C_{FF} &= \frac{1}{T_{FF}} \int_0^{T_{FF}} \bar{U} dt \\ &= \frac{A\hbar^2}{4mT_{FF}} \int_0^{T_{FF}} \frac{1}{L^2} dt - \frac{mA}{8T_{FF}} \int_0^{T_{FF}} (L\ddot{L} - \dot{L}^2) dt \\ &= \frac{A\hbar^2}{4mT_{FF}} \int_0^{T_{FF}} \frac{1}{L^2} dt + \frac{mA}{8T_{FF}} \int_0^{T_{FF}} \left( -\frac{d}{dt}(\dot{L}L) + 2\dot{L}^2 \right) dt \\ &= \frac{A\hbar^2}{4mT_{FF}} \int_0^{T_{FF}} \frac{1}{L^2} dt - \frac{mA}{4T_{FF}} \int_0^{T_{FF}} \dot{L}^2 dt. \end{aligned}$$

Using Eq. (31), one obtains

$$\begin{aligned} mA \frac{1}{4T_{FF}} \int_0^{T_{FF}} \dot{L}^2 dt &= mA \frac{1}{4T_{FF}} \int_0^{T_{FF}} \bar{v}^2 \left( \frac{t}{T_{FF}} - \frac{t^2}{T_{FF}^2} \right)^2 dt \\ &= mA \frac{\bar{v}^2}{4T_{FF}} \left( \frac{1}{3} T_{FF} - \frac{1}{2} T_{FF} + \frac{1}{5} T_{FF} \right) = \frac{mA}{120} \bar{v}^2. \end{aligned}$$

Then

$$C_{FF} = \frac{1}{T_{FF}} \int_0^{T_{FF}} \bar{U} dt = \frac{A\hbar^2}{4mT_{FF}} \int_0^{T_{FF}} \frac{1}{L^2} dt + \frac{mA}{120} \bar{v}^2. \quad (32)$$

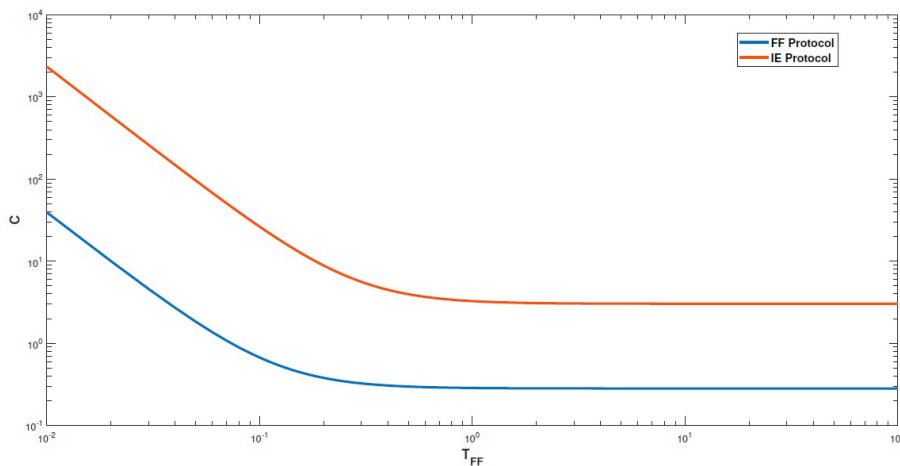


FIG. 1. Energy cost for the fast forward protocol (blue) with control parameter  $L$  given by Eq. (30) and the inverse engineering protocol (red) with the initial frequency  $\omega_0 = 1$  and the final frequency  $\omega_F = 10$

In the case of the control parameter  $L(t)$  chosen in the form

$$L(t) = L_0 + \bar{v} \left( t - \frac{T_{FF}}{2\pi} \sin \frac{2\pi}{T_{FF}} t \right), \quad (33)$$

$$\dot{L} = \bar{v} \left( 1 - \cos \frac{2\pi}{T_{FF}} t \right), \quad (34)$$

we have

$$C_{FF} = \frac{1}{T_{FF}} \int_0^{T_{FF}} \bar{U} dt = \frac{A\hbar^2}{4mT_{FF}} \int_0^{T_{FF}} \frac{1}{L^2} dt + \frac{3Am}{8} \bar{v}^2. \quad (35)$$

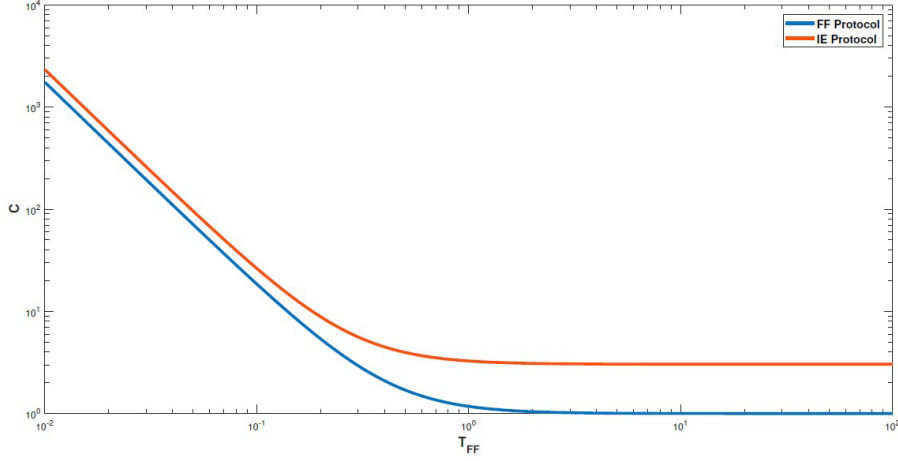


FIG. 2. Energy cost for the fast forward protocol (blue) with the control parameter  $L$  given by Eq.(30) and the inverse engineering protocol (red) with the initial frequency  $\omega_0 = 1$  and the final frequency  $\omega_F = 10$

Now, let us do similar calculations for the quantum box with moving wall. Energy  $\bar{U}$  for accelerated dynamics of the quantum box with moving wall looks as follows (for details see [7]):

$$\begin{aligned} \bar{U} &= \frac{\pi^2 \hbar^2 N^3}{24m L^2} \left[ 1 + \frac{24}{\pi^2} \left( \frac{mkT}{\hbar^2} \right)^2 \left( \frac{N}{L} \right)^{-4} + \dots \right] \\ &- \frac{N}{6} (mL\ddot{L} - m\dot{L}^2) \left[ 1 + \frac{6}{\pi^2} \frac{1}{N^2} \left( 1 + \frac{16}{3\pi^2} \left( \frac{mkT}{\hbar^2} \right)^2 \left( \frac{N}{L} \right)^{-4} + \dots \right) \right]. \end{aligned} \quad (36)$$

Here we also considered two cases: the first one takes place if the control parameter  $L(t)$  is given as polynomial function, the second one takes place if  $L(t)$  is trigonometric function. As for polynomial  $L(t)$ , it is as follows:

$$L = L_0 + \bar{v} \left( \frac{1}{2} \frac{t^2}{T_{FF}} - \frac{1}{3} \frac{t^3}{T_{FF}^2} \right). \quad (37)$$

The energetic cost is given by

$$C_{FF} = \frac{1}{T_{FF}} \int_0^{T_{FF}} \bar{U} dt = B_1 \frac{1}{24T_{FF}} \int_0^{T_{FF}} \frac{1}{L^2} + B_2 \frac{\bar{v}^2}{90}, \quad (38)$$

where  $B_1$  and  $B_2$  are the following constants:

$$B_1 = \frac{\pi^2 \hbar^2 N^3}{24m} \left[ 1 + \frac{24}{\pi^2} \left( \frac{mkT}{\hbar^2} \right)^2 \left( \frac{N}{L} \right)^{-4} + \dots \right], \quad (39)$$

$$B_2 = \frac{mN}{6} \left[ 1 + \frac{16}{3\pi^2} \left( \frac{mkT}{\hbar^2} \right)^2 \left( \frac{N}{L} \right)^{-4} + \dots \right]. \quad (40)$$

For the case of trigonometric control parameter, one has  $L(t)$  in the form

$$L(t) = L_0 + \bar{v} \left( t - \frac{T_{FF}}{2\pi} \sin \frac{2\pi}{T_{FF}} t \right). \quad (41)$$

For the energetic cost, we obtain the expression

$$C_{FF} = \frac{1}{T_{FF}} \int_0^{T_{FF}} \bar{U} dt = B_1 \frac{1}{24T_{FF}} \int_0^{T_{FF}} \frac{1}{L^2} + B_2 \frac{\bar{v}^2}{2}. \quad (42)$$

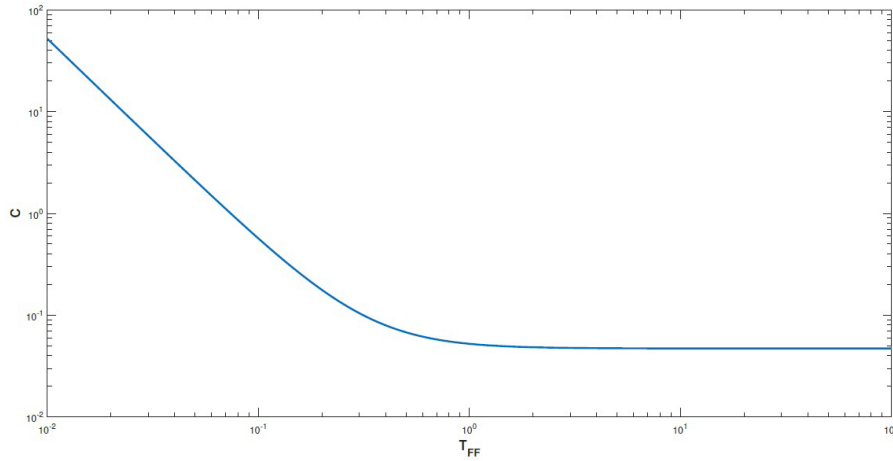


FIG. 3. Energy cost of the fast forward protocol with  $L$  given by Eq. (37) for the parameters  $L_0 = 1$  and  $L_F = 10$

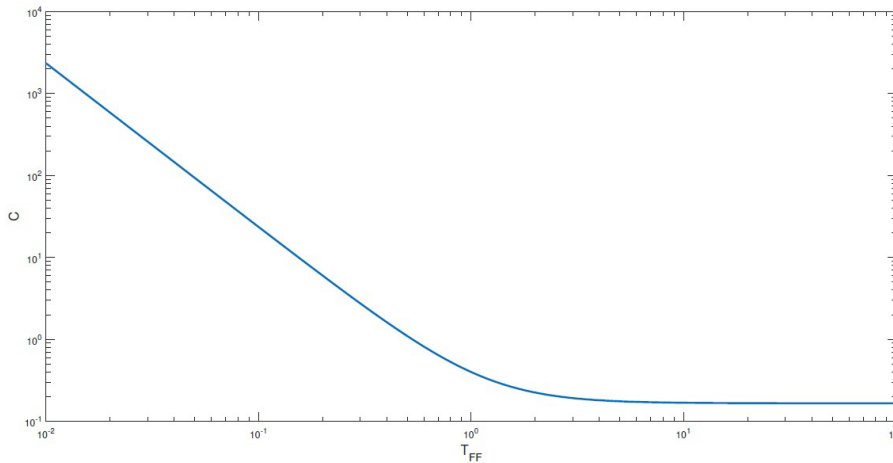


FIG. 4. Energy cost of the fast forward protocol with  $L$  given by Eq. (41) for the parameters  $L_0 = 1$  and  $L_F = 10$

Fig. 1 compares plots of the energy cost as function of time for Masuda–Nakamura’s (blue line) and the inverse engineering (IE) (red line) fast forward protocols for the time-dependent harmonic oscillator (see [12] for details). Energy cost for IE protocol is obtained numerically by using the following IE Hamiltonian [12] :

$$\langle H_{IE} \rangle = \frac{1}{2} \left[ \frac{\dot{b}^2(t)}{2\omega_0} + \frac{\omega^2(t)b^2(t)}{2\omega_0} + \frac{\omega_0}{2b^2(t)} \right] \coth \left( \frac{\beta\omega_0}{2} \right), \quad (43)$$

where  $b(t)$  is the dimensionless function satisfying the Ermakov equation:

$$\ddot{b}(t) + \omega^2(t)b(t) = \omega_0/b^3(t). \quad (44)$$

The calculations were done for the control parameter  $L(t)$  given by Eq. (30). As the plot shows, the cost for the Masuda–Nakamura protocol is much smaller than that for the inverse engineering one and the curves are almost parallel to each other. Fig. 2 presents similar plots for the form of  $L(t)$  given by Eq. (33). It can be seen that the costs are completely different than that in Fig. 1, both qualitatively and quantitatively, i.e. the cost for Masuda–Nakamura’s fast forward protocol in Fig. 1 is much smaller than that in Fig. 2. In addition, at the initial time the difference between the costs are much smaller than that at longer times. In Fig. 3, the time-dependence of the energy cost for the Masuda–Nakamura protocol is plotted for the quantum box with moving wall for the control parameter given by Eq. (30). Fig. 4 presents similar plot for the case when  $L(t)$  is given by Eq. (33). Comparing plots of the costs presented in Figs.3 and 4 with those in Figs. 1 and 2, one can conclude that the costs for the time-dependent harmonic oscillator and for the quantum box with moving wall within the Masuda–Nakamura fast forward protocol are almost equal for the same systems (provided they are estimated for the same control parameter).

## 5. Conclusion

In this paper, we proposed two models where Masuda–Nakamura’s fast forward protocol can be applied in the adiabatic regime and the energy cost for the implementation of such protocol can be computed. In particular, Masuda–Nakamura’s method for the fast-forward evolution [1, 2] is applied for the acceleration of the evolution of the time-dependent box with slowly moving wall and the harmonic oscillator with slowly varying time-dependent frequency. The quantitative comparison of the energetic cost of the Masuda–Nakamura protocol with the inverse engineering protocol is given. In particular, the plots of the energy cost for the Masuda–Nakamura and the inverse engineering protocols in Figs. 1 and 2 shows that the Masuda–Nakamura protocol requires less cost than the inverse engineering protocol. The results obtained in this paper can be used for further development of energy-efficient and resource-saving low-dimensional quantum devices.

## References

- [1] Masuda S. and Nakamura K. Fast-forward problem in quantum mechanics. *Phys. Rev. A*, 2008, **78**, P. 062108.
- [2] Masuda S. and Nakamura K. Fast-forward of adiabatic dynamics in quantum mechanics. *Proc. R. Soc. A*, 2010, **466**, P. 1135.
- [3] Masuda S. and Nakamura K. Acceleration of adiabatic quantum dynamics in electromagnetic fields. *Phys. Rev. A*, 2011, **84**, P. 043434.
- [4] Khujakulov A. and Nakamura K. Scheme for accelerating quantum tunneling dynamics. *Phys. Rev. A*, 2016, **93**, P. 022101.
- [5] I. Setiawan, Bobby Eka Gunara, S. Masuda and K. Nakamura. Fast forward of the adiabatic spin dynamics of entangled states. *Phys. Rev. A*, 2017, **96**, P. 052106.
- [6] Nakamura K., Khujakulov A., Avazbaev S. and Masuda S. Fast forward of adiabatic control of tunneling states. *Phys. Rev. A*, 2017, **95**, P. 062108.
- [7] Babajanova G., Matrasulov J., Nakamura K. Quantum gas in the fast forward scheme of adiabatically expanding cavities: Force and equation of state. *Phys. Rev. E*, 2018, **97**, P. 042104.
- [8] Nakamura K., Matrasulov J., and Izumida Y. Fast-forward approach to stochastic heat engine. *Phys. Rev. E*, 2020, **102**, P. 012129.
- [9] Matrasulov J., Yusupov J.R., Saidov A.A. Fast forward evolution in heat equation: Tunable heat transport in adiabatic regime, *Nanosystems: Physics, Chemistry, Mathematics*, 2023, **14**, P. 421–427.
- [10] Setiawan I., Sugihakim R., Gunara B.E., Masuda S., Nakamura K. Fast-forward generation of non-equilibrium steady states of a charged particle under the magnetic field. *Progress of Theoretical and Experimental Physics*, 2023, **2023**, 063A04.
- [11] Zheng Y., Campbell S., De Chiara G., Poletti D. Cost of counterdiabatic driving and work output. *Phys. Rev. A*, 2016, **94**, P. 042132.
- [12] Obinna Abah, Ricardo Puebla, Anthony Kiely, Gabriele De Chiara, Mauro Paternostro and Steve Campbell. Energetic cost of quantum control protocols. *New J. Phys.*, 2019, **21**, P. 103048.
- [13] Chen X., et al. Fast Optimal Frictionless Atom Cooling in Harmonic Traps: Shortcut to Adiabaticity. *Phys. Rev. Lett.*, 2010, **104**, P. 063002.
- [14] Guéry-Odelin D., Ruschhaup A., Kiel A., Torrontegui E., Martínez-Garaot S., Muga J.G. Shortcuts to adiabaticity: Concepts, methods, and applications. *Rev. Mod. Phys.*, 2019, **91**, P. 045001.
- [15] Erik Torrontegui, et al. Chapter 2 - Shortcuts to Adiabaticity. *Advances in atomic, molecular, and optical physics*, 2013, **62**, P. 117.
- [16] Martínez-Garaot S., et al. Vibrational Mode Multiplexing of Ultracold Atoms. *Phys. Rev. Lett.*, 2013, **111**, P. 213001.
- [17] A. del Campo. Shortcuts to Adiabaticity by Counterdiabatic Driving. *Phys. Rev. Lett.*, 2013, **111**, P. 100502.
- [18] Demirplak M., Rice S.A. Adiabatic Population Transfer with Control Fields. *J. Phys. Chem. A*, 2003, **107**, P. 9937.
- [19] Berry M.V. Transitionless quantum driving. *Journal of Physics A: Mathematical and Theoretical*, 2009, **42**, P. 365303.
- [20] Christopher Jarzynski, Sebastian Deffner, Ayoti Patra, and Yiğit Subaşı. Fast forward to the classical adiabatic invariant. *Phys. Rev. E*, 2017, **95**, P. 032122.

---

*Submitted 30 April 2024; revised 11 June 2024, 20 July 2024; accepted 21 July 2024*

### Information about the authors:

*J. D. Matrasulov* – Faculty of Physics, National University of Uzbekistan, Vuzgorodok, Tashkent 100174, Uzbekistan; Institute of Fundamental and Applied Research, National Research University TIIAME, Kori Niyoziy 39, Tashkent 100000, Uzbekistan; ORCID 0000-0001-5741-9003; jasur1362@gmail.com

*J. R. Yusupov* – Kimyo International University in Tashkent, 156 Usman Nasyr Str., 100121, Tashkent, Uzbekistan; Faculty of Physics, National University of Uzbekistan, Vuzgorodok, Tashkent 100174, Uzbekistan; ORCID 0000-0003-1758-6805; j.yusupov@yit.uz

*Kh. Sh. Matyokubov* – Urgench State Pedagogical Institute, 1 Gurlan str., 220100, Urgench, Uzbekistan; Urgench State University, 14 H. Olimjon Str., 220100, Urgench, Uzbekistan; ORCID 0000-0002-6642-5488; hikmat.shuhratovich@gmail.com

*Conflict of interest:* the authors declare no conflict of interest.

## Role of bulk and surface current carriers in resistivity of thin films of the topological insulator $\text{Bi}_2\text{Se}_3$

Alexandra N. Perevalova<sup>a</sup>, Bogdan M. Fominykh, Vasiliy V. Chistyakov, Vyacheslav V. Marchenkov<sup>b</sup>

M. N. Mikheev Institute of Metal Physics of the Ural Branch of the Russian Academy of Sciences, 620108 Ekaterinburg, Russia

<sup>a</sup>domozhirova@imp.uran.ru, <sup>b</sup>march@imp.uran.ru

Corresponding author: Alexandra N. Perevalova, domozhirova@imp.uran.ru

PACS 73.50.-h, 73.63.-b

**ABSTRACT** The temperature dependences of the electrical resistivity of topological insulator  $\text{Bi}_2\text{Se}_3$  thin films with thicknesses of 20 and 40 nm were measured in the temperature range from 4.2 to 80 K. Their resistivity was shown to depend on thickness. A method was proposed for “separation” of the bulk and surface resistivity of films, with the help of which corresponding estimates were made. It was demonstrated that the surface resistivity is more than two orders of magnitude less than the bulk resistivity at  $T = 4.2$  K.

**KEYWORDS** thin films,  $\text{Bi}_2\text{Se}_3$ , topological insulator, electrical resistivity, bulk and surface resistivities

**ACKNOWLEDGEMENTS** The research was carried out within the state assignment of Ministry of Science and Higher Education of the Russian Federation (theme “Spin” No. 122021000036-3). The authors thank J. C. A. Huang for providing thin films and E. B. Marchenkova for assistance in their characterization.

**FOR CITATION** Perevalova A.N., Fominykh B.M., Chistyakov V.V., Marchenkov V.V. Role of bulk and surface current carriers in resistivity of thin films of the topological insulator  $\text{Bi}_2\text{Se}_3$ . *Nanosystems: Phys. Chem. Math.*, 2024, **15** (4), 465–468.

### 1. Introduction

Topological insulators attract the attention of a large number of researchers due to their unusual electronic band structure and the possibility of application in spintronics and other fields [1, 2]. Topological insulators are materials that have an energy gap in the bulk and gapless states with a linear dispersion law, called the Dirac cone, on the surface. Surface states arise due to band inversion in the bulk in the presence of strong spin-orbit interactions and are protected by time-reversal symmetry. Their existence can be explained by the fact that when a topological insulator is in contact with an ordinary insulator (including vacuum) having the opposite band order, the gap closes at the boundary as the topology changes from nontrivial to trivial. Therefore, “metallic” states always exist on the surface of a topological insulator [3–5]. The current carriers in the near-surface “metallic” layer are massless Dirac fermions, the spin of which is locked to the momentum. Such carriers are protected from scattering by defects and non-magnetic impurities. Typical representatives of three-dimensional topological insulators are bismuth selenide and bismuth telluride [6, 7]. These compounds have relatively large band gap values of  $\sim 0.2 - 0.3$  eV, which is important for practical applications.

Bismuth chalcogenides, including  $\text{Bi}_2\text{Se}_3$  and  $\text{Bi}_2\text{Te}_3$ , are layered compounds with a rhombohedral lattice (space group  $R\bar{3}m$ ). The crystal structure can be represented as a set of quintuple layers (QL) perpendicular to the  $c$  axis. Each QL consists of five atomic layers alternating in the sequence Se(Te)1-Bi-Se(Te)2-Bi-Se(Te)1. Within a QL, atoms have strong ionic or covalent bonds, but QLs are bound together by weak van der Waals forces. The height of a QL is  $\sim 1$  nm. Using angle-resolved photoemission spectroscopy (ARPES), it was shown that  $\text{Bi}_2\text{Se}_3$  films exhibit a Dirac dispersion law on the surface, i.e. they manifest the properties of a topological insulator, at a thickness of 5 nanometers or more, which corresponds to 5 or more QLs [4].

Currently, there is a large number of works devoted to the study of the electronic structure and transport properties of topological insulators (see, for example, [6–12]). One of the main methods for studying Dirac surface states is ARPES, which allows one to directly observe the presence of Dirac cones on the surface of a topological insulator [7, 10]. However, this method places fairly high demands on the quality of samples. Another effective way is to analyze the quantum oscillations in magnetoresistivity and Hall resistivity [11, 12]. This method allows one to estimate the Berry phase and determine which current carriers, surface or bulk, dominate in magnetotransport, as well as estimate their parameters, such as concentration, mobility and effective mass. Determination of the contribution of surface and bulk current carriers to the transport properties of topological insulators could be useful for practical applications. It was experimentally demonstrated in [13] that the conductance of  $\text{Bi}_2\text{Se}_3$  nanodevices is determined by parallel surface and bulk contributions. Therefore,

the question arises about the possibility of “separation” of the contributions to conductivity (resistivity) from the bulk and surface in such materials.

In this work, a relatively simple method is proposed for “separation” of the bulk and surface resistivities of topological insulator films, with the help of which corresponding estimates are made for  $\text{Bi}_2\text{Se}_3$  thin films.

## 2. Experiment

Thin films of the topological insulator  $\text{Bi}_2\text{Se}_3$  with thicknesses of 20 and 40 nm were synthesized by molecular beam epitaxy on  $\text{Al}_2\text{O}_3$  substrates.

Determination of the chemical composition of the films and measurements of the temperature dependences of the electrical resistivity  $\rho(T)$  were carried out at the Collaborative Access Center “Testing Center of Nanotechnology and Advanced Materials” of M. N. Mikheev Institute of Metal Physics of the Ural Branch of the Russian Academy of Sciences. The chemical composition of the thin films was confirmed by energy dispersive X-ray microanalysis (EDXMA) using a Quanta 200 scanning microscope with an EDXMA attachment (Table 1). It can be seen that the composition is close to nominal.

TABLE 1. Results of the analysis of the chemical composition of the  $\text{Bi}_2\text{Se}_3$  films

Film thickness, nm	Content of chemical element, at.%	
	Bi	Se
20	40.05	59.95
40	39.62	60.38

Electrical resistivity  $\rho$  was measured at direct current using the four-point method with switching the direction of the current through the sample (see, for example, [14]) at temperatures from 4.2 to 80 K.

## 3. Results and discussion

Figure 1 shows the temperature dependences of the resistivity  $\rho$  for two films of  $\text{Bi}_2\text{Se}_3$  with thicknesses of 20 and 40 nm. It can be seen that the resistivity values of the films differ significantly and depend on their thickness. Thus, for the 20 nm-thick film, the electrical resistivity increases from 215 to 282  $\mu\Omega\cdot\text{cm}$ , and for the 40 nm-thick film, it increases from 420 to 523  $\mu\Omega\cdot\text{cm}$  in the temperature range from 4.2 to 80 K. It can be assumed that the difference in resistivity values is due to the difference in the “surface/bulk” ratio for the two films, that is, a significant difference in the values of bulk and surface conductivities. Similar effects were observed in [15, 16] for thin films of  $\text{Bi}_2\text{Se}_3$  and  $\text{Bi}_2\text{Te}_3$ .

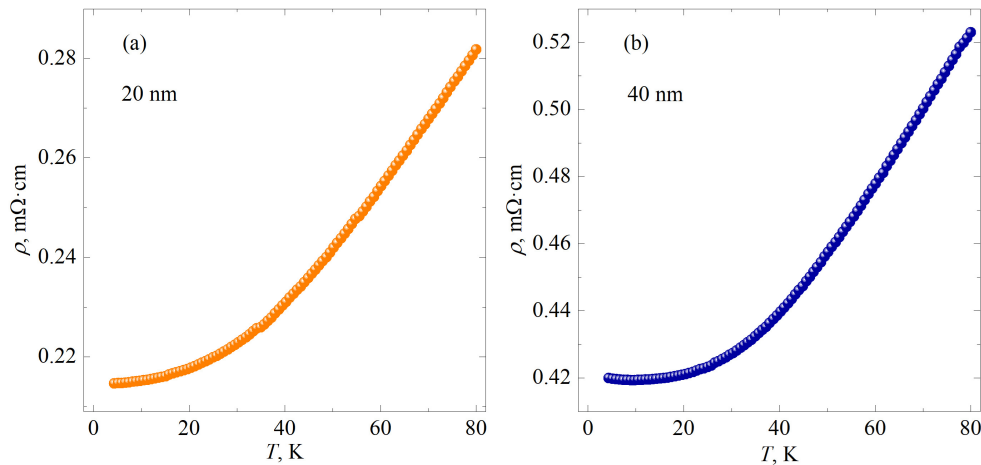


FIG. 1. Temperature dependences of the electrical resistivity of the thin films of the topological insulator  $\text{Bi}_2\text{Se}_3$  with thicknesses of 20 nm (a) and 40 nm (b)

One can try to estimate the contributions of surface and bulk resistivity (conductivity) to the total resistivity (conductivity) of the  $\text{Bi}_2\text{Se}_3$  films under study. Fig. 2 schematically shows the cross sections of the two films. Since surface and bulk conductivities in topological insulators can differ significantly, the total conductivity can be represented as a parallel connection of conductors. In this case, the resistances  $R_1$  and  $R_2$  of topological insulator thin films can be expressed as follows:

$$\frac{1}{R_1} = \frac{1}{\rho_1} \cdot \frac{a \cdot d_1}{L} \approx \frac{1}{\rho_{\text{bulk}}} \cdot \frac{a \cdot d_1}{L} + \frac{1}{\rho_{\text{surf}}} \cdot \frac{2\delta \cdot a}{L}, \quad (1)$$

$$\frac{1}{R_2} = \frac{1}{\rho_2} \cdot \frac{b \cdot d_2}{L} \approx \frac{1}{\rho_{\text{bulk}}} \cdot \frac{b \cdot d_2}{L} + \frac{1}{\rho_{\text{surf}}} \cdot \frac{2\delta \cdot b}{L}. \quad (2)$$

Here  $\rho_1$  and  $\rho_2$  are resistivities of the first and second films (Fig. 2);  $d_1$  and  $d_2$  are their thicknesses;  $a$  and  $b$  are widths of the films;  $\delta$  is a thickness of the near-surface “metallic” layer, which is much less than the thickness of the films;  $L$  is a distance between potential contacts;  $\rho_{\text{surf}}$  and  $\rho_{\text{bulk}}$  are surface and bulk resistivities, respectively. It is easy to show that  $\rho_{\text{surf}}$  and  $\rho_{\text{bulk}}$  can be represented as:

$$\rho_{\text{surf}} \approx \frac{2\delta \left( \frac{1}{d_1} - \frac{1}{d_2} \right)}{\rho_1^{-1} - \rho_2^{-1}}, \quad (3)$$

$$\rho_{\text{bulk}} \approx \frac{d_2 - d_1}{\rho_2 - \rho_1}. \quad (4)$$

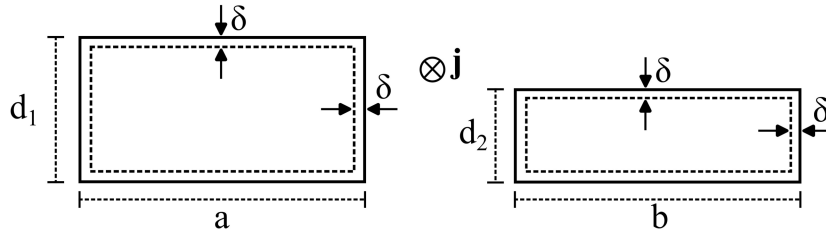


FIG. 2. Schematic representation of the cross-section of two films of a topological insulator:  $d_1$  and  $d_2$  are thicknesses of the first and second films, respectively;  $a$  and  $b$  are widths of the films;  $\delta$  is the thickness of the near-surface “metallic” layer; an electric current  $j$  is directed perpendicular to the plane of the figure

The thickness of the near-surface layer  $\delta$  was set equal to 1 nm, which corresponds to the thickness of one QL in the  $\text{Bi}_2\text{Se}_3$  crystal structure [4]. This value does not exceed the thickness of the two-dimensional conduction channel of 1.7 nm, estimated for  $\text{Bi}_2\text{Se}_3$  in [17]. Note also that in this model representation there is a sharp boundary between surface and bulk, which does not entirely correspond to reality.

Using the above expressions and assumptions, estimations of surface and bulk resistivities were performed. Fig. 3 shows the temperature dependences of the contributions to the resistivity from surface,  $\rho_{\text{surf}}$ , and bulk,  $\rho_{\text{bulk}}$ , current carriers in the  $\text{Bi}_2\text{Se}_3$  films. It can be seen that the dependence  $\rho_{\text{surf}}(T)$  exhibits metallic behaviour, i.e. the electrical resistivity grows with increasing temperature according to a power law, and the dependence  $\rho_{\text{bulk}}(T)$  exhibits semiconductor behaviour, i.e.  $\rho_{\text{bulk}}$  decreases with increasing temperature. In general, this is consistent with the presence of metallic states on the surface of a topological insulator and an energy gap in its bulk. At  $T = 4.2$  K, the surface resistivity  $\rho_{\text{surf}}$  of the films is more than 2 orders of magnitude less than the bulk resistivity  $\rho_{\text{bulk}}$ . In addition, at temperatures below 55 K, the surface resistivity  $\rho_{\text{surf}}$  depends on temperature according to a quadratic law, and a linear dependence  $\rho_{\text{surf}}(T)$  is observed at higher temperatures. The quadratic temperature dependence of the electrical resistivity can be explained by electron-electron scattering, as well as by an “electron-phonon-surface” interference scattering mechanism described in [18, 19]. However, further research is required to understand the reason for such dependence.

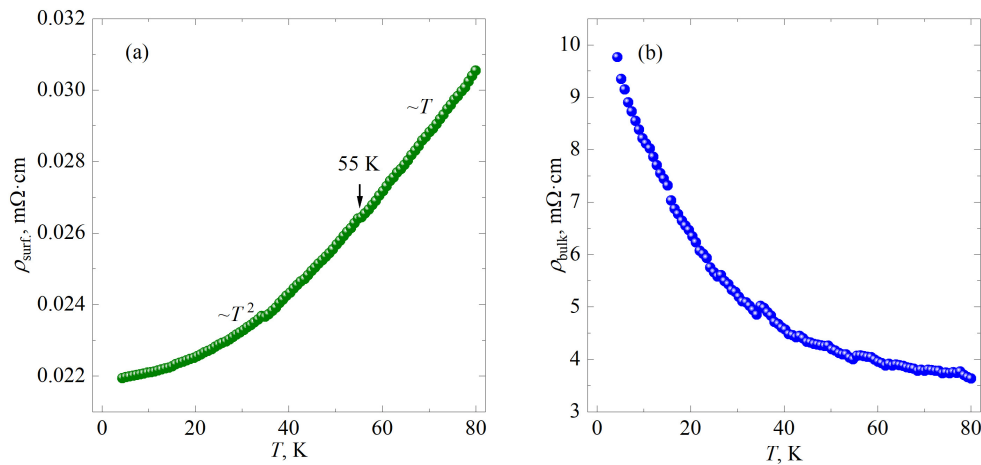


FIG. 3. Temperature dependences of the contributions of surface  $\rho_{\text{surf}}$  (a) and bulk  $\rho_{\text{bulk}}$  (b) current carriers to the resistivity of the  $\text{Bi}_2\text{Se}_3$  thin films

#### 4. Conclusion

It was found that the temperature dependences of the resistivity of the topological insulator  $\text{Bi}_2\text{Se}_3$  films demonstrate metallic behavior, and the resistivity value depends on the thickness of the film.

The relatively simple method for “separating” the bulk and surface resistivities of topological insulator films was proposed, with the help of which corresponding estimates were made for thin films of  $\text{Bi}_2\text{Se}_3$  with thicknesses of 20 and 40 nm.

The performed estimates showed that the contribution of surface carriers to the electrical resistivity of  $\text{Bi}_2\text{Se}_3$  grows with increasing temperature, whereas the contribution of bulk carriers decreases. The value of the surface resistivity is more than two orders of magnitude less than the bulk resistivity at low temperatures. In general, this is consistent with existing concepts about the presence of “metallic” states on the surface of a topological insulator and an energy gap in its bulk.

#### References

- [1] Gilbert M.J. Topological electronics. *Commun. Phys.*, 2021, **4**, 70.
- [2] He M., Sun H., He Q.L. Topological insulator: Spintronics and quantum computations. *Front. Phys.*, 2019, **14**, 43401.
- [3] Hasan M.Z., Kane C.L. Colloquium: Topological insulators. *Rev. Mod. Phys.*, 2010, **82**, 3045.
- [4] Qi X.-L., Zhang S.-C. Topological insulators and superconductors. *Rev. Mod. Phys.*, 2011, **83**, P. 1057–1110.
- [5] Xiao J., Yan B. First-principles calculations for topological quantum materials. *Nat. Rev. Phys.*, 2021, **3**, P. 283–297.
- [6] Zhang H., Liu C.-X., Qi X.-L., Dai X., Fang Z., Zhang S.-C. Topological insulators in  $\text{Bi}_2\text{Se}_3$ ,  $\text{Bi}_2\text{Te}_3$  and  $\text{Sb}_2\text{Te}_3$  with a single Dirac cone on the surface. *Nature Phys.*, 2009, **5**, P. 438–442.
- [7] Xia Y., Qian D., Hsieh D., Wray L., Pal A., Lin H., Bansil A., Grauer D., Hor Y.S., Cava R.J., Hasan M.Z. Observation of a large-gap topological-insulator class with a single Dirac cone on the surface. *Nature Phys.*, 2009, **5**, P. 398–402.
- [8] Stepina N.P., Golyashov V.A., Nenashev A.V., Tereshchenko O.E., Kokh K.A., Kirienko V.V., Koptev E.S., Goldyreva E.S., Rybin M.G., Obraztsova E.D., Antonova I.V. Weak antilocalization to weak localization transition in  $\text{Bi}_2\text{Se}_3$  films on graphene. *Physica E*, 2022, **135**, 114969.
- [9] Wang W.J., Gao K.H., Li Z.Q. Thickness-dependent transport channels in topological insulator  $\text{Bi}_2\text{Se}_3$  thin films grown by magnetron sputtering. *Sci. Rep.*, 2016, **6**, 25291.
- [10] Pan Z.-H., Vescovo E., Fedorov A.V., Gardner D., Lee Y.S., Chu S., Gu G.D., Valla T. Electronic structure of the topological insulator  $\text{Bi}_2\text{Se}_3$  using angle-resolved photoemission spectroscopy: Evidence for a nearly full surface spin polarization. *Phys. Rev. Lett.*, 2011, **106**, 257004.
- [11] Cao H., Tian J., Miotkowski I., Shen T., Hu J., Qiao S., Chen Y.P. Quantized Hall effect and Shubnikov–de Haas oscillations in highly doped  $\text{Bi}_2\text{Se}_3$ : evidence for layered transport of bulk carriers. *Phys. Rev. Lett.*, 2012, **108**, 216803.
- [12] Vedenev S.I. Quantum oscillations in three-dimensional topological insulators. *Phys.-Usp.*, 2017, **60**, 385.
- [13] Steinberg H., Gardner D.R., Lee Y.S., Jarillo-Herrero P. Surface state transport and ambipolar electric field effect in  $\text{Bi}_2\text{Se}_3$  nanodevices. *Nano Lett.*, 2010, **10**, P. 5032–5036.
- [14] Marchenkov V.V., Weber H.W., Cherepanov A.N., Startsev V.E. Experimental verification and quantitative analysis of the temperature (phonon) breakdown phenomenon in the high-field magnetoresistivity of compensated metals. *J. Low Temp. Phys.*, 1996, **102**, P. 133–155.
- [15] He H.-T., Wang G., Zhang T., Sou I.-K., Wong G.K.L., Wang J.-N. Impurity effect on weak antilocalization in the topological insulator  $\text{Bi}_2\text{Te}_3$ . *Phys. Rev. Lett.*, 2011, **106**, 166805.
- [16] Le P.H., Wu K.H., Luo C.W., Leu J. Growth and characterization of topological insulator  $\text{Bi}_2\text{Se}_3$  thin films on  $\text{SrTiO}_3$  using pulsed laser deposition. *Thin Solid Films*, 2013, **534**, P. 659–665.
- [17] Cao H., Tian J., Miotkowski I., Shen T., Hu J., Qiao S., Chen Y.P. Quantized Hall effect and Shubnikov–de Haas oscillations in highly doped  $\text{Bi}_2\text{Se}_3$ : Evidence for layered transport of bulk carriers. *Phys. Rev. Lett.*, 2012, **108**, 216803.
- [18] Startsev V.E., D'yakina V.P., Cherepanov V.I., Volkenshtein N.V., Nasyrov R.Sh., Manakov V.G. Quadratic temperature dependence of the resistivity of tungsten single crystals. Role of surface scattering of electrons. *Sov. Phys. JETP*, 1980, **52** (4), P. 675–679.
- [19] Marchenkov V.V. Quadratic temperature dependence of magnetoresistivity of pure tungsten single crystals under static skin effect. *Low Temp. Phys.*, 2011, **37**, P. 852–855.

---

*Submitted 8 May 2024; revised 14 August 2024; accepted 15 August 2024*

#### Information about the authors:

*Alexandra N. Perevalova* – M. N. Mikheev Institute of Metal Physics of the Ural Branch of the Russian Academy of Sciences, 620108 Ekaterinburg, Russia; ORCID 0000-0002-8540-8720; domozhirova@imp.uran.ru

*Bogdan M. Fominykh* – M. N. Mikheev Institute of Metal Physics of the Ural Branch of the Russian Academy of Sciences, 620108 Ekaterinburg, Russia; ORCID 0000-0002-4755-3839; bogdan.fominyh@mail.ru

*Vasiliy V. Chistyakov* – M. N. Mikheev Institute of Metal Physics of the Ural Branch of the Russian Academy of Sciences, 620108 Ekaterinburg, Russia; ORCID 0000-0002-2684-256X; saddax@yandex.ru

*Vyacheslav V. Marchenkov* – M. N. Mikheev Institute of Metal Physics of the Ural Branch of the Russian Academy of Sciences, 620108 Ekaterinburg, Russia; ORCID 0000-0003-2044-1789; march@imp.uran.ru

*Conflict of interest:* the authors declare no conflict of interest.

## Quantum graph as a benchmark for persistent current

Igor Y. Popov<sup>1,a</sup>, Anton I. Popov<sup>1,b</sup>, Pavel A. Gilev<sup>1,c</sup>, Ashok Chatterjee<sup>1,2,d</sup>

<sup>1</sup>ITMO University, St. Petersburg, Russia

<sup>2</sup>GITAM University, Rudraram, Hyderabad, Telangana, India

<sup>a</sup>popov1955@gmail.com, <sup>b</sup>popov239@gmail.com, <sup>c</sup>grandarchtemplar@gmail.com, <sup>d</sup>acsp@uohyd.ernet.in

Corresponding author: Igor Y. Popov, popov1955@gmail.com

PACS 73.23.Ra, 73.63.Nm

**ABSTRACT** The problem of persistence current in nanosystems is studied. We demonstrate some simple theoretical observation which allows one to construct a benchmark for the persistence current. It can be used for improvement of the persistence current measurement procedure. The consideration is based on the quantum graph model. The benchmark is given by a graph with finite number of rings touching at one point with a lead attached to this point. It is assumed that the graph is plane and there exists a magnetic field orthogonal to the rings.

**KEYWORDS** quantum graph; persistent current

**ACKNOWLEDGEMENTS** This work was partially financially supported by Russian Science Foundation (grant 24-21-00107, <https://rscf.ru/en/project/24-21-00107/>).

**FOR CITATION** Popov I.Y., Popov A.I., Gilev P.A., Chatterjee A. Quantum graph as a benchmark for persistent current. *Nanosystems: Phys. Chem. Math.*, 2024, **14** (4), 469–472.

### 1. Introduction

Electronic properties at low dimensions with various geometries have continued to fascinate the scientific community over the years. Among such structures quantum rings are widely celebrated due to their peculiar electronic properties. The fabrication of nanoscale quantum rings [1, 2] in semiconductor heterostructures has aided in the understanding of the theoretical results on the subject [3, 4]. Later, more complicated ring structures were studied, e.g., the Möbius strip [5–7]. An electrical current induced in a resistive circuit will rapidly decay in the absence of an applied voltage. This decay reflects the tendency of the circuit's electrons to dissipate energy and relax to their ground state. However, quantum mechanics predicts that the electrons' many-body ground state (and, at finite temperature, their thermal equilibrium state) may itself contain a “persistent” current which flows through the resistive circuit without dissipating energy or decaying. A quantum ring can host persistent current [8] when it is threaded by a magnetic flux. A magnetic flux threading the ring breaks time-reversal symmetry, allowing the persistent current to flow in a particular direction around the ring. It is a quantum effect. This current exists although the metal of the ring is resistive. Due to the small size of the ring, the electron moves as a ballistic one even for non-zero temperature. Calculations [8] show that a micron-diameter ring will support a persistent current of about 1 nA at temperatures less than 1 K. This persistent current is closely related to the Aharonov-Bohm effect [9]. A reasonable number of studies [10–23] has been devoted to confirming the existence and properties of the persistent current in ringlike quantum structures.

However, measuring the persistent current is challenging for a number of reasons [24]. For example, the persistent current flows only within the ring and so cannot be measured using a conventional ammeter. Experiments to date have mostly used SQUIDs to infer the persistent current from the magnetic field it produces. A SQUID (superconducting quantum interference device) is a very sensitive magnetometer used to measure extremely weak magnetic fields, based on superconducting loops containing Josephson junctions. Interpretation of these measurements has been complicated by the SQUIDs' low signal-to-noise ratio and the uncontrolled back action of the SQUID's ac Josephson oscillations, which may drive non-equilibrium currents in the rings.

In the present paper, we demonstrate some simple theoretical observation which allows one to construct a benchmark for the persistence current. It can be used for improvement of the persistence current measurement procedure. We consider the quantum rings in the framework of quantum graph model which shows its usefulness for description of nanosystems (see, e.g. [25–31]). The magnetic field is assumed to be orthogonal to the plane of the rings. The benchmark is given by a graph with finite number of rings touching at one point with a lead attached to this point (see Fig. 1).

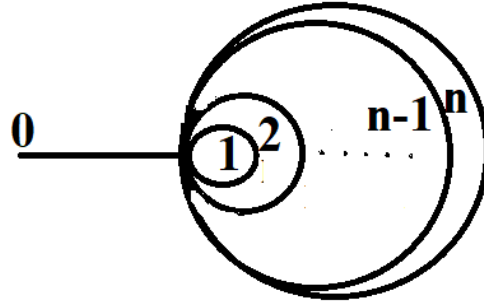


FIG. 1. Quantum graph structure. Edge numbering is shown.

**2. Model**

Consider the quantum graph  $\Gamma$  presented in Fig. 1. It consists of several rings  $\Gamma_j, j = 1, 2, \dots, n$ , and straight lead  $\Gamma_0$ . We assume that there is a homogeneous magnetic field  $\mathbf{B}$  orthogonal to the plane of the graph. We investigate the ballistic electron in this graph. Correspondingly, the model is given by the following operator acting in the space  $W_2^2(\Gamma)$ :

$$\begin{aligned} H\psi_0 &= -\frac{d^2}{dx^2}, & x \in \Gamma_0, \\ H\psi_j &= \left(i\frac{d}{dx} + B\pi R_j \Phi_0^{-1}\right)^2, & j = 1, 2, \dots, n, x \in \Gamma_j, \end{aligned} \tag{1}$$

where  $\Phi_0 = 2\pi\hbar c/|e|$  is the magnetic flux quantum playing a role of a unit for the magnetic flux in the system,  $c$  is the speed of light,  $|e|$  is the electron charge,  $x$  is the length of the arc starting with the graph vertex (counter clock wise),  $\hbar$  is the Planck constant,  $R_j$  is the radius of  $j$ -th ring,  $B$  is the magnetic field,

$$\psi = \begin{pmatrix} \psi_0 \\ \psi_1 \\ \dots \\ \psi_n \end{pmatrix}.$$

As for the graph vertex  $x_0$ , we pose here the magnetic Kirchhoff conditions named also the Griffith conditions:

$$\begin{cases} \psi_j|_{x_0} = \psi_p|_{x_0}, & j \neq p, \\ \frac{d\psi_0}{dx}|_{x_0} + \sum_{j=1}^n (-1)^{\sigma_j} \left(\frac{d}{dx} - iB\pi R_j \Phi_0^{-1}\right)\psi_j|_{x_0} = 0, \end{cases} \tag{2}$$

where  $\sigma_j = 0$  for outgoing edge and  $\sigma_j = 1$  for incoming edge.

Let us determine the persistent current in the rings. Consider the scattering problem for the graph. The electron wave function  $\psi$  in semi-infinite lead “0” has the form

$$\psi_0 = e^{ikx} + r e^{-ikx}, \tag{3}$$

where  $k$  is the wave number of the electron,  $r$  is the reflection coefficient. The magnetic field has no influence on the electron in this one-dimensional straight lead. Naturally, the situation changes in the rings. Let the  $j$ -th ring have radius  $R_j$ . Then, the wave function has the following form

$$\psi_j = a_j e^{i(k+B\pi R_j \Phi_0^{-1})x} + b_j e^{i(-k+B\pi R_j \Phi_0^{-1})x}, \quad j = 1, 2, \dots, n, \tag{4}$$

Conditions (2) gives one the following system for coefficients  $r, a_j, b_j, j = 1, \dots, n$ :

$$\begin{cases} 1 + r = a_j + b_j, & j = 1, 2, \dots, n, \\ 1 + r = a_j e^{i(k+B\pi R_j \Phi_0^{-1})2\pi R_j} + b_j e^{i(-k+B\pi R_j \Phi_0^{-1})2\pi R_j}, & j = 1, 2, \dots, n, \\ ikr - ik = ik \sum_{j=1}^n \left( a_j \left(1 - e^{i(k+B\pi R_j \Phi_0^{-1})2\pi R_j}\right) - b_j \left(1 - e^{i(-k+B\pi R_j \Phi_0^{-1})2\pi R_j}\right) \right). \end{cases} \tag{5}$$

Transformation of the first  $j$  pairs of equations from (5) gives one:

$$\left\{ \begin{array}{l} a_j = -\frac{1 - e^{i(-k+B\pi R_j \Phi_0^{-1})2\pi R_j}}{e^{i2B\pi^2 R_j^2} 2i \sin(2\pi k R_j)} (1+r), \quad j = 1, 2 \dots n, \\ b_j = \frac{1 - e^{i(k+B\pi R_j \Phi_0^{-1})2\pi R_j}}{e^{i2B\pi^2 R_j^2} 2i \sin(2\pi k R_j)} (1+r), \quad j = 1, 2 \dots n, \\ ikr - ik = ik \sum_{j=1}^n \left( a_j \left( 1 - e^{i(k+B\pi R_j \Phi_0^{-1})2\pi R_j} \right) - b_j \left( 1 - e^{i(-k+B\pi R_j \Phi_0^{-1})2\pi R_j} \right) \right). \end{array} \right. \quad (6)$$

The persistent current in the  $j$ -th ring is determined as follows [23]:

$$I_j = \frac{1}{2ki} \left( \overline{\psi_j} \frac{d}{dx} \psi_j - \psi_j \frac{d}{dx} \overline{\psi_j} - i \frac{2B\pi R_j}{\Phi_0} \overline{\psi_j} \psi_j \right). \quad (7)$$

By inserting expressions (4) in (7), one obtains:

$$I_j = |a_j|^2 - |b_j|^2. \quad (8)$$

Expressions (6) gives one

$$\left\{ \begin{array}{l} |a_j|^2 = \frac{\sin^2(-\pi k R_j + B\pi^2 R_j^2 (\Phi_0)^{-1})}{\sin^2(\pi k R_j)} |1+r|^2, \quad j = 1, 2 \dots n, \\ |b_j|^2 = \frac{\sin^2(\pi k R_j + B\pi^2 R_j^2 (\Phi_0)^{-1})}{\sin^2(\pi k R_j)} |1+r|^2, \quad j = 1, 2 \dots n. \end{array} \right. \quad (9)$$

Hence, the ratio of the persistent currents in  $j$ -th and  $s$ -th rings does not depend on the number  $n$  of rings but depends on their radii, the magnetic field and the electron energy:

$$\frac{I_j}{I_s} = \frac{\sin(2B\pi^2 R_j^2 (\Phi_0)^{-1}) \sin(2\pi k R_s)}{\sin(2B\pi^2 R_s^2 (\Phi_0)^{-1}) \sin(2\pi k R_j)}. \quad (10)$$

It allows one to construct ‘‘a benchmark’’ for the persistent current. One can add or remove rings without changing the ratio (10) for other pairs of rings. If one consider  $\ln I_j$  then the difference  $\ln I_j - \ln I_s$  does not depend on the number of rings. One can collect rings to construct a benchmark with fixed step of  $\ln I_j$  between the neighbour rings ( $\ln I_{j+1} - \ln I_j$ ). Moreover, if one chooses some pair of rings and modifies the graph by adding a ring then the step of the logarithm of the persistent current in the chosen pair of rings ( $\ln I_{j+1} - \ln I_j$ ) does not change. It means that one can extend the benchmark by adding rings without destroying the scale of the initial benchmark.

## References

- [1] Lorke A., Luyken R.J., Govorov A.O., Kotthaus J.P., Garcia J.M., Petroff P.M. Spectroscopy of Nanoscopic Semiconductor Rings. *Phys. Rev. Lett.*, 2000, **84**, P. 2223.
- [2] Fuhrer A., Luscher S., Ihn T., Heinzel T., Ensslin K., Wegscheider W., Bichler M. Energy spectra of quantum rings. *Nature*, 2001, **413**, P. 822.
- [3] Chakraborty T., Pietiläinen P. Electron-electron interaction and the persistent current in a quantum ring. *Phys. Rev. B*, 1994, **50**, P. 8460.
- [4] Halonen V., Pietiläinen P., Chakraborty T. Optical absorption spectra of quantum dots and rings with a repulsive scattering centre. *Europhys. Lett.*, 1996, **33**, P. 377.
- [5] Popov I.Y. A model of charged particle on the flat Möbius strip in a magnetic field. *Nanosystems: Phys. Chem. Math.*, 2023, **14**(4), P. 418–420.
- [6] Popov I.Y. Magnetic Schrödinger operator on the flat Möbius strip. *Banach J. Math. Anal.*, 2024, <https://doi.org/10.1007/s43037-024-00360-y>.
- [7] Guo Z.L., Gong Z.R., Dong H., Sun C.P. Möbius graphene strip as a topological insulator. *Phys. Rev. B*, 2009, **80**, P. 195310.
- [8] Büttiker M., Imry Y., Landauer R. Josephson behavior in small normal one-dimensional rings. *Phys. Lett. A*, 1983, **96**, P. 365.
- [9] Aharonov Y., Bohm D. Significance of Electromagnetic Potentials in the Quantum Theory. *Phys. Rev.*, 1959, **115**, P. 485.
- [10] Cheung H.F., Gefen Y., Riedel E.K., Shih W.H. Persistent currents in small one-dimensional metal rings. *Phys. Rev. B*, 1988, **37**, P. 6050.
- [11] Cheung H.F., Gefen Y., Riedel E.K. Isolated rings of mesoscopic dimensions. Quantum coherence and persistent currents. *IBM J. Res. Dev.*, 1988, **32**, P. 359.
- [12] Cheung H.F., Riedel E.K., Gefen Y. Persistent Currents in Mesoscopic Rings and Cylinders. *Phys. Rev. Lett.*, 1989, **62**, P. 587.
- [13] Lévy L.P., Dolan G., Dunsmuir J., Bouchiat H. Magnetization of mesoscopic copper rings: Evidence for persistent currents. *Phys. Rev. Lett.*, 1990, **64**, P. 2074.
- [14] Montambaux G., Bouchiat H., Sigeti D., Friesner R. Persistent currents in mesoscopic metallic rings: Ensemble average. *Phys. Rev. B*, 1990, **42**, P. 7647 (R).
- [15] Chandrasekhar V., Webb R.A., Brady M.J., Ketchen M.B., Gallagher W.J., Kleinsasser A. Magnetic response of a single isolated gold loop. *Phys. Rev. Lett.*, 1991, **67**, P. 3578.
- [16] Avishai Y., Hatsugai Y., Kohmoto M. Persistent currents and edge states in a magnetic field. *Phys. Rev. B*, 1993, **47**, P. 9501.
- [17] Bouzerar G., Poilblanc D., Montambaux G. Persistent currents in one-dimensional disordered rings of interacting electrons. *Phys. Rev. B*, 1994, **49**, P. 8258.
- [18] Maillé D., Chapelier C., Benoit A. Experimental observation of persistent currents in GaAs-AlGaAs single loop. *Phys. Rev. Lett.*, 1993, **70**, P. 2020.
- [19] Sankar I.V., Monisha P.J., Sil S., Ashok Chatterjee. Persistent current and existence of metallic phase in a Holstein-Hubbard quantum ring. *Physica E*, 2015, **73**, P. 175–180.
- [20] Ashok Chatterjee, Smolkina M.O., Popov I.Y. Persistent current in a chain of two Holstein-Hubbard rings in the presence of Rashba spin-orbit interaction. *Nanosystems: Physics, Chemistry, Mathematics*, 2019, **10**, P. 50–62.

- [21] Lavanya C. U., Ashok Chatterjee. Persistent Charge and Spin Currents in the 1D Holstein-Hubbard ring at half filling and at away from half filling by Bethe-ansatz approach. *J. Mag. Mag. Mat.*, 2021, **529**, P. 167711.
- [22] Mijanur Islam, Tutul Biswas, Saurabh Basu. Effect of magnetic field on the electronic properties of an  $\alpha - T_3$  ring. *Phys. Rev. B*, 2023, **108**, P. 085423.
- [23] Hisham M. Fayad, Mazen M. Abadla. Mesoscopic Transport and Persistent Current in the Aharonov-Bohm Rings. *Journal of Al Azhar University-Gaza (ICBAS Special Issue)*, 2010, **12**, P. 88–94.
- [24] Bleszynski-Jayich A.C., Shanks W.E., Peaudecerf B., Ginossar E., von Oppen F., Glazman L., Harris J.G.E.. Persistent currents in normal metal rings: comparing high-precision experiment with theory. *Science*, 2009, **326**, P. 272.
- [25] Berkolaiko G., Kuchment P. *Introduction to Quantum Graphs*. AMS, Providence, 2012.
- [26] Lipovsky J. Quantum Graphs And Their Resonance Properties. *Acta Physica Slovaca*, 2016, **66**(4), P. 265–363.
- [27] Exner P., Keating P., Kuchment P. Sunada T., Teplyaev A. Analysis on graph and its applications. AMS, Providence, 2008.
- [28] Exner P., Manko S.S. Spectra of magnetic chain graphs: coupling constant perturbations. *Journal of Physics A: Mathematical and Theoretical*, 2015, **48**(12), P. 125302.
- [29] Popov I.Y., Skorynina A.N., Blinova I.V. On the existence of point spectrum for branching strips quantum graph. *Journal of Mathematical Physics*, 2014, **55**, P. 033504/1-20.
- [30] Rakhmanov S.Z., Tursunov I.B., Matyokubov Kh.Sh., Matrasulov D.U. Optical high harmonic generation in a quantum graph. *Nanosystems: Phys. Chem. Math.*, 2023, **14**(2), P. 164–171.
- [31] Sabirov K.K., Yusupov J.R., Matyokubov Kh.Sh., Susanto H., Matrasulov D.U. Networks with point-like nonlinearities. *Nanosystems: Phys. Chem. Math.*, 2022, **13**(1), P. 30–35.

---

Submitted 09 May 2024; revised 05 August 2024; accepted 20 August 2024

*Information about the author:*

Igor Y. Popov – Center of Mathematics, ITMO University, Kroverkskiy, 49, St. Petersburg, 197101, Russia; ORCID 0000-0002-5251-5327; popov1955@gmail.com

Anton I. Popov – Center of Mathematics, ITMO University, Kroverkskiy, 49, St. Petersburg, 197101, Russia; ORCID 0000-0001-7137-4067; popov239@gmail.com

Pavel A. Gilev – Center of Mathematics, ITMO University, Kroverkskiy, 49, St. Petersburg, 197101, Russia; grandarchtemplar@gmail.com

Ashok Chatterjee – Center of Mathematics, ITMO University, Kroverkskiy, 49, St. Petersburg, 197101, Russia; GITAM School of Sciences, Department of Physics, GITAM University, Rudraram, Hyderabad 502329, Telangana, India; ORCID 0000-0002-9658-7162; acsp@uohyd.ernet.in

*Conflict of interest:* the author declares no conflict of interest.

## Diameter dependent geometrical and electrical properties of zigzag HgSe nanotubes: A density functional study

Monoj Das

Department of Physics, Gushkara Mahavidyalaya, Gushkara, 713128, India

dsmonoj@gmail.com

PACS 61.46.Fg, 71.20.-b, 73.63.Fg

**ABSTRACT** Using density functional theory, evolution of geometrical and electrical properties like wall width, binding energy, strain energy, band structure, density of states etc. of several zigzag HgSe nanotubes with diameters in the range of 11.59 to 21.74 Å are systematically investigated. It is noted that the walls of the nanotubes are gradually becoming thin with increasing tube diameter. This study reveals that the stability of the zigzag HgSe nanotube increases with increasing diameter. It is also perceived that zigzag HgSe nanotubes obey classical elasticity law. Band structure analysis reflects that all the zigzag HgSe nanotubes are direct band gap semiconductors and their band gaps slowly decrease with increasing diameter.

**KEYWORDS** nanotube, density functional theory, binding energy, band-gap

**FOR CITATION** Das M. Diameter dependent geometrical and electrical properties of zigzag HgSe nanotubes: A density functional study. *Nanosystems: Phys. Chem. Math.*, 2024, **15** (4), 473–480.

### 1. Introduction

The focal point of modern nanotechnology research is nanotubes owing to their vast potentials. Nanotubes may be successfully applied to a wide range of applications, such as field effect transistor, photovoltaic device, thermoelectric device, lasers, light emitting diodes and so on. For productive use of nanotubes in nanodevices, we must have a detail understanding of their characteristics. Synthesis of carbon nanotube [1] expedited the research on nanotubes and consequently nanotubes of many non-carbon materials like BN, SiC, CdS, ZnO, ZnS, WS<sub>2</sub>, MoS<sub>2</sub>, CdSe [2–8] etc. were synthesized. Recently, HgSe based nanostructures are seeking enormous attention attributed to their lucrative properties such as high electron mobility, high electron density, etc. [9]. In bulk form, HgSe has nearly zero band gap making it a semimetal [10]. Various types of nanostructures such as nanorods, nanowires, nano particles, quantum dots, thin film etc. of this material have already been synthesized [11–18]. In addition, HgSe nanotubes are also synthesized. R. R. Arnepalli et al. [19] first synthesized HgSe nanotubes by spray deposition of solvothermally synthesized HgSe-Iodine nanoparticles. R. R. Arnepalli et al. [20] also synthesized multi walled HgSe nanotubes by employing mercury iodide catalyst. Various forms of HgSe nanostructures are successfully utilized in mid infrared photo detector, thermoelectric devices, leds etc. [21–28]. For many years, HgSe has been the subject of many theoretical studies. By employing linear muffin-tin orbital method Delin et al. [29] reported that HgSe in zinc-blende phase exhibits semi-metallic property. Radescu et al. [30] studied the pressure-driven phase transitions in HgSe. Employing density functional theory, Duz et al. [31] investigated the mechanical properties of HgSe polymorphs under high pressure. The structural, electrical, optical and thermodynamic features of HgSe crystal are reported by Secuk et al. [32]. Using density functional theory, Li et al. [33] reported that under in plane tensile strain, HgSe monolayer endured insulator to topological insulator phase transition. Very recently, Habibes et al. [34] studied the electronic and optical properties of Mn doped HgSe for spintronic device applications. However, as of yet, no theoretical work on HgSe nanotubes has been published. To use HgSe nanotubes in a range of nanodevices, it is essential to understand their properties. Here, for the first time, the properties of zigzag HgSe nanotubes are reported using density functional theory. At this point, it is important to highlight that density functional theory underestimates the band gap value in semiconductors. However, we can get a qualitative view of the trend of band gap variation of a nanotube with respect to diameter. Moreover, several researchers have used density functional theory to study the properties of HgSe nanostructures and some findings (such as semi metallic property) agree with the experimental observations. Therefore, density functional theory can be used to predict the properties of zigzag HgSe nanotubes. In the following section, the methods and important parameters are described. The results are enumerated in Section 3 and finally the significant findings are summarized in Section 4.

### 2. Approach and method

The geometrical and electronic properties of zigzag HgSe nanotubes are extracted by using SIESTA package [35, 36] that implements Density Functional Theory. The exchange and correlation energy is represented by generalized gradient approximated (GGA) Perdew–Burke–Ernzerhof (PBE) functional [37]. The Monkhorst–Pack method [38] with

a  $25 \times 1 \times 1$  K-point mesh is used to sample the Brillouin Zone. Throughout the calculations, the real space mesh cut-off energy is taken as 460 Ry. The energy convergence limit for self-consistent fields (SCF) is set at  $10^{-5}$  eV. During all the calculations, a vacuum space of 25 Å is kept so as to neglect interaction between the nanotube and its periodic image. The most favourable geometry is obtained by setting force convergence limit to 0.001 eV/Å.

In this study, HgSe nanosheet (HgSeNS) as depicted in Fig. 1 is rolled along the chiral vector  $\vec{C} = x\vec{u} + y\vec{v}$  to obtain HgSe( $x, y$ ) nanotube. The tube axis is always perpendicular to the chiral vector. For zigzag nanotubes,  $y = 0$ . Here, the properties of HgSe(8,0) to HgSe(15,0) are investigated systematically.

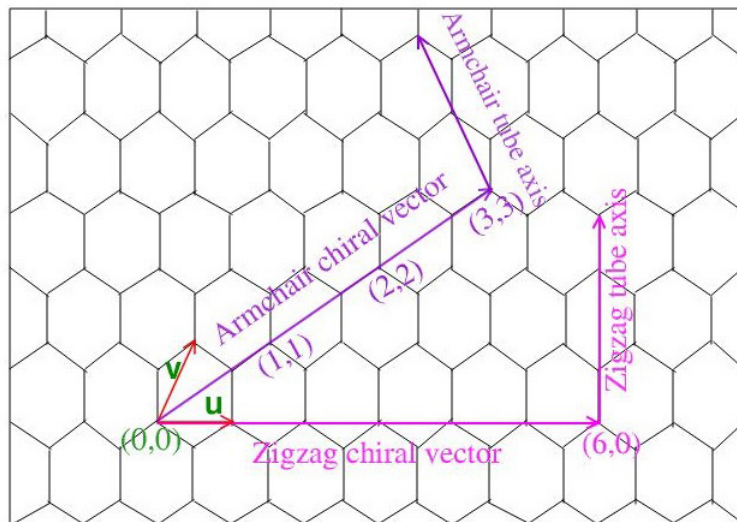


FIG. 1. The chiral vector and tube axis in HgSe nanosheet

### 3. Results and discussions

Initially, the HgSe nanosheet's relaxed geometrical structure is identified. It is perceived that the relaxed HgSeNS is buckled like having a buckled height of 0.39 Å. The mean Hg–Se bond length in HgSeNS is 2.62 Å. The optimized structure of HgSeNS is displayed in Fig. 2.

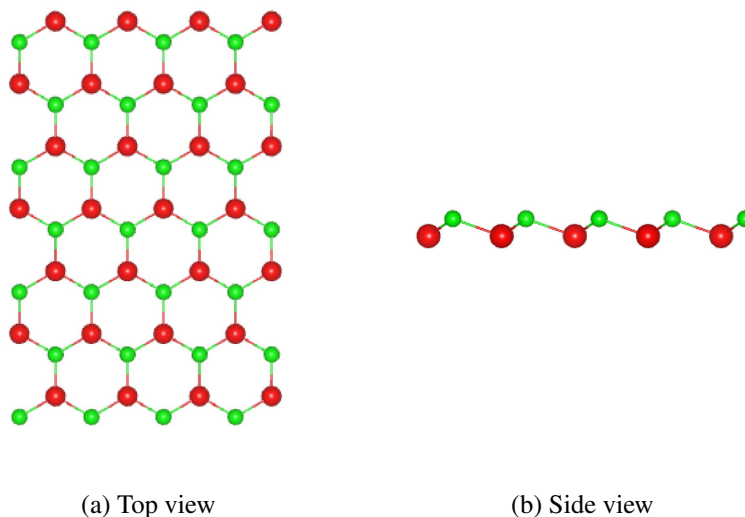


FIG. 2. Optimized geometrical structure of HgSe nanosheet. The bigger (red) spheres represent Hg atoms and smaller (green) spheres denote Se atoms respectively

This optimized nanosheet is adopted to construct various zigzag HgSe nanotubes (ZHgSeNTs) by folding this sheet along various zigzag chiral vectors. These nanotubes are allowed to undergo further relaxation. After relaxation, the nanotube surfaces take wave like pattern as depicted in Fig. 3. The more electronegative Se atoms move away from the axis compared to the Hg atoms. Thus, it appears that the surface of the nanotube is composed of two coaxial cylinders, with Se atoms arranged on the outer cylinder and Hg atoms on the inner cylinder. Note that, the strong covalent bonds continue

to hold the Hg atoms in the inner cylinder and the Se atoms in the outer cylinder together. Similar surface configurations have also been observed in nanotubes made of AlN, CdS, ZnTe [39–41] etc. The wall width of the nanotubes can be calculated by measuring the difference in radius between the inner and outer cylinders. Wall widths of all the nanotubes are estimated and are displayed in the Table 1. The variation of wall width with respect to diameter is also presented in Fig. 4. Calculations show that the wall width of zigzag HgSe nanotube steadily decreases from 0.547 to 0.421 Å upon increasing diameter from 11.59 to 21.74 Å. Therefore, nanotube walls are progressively becoming thin with enlarging tube diameter. It is important to mention that wall thickness is an indicator of surface buckling in nanotubes. When a nanosheet is rolled into a nanotube, strain or deformation related to this process causes buckling in the nanotube surface. In comparison to larger diameter nanotubes, those with a smaller diameter exhibit more buckling and, thus, a thicker wall due to their higher strain energy.

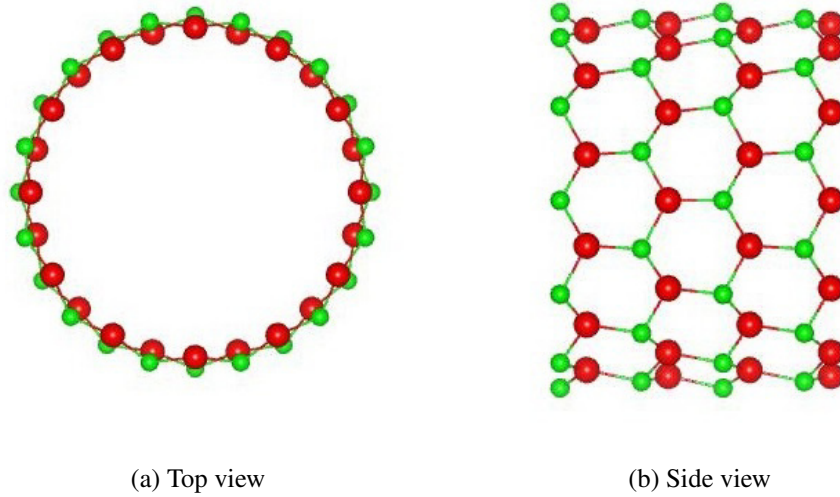


FIG. 3. Energetically relaxed geometrical structure of HgSe(12,0) nanotube. The bigger (red) spheres indicate Hg atoms and smaller (green) balls represent Se atoms respectively

TABLE 1. Diameter, wall thickness, binding energy, strain energy, band gap values of various zigzag HgSe nanotubes

Nanotube	Diameter (Å)	Wall Thickness (Å)	Binding Energy (eV)	Strain Energy (eV)	Band Gap (eV)
HgSe(8,0)	11.59	0.547	1.918	0.071	0.60
HgSe(9,0)	13.08	0.523	1.927	0.062	0.55
HgSe(10,0)	14.50	0.502	1.934	0.055	0.51
HgSe(11,0)	15.96	0.483	1.940	0.049	0.47
HgSe(12,0)	17.40	0.466	1.944	0.045	0.43
HgSe(13,0)	18.85	0.450	1.948	0.041	0.39
HgSe(14,0)	20.30	0.435	1.951	0.038	0.35
HgSe(15,0)	21.74	0.421	1.954	0.035	0.32

The stability of HgSe nanosheet and various zigzag HgSe nanotubes can be assessed by determining their binding energies using the following formula:

$$E_{BE} = -\frac{E(\text{HgSe}) - NE(\text{Hg}) - NE(\text{Se})}{2N}.$$

Here,  $E(\text{HgSe})$  represents the total energy of relaxed HgSe nanosheet or nanotube consisting of  $N$  Hg and  $N$  Se atoms.  $E(\text{Hg})$  and  $E(\text{Se})$  denote energy of isolated Hg and Se atom, respectively. It is observed that the binding energy of

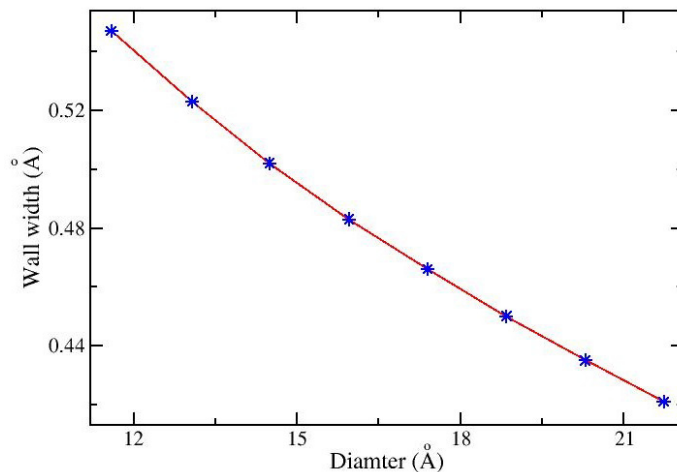


FIG. 4. Plot of wall thickness vs. diameter of zigzag HgSe nanotubes

HgSeNS is 1.989 eV. The binding energies of ZHgSeNTs are determined and written in Table 1. The variation of binding energy with respect to diameter is also graphically plotted in Fig. 5. The binding energy of ZHgSeNT is increasing from 1.918 to 1.954 eV when the diameter is altered from 11.59 to 21.74 Å. Therefore, ZHgSeNTs with smaller diameters are relatively less stable than those with greater diameters. This can be explained by the fact that decreasing the diameter causes the bond to bend more, reducing the stability.

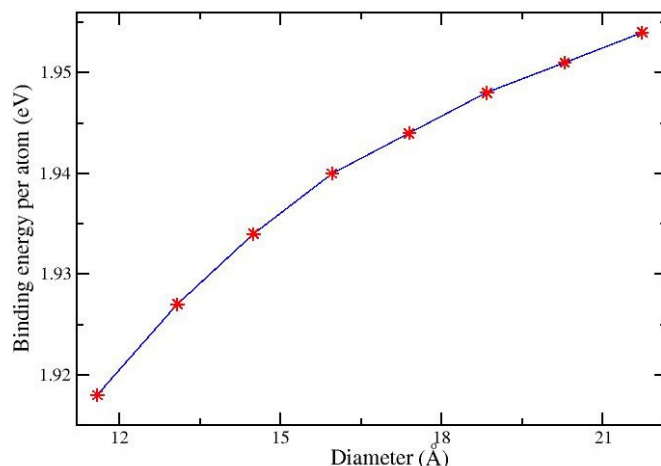


FIG. 5. Variation of binding energy per atom as a function of tube diameter of zigzag HgSe nanotubes

To figure out the energy required to create HgSe nanotubes with different diameters from HgSe nanosheet, the strain energies of HgSe nanotubes are evaluated. The strain energy,  $E_s$  is just the binding energy difference between HgSeNS and ZHgSeNT, i.e.

$$E_s = E_{BE}(\text{HgSeNS}) - E_{BE}(\text{ZHgSeNT}).$$

Here,  $E_{BE}(\text{HgSeNS})$  and  $E_{BE}(\text{ZHgSeNT})$  represent binding energy of HgSe nanosheet and zigzag HgSe nanotube, respectively. The estimated strain energy of every nanotube is displayed in Table 1. The classical continuum elasticity theory reflects that strain energy,  $E_s$ , must vary as  $E_s = m/D^2 + c$  against diameter ( $D$ ) where  $m$  and  $c$  are constants [42]. The strain energy is plotted against  $1/D^2$  in Fig. 6 to determine whether ZHgSeNTs comply with classical elasticity theory or not. The straight line nature of the plot signifies that ZHgSeNTs obey classical elasticity theory. The values of the constants  $m$  and  $c$ , according to least square fitting, are 6.744 and 0.022, respectively.

One of the important electrical characteristics of a material is its band gap, which dictates the material's use in technological applications. In nanoelectronics, figuring out different ways to accomplish band gap engineering is also crucial. The band gaps of HgSeNS and ZHgSeNTs are estimated in order to evaluate the importance of these nanostructures in different technological applications. The findings are shown in Table 1. The variation of band gap in terms of nanotube diameter is also plotted in Fig. 7. It is marked that HgSeNS is a low direct band gap semiconductor with a band gap of 0.12 eV as shown in Fig. 8. Band structures of various ZHgSeNTs are also depicted in Fig. 9. It is perceived that all

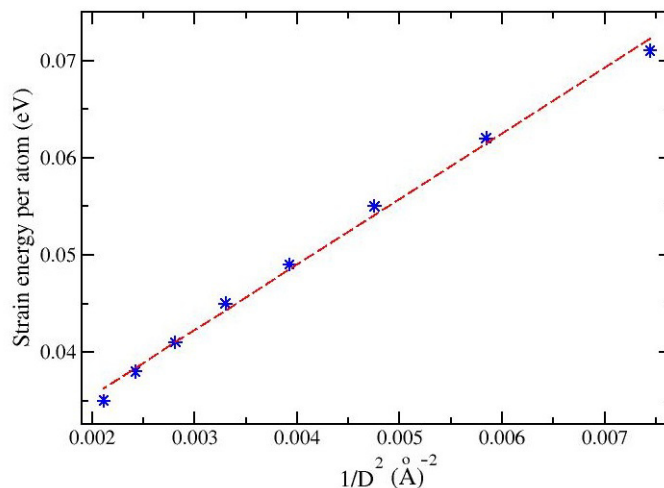


FIG. 6. The plot of strain energy per atom as a function of  $1/D^2$ . The best fit curve is shown by the dotted line

the ZHgSeNTs are direct band gap semiconductors and their band gaps are slowly decreasing from 0.60 to 0.32 eV when diameter is increased from 11.59 to 21.74 Å. Therefore, one can tune band gap within a range of 0.28 eV by altering diameter from 11.59 to 21.74 Å. This trend of decreasing band gap with increasing tube diameter is in the same line with other II–VI semiconductors like CdS, ZnTe, ZnO, ZnS etc. nanotubes [40, 41, 43, 44]. It is commonly recognised that II–VI semiconductors show the quantum confinement effect, in which the band gap widens as the nanostructure’s size decreases. This quantum confinement effect can account for the band gap rise in zigzag HgSe nanotubes with decreasing nanotube diameter.

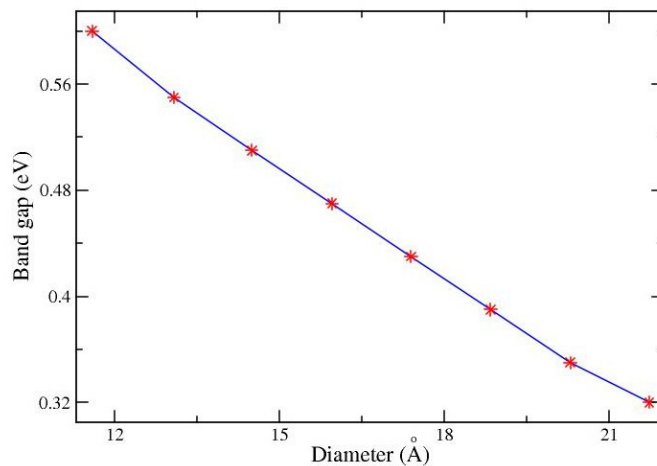


FIG. 7. Band gap vs. diameter plot of zigzag HgSe nanotubes

To support the pattern of decreasing band gap with increasing tube diameter, the total density of states of various ZHgSeNTs are determined and displayed in Fig. 10. This graph makes it very evident that the band gap becomes smaller for nanotube of larger diameter.

#### 4. Summary

In conclusion, density functional theory is used to present the variation of geometrical and electrical properties with respect to diameter of various zigzag HgSe nanotubes. It is predicted that the walls of the nanotubes gradually get thinner as the diameters of the nanotubes increase. It is further noticed that zigzag HgSe nanotubes become increasingly stable on increasing their diameter. Strain energy analysis manifests that all the zigzag HgSe nanotubes adhere to the classical elasticity law. Band structure calculation signifies that the variation of band gap with diameter is congruous with other II–VI semiconductor nanotubes and the band gap energy may be calibrated over practically useful range of 0.32 to 0.60 eV. These results might help to expedite future studies on HgSe nanotubes.

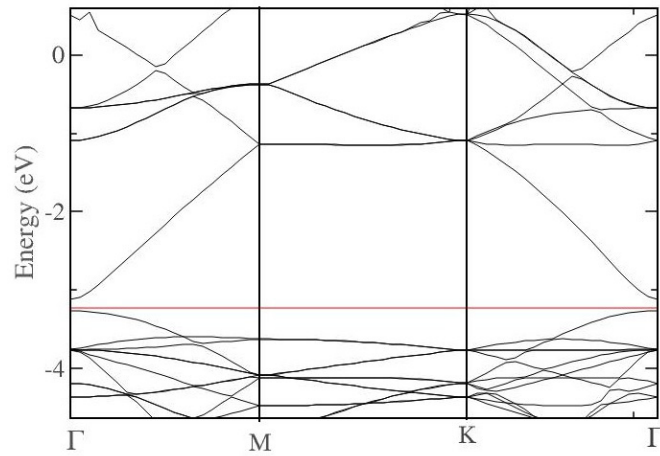


FIG. 8. Band structure plot of HgSe nanosheet. The fermi energy level is shown by the solid red line

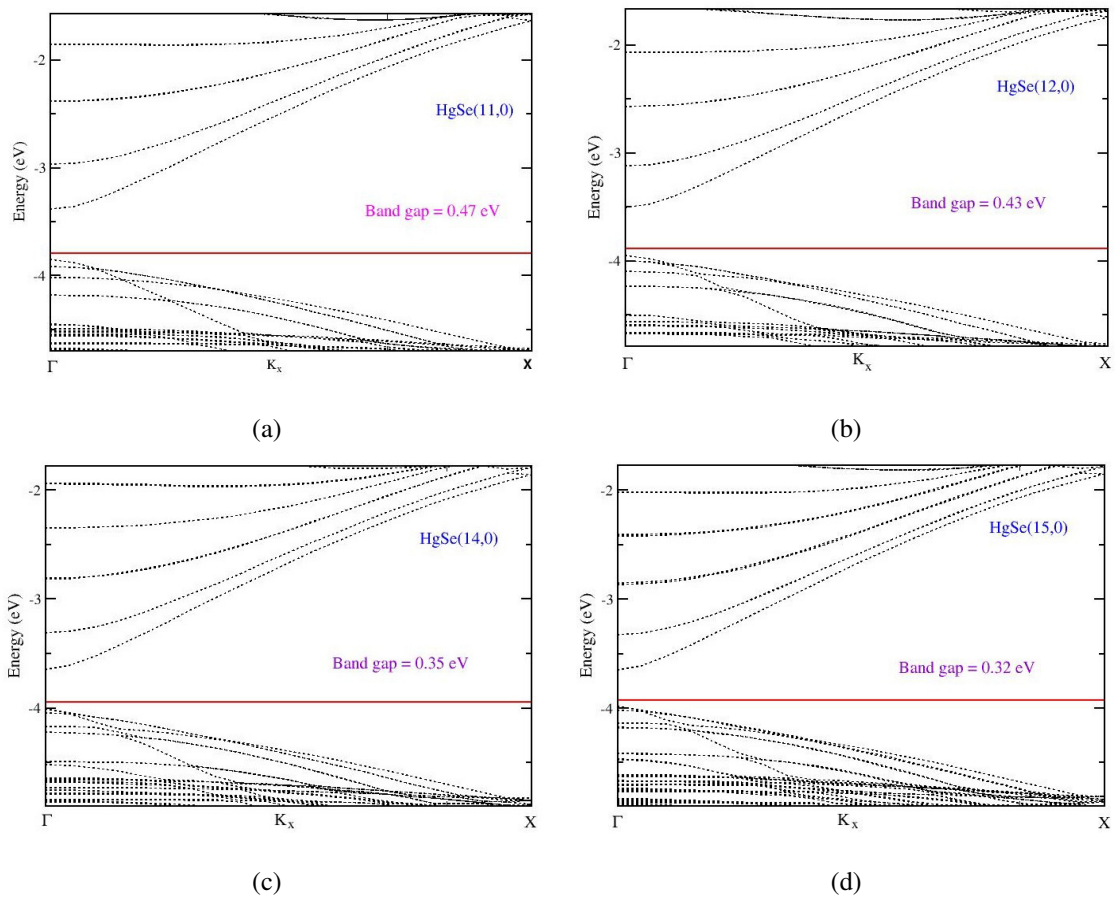


FIG. 9. Band structure plots of various zigzag HgSe nanotubes. The fermi energy level is represented by the solid red line

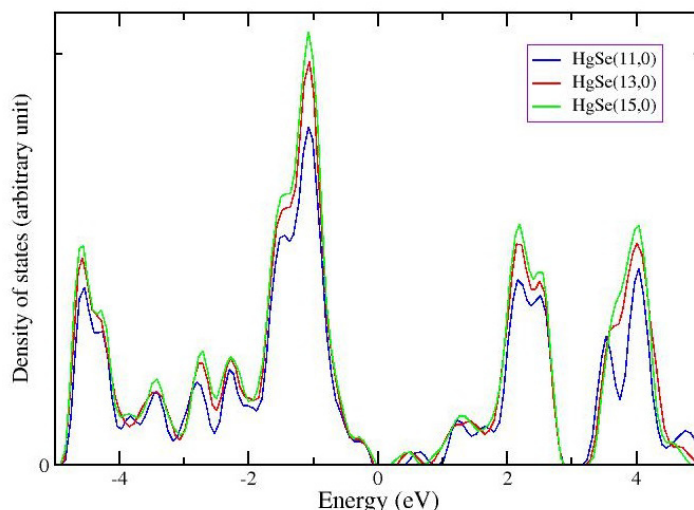


FIG. 10. The total density of states plot of different zigzag HgSe nanotubes. Here, the Fermi energy is scaled down to zero

## References

- [1] Iijima S. Helical microtubules of graphitic carbon. *Nature*, 1991, **354**, P. 56–58.
- [2] Chopra N.G. et al. Boron Nitride Nanotubes. *Science*, 1995, **269** (5226), P. 966–967.
- [3] Huu C.P., Keller N., Ehret G., Ledoux M.J. The First Preparation of Silicon Carbide Nanotubes by Shape Memory Synthesis and Their Catalytic Potential. *J. of Catalysis*, 2001, **200** (2), P. 400–410.
- [4] Ling T., Wu M., Du X. Template synthesis and photovoltaic application of CdS nanotube arrays. *Semiconductor Science and Technology*, 2012, **27** (5), 055017.
- [5] Madlol R.A.A. Structural and optical properties of ZnO nanotube synthesis via novel method. *Results in Physics*, 2017, **7**, P. 1498–1503.
- [6] Guo M., Song M., Li S., Yin Z., Song X., Bu Y. Facile and economical synthesis of ZnS nanotubes and their superior adsorption performance for organic dyes. *Cryst. Eng. Comm.*, 2017, **19**, P. 2380–2393.
- [7] Sinha S.S., Yadgarov L., Aliev S.B., Feldman Y., Pinkas I., Chithaiah P., Ghosh S., Idelevich A., Zak A., Tenne R. MoS<sub>2</sub> and WS<sub>2</sub> Nanotubes: Synthesis, Structural Elucidation, and Optical Characterization. *The J. of Physical Chemistry C*, 2021, **125** (11), P. 6324–6340.
- [8] Shen Q., Jiang L., Miao J., Hou W., Zhu J.J. Sonochemical synthesis of CdSe nanotubes. *Chem. Commun.*, 2008, **14**, P. 1683–1685.
- [9] Ren J., Eason D.B., Churchill L.E., Yu Z., Boney C., et al. Integrated heterostructure devices composed of II–VI materials with Hg-based contact layers. *J. of Crystal Growth*, 1994, **138**, P. 455–463.
- [10] Truchseß M.V., Pfeuffer-Jeschke A., Becker C.R., Landwehr G., Batke E. Electronic band structure of HgSe from Fourier transform spectroscopy. *Phys. Rev. B*, 2000, **61**, 1666.
- [11] Ding T., Zhang J.R., Hong J.M., Zhu J.J., Chen H.Y. Sonochemical synthesis of taper shaped HgSe nanorods in polyol solvent. *J. of Crystal Growth*, 2004, **260**, P. 527–531.
- [12] Zare M.E., Niasari M.S., Sobhani A. Simple sonochemical synthesis and characterization of HgSe nanoparticles. *Ultrasonics Sonochemistry*, 2012, **19** (5), P. 1079–1086.
- [13] Ding T., Zhu J.J., Hong J.M. Sonochemical preparation of HgSe nanoparticles by using different reductants. *Materials Letters*, 2003, **57**, P. 4445–4449.
- [14] Wang S., Guo T., Cao S. The Influence of Synthetic Parameters on HgSe QDs. *ACS Omega*, 2023, **8** (47), P. 44804–44811.
- [15] Mahalingam T., Kathalingam A., Sanjeeviraja C., Chandramohan R., Chu J.P., Kim Y.D., Velumani S. Electrodeposition and characterization of HgSe thin films. *Materials Characterization*, 2007, **58** (8–9), P. 735–739.
- [16] Hankare P.P., Bhuse V.M., Garadkar K.M., Jadhav A.D. A novel method to grow polycrystalline HgSe thin film. *Materials Chemistry and Physics*, 2001, **71** (1), P. 53–57.
- [17] Hankare P.P., Bhuse V.M., Garadkar K.M., Delekar S.D., Mulla I.S. Chemical deposition of cubic CdSe and HgSe thin films and their characterization. *Semiconductor Science and Technology*, 2004, **19**, 70.
- [18] Bazarganipour M., Sadri M., Davar F., Niasari M.S. Mercury selenide nanorods: Synthesis and characterization via a simple hydrothermal method. *Polyhedron*, 2011, **30** (6), P. 1103–1107.
- [19] Arnepalli R.R., Dutta V. Nanotubes in Low Temperature Spray Deposited Nanocrystalline HgSe: I thin films. *MRS Online Proceedings Library*, 2006, **922**, 209.
- [20] Arnepalli R.R., Dutta V., Singh V.N. Multiwalled HgX (X = S, Se, Te) Nanotubes Formed with a Mercury Iodide Catalyst in Nanocrystalline Thin Films Spray-Deposited at Low Temperature. *Advanced Materials*, 2008, **20** (10), P. 1945–1951.
- [21] Jana M.K., Chithaiah P., Murali B., Krupanidhi S.B., Biswasa K., Rao C.N.R. Near infrared detectors based on HgSe and HgCdSe quantum dots generated at the liquid-liquid interface. *J. Mater. Chem. C*, 2013, **1**, P. 6184–6187.
- [22] Chen M., Hao Q., Luo Y., Tang X. Mid-Infrared Intraband Photodetector via High Carrier Mobility HgSe Colloidal Quantum Dots. *ACS Nano*, 2022, **16** (7), P. 11027–11035.
- [23] Zhao X., Mu G., Tang X., Chen M. Mid-IR Intraband Photodetectors with Colloidal Quantum Dots. *Coatings*, 2022, **12** (4), 467.
- [24] Hao Q., Ma H., Xing X., Tang X., Wei Z., Zhao X., Chen M. Mercury Chalcogenide Colloidal Quantum Dots for Infrared Photodetectors. *Materials*, 2023, **16** (23), 7321.
- [25] Prudnikau A., Roshan H., Paulus F., García B.M., Hübner R., Jalali H.B., Franco M.D., Prato M., Stasio F.D., Lesnyak V. Efficient Near-Infrared Light-Emitting Diodes Based on CdHgSe Nanoplatelets. *Advanced Functional Materials*, 2024, **34**, 2310067.

- [26] Hodges J.M., Hao S., Grovogui J.A., Zhang X., Bailey T.P., Li X., Gan Z., Hu Y.Y., Uher C., Dravid V.P., Wolverton C., Kanatzidis M.G. Chemical Insights into PbSe –  $x\%$  HgSe: High Power Factor and Improved Thermoelectric Performance by Alloying with Discordant Atoms. *J. of the American Chemical Society*, 2018, **140** (51), P. 18115–18123.
- [27] Yun J., Cho K., Park Y., Yang S., Choi J., Kim S. Thermoelectric characteristics of nanocomposites made of HgSe and Ag nanoparticles for flexible thermoelectric devices. *Nano Research*, 2017, **10** (2), P. 683–689.
- [28] Tang X., Wua G.F., Lai K.W.C. Plasmon resonance enhanced colloidal HgSe quantum dot filterless narrowband photodetectors for mid-wave infrared. *J. Mater. Chem. C*, 2017, **5**, P. 362–369.
- [29] Delin A., Klüner T. Excitation spectra and ground-state properties from density-functional theory for the inverted band-structure systems  $\beta$ -HgS, HgSe, and HgTe. *Phys. Rev. B*, 2002, **66**, 035117.
- [30] Radescu S., Mujica A., López-Solano J., Needs R.J. Theoretical study of pressure-driven phase transitions in HgSe and HgTe. *Phys. Rev. B*, 2011, **83**, 094107.
- [31] Duz I., Kart S.O., Erdem I., Kuzucu V. DFT study on phase transition behavior and mechanical properties of HgSe polymorphs under high pressure. *Current Applied Physics*, 2018, **18** (4), P. 424–436.
- [32] Secuk M.N., Aycibin M., Erdinc B., Gulebaglan S.E., Dogan E.K., Akkus H. Ab-initio Calculations of Structural, Electronic, Optical, Dynamic and Thermodynamic Properties of HgTe and HgSe. *American J. of Condensed Matter Physics*, 2014, **4** (1), P. 13–19.
- [33] Li J., He C., Meng L., Xiao H., Tang C., Wei X., Kim J., Kioussis N., Stocks G.M., Zhong J. Two-dimensional topological insulators with tunable band gaps: Single-layer HgTe and HgSe. *Scientific Reports*, 2015, **5** (1), 14115.
- [34] Habibes N.E.H., Boukourt A., Meskine S., Benbedra A., Mamouni Y., Bennacer H. Electronic and Optical Properties of Mn-Doped HgSe Topological Insulator for Spintronic Devices. *ECS J. Solid State Sci. Technol.*, 2024, **13**, 013013.
- [35] Ordejón P., Artacho E., Soler J.M. Self-consistent order N density functional calculations for very large systems. *Phys. Rev. B*, 1996, **53** (16), R10441–R10444.
- [36] Soler J.M., Artacho E., Gale J.D., García A., Junquera J., Ordejón P., Portal D.S. The SIESTA method for ab initio order-N materials simulation. *J. Phys. Condens. Matter*, 2002, **14** (11), P. 2745–2779.
- [37] Perdew J.P., Burke K., Ernzerhof M. Generalized Gradient Approximation Made Simple. *Phys. Rev. Lett.*, 1997, **78**, 1396.
- [38] Monkhorst H.J., Pack J.D. Special points for Brillouin-zone integrations. *Phys. Rev. B*, 1976, **13**, 5188.
- [39] Zhao M., Xia Y., Zhang D., Mei L. Stability and electronic structure of AlN nanotubes. *Phys. Rev. B*, 2003, **68**, 235415.
- [40] Das M., Mukherjee P., Chowdhury S., Gupta B.C. Tunable structural and electrical properties of zigzag CdS nanotubes: A density functional study. *Phys. Status Solidi B*, 2017, **254** (9), 1700038.
- [41] Das M., Chowdhury S., Gupta B.C. Atomic-Ordering-Induced Modulated Properties of Zigzag ZnTe Nanotubes. *Phys. Status Solidi B*, 2021, **258** (8), 2100115.
- [42] Senger R.T., Dag S., Ciraci S. Chiral Single-Wall Gold Nanotubes. *Phys. Rev. Lett.*, 2004, **93**, 196807.
- [43] Pan H., Feng Y.P. Semiconductor Nanowires and Nanotubes: Effects of Size and Surface-to-Volume Ratio. *ACS Nano*, 2008, **2** (11), P. 2410–2414.
- [44] Xiang H.J., Yang J., Hou J.G., Zhu Q. Piezoelectricity in ZnO nanowires: A first-principles study. *Appl. Phys. Lett.*, 2006, **89**, 223111.

---

*Submitted 3 August 2024; revised 13 August 2024; accepted 14 August 2024*

*Information about the authors:*

Monoj Das – Department of Physics, Gushkara Mahavidyalaya, Gushkara, 713128, India; ORCID 0000-0001-9367-2612; dsmonoj@gmail.com

## Crystalline $\text{LiYF}_4:\text{Nd}^{3+}$ nanoparticles synthesized via laser ablation method in water solutions of ethanol

Anna L. Dymova<sup>1,a</sup>, Vadim A. Prikazchikov<sup>1</sup>, Anna V. Astrakhantseva<sup>1</sup>, Timur M. Minnebaev<sup>1</sup>, Mintimir R. Zaitov<sup>1</sup>, Maksim S. Pudovkin<sup>1</sup>, Alexey S. Nizamutdinov<sup>1,b</sup>

<sup>1</sup>Kazan Federal University, Kazan, Russian Federation

<sup>a</sup>anyuta.dymova@mail.ru, <sup>b</sup>anizamutdinov@mail.ru

Corresponding author: Anna L. Dymova, anyuta.dymova@mail.ru

PACS 78.67.Bf, 81.16.-c

**ABSTRACT** In this work, a set of crystalline  $\text{LiYF}_4:\text{Nd}^{3+}$  nanoparticles with an average size of about 35 nm, were successfully synthesized via laser ablation method in liquid (combination of ethanol and water). The samples have trigonal structure corresponding to  $\text{LiYF}_4$  host. The spectral and kinetic characteristics of the synthesized nanoparticles corresponded to the characteristics of the target  $\text{LiYF}_4:\text{Nd}^{3+}$  bulk crystal. In particular, the luminescence decay curves for the  ${}^4\text{F}_{3/2} \rightarrow {}^4\text{I}_{11/2}$  radiative transition ( $\text{Nd}^{3+}$ ) are single-exponential and the decay times were around 517  $\mu\text{s}$ , which is typical for  $\text{Nd}^{3+}$  in  $\text{LiYF}_4$  host. It has been established that the decrease in the power density of laser radiation energy leads to the increase of the average particle size.

**KEYWORDS** laser ablation, laser ablation in liquids,  $\text{LiYF}_4$  nanoparticles,  $\text{Nd}^{3+}$  nanoparticle synthesis

**ACKNOWLEDGEMENTS** This research was funded by the subsidy allocated to Kazan Federal University for the state assignment in the sphere of scientific activities: FZSM-2023-0012.

**FOR CITATION** Dymova A.L., Prikazchikov V.A., Astrakhantseva A.V., Minnebaev T.M., Zaitov M.R., Pudovkin M.S., Nizamutdinov A.S. Crystalline  $\text{LiYF}_4:\text{Nd}^{3+}$  nanoparticles synthesized via laser ablation method in water solutions of ethanol. *Nanosystems: Phys. Chem. Math.*, 2024, **15** (4), 481–486.

### 1. Introduction

In the past two decades, one of the most rapidly growing areas of science and industry has been the synthesis of nanoparticles with specified morphology and desirable physicochemical properties. Among many methods for the synthesis of nanomaterials, the laser ablation in liquid plays a special role. Indeed, laser ablation is a relatively simple and time consuming method of the nanoparticle synthesis, which allows obtaining metal nanoparticles [1, 2], nanoparticles of semiconductor compounds [3, 4], as well as dielectric ones (in particular, fluoride and oxide compounds [5, 6]). The laser ablation method in liquid has a number of advantages: firstly, it is a relatively fast method of producing particles that does not require such specialized conditions as high temperature, pressure, and the use of toxic compounds or acids as reaction environment. Secondly, it allows controlling such properties of the resulting nanoparticles as shape, size, and size distribution by varying the laser irradiation parameters (wavelength, frequency and duration of the pulses, power density). The characteristics of the liquid (pH level, chemical composition of the solvent and its polarity) have a notable impact on the above-mentioned characteristics [7–11]. In particular, in [12, 13], it was shown that an increase in the power density of laser irradiation increases the average size of the nanoparticles. Despite a number of advantages, laser ablation in liquid is not widely used as a method of industrial synthesis. The main reason is the low productive capacity of the process compared to chemical methods. There is large dispersion of the resulting nanoparticles in shape and size (width of the size distribution is from approximately 1–5 nm to 100–150 nm) in the case of non-optimal choice of the laser irradiation parameters [7].

This work demonstrates the possibility of the  $\text{LiYF}_4:\text{Nd}^{3+}$  nanoparticle synthesis via laser ablation in the liquid using a bulk crystal of a similar composition as a target for laser irradiation. It was previously shown that the laser ablation torch of this crystal, there are all the necessary components for the synthesis of this nanosized compound [14]. The possibility of the synthesizing of the thin films [15] and nanoparticles [16] of this compound by laser ablation was also shown. The main objective of this work is to study the dependence of laser irradiation parameters and liquid parameters on characteristics of  $\text{LiYF}_4:\text{Nd}^{3+}$  nanoparticles. The mechanisms explaining the obtained results were suggested [17–21].

The choice of  $\text{LiYF}_4$  host is based on the fact, that it has low phonon energy resulting in lower probability of non-radiative multiphonon relaxation. It also demonstrates high chemical, mechanical and thermal stability [22–24]. In its turn,  $\text{Nd}^{3+}$  ion has a unique electron level structure and can be optically excited in the broad spectral range including so-called “biological window”. Due to the thermally coupled Stark components of the luminescence peaks nanoparticles doped with  $\text{Nd}^{3+}$  ions can serve as luminescent thermometers operating in the physiological temperature range. Specifically,  $\text{Nd}^{3+}$  doped fluoride nanoparticles were successfully utilized for hyperthermia with simultaneous remote optical temperature

sensing for phantom tissue [25]. On the other hand,  $\text{Nd}^{3+}$  doped  $\text{SrF}_2$  nanoparticles demonstrated their efficiency in bioimaging of mouse organs in the biological window (1000–1400 nm) [26].

## 2. Materials and methods

### 2.1. Synthesis of $\text{LiYF}_4:\text{Nd}^{3+}$ nanoparticles

The nanoparticles were synthesized using a pulsed Nd:YAG laser (LQ529B) generating 532 nm nanosecond pulse irradiation (pulse duration and pulse repetition rate were 10 ns and 10 Hz, respectively). The target  $\text{LiYF}_4:\text{Nd}^{3+}$  (1.0 at.%) bulk crystal was grown by the Bridgman-Stockbarger method. Irradiation was carried out in solution of deionized water with 10% volume fraction of ethanol. The effect of laser energy power density on the nanoparticle size in the water/ethanol = 90/10% solution was also investigated. The chosen power densities were 0.9, 1.1, and 1.5  $\text{J}/\text{cm}^2$ . Particles were collected from the colloidal solution using a syringe. Next, the nanoparticles were dried in a dustproof chamber in air. The scheme of the experimental set-up is presented in Fig. 1. To record the luminescence spectra, a CCD StellarNet spectrometer was used (1–2 nm resolution and 200–1200 nm spectral range). To record the luminescence decay curves, a combination of an MDR-23 monochromator (resolution 0.1 nm, spectral range 200–2000 nm), a photomultiplier tube (FEU-62) and a Bordo oscilloscope (10 bit, bandwidth 200 MHz) was used.

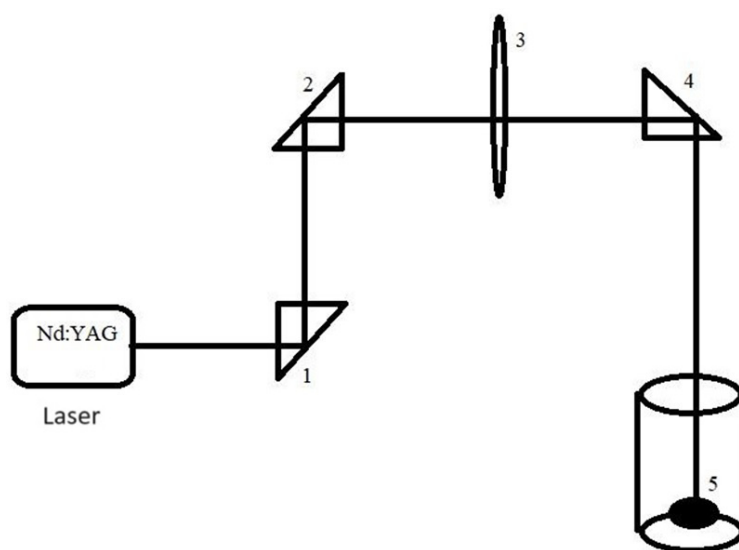


FIG. 1. Experimental set-up for synthesis via laser ablation consisting of a set of prisms (1, 2, and 4), lens (3), and the target (5) in the liquid

### 2.2. Physicochemical characterization of the samples

The work examined the morphology of nanoparticles, as well as the phase composition. The study of all the samples was carried out in three stages. The phase composition of the samples was studied via X-ray diffraction (XRD) using an MD-10 EFA setup ( $\text{FeK}_\alpha$  radiation at  $\lambda=1.93597$  wavelength). The scanning electron microscope EVO 50 XVP Carl Zeiss was used to investigate the morphology and size of the samples.

## 3. Results and discussion

The XRD pattern of the  $\text{LiYF}_4:\text{Nd}^{3+}$  nanoparticles is represented in Fig. 2.

The obtained XRD pattern corresponds to the  $\text{LiYF}_4$  host. The impurity peaks or double phase as well as the presence of the amorphous phase were not found. The calculated lattice parameters were  $a=0.513(6)$ ,  $c=1.070(7)$  are typical for the  $\text{LiYF}_4$  host [20]. SEM image of the nanoparticles synthesized in water/ethanol = 90/10% solution presented in Fig. 3.

It can be seen, that the nanoparticles have predominantly spherical shape. The size distribution histograms of the obtained nanoparticles are presented in Fig. 4.

The mechanism of nanoparticle formation is the crystallization from the gas phase. In particular, under the influence of a laser pulse, the target material is heated and evaporates, forming a drop in a bubble, and then crystallizes as a result of cooling [9, 11–13]. Since the thermal conductivity of water is high, the molten droplets dispersed in solvent will quickly condense to form large sized particles. For solvents having lower thermal conductivity, the initial particles exist longer in the melted condition and fractionize into smaller particles. The ethanol molecules can act as a shell that prevents the aggregation of nanoparticles [18, 19]. It is of interest to consider the influence of laser radiation energy density on the sizes of nanoparticles. Fig. 4 shows graphs of particle size distribution. According to the data obtained, it can be said that

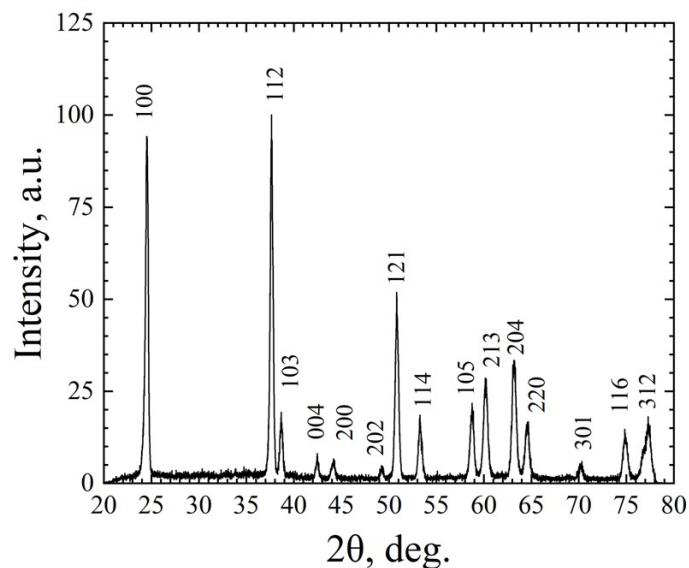


FIG. 2. XRD pattern of the  $\text{LiYF}_4:\text{Nd}^{3+}$  nanoparticles

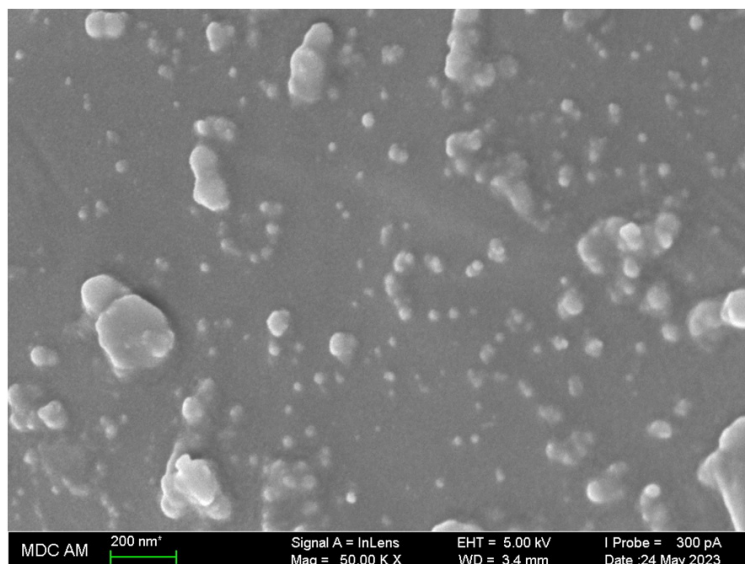


FIG. 3. SEM image of the nanoparticles synthesized in water/ethanol = 90/10% solution obtained for laser radiation energy density  $0.9 \text{ J/cm}^2$

with the increase of power density of laser radiation energy, the average particle size increases. This can be related to the fact that higher energy heats up the nanoparticles more efficiently, which leads to their aggregation and fusing into one crystalline agglomerate [20, 21].

Optical excitation of nanoparticles was carried out by laser irradiation at 790 nm wavelength ( $^4\text{I}_{9/2} \rightarrow ^4\text{F}_{5/2}$  absorption band of  $\text{Nd}^{3+}$  ions). Fig. 5a shows the luminescence spectrum of  $\text{LiYF}_4:\text{Nd}^{3+}$  nanoparticles recorded at room temperature. The spectrum contains luminescence bands corresponding to the  $^4\text{F}_{3/2} \rightarrow ^4\text{I}_{9/2}$  (849–950 nm) and  $^4\text{F}_{3/2} \rightarrow ^4\text{I}_{11/2}$  (1039–1080 nm) radiative transitions of  $\text{Nd}^{3+}$  ions [15, 22].

Fig. 5b demonstrates the luminescence decay curve at 1046 nm ( $^4\text{F}_{3/2} \rightarrow ^4\text{I}_{11/2}$  radiative transition of  $\text{Nd}^{3+}$  ions) upon excitation at 790 nm. The curve has a single-exponential dependence with a calculated decay around  $517 \mu\text{s}$ , which is typical for  $\text{LiYF}_4:\text{Nd}^{3+}$  phosphors [15]. In addition, the single-exponential nature of the luminescence decay suggests that  $\text{Nd}^{3+}$  ions are distributed homogeneously in the nanoparticles and do not form clusters. In particular, during clustering,  $\text{Nd}^{3+}$  ions interact more effectively with each other in clusters, which can lead to enhanced quenching of the  $^4\text{F}_{3/2}$  state due to concentration quenching and/or cross-relaxation. This can lead to the appearance of a short-lived component in the kinetics of luminescence decay [22].

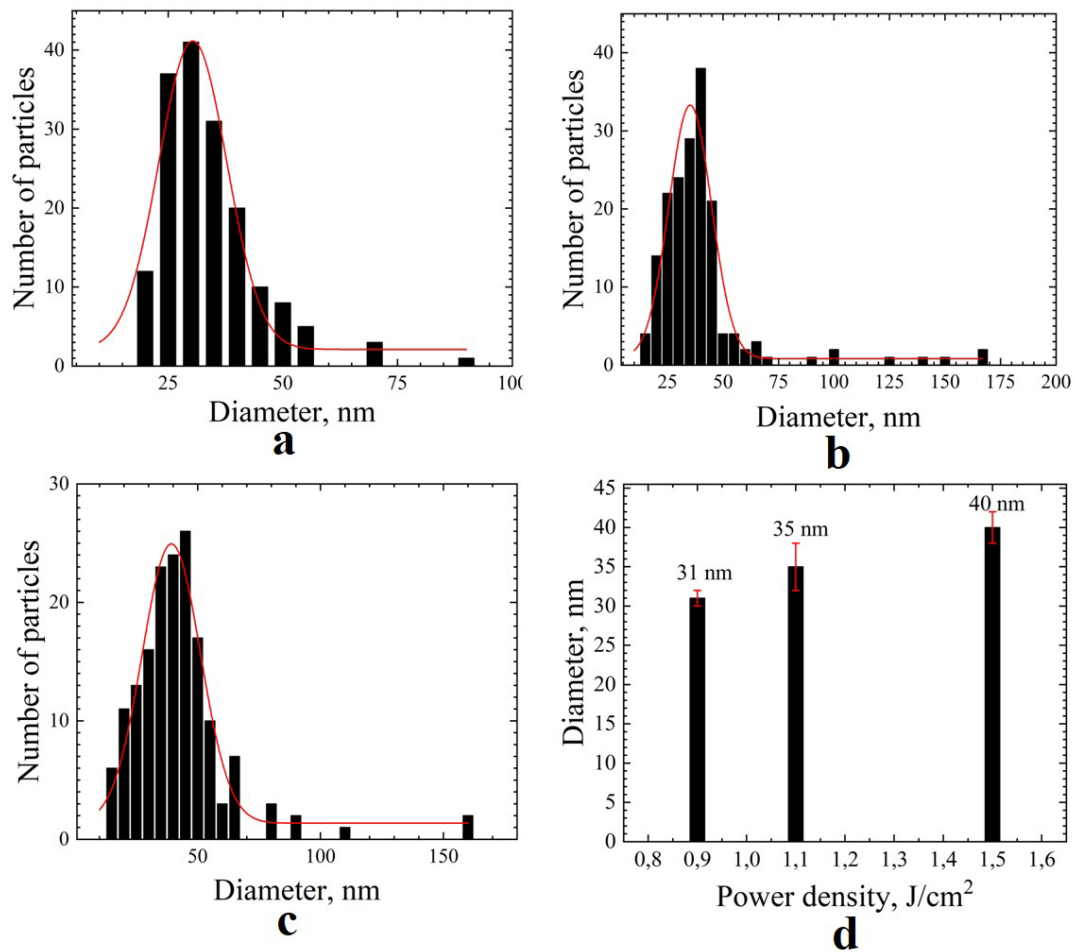


FIG. 4. The nanoparticle size distribution obtained for laser radiation energy density a) 0.9, b) 1.1, c) 1.5 J/cm<sup>2</sup>; d) The nanoparticle size dependence on the energy density of laser radiation

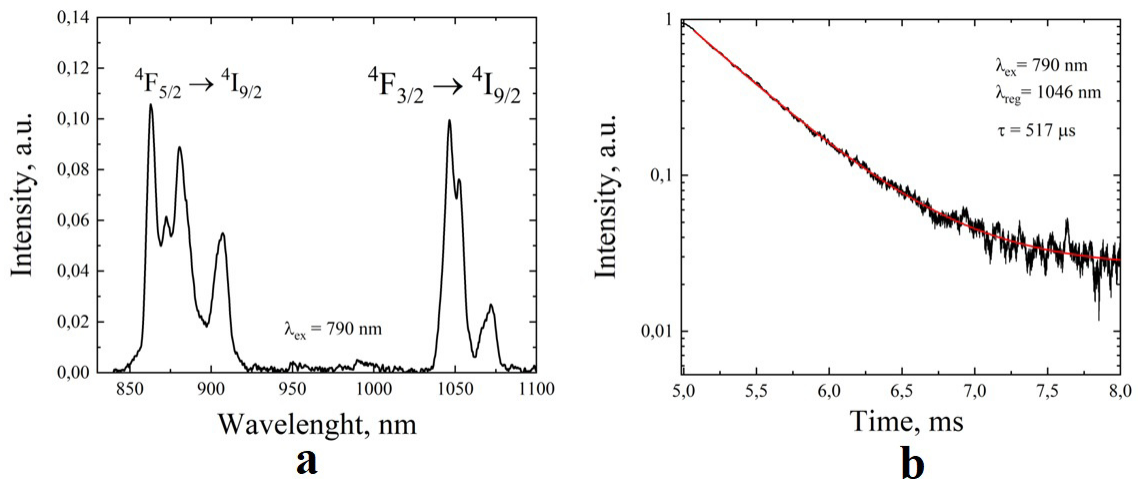


FIG. 5. Room temperature luminescence spectrum of LiYF<sub>4</sub>:Nd<sup>3+</sup> nanoparticles (a) and luminescence decay kinetic at the registration wavelength  $\lambda = 1046$  nm (b) for a sample synthesized from a solution with a volume fraction of ethanol 10%, excitation wavelength  $\lambda = 790$  nm

#### 4. Conclusions

Nanoparticles of LiYF<sub>4</sub>:Nd<sup>3+</sup> were successfully synthesized by laser ablation in liquid. Specifically, the laser irradiation was carried out in solutions of deionized water with volume fractions of ethanol in solution of 10%. The effect of laser energy power density on the nanoparticle size in the water/ethanol = 90/10% solution was also investigated. The chosen power densities were 0.9, 1.1, and 1.5 J/cm<sup>2</sup>. The resulting samples had a trigonal structure corresponding to the LiYF<sub>4</sub> host. The nanoparticles synthesized in aqueous solutions with ethanol, have the average particle size around 72 nm. The hypothesis explaining the observed results was made. Specifically, the thermal conductivity of water is high, the molten droplets dispersed in solvent will quickly condense to form large sized particles. For solvents having higher thermal conductivity, the initial particles exist longer in the melted condition and fractionize into smaller particles. The ethanol molecules can act as a shell that prevents the aggregation of nanoparticles. It is also shown, that with the increase of the power density of laser radiation energy, the average particle size increases. This can be related to the fact that higher energy heats up the nanoparticles more efficiently, which leads to their aggregation and fusing into one crystalline agglomerate. The spectral and kinetic characteristics of the synthesized nanoparticles also corresponded to the target bulk crystal. In particular, upon 790 nm excitation, a characteristic luminescence spectrum was observed for the <sup>4</sup>F<sub>3/2</sub> → <sup>4</sup>I<sub>9/2</sub> (849–950 nm) and <sup>4</sup>F<sub>3/2</sub> → <sup>4</sup>I<sub>11/2</sub> (1039–1080 nm) radiative transitions of Nd<sup>3+</sup> ions. The curve has a single-exponential dependence with a calculated decay around 517 μs, which is typical for LiYF<sub>4</sub>:Nd<sup>3+</sup> phosphors.

#### References

- [1] Compagnini G., Scalisi A.A., Puglisi O. Production of gold nanoparticles by laser ablation in liquid alkanes. *Journal of Applied Physics*, 2003, **94**(12), P. 7874–7877.
- [2] Lau Truong S., Levi G., Bozon-Verduraz F., Petrovskaya A.V., Simakin A.V., Shafeev G.A. Generation of Ag nanopikes via laser ablation in liquid environment and their activity in SERS of organic molecules. *Applied Physics A*, 2007, **89**, P. 373–376.
- [3] Sajti C.L., Giorgio S., Khodorkovsky V., Marine W. Femtosecond laser synthesized nanohybrid materials for bioapplications. *Applied Surface Science*, 2007, **253**(19), P. 8111–8114.
- [4] Usui H., Shimizu Y., Sasaki T., Koshizaki N. Photoluminescence of ZnO nanoparticles prepared by laser ablation in different surfactant solutions. *The Journal of Physical Chemistry B*, 2005, **109**(1), P. 120–124.
- [5] Amans D., Malaterre C., Diouf M., Mancini C., Chaput F., Ledoux G., Perriat P. Synthesis of oxide nanoparticles by pulsed laser ablation in liquids containing a complexing molecule: impact on size distributions and prepared phases. *The Journal of Physical Chemistry C*, 2011, **115**(12), P. 5131–5139.
- [6] Ledoux G., Amans D., Dujardin C., Masenelli-Varlot K. Facile and rapid synthesis of highly luminescent nanoparticles via pulsed laser ablation in liquid. *Nanotechnology*, 2009, **20**(44), P. 445605.
- [7] Makarov G.N. Laser applications in nanotechnology: nanofabrication using laser ablation and laser nanolithography. *Physics-Uspekhi*, 2013, **56**(7), P. 643.
- [8] Buesser B., Groehn A.J. Multiscale Aspects of Modeling Gas Phase Nanoparticle Synthesis. *Chemical Engineering & Technology*, 2012, **35**(7), P. 1133–1143.
- [9] Naser H., Alghoul M.A., Hossain M.K., Asim N., Abdullah M.F., Ali M.S., Amin N. The role of laser ablation technique parameters in synthesis of nanoparticles from different target types. *Journal of Nanoparticle Research*, 2019, **21**, P. 1–28.
- [10] Wang Y.L., Xu W., Zhou Y., Chu L.Z., Fu G.S. Influence of pulse repetition rate on the average size of silicon nanoparticles deposited by laser ablation. *Laser and Particle Beams*, 2007, **25**(1), P. 9–13.
- [11] Al-Azawi M.A., Bidin N., Bououdina M., Abbas K.N., Al-Asedy H. J., Ahmed O.H., Thahe A.A. The effects of the ambient liquid medium on the ablation efficiency, size and stability of silver nanoparticles prepared by pulse laser ablation in liquid technique. *J. Teknol*, 2016, **78**(3), P. 7–11.
- [12] Pereira H., Moura C.G., Miranda G., Silva F.S. Influence of liquid media and laser energy on the production of MgO nanoparticles by laser ablation. *Optics & Laser Technology*, 2021, **142**, P. 107181.
- [13] Wang H., Odawara O., Wada H. Facile and chemically pure preparation of YVO<sub>4</sub>:Eu<sup>3+</sup> colloid with novel nanostructure via laser ablation in water. *Scientific Reports*, 2016, **6**(1), P. 20507.
- [14] Barsanti S., Favilla E., Bicchi P. Emission and electron/ion analysis of the ablated plume from LiYF<sub>4</sub> crystals doped with Tm<sup>3+</sup> or Nd<sup>3+</sup> ions. *Radiation Physics and Chemistry*, 2007, **76**(3), P. 512–515.
- [15] Barsanti S., Cornacchia F., Di Lieto A., Toncelli A., Tonelli M., Bicchi P. Nd<sup>3+</sup>-doped fluoride film grown on LiYF<sub>4</sub> substrate by pulsed laser deposition. *Thin Solid Films*, 2008, **516**(8), P. 2009–2013.
- [16] Lukinova E., Farukhshin I., Nizamutdinov A., Madirov E., Semashko V., Pudovkin M. Ce<sup>3+</sup> doped LiYF<sub>4</sub> nanoparticles fabrication by laser ablation. In EPJ Web of Conferences, 2017, **161**, P. 03014.
- [17] Rawat R., Tiwari A., Arun N., Rao S.N., Pathak A.P., Tripathi A. Solvents effect on the morphology and stability of Cu/CuO nanoparticles synthesized at high fluence laser ablation. *ChemistrySelect*, 2019, **4**(35), P. 10471–10482.
- [18] Naderi-Samani H., Razavi R.S., Mozaffarinia R. Investigating the effect of 532 nm and 1064 nm wavelengths and different liquid media on the qualities of silver nanoparticles yielded through laser ablation. *Materials Chemistry and Physics*, 2023, **305**, P. 128001.
- [19] Goncharova D.A., Kharlamova T.S., Reutova O.A., Svetlichnyi V.A. Water–ethanol CuOx nanoparticle colloids prepared by laser ablation: Colloid stability and catalytic properties in nitrophenol hydrogenation. *Colloids and Surfaces A: Physicochemical and Engineering Aspects*, 2021, **613**, P. 126115.
- [20] Thoma R.E., Brunton G.D., Penneman R.A., Keenan T.K. Equilibrium relations and crystal structure of lithium fluorolanthanate phases. *Inorganic Chemistry*, 1970, **9**(5), P. 1096–1101.
- [21] Alakshin E.M., Kondratyeva E.I., Nuzhina D.S., Iakovleva M.F., Kuzmin V.V., Safullin K.R., Tagirov M.S. The self-assembly of DyF<sub>3</sub> nanoparticles synthesized by chloride-based route. *Journal of Nanoparticle Research*, 2018, **20**, P. 1–11.
- [22] Pudovkin M.S., Ginkel A.K., Morozov O.A., Kiiamov A.G., Kuznetsov M.D. Highly-sensitive lifetime optical thermometers based on Nd<sup>3+</sup>, Yb<sup>3+</sup>:YF<sub>3</sub> phosphors. *Journal of Luminescence*, 2022, **249**, P. 119037.
- [23] Anbharasi L., Rekha E.B., Rahul V.R., Roy B., Gunaseelan M., Yamini S., Senthilselvan J. Tunable emission and optical trapping of upconverting LiYF<sub>4</sub>: Yb, Er nanocrystal. *Optics & Laser Technology*, 2020, **126**, P. 106109.

- [24] Fedorov P.P., Semashko V.V., Korableva S.L. Lithium rare-earth fluorides as photonic materials: 1. Physicochemical characterization. *Inorganic Materials*, 2022, **58**(3), P. 223–245.
- [25] Ximendes E.C., Rocha U., Kumar K.U., Jacinto C., Jaque D. LaF<sub>3</sub> core/shell nanoparticles for subcutaneous heating and thermal sensing in the second biological-window. *Applied Physics Letters*, 2016, **108**(25).
- [26] Villa I., Vedda A., Cantarelli I.X., Pedroni M., Piccinelli F., Bettinelli M., Garcna D.J. 1.3  $\mu\text{m}$  emitting SrF<sub>2</sub>:Nd<sup>3+</sup> nanoparticles for high contrast in vivo imaging in the second biological window. *Nano Research*, 2015, 8, P. 649–665.

---

*Submitted 3 December 2023; revised 18 July 2024; accepted 19 July 2024*

*Information about the authors:*

*Anna L. Dymova* – Kazan Federal University, 18 Kremlyovskaya str, Kazan, 420008, Russian Federation; anyuta.dymova@mail.ru

*Vadim A. Prikazchikov* – Kazan Federal University, 18 Kremlyovskaya str, Kazan, 420008, Russian Federation

*Anna V. Astrakhantseva* – Kazan Federal University, 18 Kremlyovskaya str, Kazan, 420008, Russian Federation; ORCID 0000-0002-1670-3064

*Timur M. Minnebaev* – Kazan Federal University, 18 Kremlyovskaya str, Kazan, 420008, Russian Federation

*Mintimir R. Zaitov* – Kazan Federal University, 18 Kremlyovskaya str, Kazan, 420008, Russian Federation; ORCID 0009-0003-3621-0982

*Maksim S. Pudovkin* – Kazan Federal University, 18 Kremlyovskaya str, Kazan, 420008, Russian Federation; ORCID 0000-0002-7455-9611

*Alexey S. Nizamutdinov* – Kazan Federal University, 18 Kremlyovskaya str, Kazan, 420008, Russian Federation; ORCID 0000-0003-1559-6671; anizamutdinov@mail.ru

*Conflict of interest:* the authors declare no conflict of interest.

## Colloidal chemical properties of the sol $V_2O_5 \cdot nH_2O$

Hein Myat Lwin<sup>a</sup>, Oksana V. Yarovaya<sup>b</sup>

D. I. Mendeleev University of Chemical Technology of Russia, Moscow, Russia

<sup>a</sup>heinmyatlwin2468@gmail.com, <sup>b</sup>iarovaia.o.v@muctr.ru

Corresponding author: Oksana V. Yarovaya, iarovaia.o.v@muctr.ru

PACS 82.70.Dd

**ABSTRACT** The colloidal properties of the lyophilic dispersion system  $V_2O_5 \cdot nH_2O$  sol studied in this work was obtained by the thermolysis of  $V_2O_5$  powder with hydrogen peroxide. The dispersion phase exists in the form of nanorods. The optimal mole ratio of  $V_2O_5$  and  $H_2O_2$  for synthesizing the sol is 1:30, and the possible concentration of  $V_2O_5$  in the entire colloidal system ranges between 0.3 to 1.6 mass percent. The existence of nanoparticles in this colloidal system and the pH range that maintains the stability of the sol conform to the phase diagram of vanadium (V) in an aqueous medium. The absolute value of the zeta potential of the sol increases when the initial concentration of the sol during synthesis increases and the ionic strength of the dispersion medium decreases. Potential curves of pair interaction between nanoparticles were also constructed according to the DLVO theory.

**KEYWORDS**  $V_2O_5 \cdot nH_2O$ , thermolysis, nanorods, lyophilic colloidal system, stability, DLVO theory

**FOR CITATION** Lwin H.M., Yarovaya O.V. Colloidal chemical properties of the sol  $V_2O_5 \cdot nH_2O$ . *Nanosystems: Phys. Chem. Math.*, 2024, **15** (4), 487–497.

### 1. Introduction

In recent years, one can see rapid progress in the field of nanotechnology with a particular focus on the synthesis and applications of nano-scale materials. Among these, vanadium (V) oxide ( $V_2O_5$ ) sol has attracted significant attention due to its unique properties and potential applications in such fields as catalysis, energy storage, sensors, and optics [1–3].  $V_2O_5$  is a widely studied transition-metal oxide with a layered crystal structure, featuring strong Vanadium-Oxygen bonds [4, 5]. In the field of catalysis,  $V_2O_5$  has demonstrated exceptional performance as a catalyst for oxidation, hydrogenation, and dehydrogenation reactions due to its high surface area and redox properties [6–11]. Moreover,  $V_2O_5$  shows promise for use in energy storage devices, such as lithium-ion batteries and supercapacitors, owing to its electronic conductivity and electrochemical stability [12, 13]. Additionally, the potential use of  $V_2O_5$  in gas sensing, electrochromic devices, and optical coatings further highlights its significance in emerging technologies [14–16].

$V_2O_5$  sol, comprising nanoscale  $V_2O_5$  particles suspended in a liquid medium, offers significant advantages such as high surface area, tunable properties, and enhanced reactivity, thereby opening up new perspectives for its practical utilization. The preparation of  $V_2O_5$  sol involves the synthesis of nanoscale  $V_2O_5$  particles, followed by their dispersion in a suitable liquid medium. Over the years, various methods have been developed to prepare  $V_2O_5$  sol, each offering distinct advantages and disadvantages. The choice of synthesis method is critical in determining the particle size, morphology, and surface properties of the resulting  $V_2O_5$  sol, which in turn dictate its performance in different applications [17–26].

The sol-gel method has been used to create  $V_2O_5$  thin films and nanopowders from  $V_2O_5$  sols, which were prepared by ion exchange [17, 18], alkoxide hydrolysis [19, 20], solidification melting [21–23] and hydrolysis/thermolysis of  $V_2O_5$  using hydrogen peroxide [24–26]. Among these methods, the method of hydrolysis/thermolysis of  $V_2O_5$  using hydrogen peroxide is attractive due to its environmental safety, low cost, and simplicity of the process [27]. There are many articles [24–30] on the process and application of the  $V_2O_5 \cdot nH_2O$  sol/gel obtained by this method. However, the assessment of the colloidal stability of the sol obtained by these methods was not reported in the available literatures.

The colloidal chemical properties of  $V_2O_5$  sols play a crucial role in determining their performance in diverse applications. Studying the colloidal stability of  $V_2O_5$  sols can provide valuable insights into the underlying physicochemical mechanisms, such as particle-particle interactions, surface properties, and the influence of various factors (pH, ionic strength, concentration, etc.). This fundamental understanding is essential for the rational design and optimization of  $V_2O_5$ -based materials and systems.

By gaining a deeper understanding of the colloidal properties of  $V_2O_5$  sols, researchers can optimize their performance and develop new applications with enhanced reactivity, stability, and sensitivity. For instance, improved colloidal stability can lead to enhanced dispersibility, processability, and long-term performance of  $V_2O_5$ -based materials in various fields, including catalysis, energy storage, and functional coatings. Therefore, the synthesis of  $V_2O_5$  and a comprehensive

investigation of its colloidal properties become important areas of study. This study can provide valuable insights for the development of advanced  $V_2O_5$ -based materials and technologies.

## 2. Materials and methods

### 2.1. Materials

The following reagents were used in the work: vanadium (V) oxide, “analytical grade”; and hydrogen peroxide  $H_2O_2$ , “special purity grade” are used as the sources of sol preparation.

### 2.2. Method for preparation of sol

Distilled water was added to the round bottom flask containing  $V_2O_5$  powder and dispersed by stirring. Then the calculated volume of hydrogen peroxide solution was added and stirred until a homogeneous yellow mass was formed. Then the required amount of water was added and heated to a boil using a reverse refrigerator. After boiling for 5 minutes, the color changes from yellow to orange, and then after 3 minutes, it turns into dark red resulting  $V_2O_5 \cdot nH_2O$  sol.

### 2.3. Method for determining the concentration of vanadium (V) in solutions and sols

To determine vanadium (V), titrated using Mohr’s salt  $(NH_4)_2Fe(SO_4)_2$ . Previously, 5 M sulfuric acid was added to the analyzed solution in a volume ratio of 1:1. Phenylanthranilic acid was used as an indicator, based on the acidity of the medium. The equivalence point was determined when the solution transitioned from violet to green. The permissible absolute total error of the analysis is 0.7 %, with a confidence level of  $P = 0.95$  [31].

The reaction occurred during titration is described in eq. (1).



The concentration of vanadium (V) content was calculated using formulas (2) and (3).

$$\text{Vanadium(V) concentration, mole/liter} = \frac{V_{\text{avg}} \times N}{V_{\text{analyz}} \times 2}, \quad (2)$$

$$V_2O_5, \text{ g/l} = \frac{V_{\text{avg}} \times N \times 91}{V_{\text{analyz}}}, \quad (3)$$

where:  $N$  is the normality of Mohr’s salt solution  $(NH_4)_2Fe(SO_4)_2$ , mole/liter;  $V_{\text{avg}}$  is the average volumes of Mohr’s salt used for titration, ml;  $V_{\text{analyz}}$  is the volume of the analyzed solution (10 ml); 91 is the equivalent mass of vanadium oxide.

### 2.4. Characterization

The morphology and particle size of nanoparticles were analyzed by the Transmission Electron Microscope (TEM) LIBRA 200 FE HR (Germany). Absorption spectra of sol were recorded on a brand spectrophotometer LEKI SS2110UV in plastic cuvettes with an absorbing layer thickness of 10 mm in the wavelength range 500 – 800 nm. pH determination was carried out on a pH-meter/milivoltmeter (pH-420) OOO device using a glass electrode, the measurement range of which is from 0.5 to 14. The determination of zeta potential was carried out on a Compact-Z device using standard round cuvettes measuring  $15 \times 45$  mm with a capacity of 4 ml, with a relative measurement error of  $\pm 1$  %.

The content of particles in the resulting sol was determined by acidimetric titration according to the method in Section 2.3. First, we analyzed the total vanadium (V) content and the vanadium (V) content in the filtrate, which was obtained after ultrafiltration using an ultrafiltration cell with a UPM-450 polymer membrane. Based on these experimental results of total concentration and the concentration of filtrate, the content of vanadium (V) particles was determined. The ionic strength of the dispersion medium was calculated based on the obtained data on the concentration of dissolved  $V_2O_5$  in the resulting filtrate.

The threshold for rapid coagulation is determined by the threshold volume of the electrolyte at which the optical density of the sol reaches its maximum value, and does not change with further addition of electrolyte. Coagulation threshold values  $C_{\text{crit}}$  were calculated using eq. (4).

$$C_{\text{crit}} = \frac{C_{\text{elect}} \times V_{\text{crit}}}{V}, \quad (4)$$

where:  $C_{\text{elect}}$  is the concentration of electrolyte (mol/l),  $V$  is the volume of the system (ml).

The morphology of the thin layer was analyzed by Scanning Electron Microscope (SEM) JEOL 1610LV (JEOL, Japan). The crystallographic structure of the sample was analyzed using powder X-ray diffraction DX-2700BH (XRD, with  $CuK\alpha$  radiation).

## 2.5. Calculation method for potential energy of paired particle interactions using DLVO theory

At first, the value of the complex Hamaker constant was calculated. According to the DLVO theory, for the electrolyte concentration equals to the rapid coagulation threshold, the potential curve of the dispersed system is in the region of negative values. Only its maximum, corresponding to the zero potential barrier, lies on the abscissa axis. So, the value of the complex Hamaker constant for the hydrosols was determined graphically, taking the ionic strength of the dispersion medium equal to the sum of the ionic strength of a freshly prepared sol and the value of the rapid coagulation threshold in the presence of an indifferent electrolyte of type 1–1 ( $NaNO_3$ ).

Assuming that the particles are in the form of cylinders, the molecular component of the potential energy of pair interaction for two particles through a layer of dispersion medium was calculated using equation (5) [32]:

$$U_{m,cylinder} = -\frac{A_{131}l}{12\sqrt{2}h^{3/2}} \left[ \frac{a_1 a_2}{a_1 + a_2} \right]^{1/2}, \quad (5)$$

where:  $A_{131}$  is the complex Hamaker constant, characterizing the interaction of two particles of a certain nature through a layer between them, Joule (1 indicates the nature of the interacting particles, 3 – the layer);  $h$  is the distance between particles, m;  $a_1$  and  $a_2$  are the radii of the interacting particles, m;  $l$  is the length of the cylindrical particle, m.

The electrostatic component was calculated using eq. (6) [33, 34]:

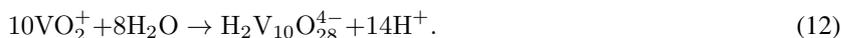
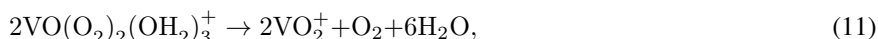
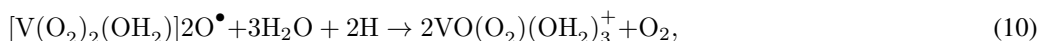
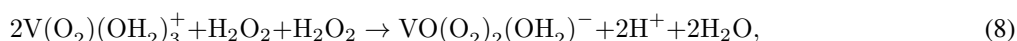
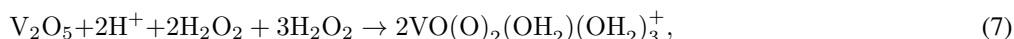
$$U_{ele,cylinder} = \sqrt{\pi}\epsilon\epsilon_0 \sqrt{\frac{ka_1 a_2}{a_1 + a_2}} \cdot \left[ 2\sqrt{2}z_1 z_2 \zeta_1 \zeta_2 e^{-kh} - (z_1^2 \zeta_1^2 + z_2^2 \zeta_2^2) e^{-2kh} \right], \quad (6)$$

where  $\zeta$  is the electrokinetic potential, mV;  $z_i$  is the counterion charge;  $k$  is the inverse value of the thickness of the diffuse part of the electric double layer,  $m^{-1}$ ;  $\epsilon_0$  is the dielectric constant.

## 3. Results and discussion

### 3.1. Determination of the optimal mole ratio and range of the initial concentration of the sol

According to literature [28–30] dealt with studies based on 51 V NMR method, the reaction mechanism of  $V_2O_5 \cdot nH_2O$  sol can be described as follows. First,  $V_2O_5$  dissolves in the presence of excess  $H_2O_2$ , forming an orange solution of diperoxoanions  $[VO(O_2)_2]^-$ . These peroxy ions are unstable in solution and gradually decompose, forming monoperoxo ions  $[VO(O_2)]^+$  and then vanadate compounds. As a result, oxygen gas is released. Finally,  $VO_2^+$  and  $[H_2V_{10}O_{28}]^{4-}$  ions are obtained. Decavanadic acid  $[H_2V_{10}O_{28}]^{4-}$  then spontaneously dissociates, leading to the polymerization of  $V_2O_5 \cdot nH_2O$ . The conversion path of peroxovanadate solutions during synthesis, according to the literatures [26] can be described as below:



Therefore, based on the above literature data [26, 28–30], the reaction steps can be briefly written as shown in Fig. 1.

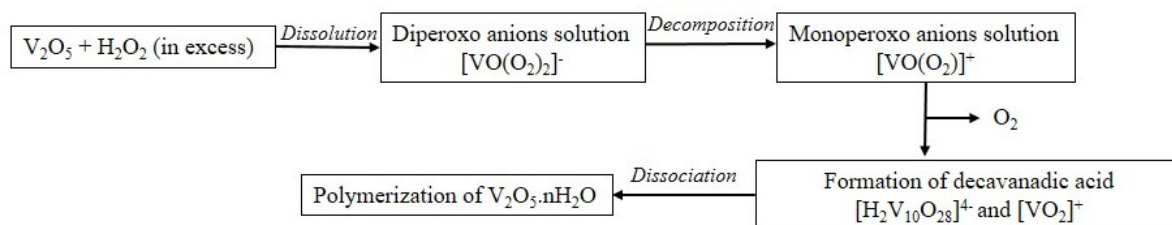


FIG. 1. Reaction steps for preparing  $V_2O_5 \cdot nH_2O$  sol [26, 28–30]

To determine the optimal molar ratio for the preparation of the sol, the same mass percentage of 0.5 % was chosen under the same synthesis condition (initial mass of 0.5 g of  $V_2O_5$  in a total sol volume of 100 ml during synthesis) according to the method of preparation shown in Section 2.2. It has been shown that at a molar ratio of  $[V_2O_5]:[H_2O_2]$  less than  $[1]:[30]$ , at the step of dissolving the  $V_2O_5$  powder, which was the first stage of sol preparation, the powders do not completely dissolve. So for further studies, to synthesize the sols, as the minimum and optimal mole ratio for

vanadium pentoxide and hydrogen peroxide [1]:[30] was chosen. The range of sols concentrations obtained in this mole ratio that keep the sol stable for about 6 months is from 0.3 to 1.6 wt.%  $V_2O_5$ . At a content of less than 0.3 wt.% the system was in the form of a solution with precipitation, and above 1.6 % an extreme exothermic reaction occurred, and both types of sol and gel were formed. The morphology of  $V_2O_5 \cdot nH_2O$  nanoparticles is shown in Fig. 2. According to Fig. 2, the solid phase is in the form of nanorods (the thickness is approximately 2 nm, the width is 15 – 25 nm, the length is 0.3 – 0.8  $\mu m$ ).

### 3.2. Determination of the actual concentration of particles and the zeta potential of the sol $V_2O_5 \cdot nH_2O$

To determine the actual content of  $V_2O_5 \cdot nH_2O$  nanoparticles in the sol and the loss of  $V_2O_5$  into ionic form in aqueous medium during the synthesis of the sol  $V_2O_5 \cdot nH_2O$ , the ultrafiltration was carried out, and the resulting filtrate was analyzed according to the analysis procedure shown in Section 2.3. Fig. 3 shows the dependence of the percentage of  $V_2O_5 \cdot nH_2O$  particles content on the amount of  $V_2O_5$  during sol synthesis. The concentration of  $V_2O_5 \cdot nH_2O$  nanoparticles increased with increasing total concentrations of vanadium (V) and it can be found that this relationship follows correctly the phase diagram of vanadium (V) in aqueous medium [35]. In addition, with increasing concentrations of vanadium (V) in the system during synthesis, the absolute value of the zeta potential of the nanoparticles increases. This occurs due to a decrease in ionic strength, since the content of dissolved vanadium ions decreases with increasing total vanadium (V) concentration of sol. The dependence of the zeta potential and ionic strength of sols on the initial concentration of  $V_2O_5$  during synthesis are shown in Fig. 4.

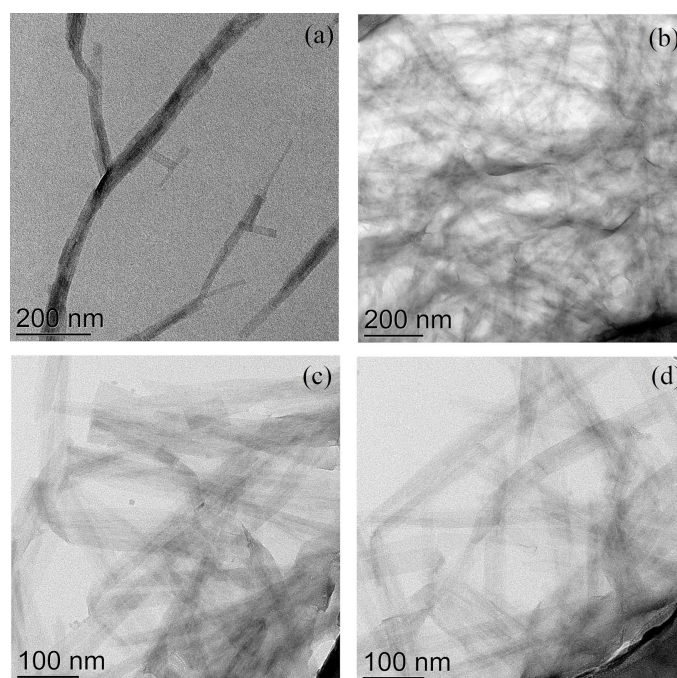


FIG. 2. TEM image of  $V_2O_5 \cdot nH_2O$  nanoparticles

### 3.3. Determination of optical properties and the pH regions that keep the stability of sol

The optical density of the sol was analyzed using a LEKI SS2110UV spectrophotometer. To find the absorption spectrum, the sol ( $\omega\% V_2O_5 = 1$ ) was diluted with the same pH value, and it was found that the maximum absorption spectrum was observed at 378 nm (Fig. 5). The increase in optical density with increasing concentration clearly obeys the Beer–Lambert–Bouguer law (Fig. 6).

To study the pH range that maintains the stability of the sol, it must be diluted due to the high concentration of the sol and the high optical density. The sol having a total concentration of 1 wt%  $V_2O_5$ , was diluted with the same pH number 20 times to 0.05 wt%. The initial pH of the sol is 2.45. It was found that the pH range that keeps the stability of sols is from 2.35 to 3.6, since according to the diagram of vanadium (V) in an aqueous solution [35], the solid phase of vanadium (V) exists only in a very narrow pH range in an acidic environment. As the pH decreased, the particles precipitated and then dissolved. As the pH increases, the optical density first increases, which is associated with the strengthening of the formed complex. With a further increase in pH, the optical density of the solution decreases because of the decomposition of the complex, and with a further increase in pH, partial dissolution of yellow-colored nanoparticles occurs. Optical density of the sol as a function of pH at a wavelength of 550 nm is described in Fig. 7(a).

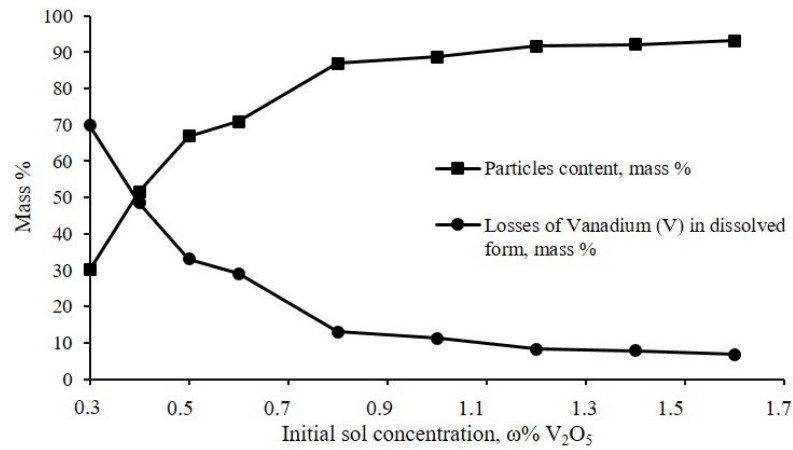


FIG. 3. Dependence of particle content and mass loss of  $V_2O_5$  in dissolved form on the amount of  $V_2O_5$  during sol synthesis

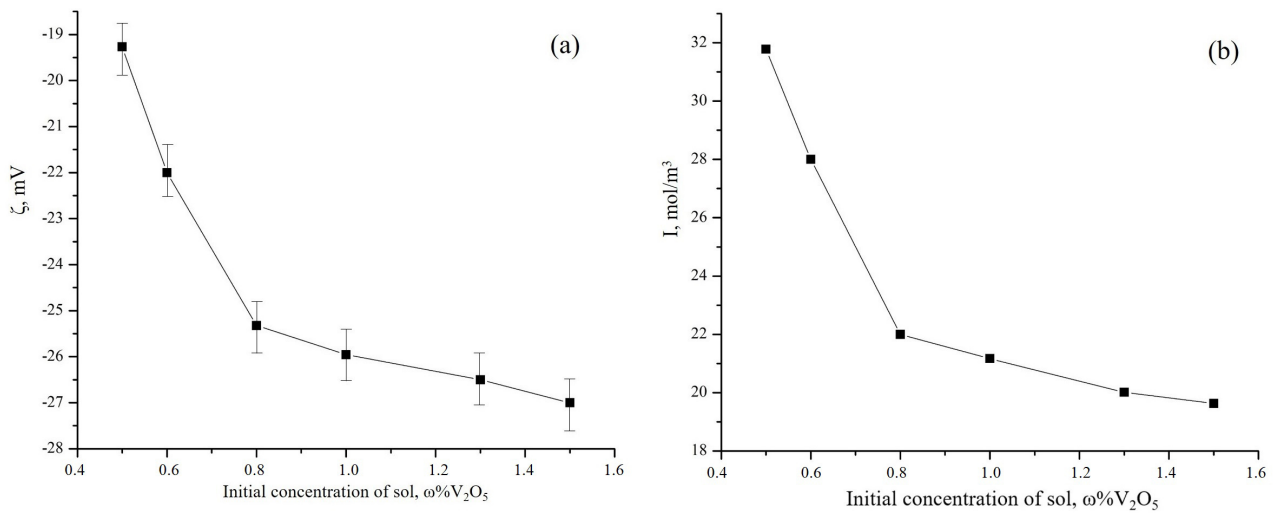


FIG. 4. Dependence of zeta potential  $\zeta$  (a) and ionic strength (b) on the initial mass percentage of  $V_2O_5$  during synthesis

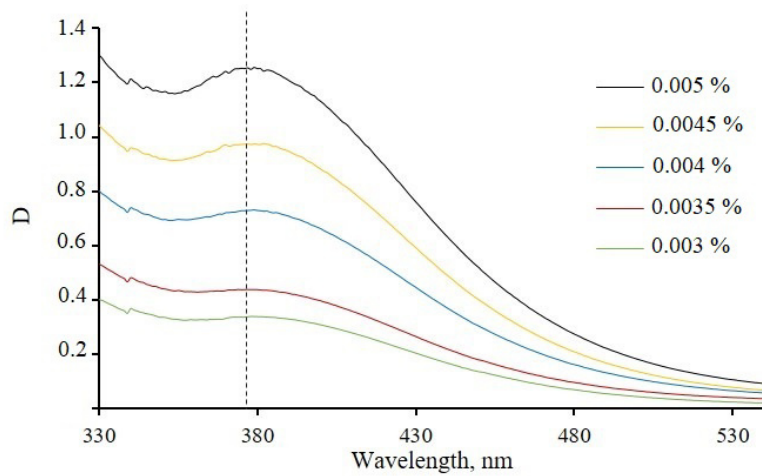


FIG. 5. Absorption spectra of sols with concentrations from 0.003 to 0.005 mass % (diluted from the initial concentration of 1 % mass)

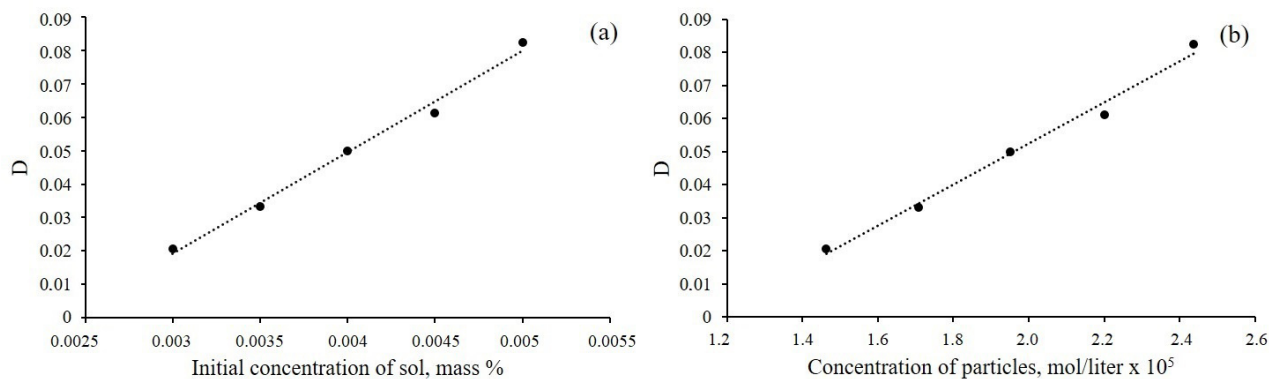


FIG. 6. Optical density of samples with different sol concentrations (a) and with different concentrations of particles at a wavelength of 378 nm (b) (diluted from the initial concentration of 1 % mass)

The dependence of the value of the zeta potential of nanoparticles on the pH of the dispersion medium was also studied, and the results are shown in Fig. 7(b). The initial value of pH is 2.45, and the concentration of sol for this experiment was taken 1 % mass  $V_2O_5$ . It was found that with increasing or decreasing the pH value from the initial pH value within the pH value that keeps sol stability, the absolute value of zeta potential is decreased. Decreasing the absolute value of zeta potential with decreasing the pH is due to the fact that point zero charge of  $V_2O_5 \cdot nH_2O$  lines about at pH value 2 [36, 37]. Decreasing the absolute value of zeta potential with increasing pH is due to the dissolution of nanoparticles.

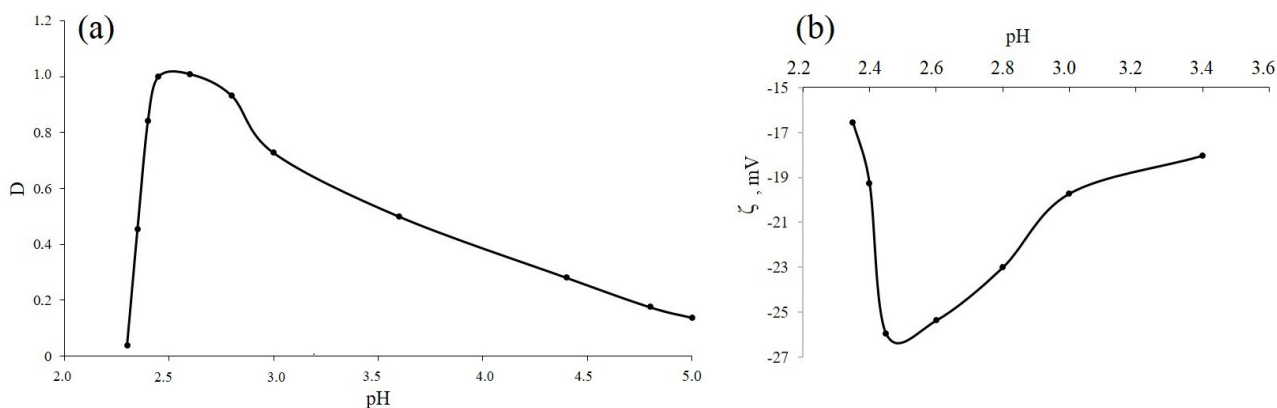


FIG. 7. Optical density of the sol (wt.% = 0.05 %, diluted from the initial concentration of 1 % wt., initial pH = 2.45) as a function of pH at a wavelength of 550 nm (a) and the dependence of the value of the zeta potential of nanoparticles on pH of the dispersion medium (concentration of sol – 1 % mass.  $V_2O_5$ , pH – 2.45) (b)

### 3.4. Rheological properties of the sol $V_2O_5 \cdot nH_2O$

The changes in viscosity of sol on the dependence of concentration are shown in Fig. 8(a). The viscosity of sols increases with increasing their concentration. Viscosity of sol sharply increased after the concentration of sol 1 % mass. This is due to the inner structure formation of particles. Therefore, the viscosity of sol is not linearly dependent on the concentration of sol; the system represents the lyophilic colloidal system [38]. To define the particle shape factor according to Einstein's formula [39], built the graph of the dependence of the relative viscosity of sol on the volume fraction of sol from the concentration of 0.3 to 0.9 mass % (Fig. 8(b)) as during this region the liner dependence of viscosity and concentration of sol was obtained. The particle shape factor was defined by the liner coordinate eq. (14), and its value is approximately 9.608 with a relative error value of less than 0.5 %.

$$\eta = \eta_0(1 + \alpha\varphi_{\text{effective}}), \quad (13)$$

$$\frac{\eta}{\eta_0} = 1 + \alpha\varphi_{\text{effective}}. \quad (14)$$

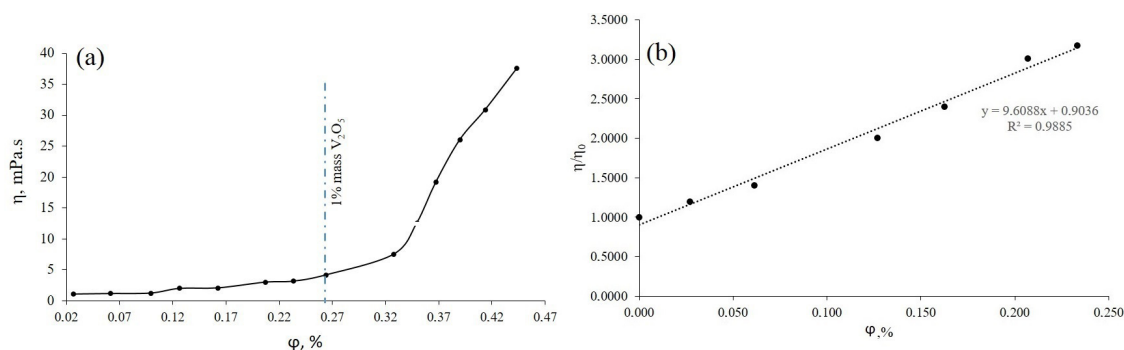


FIG. 8. The changes of viscosity of the sol on the volume fraction of the sol  $\varphi$  from the concentration of 0.3 to 1.6 mass % (a) and the dependence of the relative viscosity of sol  $\eta/\eta_0$  on the volume fraction of sol  $\varphi$  from the concentration of 0.3 to 0.9 mass % (b)

### 3.5. The influence of the electrolyte on the stability of sol $V_2O_5 \cdot nH_2O$

The stability of the sol in the presence of other electrolytes in the colloidal system is one point to study the properties of sol. To determine the threshold for rapid coagulation by the optical method, the sol ( $\omega V_2O_5 - 1\%$ ,  $pH = 2.45$ ) was diluted with the same pH value into 0.02, 0.0225, 0.025, 0.0275, 0.03, 0.04, and 0.05 mass % respectively.  $NaNO_3$ , singly charged counterions is used as an electrolyte. The value of the threshold for rapid coagulation is 0.03 mol/l  $NaNO_3$ . The dependence of the optical density of sol on the concentration of electrolyte ( $\omega V_2O_5 - 0.03\%$ ,  $pH = 2.45$ ) is shown in Fig. 9(a). The dependence of rapid threshold coagulation on the presence of  $NaNO_3$  at different pH was also studied. It was found that at the pH around 2.45 – 2.75, the rapid threshold coagulation is maximum, with increasing and decreasing the pH, the value of threshold coagulation decreases as the stability of sol also decreases (Fig. 9(b)).

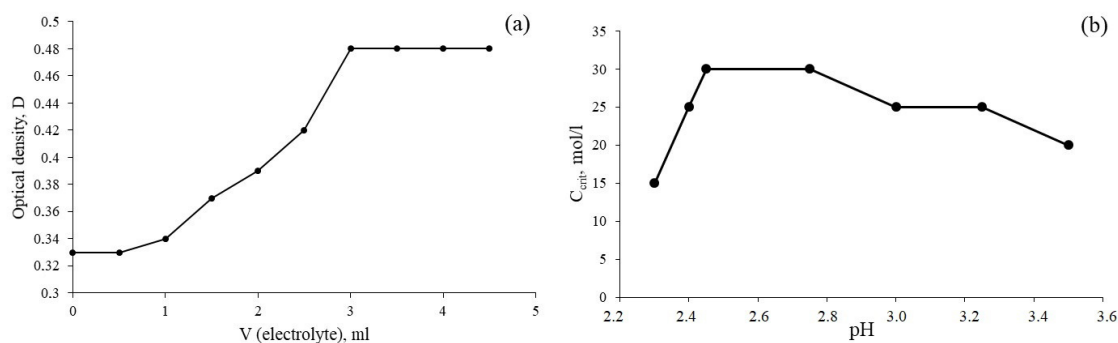


FIG. 9. The dependence of optical density of sol on the volume of electrolyte  $NaNO_3$  ( $\omega V_2O_5 - 0.03\%$ ,  $pH = 2.45$ ) (a) and the dependence of rapid threshold coagulation at the presence of  $NaNO_3$  at different pH (b)

At high sol concentrations in the presence of electrolyte, the system tends to form a gel state. The dependence of the viscosity of sol (1 % mass) on the concentration of the electrolyte  $NaNO_3$  is shown in Fig. 10. The viscosity of lyophilic colloid sols  $V_2O_5 \cdot nH_2O$  falls at small concentrations of added electrolyte  $NaNO_3$  to 0.013 mol/l, and then, when the electrolyte concentration increases, it begins to increase sharply. This process can be explained by the fact that low concentrations of electrolyte destroy the internal structure of the sol due to peptization, and then at high concentrations of electrolyte, coagulation occurs and the viscosity begins to increase.

The influence of the concentration of electrolyte on the value of zeta potential of the sol was also studied (Fig. 11(a)). The zeta potential of a sol decreases when the concentration of electrolytes is increased due to the phenomenon of electrical double layer compression. When electrolytes are added to sol, they dissociate into ions, which can interact with the charged particles in the sol, neutralizing their charges. This leads to a decrease in the electrical potential at the slipping plane and thus, a decrease in the zeta potential. Additionally, the increased concentration of electrolytes can lead to the formation of a more compact and thick electrical double layer around the particles, which further reduces the magnitude of the zeta potential.

Based on the experimental results of the dependence of zeta potential on the concentration of electrolyte, the calculated value of ionic strength (I) and diffuse layer thickness ( $\lambda$ ), and constructed natural logarithm of the zeta potential  $\ln \zeta$  on the dependence of  $1/\lambda$  according to liner coordinate equation Gouy–Chapman – eq. (16) [39] and the graphic is shown in Fig. 11(b).

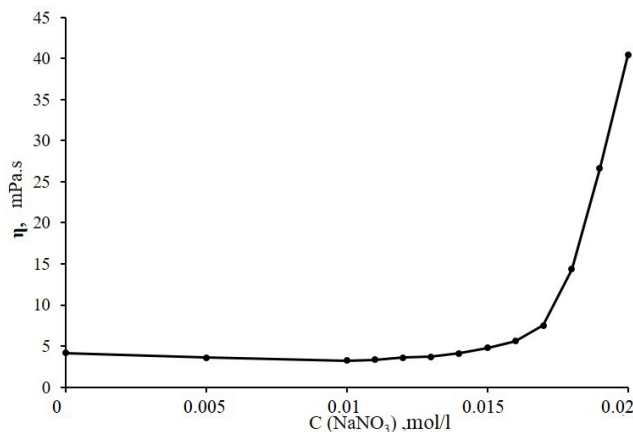


FIG. 10. The dependence of the viscosity of sol (1 % mass) on the concentration of the electrolyte NaNO<sub>3</sub>

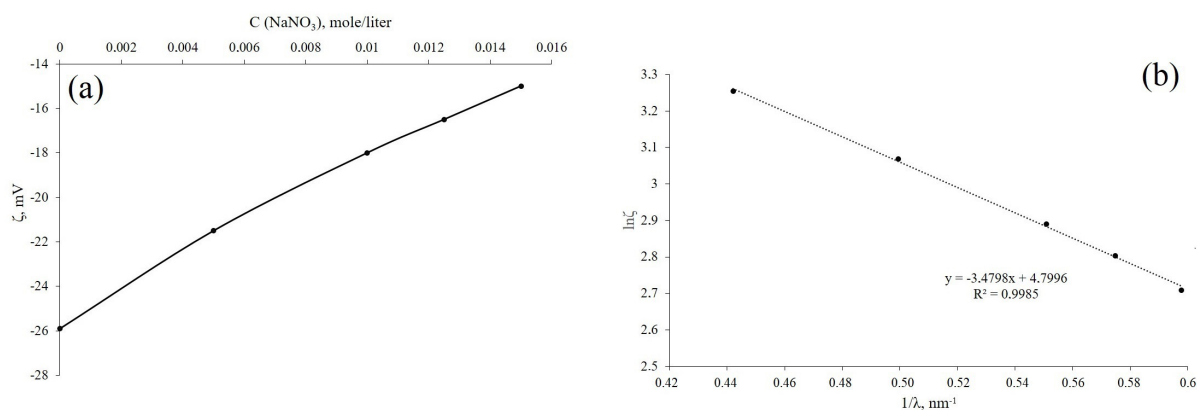


FIG. 11. The influence of the concentration of electrolyte on the value of zeta potential of the sol (concentration of sol – 1 % mass.) (a) and the dependence of natural logarithm of zeta potential  $\ln \zeta$  on the value of  $1/\lambda$  (b)

Gouy–Chapman equation:

$$\zeta = \varphi_{\delta} e^{-l/\lambda}, \quad (15)$$

$$\ln \zeta = \ln \varphi_{\delta} - \frac{l}{\lambda}, \quad (16)$$

where:  $\zeta$  is the value of the zeta potential (mV),  $\varphi_{\delta}$  is the value of the diffuse layer potential (mV),  $l$  is the distance from the Helmholtz layer to the slip plane, nm.

### 3.6. Calculation of potential energy of paired particle interactions using DLVO theory

Graphic of determining the value of the complex Hamaker constant for cylindrical particles of V<sub>2</sub>O<sub>5</sub> sol is shown in Fig. 12(a). The graphically calculated value of the complex Hamaker constant is  $2.6 \times 10^{-20}$  J. As the sol V<sub>2</sub>O<sub>5</sub> · nH<sub>2</sub>O is very stable for about 6 months, the experimental results of potential energy of the paired particle interactions using the DLVO theory is acceptable as the energy barrier is essentially higher than the secondary minima (Fig. 12(b)).

### 3.7. Determination of the dispersion phase of sol

To confirm the phase composition of dispersion phase, the sol was dried at room temperature on the glass plate. The forming thin layer was analyzed by XRD method. X-ray diffraction patterns and electron diffraction patterns of xerogel obtained after drying the sol V<sub>2</sub>O<sub>5</sub> · nH<sub>2</sub>O at room temperature and are shown in Fig. 13. Its X-ray diffraction peaks in Fig. 13 were in good agreement with the standard X-ray diffraction patterns of V<sub>2</sub>O<sub>5</sub> · 1.6H<sub>2</sub>O (JCPDS card No. 40-1296) with orthorhombic crystal system. The crystallite size in the crystallographic direction [001] was calculated using the Scherrer method and amounted to about 11 nm. The results of the interplanar distances calculated from electron diffraction data are shown in Table 1. The formation of thin layer xerogel V<sub>2</sub>O<sub>5</sub> · 1.6H<sub>2</sub>O on the surface of ceramic membrane is shown in Fig. 14.

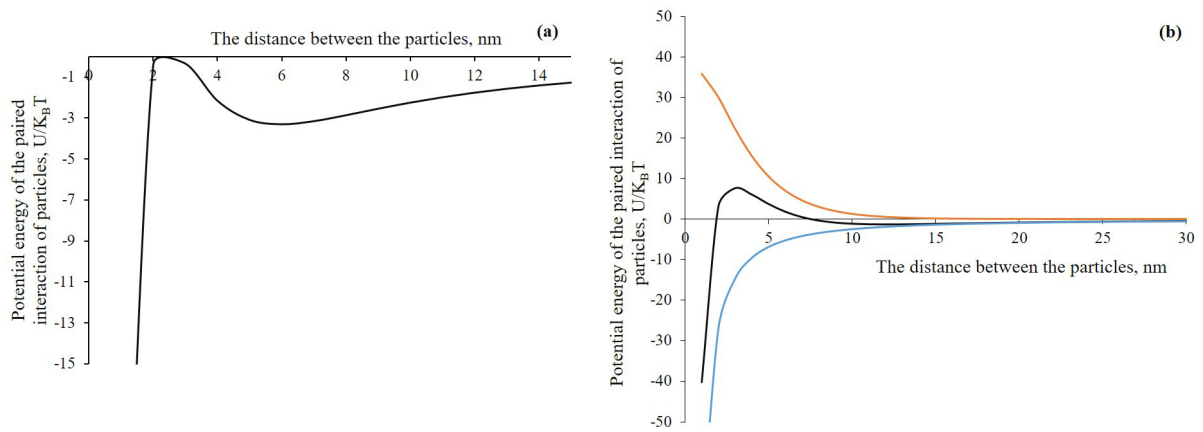


FIG. 12. Potential curves of pair interaction of  $V_2O_5 \cdot nH_2O$  nanoparticles for determining the complex Hamaker constant (a) and potential curves of pair interaction of  $V_2O_5 \cdot nH_2O$  nanoparticles (b)

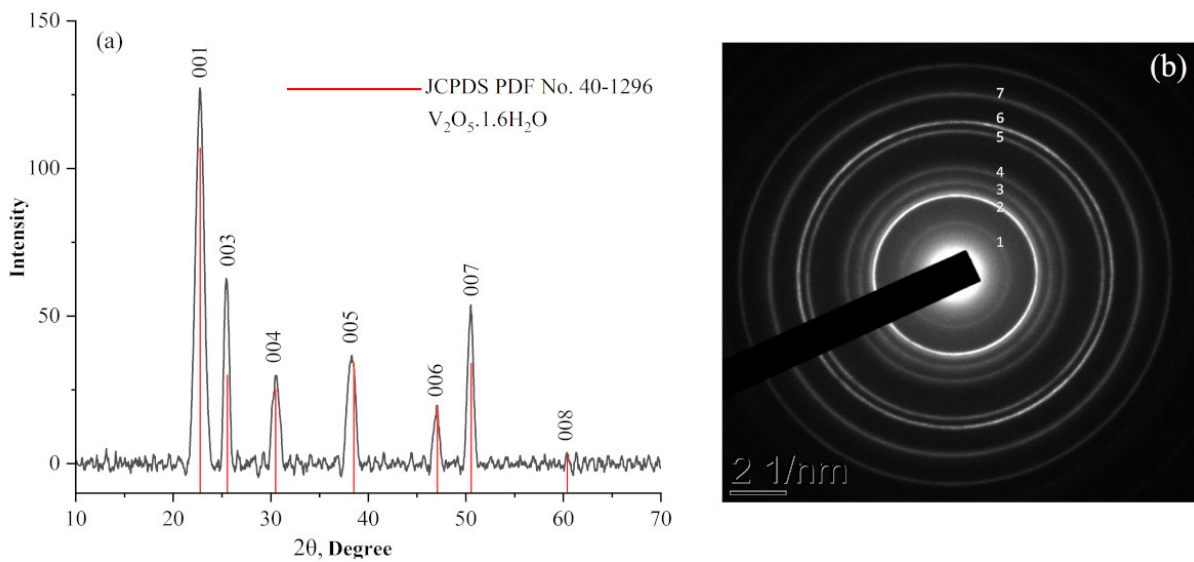


FIG. 13. X-ray diffraction patterns (a) and electron diffraction patterns (b) of xerogel obtained after drying the sol  $V_2O_5 \cdot nH_2O$  at room temperature

TABLE 1. The results of comparing the interplanar distances calculated from electron diffraction data with those for the  $V_2O_5 \cdot 1.6H_2O$  compound (PDF-2 No. 40-1296)

The point in Fig. 13(b)	Interplanar distances ( $d$ ) according to the electron diffraction data (Fig. 13(b)), Å	Miller indices $hkl$ of $V_2O_5 \cdot 1.6H_2O$ compound reflections
1	3.902	001
2	3.482	003
3	2.925	004
4	2.345	005
5	1.927	006
6	1.808	007
7	1.534	008

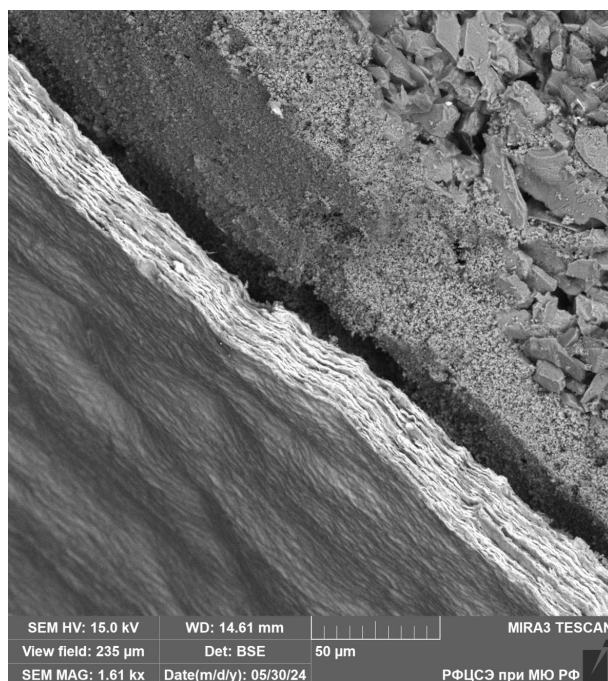


FIG. 14. SEM image of the thin film layer  $V_2O_5 \cdot 1.6H_2O$ , which was obtained after drying on ceramic

#### 4. Conclusion

This study explored the colloidal chemical properties of the lyophilic dispersion system  $V_2O_5 \cdot nH_2O$  sol. The key findings are as follows.

1. Optimal synthesis conditions. The optimal mole ratio of  $V_2O_5$  and  $H_2O_2$  for the synthesis of the sol is 1:30. The optimal concentration range that maintains the sol's stability is 0.3 to 1.6 % by mass of  $V_2O_5$ .
2. Particles content in sols. The concentration of  $V_2O_5 \cdot nH_2O$  particles increased with increasing total concentrations of vanadium (V) and it can be found that this relationship follows correctly the phase diagram of vanadium (V) in aqueous medium.
3. Zeta potential. As the concentration of vanadium (V) in the system increases during synthesis, the absolute value of the zeta potential of the nanoparticles also increases as the ionic strength of the dispersion medium decreases.
4. Optical properties. The maximum absorption spectrum of the prepared sols was observed at 378 nm. The increase in optical density with increasing concentration clearly obeys the Beer-Lambert-Bouguer law.
5. pH range. The pH range that maintains the sol's stability is between 2.35 and 3.6.
6. Viscosity. The viscosity of the sol sharply increases after the concentration reaches 1 % by mass.
7. Particle shape factor. The particle shape factor is approximately 9.608, with a correlation coefficient of 0.9885.
8. The influence of the electrolyte on the stability of sol  $V_2O_5 \cdot nH_2O$ . The rapid threshold coagulation in the presence of  $NaNO_3$  (singly charged counterions) is maximum around pH 2.45 – 2.75. At high sol concentrations in the presence of an electrolyte, the system tends to form a gel state. The zeta potential of the sol decreases when the concentration of electrolytes is increased due to the phenomenon of electrical double layer compression.
9. DLVO theory. Calculations of the potential energy of paired particle interactions using DLVO (Derjaguin–Landau–Verwey–Overbeek) theory were carried out. The experimental results of the potential energy of paired particle interactions using the DLVO theory are acceptable, as the energy barrier is significantly higher than the secondary minima.

Overall, this study provides valuable insights into the colloidal chemical properties of the  $V_2O_5 \cdot nH_2O$  sol, which can be useful for various applications, such as in the development of functional materials and catalysts.

#### References

- [1] Top K. Le, Phuong V. Pham. Recent advances in vanadium pentoxide ( $V_2O_5$ ) towards related applications in chromogenics and beyond: fundamentals, progress, and perspectives. *J. of Materials Chemistry C*, 2022, **10**, P. 1–55.
- [2] Xuyan L., Jiahuan Z.  $V_2O_5$ -Based nanomaterials: synthesis and their applications. *RSC Adv.*, 2018, **8**, P. 4014–4031.
- [3] Ehsan K. Recent advances in synthesis, properties, and applications of vanadium oxide nanotube. *Microchemical J.*, 2019, **145**, P. 966–978.
- [4] Thi Dieu H.N., Vo K.D. Electronic and optical excitation properties of vanadium pentoxide  $V_2O_5$ . *Computational Materials Science*, 2022, **198**, P. 1–8.
- [5] Sukrit S., Gaihua Ye.  $V_2O_5$ : A 2D van der Waals Oxide with Strong In-Plane Electrical and Optical Anisotropy. *ACS Appl Mater Interfaces*, 2017, **9** (28), P. 23949–23956.

- [6] Ryan R.L., David M.K. Catalytic Applications of Vanadium: A Mechanistic Perspective. *Chemical Reviews*, 2019, **119**, P. 2128–2191.
- [7] Kaichev V., Popova G.Y. Selective oxidation of methanol to form dimethoxymethane and methyl formate over a monolayer  $V_2O_5/TiO_2$  catalyst. *J. of Catalysis*, 2014, **311**, P. 59–70.
- [8] David V.F., William J.M. The formation of propane, propylene, and acetone from 2-propanol over vanadium pentoxide and modified vanadium pentoxide catalysts. *Canadian J. of Chemistry*, 1978, **56**, P. 28–39.
- [9] Bars J. Le, Auroux A. Active Sites of  $V_2O_5/\gamma-Al_2O_3$  catalysts in the oxidative dehydrogenation of ethane. *J. of Catalysis*, 1996, **162**, P. 250–259.
- [10] Lemke K., Ehrlich H. Selective hydroxylation of benzene to phenol over supported vanadium oxide catalysts. *Appl. Catal. A Gen.* 2003, **243**, P. 41–51.
- [11] Lukasz W., Maria Z. Insight into pathways of methylene blue degradation with  $H_2O_2$  over mono and bimetallic Nb, Zn oxides. *Applied Catalysis B: Environmental*, 2017, **224**, P. 634–647.
- [12] Alain M., Christian M.J.  $V_2O_5$  thin films for energy storage and conversion. *AIMS Materials Science*, 2018, **5** (3), P. 349–401.
- [13] Huguenin F., Martins A.R. Nanocomposites from  $V_2O_5$  and Lithium-Ion Batteries. In: Souza F., Leite E. (eds) *Nanoenergy*, 2017, P. 223–249.
- [14] Lai V.D., To T.N. Light-assisted room temperature ammonia gas sensor based on porphyrin-coated  $V_2O_5$  nanosheets. *Sensors and Actuators B: Chemical*, 2024, **409**, P. 135–150.
- [15] Dongwon S., Jiseon K. Evaluation of  $V_2O_5$  Film-Based Electrochromic Device with Dry-Deposited Ion Storage Layer. *Int. J. Precis. Eng. Manuf.*, 2023, **24**, P. 119–128.
- [16] Ma O., Batal F.E. Impact of  $V_2O_5$  and Gamma Ray Irradiation on the Optical and Structural FTIR Spectra of Lithium Phosphate Glass. *Global J. Eng. Sci.*, 2019, **3** (4), P. 1–8.
- [17] Gary A.P., Lisa W. Effects of Aging Time on  $V_2O_5$  Sol-Gel Coatings. *J. of Sol-Gel Science and Technology*, 1994, **3**, P. 57–62.
- [18] Keiji Y., Tatsuro M. Dynamics of  $V_2O_5$  Sol by Measurement of Ultrasonically Induced Birefringence. *J. Appl. Phys.*, 1994, **33**, P. 2901–2904.
- [19] Gotic M., Popovic S. Music Sol-gel synthesis and characterization of  $V_2O_5$  powders. *Materials Letters*, 2003, **57**, P. 3186–3192.
- [20] Sanchez C., Nabavi M. Synthesis and characterization of vanadium oxide gels from alkoxy-vanadate precursors. *Mat. Res. Soc. Symp. Proc.*, 1988, **121**, P. 93–104.
- [21] Wen C., Junfeng P. Synthesis of vanadium oxide nanotubes from  $V_2O_5$  sols. *Materials Letters*, 2004, **58**, P. 2275–2278.
- [22] Jay Singh, Kshitij RB Singh, Manish Kumar, Rahul Verma, Ranjana Verma, Priya Malik, Saurabh Srivastava, Ravindra Pratap Singh, Devendra Kumar. Melt-quenched vanadium pentoxide stabilized chitosan nanohybrids for efficient hydrazine detection. *Materials Advances*, 2021, **2**, P. 6665–6675.
- [23] Yu H.C.W., Dai Y.M.L. Preparation and Optical Properties of  $V_2O_5$  Nanotube Arrays. *J. of Wuhan University of Technology – Mater. Sci. Ed.*, 2006, **21**, P. 38–41.
- [24] Wang N., Magdassi S., Mandler. D. Simple sol-gel process and one-step annealing of vanadium dioxide thin films: Synthesis and thermochromic properties. *Thin Solid Films*, 2013, **534**, P. 594–598.
- [25] Huali W., Xuanxuan B. Open-structured  $V_2O_5 \cdot nH_2O$  nanoflakes as highly reversible cathode material for monovalent and multivalent intercalation batteries. *Advanced Energy Materials*, 2017, **7**, P. 1–8.
- [26] Orhan Ö., Pinar F.G. Nano-Crystal  $V_2O_5 \cdot nH_2O$  Sol-Gel Films Made by Dip Coating. *AIP Proceedings*, 2012, **1476**, P. 233–240.
- [27] Nathalie S., Jacques L. Rational design of one-dimensional vanadium (V) oxide nanocrystals: an insight into the physico-chemical parameters controlling the crystal structure, morphology and size of particles. *Cryst. Eng. Comm.*, 2015, **17**, P. 6780–6795.
- [28] Bruno A., Jacques L. Synthesis of Vanadium Oxide Gels from Pyrovanadic Acid Solutions: A 51V NMR Study. *J. of Solid-State Chemistry*, 1999, **148**, P. 16–19.
- [29] Craig J.F., Jerzy W.W. Vanadia Gel Synthesis via Peroxovanadate Precursors. 1. In Situ Laser Raman and 51V NMR Characterization of the Gelation Process. *J. Phys. Chem. B*, 2000, **104**, P. 11622–11631.
- [30] Ahmed S.E., Andrew J.P. Insights into the Exfoliation Process of  $V_2O_5 \cdot nH_2O$  nanosheet Formation Using Real-Time 51V NMR. *ACS Omega*, 2019, **4**, P. 10899–10905.
- [31] Muggin V.N., Khamina L.B. *Analytical chemistry of vanadium*. Publishing house “Science”, Moscow, 1981, 109 p.
- [32] Kirsch V.A., Kirsch V.A. Calculation of the van der Waals force between a spherical particle and an infinite cylinder. *Advances in Colloid and Interface Science*, 2003, **104**, P. 311–324.
- [33] Ohshima H. *Theory of colloid and interfacial electric phenomena*. Elsevier: Ac. Press., Tokyo, 2006, 490 p.
- [34] Ohshima H. *Biophysical chemistry of biointerfaces*. Wiley, Tokyo, 2010, 567 p.
- [35] Povar I., Spinu O., Zinicovscaia I., Pintilie B., Ubaldini S. Revised Pourbaix diagrams for the vanadium-water system. *J. Electrochemical. Sci. Eng.*, 2019, **9**, P. 75–84.
- [36] Sherif H.K., Zakya H.K. *Science and Technology of Polymers and Advanced Materials: Emerging*. Springer Science + Business Media LLC. New York, 1998, 900 p.
- [37] Michael S., Karge H.G. *Advanced Zeolite Science and Applications*. Studies in Surface and Catalysts, Netherlands, 1994, 700 p.
- [38] Belokon N.E. *Technical reference book for railway workers, physical and mathematical*. State Transport Railway Publishing House, Moscow, 1951, 663 p.
- [39] Nazarov V.V. *Colloidal chemistry: Textbook*. Delhi Plus, Moscow, 2015, 250 p.

---

Submitted 22 May 2024; revised 17 August 2024; accepted 22 August 2024

#### Information about the authors:

Hein Myat Lwin – D. I. Mendeleev University of Chemical Technology of Russia, Department of Colloidal Chemistry, Miusskaya square, 9, Moscow, 125047, Russia; ORCID 0009-0000-6975-2380; heinmyatlwin2468@gmail.com

Oksana V. Yarovaya – D. I. Mendeleev University of Chemical Technology of Russia, Department of Colloidal Chemistry, Miusskaya square, 9, Moscow, 125047, Russia; ORCID 0000-0001-8661-3235; iarovaia.o.v@muctr.ru

Conflict of interest: the authors declare no conflict of interest.

## Kinetic of colloidal-chemical transformations during the decomposition of ammonia complexes of Zn(II) in alkaline solutions

Maria A. Maksimova<sup>1,a</sup>, Evgeny V. Polyakov<sup>1,b</sup>, Ilya V. Volkov<sup>1</sup>,  
Aleksandr P. Tyutyunnik<sup>1</sup>, Alexey A. Ioshin<sup>1,c</sup>

<sup>1</sup>ISSC UB RAS, Ekaterinburg, Russia

<sup>a</sup>msalimova1993@gmail.com, <sup>b</sup>polyakov@ihim.uran.ru, <sup>c</sup>aaioshin@yandex.ru

Corresponding author: Maria A. Maksimova, msalimova1993@gmail.com

PACS 81.15.-z

**ABSTRACT** For the closed system ( $\Sigma$ ):  $Zn^{2+}-NH_{3,aq}-NH_{3,gas}$ ,  $H^+-OH^- -N_{2,gas}$ , experimental data on the change in the concentration of in the composition of the ammonia complex  $Zn(NH_3)_4^{2+}$  in solution, colloidal particles  $Zn(OH)_2/ZnO$  in solution and growing film on the reactor walls are presented depending on the synthesis time, zinc concentration and synthesis temperature  $T_s$  in the range of 50–99 °C. It has been established that up to 95 °C the ion-molecular growth of  $Zn(OH)_2/ZnO$  clusters in solution ( $\Sigma$ ) proceeds in a diffusion-controlled mode of homogeneous growth until reaching of their critical size. Further growth of their critical clusters is followed by aggregation and coalescence of critical sized clusters into microcrystals with the formation of a film on a glass substrate of various morphologies. The solubility of such a film is determined by the size of critical clusters, which preserves in the growing polycrystal in the form of coherent scattering region (*CSR*). With an increase in the synthesis temperature to 99 °C, the aggregation mechanism is replaced by a faster diffusion-controlled attachment of Zn (II) ammonia complex to the end surface of the growing microcrystals simultaneously in colloid solution and in the film.

**KEYWORDS** Zn(II), ammonia complex,  $Zn(OH)_2/ZnO$ , colloid, film, growth, mechanism

**ACKNOWLEDGEMENTS** The work was carried out with the support of the State Program of Fundamental Scientific Research of the Russian Federation (project No. 124020600007-8).

**FOR CITATION** Maksimova M.A., Polyakov E.V., Volkov I.V., Tyutyunnik A.P., Ioshin A.A. Kinetic of colloidal-chemical transformations during the decomposition of ammonia complexes of Zn(II) in alkaline solutions. *Nanosystems: Phys. Chem. Math.*, 2024, **15** (4), 498–509.

### 1. Introduction

The colloidal-chemical nature of laminar systems formation in the liquid phase (thin films, layers, coatings) was first studied systematically at the beginning of the last century [1]. That work was further developed under the general motto of “chemical bath deposition” (CBD) methods [2–5]. The interest of technologists in CBD methods is due to the relative simplicity of their implementation, cost-effectiveness, the ability to scale up the technique of applying thin films, layers, coatings on substrates without the use of expensive and special equipment, high temperatures and pressures. This method can also be used to produce thin films with controlled structure and morphology, such as nanocrystalline flowers, oriented nanowires, and nanoribbons. They are recommended for the manufacture of films formed by particles of any shape, such as flat, spherical, porous and tubular structures [2].

The disadvantage of the methods is their relatively low reproducibility compared to physical deposition methods. This limitation is eliminated by optimizing the growth parameters [6]. Among the diverse objects of film synthesis by CBD methods, chalcogenide films are in the first place [4, 7]. In recent decades, the production of 1-D films of metal-oxide nanoscale compounds and semiconductors, such as ZnO, was of particular interest. Their synthesis makes it possible to create ultrafine wires and rods on inorganic and polymer substrates for use as elements of solar converters, electronic circuits, radiation shields, light concentrators, and radiation coolers [8–13]. The kinetics of growth of thin films of oxides and chalcogenides from aqueous and mixed water-organic solutions differs depending on whether the mechanism of homogeneous or heterogeneous growth (heteronucleation) prevails during their formation [2, 3, 5]. Hydroxides, oxides, chalcogenides of Zn(II) belong to the group of compounds prone to the formation of colloidal solutions at relatively low values of supersaturation for metal ions. Heteronucleation is thought to be the main mechanism of film growth for them [5, 14]. After the first experimental studies of the initial stage of the colloidal-chemical mechanism of semiconducting film growth, it became clear that chalcogenide film formation on untreated surfaces proceeds only if a metal hydroxide film has been preliminarily formed [15, 16]. For example, the initial stage of sulfide film growth includes the formation of nanoclusters of the future hydroxide phase in a supersaturated ammonia solution. Then the nanoclusters cover the surface

of the substrate. This stage is responsible for the observed induction period of growth of many sulfide films from ammonia solutions [16]. The hydroxide phase acts as a natural surface activator. Its subsequent ion-exchange interaction [15–17] with the sulfide ions of the solution ensures the chemical modification of hydroxide into sulfide and the heterogeneous growth of the latter. At the same time, colloidal particles are formed in the volume of the solution (clusters, [18]), and their distribution at the film – solution phases interface is governed by the mechanism of heteronucleation [1, 3, 5, 16].

According to the cluster theory of crystal growth in solution, the size of primary colloidal particles ( $r$ ) determines the relative solubility of the growing crystals as Gibbs-Thomson relation [18, 19]

$$RT_s \ln \frac{a}{a_0} = \frac{\sigma \bar{V}}{r}, \quad (1)$$

where  $R$ ,  $T_s$ ,  $\bar{V}$ ,  $\sigma$ ,  $a$ ,  $a_0$  are respectively the universal gas constant (J/mol, K), the synthesis temperature (K), the molar volume of crystals ( $\text{m}^3/\text{mol}$ ), the surface tension ( $\text{J}/\text{m}^2$ ), the activity (concentration) of crystals in the supersaturated and equilibrium solution (mol/kg). If there are factors that impede the growth of nanocrystals in the volume of solution (large surface charge, phase transformations in the surface layer of the nanocrystals with the formation of a non-autonomous phase [20] etc.), their size may fluctuate near the critical cluster [18]. Further accumulation of critical clusters leads to a transition from a homogeneous to a heterogeneous growth mechanism.

The lack of experimental data on the initial stages of the colloidal-chemical process in aqueous-ammonia solutions with the participation of hydroxides determines the importance of studying the kinetics of thermal hydrolysis of ammonia complexes of d-metals as a significant element of the general mechanisms of oxide and chalcogenides film growth [21, 22]. Regardless of the type of organic ligand (urea, hexamethylenetetramine, mono-, di-, triethanolamine, dimethylamine, tetramethylammonium, etc.), the destruction of ammonia zinc complexes with increasing temperature leads to alkaline hydrolysis with the subsequent formation of a hydroxide/oxide phase [23–30].

The results of the thermodynamic analysis of the concentration and temperature regions of predominance of  $\text{Zn}(\text{OH})_2$ – $\text{ZnO}$  in the system ( $\Sigma$ ): “ $\text{Zn}^{2+}$ – $\text{NH}_3$ , $_{aq}$ – $\text{NH}_3$ , $_{gas}$ ,  $\text{H}^+$ – $\text{OH}^-$ – $\text{N}_2$ , $_{gas}$ ”, show [29, 30] that the formation of the solid phase begins at  $\text{pH} > 6 - 7$  and depends on the temperature. The reactions in aqueous-ammonia solution with the participation of  $\text{Zn}(\text{OH})_2$ – $\text{ZnO}$  particles are characterized by the presence of some volatile components of ( $\Sigma$ ) in both the gaseous and liquid phases ( $\text{NH}_3$ (a,g),  $\text{H}_2\text{O}$ (a,g)) (Fig. 1) and the in the state of nano- and microbubbles in solution. The topics of gas bubbles origin and methods of their detecting in electrolyte solution are under discussion up to now [31]. Among adequate methods used for gas nanoparticles size and surface charge monitoring in water solution are instrumental methods of dynamic light scattering (DLS) coupled with laser Doppler electrophoresis (LDE) [32]. In our previous research we used both DLS and LDE method with the help of a Zetasizer Nano ZS particle analyzer (Malvern Panalytical Ltd.).

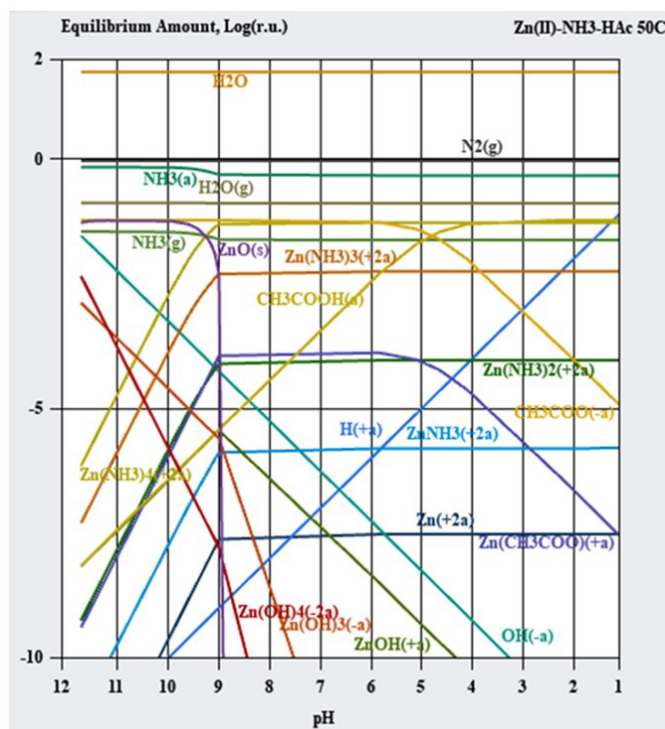


FIG. 1. Example of predominance diagram of chemical species in the system ( $\Sigma$ ) at 50 °C calculated with the help of HSC Chemistry 8 software

The growth of a hydroxide film on the surface of the substrate with the participation of gas bubbles at a relatively low temperature (less than 65 °C) gives a film with a  $\text{Zn}(\text{OH})_2$  (Wulfingit) structure and a foam-like morphology [29]. Above 80 °C, the films on the glass substrate acquire an orientation in the direction normal to the substrate surface, the hexagonal habit of ZnO (Wurtzite) and the morphology of druzen (nanoflowers) growing from a common center of crystallization, Fig. 2 and [22, 30, 33, 34]. The synthesis temperature also affects the ratio of  $\text{Zn}(\text{OH})_2/\text{ZnO}$  phases in films, the optical width of the solid phase slit, and the luminescence intensity during the transition from  $\text{Zn}(\text{OH})_2$  to ZnO [35, 36].

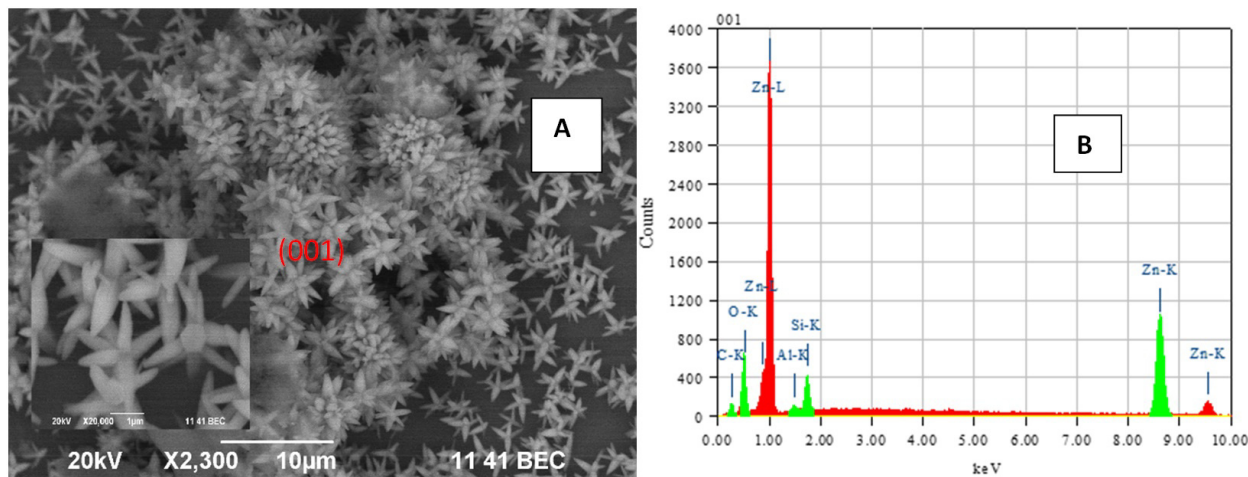


FIG. 2. (A) An example of the morphology of a ZnO film on a fragment of the glass wall of a test tube according to SEM data (enlarged fragment is shown in the inset). (B) X-ray fluorescence spectrum of ZnO particles at point (001). Synthesis duration 35 min,  $T_s = 85$  °C

We have previously shown that the driving force behind the formation of  $\text{Zn}(\text{OH})_2\text{-ZnO}$  nanoparticles in a closed initially homogeneous system ( $\Sigma$ ) is the difference in the chemical potentials of ionic particles at 25 °C and at elevated synthesis temperature  $T_s$  (supersaturated system). By using the methods of vibrational spectroscopy, X-ray phase and chemical analysis, diffuse light scattering and electrophoresis we have established that the phase transition of  $\text{Zn}(\text{OH})_2$  to ZnO in the studied system occurs in the region of  $T_s = 85 - 90$  °C, but at lower temperatures ZnO is also present in the solid as an impurity. The increase in the concentration of colloid and film, as well as in the electrical conductivity of the solution with the time of synthesis, obeys the equation of the 1st order irreversible reaction for zinc ions.

The transformation of ionic particles of  $\text{Zn}(\text{NH}_3)_4^{2+}$  into colloidal microcrystals of the composition  $\text{Zn}(\text{OH})_2\text{-ZnO}$  is a multistage process. The first stage takes place predominantly in the volume of the solution with the participation of the surfaces of the “gas bubbles-solution” interface as a result of rapid formation, growth and removal of gas bubbles from the solution during heating.

By comparing the variation in the size of colloid particles, their  $\zeta$ -potential and  $\zeta$ -potential of gas bubbles in the solution as a function of reaction time we have concluded [29] that the interaction of positively charged  $\text{Zn}(\text{OH})_2$  nanoparticles with the negatively charged surface of gas bubbles may lead to the growth of colloidal aggregates “bubble|surface film” of hydroxide nanoparticles in the form of solid foam-like surface. Such morphology is seen on SEM pictures of films, synthesized at the induction stage of film growth.

After degassing of the electrolyte solution at the second stage of film formation, the morphology of the film changes drastically. On the SEM pictures we can see nucleation and growth of columnar microcrystals  $\text{Zn}(\text{OH})_2\text{-ZnO}$ , which look like three-dimensional stars with conical spikes of hexagonal cross-section, Fig. 2. It is of interest to trace the relationship between the conditions of formation of nanocrystals as a result of thermal decomposition of the most stable complex  $\text{Zn}(\text{NH}_3)_4^{2+}$  (or, more precisely, the ion pair  $\text{Zn}(\text{NH}_3)_4(\text{OH})_2$ ) and the parameters of colloidal aggregates in the volume of the solution and at the interface surfaces.

The aim of this work was to determine the kinetic regularities of the growth of  $\text{Zn}(\text{OH})_2$  films on the glass surface in thermally nonequilibrium alkaline ammonia solutions with the participation of the  $\text{Zn}(\text{NH}_3)_4(\text{OH})_2$  complex. We aimed also on establishing a relationship between the value of solubility of growing colloidal particles  $\text{Zn}(\text{OH})_2\text{-ZnO}$ , the clusters of critical size in solution (hereinafter referred to as “critical clusters”,  $r$ ) according to equation (1), and the value of the coherent scattering region ( $CSR$ ) in polycrystalline growth products according to X-ray phase analysis of  $\text{Zn}(\text{OH})_2\text{-ZnO}$  films.

TABLE 1. The estimates of *CSR* sizes of the Wulffingit film by Williams–Hall method [37]. Temperature of the synthesis 50 °C, duration of the synthesis 80 min

Plane	Size, nm	Strain, 10 <sup>4</sup>	No. of reflections
All reflection	64.21	1.78	211
100	66.68	3.07	2
010	66.04	2.62	2
001	62.98	1.51	4
111	64.49	1.98	3

## 2. Experimental

To prepare a work solution, 4.39 g of  $\text{Zn}(\text{CH}_3\text{COO})_2 \times 2\text{H}_2\text{O}$  was dissolved in a small amount of water, 10 ml of concentrated ammonia was added and brought to a volume of 100 ml with deionized water (Millipore water treatment system). To adjust the pH to 10.2 – 10.3, 67 ml of NaOH solution with a concentration of 0.05 M was added drop by drop. The final volume of the obtained starting solution (167 ml) contained (mol/l)  $\text{Zn}(\text{II})=0.12$ ,  $\text{NH}_3=1.0$ ,  $\text{NaOH}=0.02$ . The kinetics of the synthesis of the  $\text{Zn}(\text{OH})_2\text{--ZnO}$  colloid and the film was studied in a series of test tubes made of heat-resistant glass filled with a 5.0 ml work  $\text{Zn}(\text{II})$  solution. The test tubes were closed with a rubber stopper. A Termex thermostat with water heat-carrier provided temperature stability and uniformity of the temperature field in the working area of the thermostat coolant,  $\pm 1$  °C. At specified time intervals, the corresponding test tube with the work solution was removed from the heat-carrier and the concentration of zinc was analyzed in the filtrate after acidifying the filtrate to a concentration of 1.8 – 2.0 mol/l with hydrochloric acid. The colloid part was separated from the solution by ultrafiltration through a double cellulose filter with a pore size of less than 100 nm under vacuum. The precipitate on the filter was sequentially dried and dissolved in 2 mol/l of hydrochloric acid (qualification “chemically pure”) of a given volume. The mass of  $\text{Zn}(\text{II})$  was determined in this volume by mass spectrometry with inductively coupled plasma and then the mass (mol) of metal in the form of a colloid in the system ( $\Sigma$ ) under study was calculated at a given time. The zinc content in the film on the walls of the glass reactor was determined after dissolving the layer with hydrochloric acid of 2 mol/l in a volume equal to the volume of the solution under study (5.0 ml). The method of elemental analysis of solution, colloid, and film is described in more detail elsewhere [22, 24].

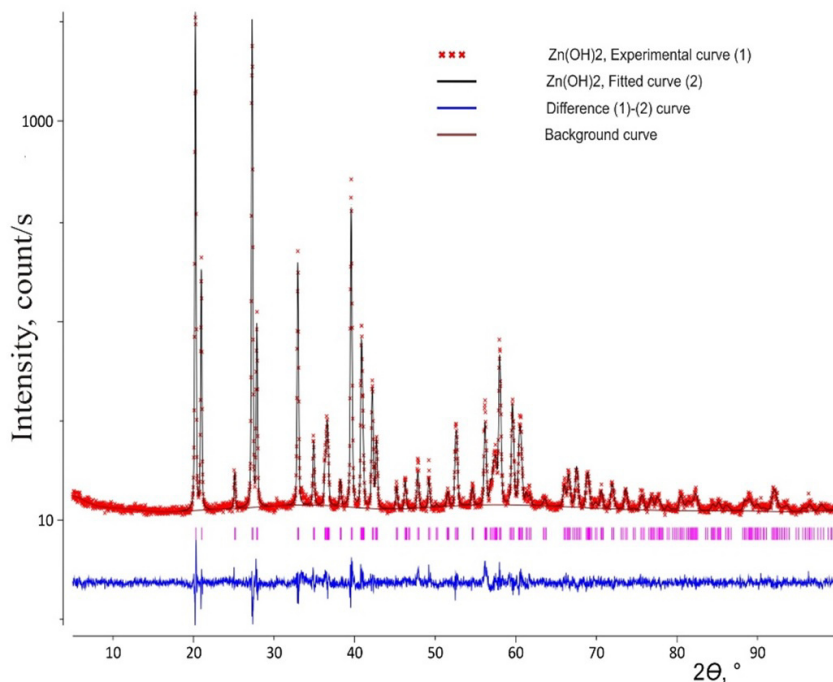


FIG. 3. Example of diffractogram of  $\text{Zn}(\text{OH})_2$  film (Wulffingit) on the glass substrate, which was performed on a STADI-P X-ray powder automatic diffractometer (STOE) with  $\text{CuK}_{\alpha 1}$  radiation

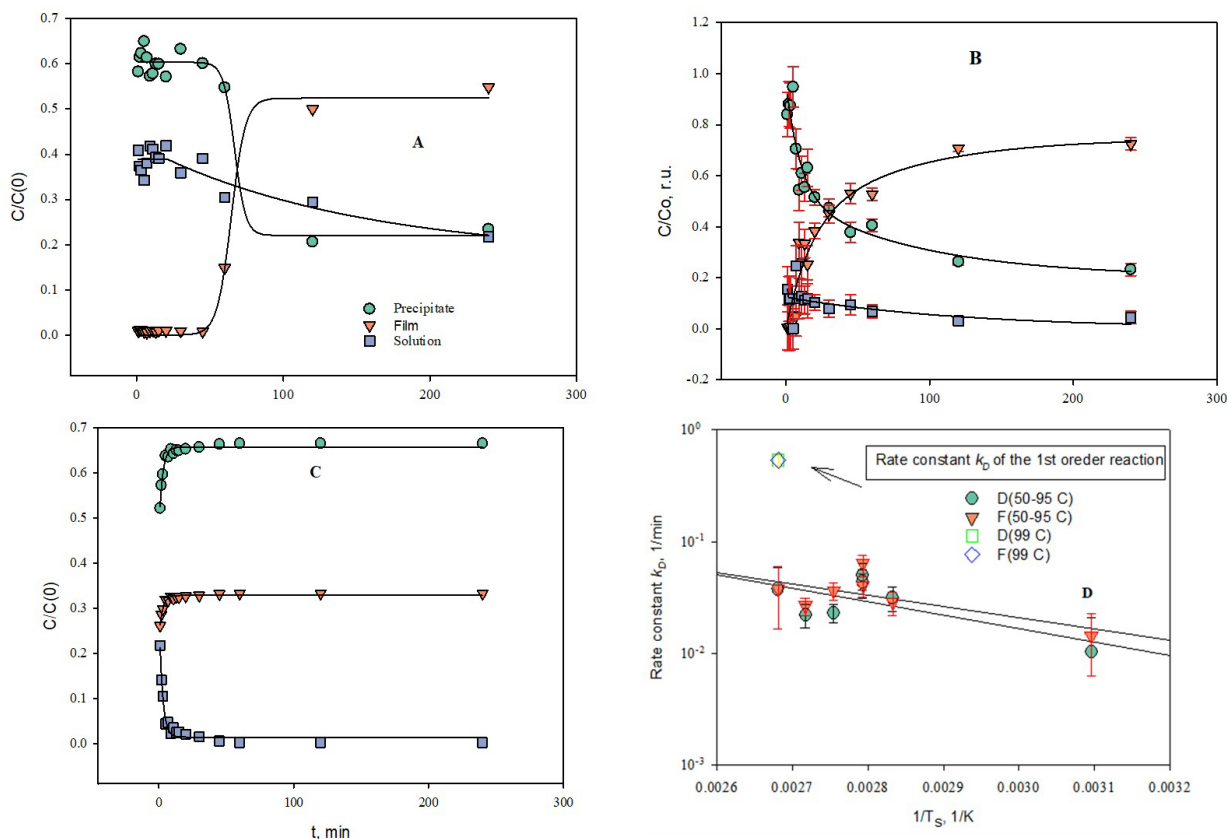


FIG. 4. Change of concentration of  $\text{Zn}(\text{OH})_2$ ,  $C/C(0)$  in the solution  $\text{NH}_3\text{-ZnAc}_2$  versus the reaction time at different temperatures of the synthesis.  $C$ ,  $C(0)$  are the current and initial concentration of zinc in the volume of the solution respectively. Synthesis temperature: (A) 50 °C, (B) 85 °C, (C) 99 °C. (D) the dependences of the rate constant ( $k_D$ ) on  $T_s$  of the 1st order irreversible reaction of the disappearance of the sol ( $D$ ) and the formation ( $F$ ) of the film  $\text{Zn}(\text{OH})_2\text{-ZnO}$  in the coordinates of the Arrhenius equation: the activation energies  $E_a$  of film growth ( $19 \pm 9$ ) kJ/mol and of disappearance of the sol ( $23 \pm 10$ ) kJ/mol. pH=10.3. The arrow shows the velocity constants at 99 °C

Thermodynamic analysis using the HSC Chemistry 8 program showed that the homogeneous state of the system ( $\Sigma$ ) remains at a zinc concentration of 0.06 mol/l and a pH of 10.0 – 10.5 up to a temperature of 35 °C [35]. Further increase in the temperature creates supersaturation in the solution relative to the mixture of phases  $\text{Zn}(\text{OH})_2$  (Wulffingit)– $\text{ZnO}$  (Zincite). As the temperature rises, the partial pressure of ammonia and water in the gas phase increases also. The concentration of ammonia dissolved in water changes little if at all. However, the partial pressure of the gases (primarily  $\text{H}_2\text{O}(\text{g})$ ,  $\text{NH}_3(\text{g})$ ) increases [38], and the colloidal phase of zinc hydroxide is formed. From the experimental data, it follows that the appearance of a colloidal solution is accompanied by the formation of zinc hydroxide particles of foamy morphology in the volume of the solution and on the surface of the walls of the glass reactor. The phase analysis of the films on the glass substrate and of the colloid particles, which was performed on a STADI-P X-ray powder automatic diffractometer (STOE) with  $\text{CuK}\alpha$  radiation, Fig. 3, has shown that due to the broadening of diffraction lines, they may be attributed to the presence of polycrystalline phases of Wulffingit and/or Zincite. These broadenings, Table 1, may be attributed to the presence of  $CSR$ s with a structure of  $\text{Zn}(\text{OH})_2$  and  $\text{ZnO}$ , as well as to distortions in their lattice [37].

We found the  $CSR$  sizes of the obtained films by using the Williams–Hall method for reflexes from the planes  $\langle 001 \rangle$ ,  $\langle 010 \rangle$ ,  $\langle 001 \rangle$ ,  $\langle 111 \rangle$  of the lattice of nanocrystals [37]. The width of the 90 % confidence interval of  $CSR$ s for this estimate varied within 2.7 nm for  $\text{Zn}(\text{OH})_2$  and 3.1 nm for  $\text{ZnO}$ , Table). It did not exceed 3 – 5 % of the  $CSR$  values of polycrystals in various diffraction planes. Since  $CSR$ s characterize the size of a single crystal region in the directions orthogonal to diffraction planes, the mean  $CSR$  value characterizes these single crystals as spherical particles at the 90 % confidence level regardless of their phase composition [39].

The Raman spectroscopy study of the samples of the  $\text{Zn}(\text{OH})_2\text{-ZnO}$  films on the surface of the walls of a glass reactor was carried out at room temperature using a Via Reflex spectrometer, Renishaw ( $\lambda = 532$  nm,  $P = 10$  mW, exposure time 10 s). The samples were prepared in the following way: a test tube with a reaction solution was placed in a thermostat at a given synthesis temperature and was kept there for a sufficient time to complete the reaction of film formation on the walls of the tube and the formation of the  $\text{Zn}(\text{OH})_2\text{-ZnO}$  precipitate at its bottom. The tube was then removed from

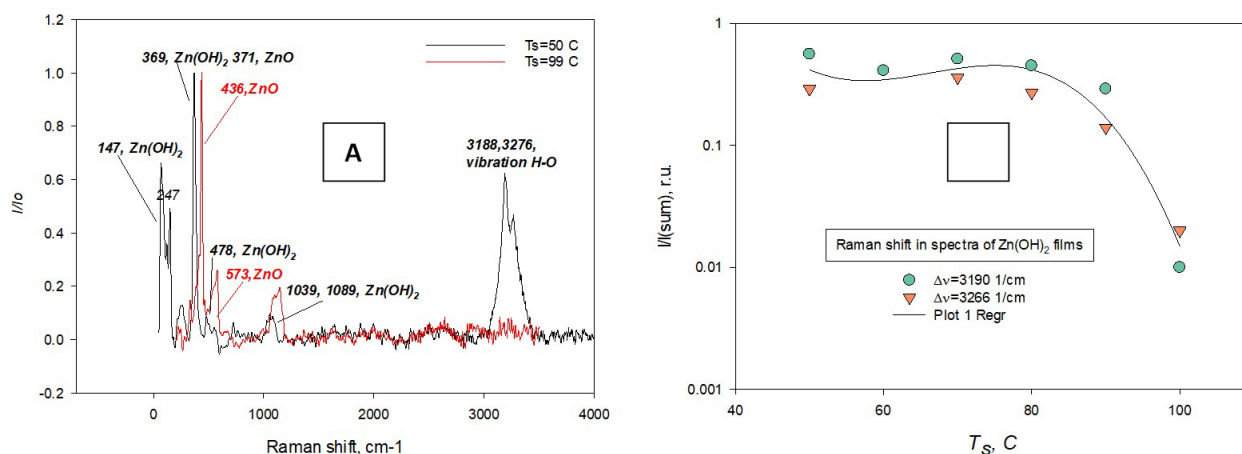
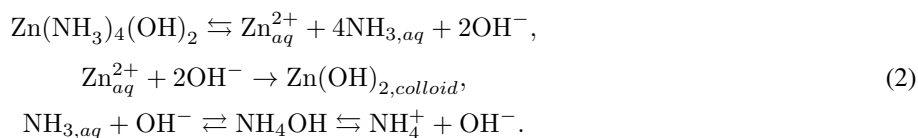


FIG. 5. (A) Examples of Raman spectra of  $\text{Zn(OH)}_2\text{-ZnO}$  film samples on the glass substrate, synthesized at temperatures  $T_s = 50$  and  $99$  °C.  $I/I_0$  – integral intensity ( $I$ ) of the Raman band normalized to the highest bands intensity ( $I_0$ ) in the spectrum. Identification of Raman shifts of  $\text{Zn(OH)}_2\text{-ZnO}$  is taken from [17]. (B) Changes in the relative intensity  $I/I_{sum}$  of vibration bonds of (OH)-groups belonging to  $\text{Zn(OH)}_2$  films with temperature  $T_s$  in the Raman shift range from  $3190$  and to  $3266$   $\text{cm}^{-1}$  according to Raman spectroscopy data.  $I_{sum}$  is the sum of all band's intensities in the spectrum range  $0 - 4000$   $\text{cm}^{-1}$ . Repr – line of quadratic regression

the thermostat, the suspension was removed from the tube, the tube with the precipitated film was rinsed with water and dried at  $23$  °C until it became air-dry. After that, the test tube was fragmented. Fragments convenient for imaging the Raman spectrum were selected, and spectra were taken. The mass concentration of  $\text{Zn(OH)}_2\text{-ZnO}$  in the films (thickness) with the same composition of the solution changed little if at all, which made it possible to consider the geometry of the survey unchanged. The morphology of the ZnO layers on the substrate was studied on fragments prepared for Raman spectroscopy study by applying scanning electron microscopy (SEM) and EDX elemental analysis using a JSM JEOL 6390LA facility.

### 3. Experimental results

The results of analysis of the layers at the final stage of precipitation by SEM and EDX methods are presented in Fig. 2. One can see that the zinc hydroxide layer on the glass substrate is represented in the form of flower-like bunches of crystals with hexagonal section. The X-ray fluorescent spectrum of the layer reveals  $K_\alpha$  and  $L_\alpha$  lines of the principal elements Zn, O and minor lines of C, Si, Al which reflect the composition of the glass substrate. In the framework of thermodynamic analysis of the initially homogeneous system ( $\Sigma$ ) we have refined our previous calculations using the HSC Chemistry 8 program. We included acetic acid ( $0.06$  mol/l) and acetic complexes of Zn(II) in ( $\Sigma$ ). The results showed that the homogeneous state of the system ( $\Sigma$ ) remains at a zinc concentration of  $0.06$  mol/l and a pH of  $10.0 - 10.5$  up to a temperature of  $35$  °C and the concentration of  $\text{Zn(CH}_3\text{COO)}_2$ ,  $\text{Zn(Ac)}_2$  species in it two orders of magnitude lower than that of  $\text{Zn(NH}_3\text{)}_4\text{(OH)}_2$ , Fig. 1. The increase in the number and size of nanoparticles with temperature in the system ( $\Sigma$ ) results in an increase in the ionic conductivity of the electrolyte solution due to the thermal decomposition of the ammonia complex  $\text{Zn(NH}_3\text{)}_4\text{(OH)}_2$  followed by hydrolysis of ammonia molecules according to the scheme



This leads to supersaturation relative to  $\text{Zn(OH)}_2$ , the formation of hydroxide particles in the form of colloidal clusters, and an increase in the concentration of ammonium ions in solution (2). The change in the concentration of Zn(II) ions in the reaction solution over the time of synthesis follows the equation of the irreversible reaction of the 1st order, (3), Fig. 4. The same relationship describes the change in the conductivity of the solution. As can be seen from Fig. 4, at  $T_s = 50$  °C, the change in the concentration of particles in the film is characterized by an induction period. With an increase in temperature  $T_s > 50$  °C, the duration of the induction period is reduced to zero, and the kinetics of film growth is determined by the loss rate of the number of colloidal nanocrystals in the solution due to the transfer of Zn(II) to the surface of the solution-reactor wall interface governed by an irreversible reaction of the 1st order.

The mean activation energy of the rate of colloid vanishing in solution and of the hydroxide film growth on the interface in this temperature range is  $E_a = (21 \pm 9)$  kJ/mol, Fig. 4D, [38]. At a temperature close to the boiling point of the electrolyte solution, the growth rate of the solid phase in the colloid system changes dramatically, Fig. 4C. Both processes

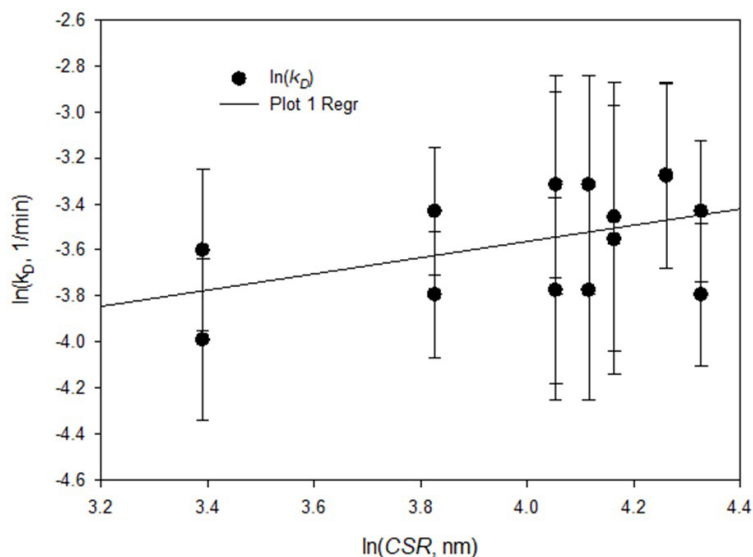


FIG. 6. Linear correlation between the mass growth (disappearance for the precipitate) rate constant  $\ln(k_D)$  and  $CSR \approx r$  for film and precipitate. The parameters of regression equation (4) estimated by the Least Square method are as follows:  $b[0] = \ln(4\pi D) = -(5.00 \pm 0.75)$ ,  $b[1] = x = (0.35 \pm 0.20)$

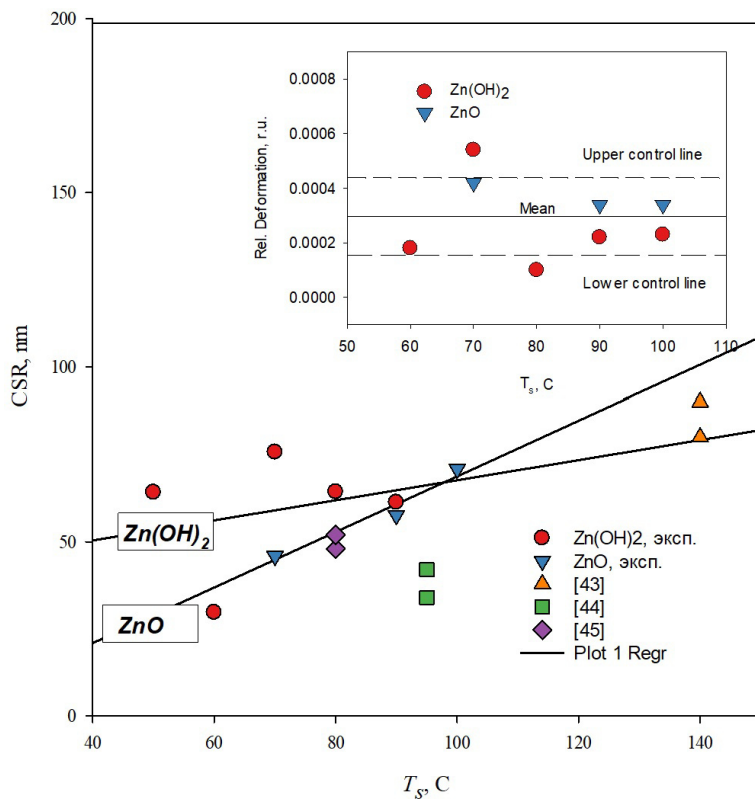


FIG. 7. Change in the mean value of the coherent scattering region ( $CSR$ ) of  $Zn(OH)_2$ - $ZnO$  nanocrystals in a film with synthesis temperature ( $T_s$ ). The regression lines (Regr) characterize the change in the compared our experimental data. In square brackets next to the dot symbols, the numbers of available data sources [42–44] are shown, which are related to the  $CSR$  of  $ZnO$  according to the list of references. In the inset: the effect of the synthesis temperature on the mean relative deformation of nanocrystals in (001, 010, 001, 111) planes according to X-ray phase analysis data

of colloid and film growth begin to proceed in parallel at the same rate in accord with the first-order reaction relative to the concentration of Zn(II) ions.

Figure 5 shows typical Raman spectra of the Zn(OH)<sub>2</sub> film, which is formed on the glass substrate at  $T_s = 55 - 95$  °C due to the thermal decomposition of the ammonia complex Zn(NH<sub>3</sub>)<sub>4</sub>(OH)<sub>2</sub> and hydrolysis of ammonia molecules according to scheme (2). We can see that the pure zinc oxide phase is formed at a temperature near the boiling point of the solution.

According to the classical theory of crystallization from a homogeneous solution, the initial stage of formation and growth of hydroxide/oxide clusters is determined by the diffusion flow of ammonia complex Zn(NH<sub>3</sub>)<sub>4</sub>(OH)<sub>2</sub> to the surface of the growing cluster, the chemical reaction (2) of decomposition of the complex on the surfaces of the growing cluster, or by the mixed regime [18, 40, 41]. Under the conditions of Zn(OH)<sub>2</sub>-ZnO clusters film growth at the surface of the reactor wall, a mixed growth mode is most likely. In that case, the monomer flux ( $J_D$ ) to the growing cluster is related to the size of the growing cluster ( $r$ ) by equation [40]:

$$J_D = \frac{dC}{dt} = -k_D(C - C_i), \quad k_D = 4\pi D r^x, \quad x = 1. \quad (3)$$

In (3),  $C$  and  $C_i$  are the concentrations of zinc ammonia complex in the volume of the solution and at the surface of the "cluster-solution" interface;  $k_D$  is the 1st order irreversible reaction rate coefficient for zinc ions measured in the experiment; and  $D$  is the diffusion coefficient.  $k_D$  depends on the current size of the cluster ( $r$ ), which changes during growth and is a function of the concentration gradient ( $C - C_i$ ). Therefore, the experimental dependence of  $k_D$  on the size of the cluster in the coordinates of equation (3) is of the form, in which the exponent ( $x$ ) of the variable ( $r$ ) characterizes the average value from zero to a maximum value of 1 or 2, depending on which mechanism of solid formation, diffusion growth and/or surface growth prevails. This conclusion follows from the results of comparison of the experimentally obtained relationship between the growth rate constant ( $k_D$ ) and the  $CSR$  value, which we chose as an estimate of the average size of the critical cluster ( $r$ ) in the film in the form of equation (4), Fig. 6,

$$\ln(k_D) = \ln(4\pi D) + x \ln(CSR) = b[0] + b[1] \ln(CSR), \quad b[0] = \ln(4\pi D), \quad b[1] = x. \quad (4)$$

The mean value of exponent  $b[1] = x = 0.35 \pm 0.20$  rel. units in equation (4) is close to, but less than unity, which does not contradict the diffusion or mixed diffusion model [41]. The diffusive nature of the cluster size growth is confirmed also by the coincidence of the determined activation energy of the film growth rate,  $E_a = (21 \pm 9)$  kJ/mol, and the activation energy of diffusion of Zn(II) cations in the electrolyte solution (26 kJ/mol) [45].

The external diffusion transfer of Zn(II) ions to the surface of growing clusters in the form of the ammonia complex Zn(NH<sub>3</sub>)<sub>4</sub>(OH)<sub>2</sub> explains the observed first order of the film growth reaction for Zn(II) ions. At the same time, clusters tend to form aggregates and that proceeds to the growth of the film as a whole. The Raman spectra of the layers, which grow on the solution-glass walls interface, show that the hydroxide phase is the main phase in the  $T_s$  range 50 - 95 °C, Fig. 5. According to the analysis of diffraction peak broadening, the polycrystalline film of the growing phase of Zn(OH)<sub>2</sub>-ZnO is composed of spherical nanocrystals, the size of which is equal to the coherent scattering region,  $CSR$  [37]. The  $CSR$  depends on  $T_s$ , Fig. 7, but the crystal lattice parameters of the nanocrystals of both zinc hydroxide and oxide in the film composition remain constant across the entire range of  $T_s$ . Since the average value of the relative strain of nanocrystals of hydroxide and oxide phases in  $\langle 001 \rangle$ ,  $\langle 010 \rangle$ ,  $\langle 001 \rangle$ ,  $\langle 111 \rangle$  planes do not depend on the synthesis temperature  $T_s$ , Fig. 7 (inset), and does not exceed 0.04 %, the size factor can be considered to be the main reason for the observed widening of diffraction peaks [37].

The nanocrystals that make up the zinc hydroxide/oxide film have sizes ( $CSR$ ) ranging from 20 to 60 nm, depending on the synthesis temperature, Fig. 7. From the point of view of the crystal growth theory [18], when the degree of supersaturation of the solution of Zn(NH<sub>3</sub>)<sub>4</sub>(OH)<sub>2</sub> changes with temperature, only those clusters are formed and remain stable that reach the critical size relative to the zinc hydroxide/oxide phase ( $r$ ) [18, 19, 40]. The emergence of stable clusters of critical size opens a new route for colloid formation, consisting in the aggregation of these clusters. If the rate of aggregation of critical clusters significantly exceeds the rate of generation, the growing polycrystalline phase remains monodisperse, and the size of the nanocrystals corresponds to the size of the  $CSR$  observed in the experiment. With this exception, the schema of microcrystals formation at the final stage of the growth agrees well with the proposed earlier route of ZnO nanoflower growth [46, 47].

Let us analyze this hypothesis by applying the classical theory of crystallization as a model of the growing film of the Zn(OH)<sub>2</sub>-ZnO composition. Let us represent the equilibrium solubility equation of nanocrystals (1) as (5), where the size of the critical cluster  $r$  is taken as an estimate of the size of the crystal ( $r$ )

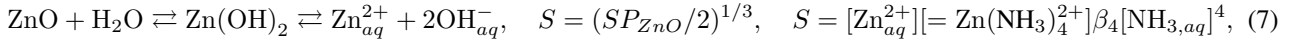
$$RT \ln(S/S_0) = \frac{\sigma \bar{V}}{\langle r \rangle}. \quad (5)$$

To assess the solubility of crystals ( $S$ , mol/l), we use the experimental values of the equilibrium concentration of zinc ions Zn(II) in a film synthesis solution at a given temperature  $T_s$  (equilibrium data for the "solution" curves, Fig. 4). The total concentration of zinc ions in the solution according to (5) depends on the degree of cation complexity in the

supernatant solution



To estimate the solubility, write the expression for  $S$  using reaction equations (6, 7) [18],



where  $SP$  is the solubility product of ZnO, and  $\beta_4$  is the stability constant of the ammonia complex according to (6).

The peculiarity of using equation (7) to describe the experimental data for Zn(OH)<sub>2</sub>-ZnO nanoparticles is that their solubility is considered simultaneously as a function of the equilibrium temperature  $T_s$  and the size of the critical cluster  $\langle r \rangle \sim CSR$ :

$$\ln(S) = \ln(S_0) + \left(\frac{\sigma\bar{V}}{R}\right)\left(\frac{1}{T_s}\right)\left(\frac{1}{\langle r \rangle}\right) = \ln(S_0) + \left(\frac{\sigma\bar{V}}{R}\right)\left(\frac{1}{T_s} \times \frac{1}{CSR}\right). \quad (8)$$

Reaction (6) is shifted to the right under the conditions of the experiment. Therefore, the experimentally measured solubility at different synthesis temperatures ( $S$ ) is determined by the concentration of the Zn(NH<sub>3</sub>)<sub>4</sub>(OH)<sub>2</sub> complex. The term ( $S_0$ ) in equation (6) characterizes the solubility component of single crystals Zn(OH)<sub>2</sub>-ZnO, which does not depend on  $T_s$  in the selected temperature range. We believe that in the considered temperature range the surface tension and molar volume of nanoparticles do not change significantly. Taking into account equation (7) and predominance of hydroxide in the  $T_s$  range 50 – 90 °C, Fig. 5, we cannot distinguish between impacts of ZnO and Zn(OH)<sub>2</sub> phases on the solubility of the film as a whole. Thus, the experimental solubility ( $S$ ) may be considered as a thermodynamic solubility of Zn(OH)<sub>2</sub>-ZnO films in the framework of equation (8).

The purpose of using the nanocrystal solubility equation (8) was to test the assumption that the  $CSR$  of the growing polycrystalline film does not differ from the size of the critical cluster  $\langle r \rangle$  in the supernatant solution. To test this assumption, consider equation (8) in a form convenient for linear regression analysis (9):

$$\ln(S) = \ln([\text{Zn}_{aq}^{2+}]) = \ln[\text{Zn}(\text{NH}_3)_4^{2+}] - \ln(\beta_4[\text{NH}_{3,aq}]^4) = \ln([\text{Zn}_{aq}^{2+}]_0) + \left(\frac{\sigma\bar{V}}{R}\right)\left(\frac{1}{T_s}\right) \times \frac{1}{CSR}. \quad (9)$$

In (9), the independent variable ( $X$ ) is the product of the inverse synthesis temperature  $T_s$  and the inverse value of the  $CSR$ :

$$\begin{aligned} \ln[\text{Zn}(\text{NH}_3)_4^{2+}] &= \ln([\text{Zn}_{aq}^{2+}]_0) + \ln(\beta_4[\text{NH}_{3,aq}]^4) + \left(\frac{\sigma\bar{V}}{R}\right)\left(\frac{1}{T_s} \times \frac{1}{CSR}\right), \\ Y = A + B \times X, \quad Y &= \ln[\text{Zn}(\text{NH}_3)_4^{2+}], \quad X = \left(\frac{1}{T_s} \times \frac{1}{CSR}\right), \end{aligned} \quad (10)$$

$$A = \ln([\text{Zn}_{aq}^{2+}]_0) + \ln(\beta_4[\text{NH}_{3,aq}]^4), \quad B = \frac{\sigma\bar{V}}{R}.$$

Figure 7 also shows foreign literature data, in which the conditions of deposition of ZnO films from aqueous ammonia solution contain the information on  $T_s$  and the value of the oxide film  $CSR$  [42–44].

The experimental solubility of Zn(OH)<sub>2</sub> and ZnO nanocrystals in the coordinates of equation (10) and the regression line  $Y = A + B \times X$  based on the results of  $CSR$  analysis are shown in Fig. 8. It can be seen that the standard error in estimating the regression line,  $Fit Std Err = 1.10$ , is close to the error in estimating the concentration of Zn(II) ions in solution, (1.2 – 1.6) log. units. Therefore, equation (10) adequately describes the simultaneous effect of  $T_s$  and  $CSR$  on the solubility of Zn(OH)<sub>2</sub>-ZnO nanocrystals in the film composition. The value of  $CSR$  can be identified with the size of critically sized clusters  $\langle r \rangle$ , the aggregation of which ensures the growth of polycrystalline film by the mechanism of heteronucleation, facilitated by their low zeta potential.

From the data of Fig. 7 it can be seen that the size of  $CSR$  forming the film of hydroxide and zinc oxide depends differently on the synthesis temperature in the region of 50 – 95 °C. The  $CSR$  of hydroxide changes slightly in the entire region of its stability up to  $T_s < 85 - 95$  °C. On the contrary, the  $CSR$  of oxide particles increases markedly with the growth of  $T_s$ .

If we extrapolate the  $CSR(T_s)$  linear regression curve to the region of  $T_s=100$  °C and above, we can see that with increasing  $T_s$  the  $CSR(T_s)$  lines of hydroxide and zinc oxide intersect in the temperature zone of  $CSR= (50 - 100 \text{ nm})$ . This size of  $CSR$  is comparable with the transverse dimensions of columnar microcrystals growing on the glass substrate (Fig. 2, inset). In this zone, we believe that the bulk growth speed of polycrystals from critical clusters in solution and the speed of parallel chemical reaction (2) on the surface of the fastest growing end face of hexagonal microcrystals become equal. The proposed change in the mechanism of high-temperature growth of ZnO microcrystals explain a sharp increase in the growth rate of the ZnO film and a visible transition to a parallel increase in the size of colloidal particles in solution and in film at 99 °C, Fig. 4C,D. Such interpretation is also consistent with the literature data [42–44, 47].

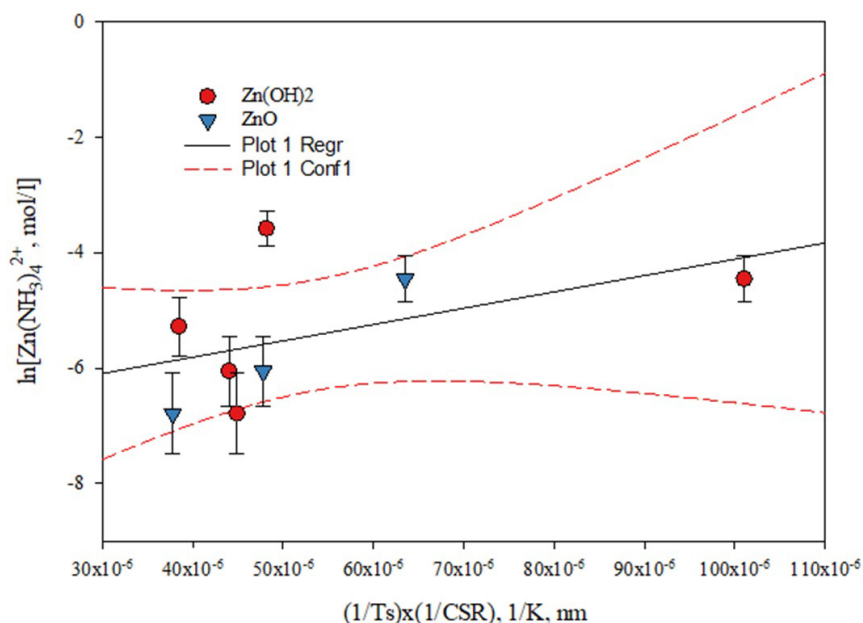


FIG. 8. Dependence of the molar solubility of zinc oxide in the system ( $S \sim [\text{Zn}(\text{NH}_3)_4(\text{OH})_2]$ ) on the product of  $(1/T_s) \times (1/CSR)$  in the coordinates of equation (10) according to the data on the equilibrium composition of the solution and film  $\text{Zn}(\text{OH})_2\text{-ZnO}$  in 1 mol/l  $\text{NH}_3$ ,  $\text{pH}=10.3$ . Parameters of the regression equation  $Y = A + B \times X$ ,  $A = (-6.90 \pm 1.10)$ ,  $B = (2.80 \pm 2.00)10^4$ , K, nm,  $\text{Fit Std Err}=1.10$ , F-value = 5. Regr – regression line, conf1 – 90 %-confidence intervals of regression

#### 4. Conclusion

By using experimental methods of XRD, Raman spectroscopy, kinetic analysis along with thermodynamic modelling we have determined that the thermal impact on the dominated ammonia complex  $\text{Zn}(\text{NH}_3)_4(\text{OH})_2$  in aqueous ammonia solutions leads to its decomposition, formation and growth of  $\text{Zn}(\text{II})$  hydroxide/oxide clusters. According to the classical theory of crystallization from a homogeneous solution, this is a mixed process, the speed of which includes (i) – diffusion of ammonia complex  $\text{Zn}(\text{NH}_3)_4(\text{OH})_2$  to the surface of the growing cluster and (ii) – the chemical reaction of decomposition of the complex on the surface of the cluster. The growth of  $\text{Zn}(\text{OH})_2\text{-ZnO}$  clusters in solution and on the surface of the test tube glass is governed by the first order reaction regarding  $\text{Zn}(\text{II})$ . Process (i) prevails in the  $T_s$  range 50 – 95 °C. At  $T_s = 99$  °C, processes (i) and (ii) proceed in parallel at an order of magnitude higher speed.

The colloid-chemical mechanism of growth of  $\text{Zn}(\text{OH})_2\text{-ZnO}$  clusters in solution and on the surface of glass substrate leads to the formation of microcrystals consisting of hydroxide/oxide nano-size clusters. Their average dimensions are equal to  $CSR$  of the microcrystals determined by the Williams-Hall method.

Relation (1) adequately describes the simultaneous effect of temperature  $T_s$  and  $CSR$  on the solubility of  $\text{Zn}(\text{OH})_2\text{-ZnO}$  nanocrystals in the film composition. The value of  $CSR$  can be identified with the size of critically sized clusters, the aggregation of which ensures the growth of colloidal particles and their transfer to the polycrystalline film by the mechanism of heteronucleation. Such interpretation allows one to explain the microcrystalline morphology and monodisperse composition of the growing film.

Establishing of the picture of high-temperature colloid-chemical growth of  $\text{ZnO}$  layers from ammonia aqueous solutions in the  $T_s$  region above 100 °C in more details is a separate task, which requires further research.

#### References

- [1] Mokrushin S.G. Experimental study of laminar systems. *Zhurnal Fizicheskoi Khimii (Journal of Physical Chemistry)*. 1934, 5(8), P. 1082–1091.
- [2] Fabian I. Ezema, Chandrakant D. Lokhande, Rajan Jose, [Eds.]. *Chemically Deposited Nanocrystalline Metal Oxide Thin Films/Synthesis, Characterizations, and Applications*. Springer Cham., 2021, 926 p.
- [3] Guire M.R.D., Bauermann L.P., Parikh H., Bill J. Chemical Bath Deposition. In: *Chemical Solution Deposition of Functional Oxide Thin Films*. [Eds.] Waser R., Kosec M., Payne D. Schneller T. Vienna, Springer, 2013, 350 p.
- [4] Kozhevnikova N.S., Markov V.F., Maskaeva L.N. Chemical precipitation of metal sulfides from aqueous solutions: from thin films to colloidal particles. *Journal of Physical Chemistry*, 2020, **94**(12), P. 1752–1766.
- [5] Maskaeva L.N., Markov V.F., Tulenin S.S., Forostyanaya N.A. *Hydrochemical Deposition of Thin Films of Chalcogenide Films: Practicum*. [Ed.] V.F. Markov. Ekaterinburg: M-vo obrazovaniya i nauki Ros. Federation, Urals. Feder. University, 284 p. (in Russian).
- [6] Fatehah M.O. Hamidi A.A., Serge S. Stability of  $\text{ZnO}$  nanoparticles in solution. Influence of pH, dissolution, aggregation and disaggregation effects. *Journal of Colloid Science and Biotechnology*, 2014, **3**(1), P. 75–84.
- [7] Majid A., Bibi M. Wet Chemical Synthesis Methods. In: *Cadmium based II-VI Semiconducting Nanomaterials*. Topics in Mining, Metallurgy and Materials Engineering. Cham. Springer, 2018.

- [8] Guillemin S., Rapenne L., Roussel H., Sarigiannidou E., Brémond G., Consonni V. Formation Mechanisms of ZnO Nanowires: The Crucial Role of Crystal Orientation and Polarity. *Journal of Physical Chemistry C*, 2013, **117**(40), P. 20738–20745.
- [9] He H., Lao C.S., Chen L.J., Davidovic D., Wang Z.L. Large-scale Ni-doped ZnO nanowire arrays and electrical and optical properties. *Journal of the American Chemical Society*, 2005, **127**, P. 16376–16377.
- [10] Comini E., Faglia G., Sberveglieri G., Pan Z.W., Wang Z.L. Stable and high-sensitive gas sensors based on semiconducting oxide nanobelts. *Applied Physics Letters*, 2002, **81**, P. 1869–1871.
- [11] He H., Hsin C.-L., Liu J., Chen L.J., Wang Z.L. Piezoelectric gated diode of a single ZnO nanowire. *Advance Materials*, 2007, **19**, P. 781–784.
- [12] Sun X., Li Q., Jiang J., Mao Y. Morphology-tunable synthesis of ZnO nanoforest and its photoelectrochemical performance. *Nanoscale*, 2014, **6**(15), P. 8769–8780.
- [13] Woo H.Y., Choi Y., Chung H. et al. Colloidal inorganic nano- and microparticles for passive daytime radiative cooling. *Nano Convergence*, 2023, **10**, P. 17–23.
- [14] M. Li, L. Tonggu, X. Zhan, T.L. Mega, L. Wang. Cryo-EM Visualization of Nanobubbles in Aqueous Solutions. *Langmuir*, 2016, **32**(43), P. 11111–11115.
- [15] Betenekov N.D., Medvedev V.P., Kitaev G.A. Deposition of cadmium sulfide films from solutions on the surface of glass. *Radiochemistry*, 1978, **20**(3), P. 431–438. (in Russian)
- [16] Kitaev G.A. *Investigation of the Processes of Obtaining Metal Chalcogenide Films in Aqueous Solutions Containing Tio-, Selenourea and Sodium Selenosulfate*. Doctor thesis. Sverdlovsk, USSR : UPI afer S.M. Kirov, 1978. (in Russian)
- [17] Lutz H.D., Jung C., Mortel R., Jacobs H., Stahl R. Hydrogen bonding in solid hydroxides with strongly polarizing metal ions, b-Be(OH)<sub>2</sub> and o-Zn(OH)<sub>2</sub>. *Spectrochimica Acta Part A*, 1998, **54**, P. 893–901.
- [18] Adamson A. *Physical Chemistry of Surfaces* (in Russian). [Eds.] B.V. Deryagin, Z.M. Zorin V.M. Muller. Moscow : Mir Publ., 1979, 568p
- [19] Kapta G. The Gibbs Equation versus the Kelvin and the Gibbs-Thomson Equations to Describe Nucleation and Equilibrium of Nano-Materials. *Journal of Nanoscience and Nanotechnology*, 2011, **12**, P. 1-9.
- [20] Gusarov V.V. The Role of Non-Autonomous Phases in the Transformations and Properties of Oxide Materials. [Ed.] N.V. Gelfond. Novosibirsk, INH SB RAS, 2023. Thermodynamics and Materials Science. Abstracts of the XV Symposium with international participation. June 3–5, 2023, P. 10.
- [21] Polyakov E.V., Tzukanov R.R., Volkov I.V., Buldakova L.Yu., Baklanova I.V., Lipina O.A., Zhukov V.P., Kuznetsova Yu.V., Tyutyunnik A.P., Maksimova M.A. Synthesis and comparative photocatalytic activity of CuO layers on SiO<sub>2</sub> substrates. *Nanosystems: Physics, Chemistry, Mathematics*, 2020, **11**(5), P. 601–607.
- [22] Polyakov E.V., Tsukanov R.R., Buldakova L.Yu., Kuznetsova Yu.V., Volkov I.V., Zhukov V.P., Maksimova M.A., Dmitriev A.V., Baklanova I.V., Lipina O.A., and Tyutyunnik A.P. Chemical Bath Precipitation and Properties of β-Ni(OH)<sub>2</sub> Films Prepared in Aqueous Ammoniac Solutions. *Russian Journal of Inorganic Chemistry*, 2002, **67**(6), P. 912–920.
- [23] Le Pivert M., Martin N., Leprince-Wang Y. Hydrothermally grown ZnO nanostructures for water purification via photocatalysis. *Crystals*, 2022, **12**(308), P. 1–16.
- [24] Pérez-Hernández R., Velázquez Salazar J.J., Yacamán M.J. Low-Temperature Synthesis and Growth Mechanism of ZnO Nanorods on Crystalline Si Substrate. *Journal of Nano Research*, 2011, **14**, P. 69–82.
- [25] Wang M., Jiang L., Jung Kim E., Hahne S.H. Electronic structure and optical properties of Zn(OH)<sub>2</sub>: LDA+U calculations and intense yellow luminescence. *RSC Advances*, 2015, **5**, P. 87496–87503.
- [26] Alnoor H., Chey Ch.O., Pozina G., Liu X., Khranovskyy V., Willander M., Nur O. Effect of precursor solutions stirring on deep level defects concentration and spatial distribution in low temperature aqueous chemical synthesis of zinc oxide nanorods. *AIP Advances*, 2015, **5**, P. 087180.
- [27] Baviskar P.K., Nikam P.R., Gargote S.S., Ennaoui Ah., Sankapal B.R. Controlled synthesis of ZnO nanostructures with assorted morphologies via simple solution chemistry. *Journal of Alloys and Compounds*, 2013, **551**, P. 233–242.
- [28] Znaidi L. Sol-gel-deposited ZnO thin films: A review. *Materials Science and Engineering: B*, 2010, **174**(1-3), P. 18–30.
- [29] Polyakov E.V., Maksimova M.A., Kuznetsova Yu.V., Buldakova L.Yu. Colloidal-chemical mechanism of Zn(OH)<sub>2</sub>-ZnO layer formation at the glass – ammonia solution – Zn(II) interface. *Nanosystems: Physics, Chemistry, Mathematics*, 2023, **14**(2), P. 231–241.
- [30] Gonzalez-Chan I.J., Moguel Z.P., Oliva A.I. Deposition of ZnO thin films by chemical bath technique: physicochemical conditions and characterization. *ECS Journal of Solid State Science and Technology*, 2019, **8**(9), P. 536–544.
- [31] Craig V.S.J., Krafft M.P. Hot Topic – Nanobubbles and Nanodroplets Nanobubbles and Nanodroplets: from Basics to Applications. *Current Opinion in Colloid & Interface Science*, 2021, **55**, P. 101516.
- [32] Xu-yu Zhang, Qian-shuai Wang, Zhong-xian Wu, Dong-ping Tao. An experimental study on size distribution and zeta potential of bulk cavitation nanobubbles. *International Journal of Minerals, Metallurgy and Materials*, 2020, **27**(2), P. 152–161.
- [33] Kahraman S., Çakmak H.M., Çetinkaya S., Çetinkara H.A., Güder H.S. CBD grown ZnO nanostructures: effects of solution temperature. *International Journal of Materials Research*, (formerly Z. Metallkd.), 2013, **104**(8), P. 798–804.
- [34] Trejo-Ramos A.I., Martín-Varguez P.E., Gonzalez-Chan I.J., Oliva A.I. Algorithm to obtain the species distribution diagrams and solubility curves for depositing ZnS, ZnO, and Zn(OH)<sub>2</sub> films in aqueous solution. *Computational and Theoretical Chemistry*, 2021, **1202**(113325), P. 1–8.
- [35] Molefe F.V., Koao L.F., Dejene B.F., Swart H.C. Phase formation of hexagonal wurtzite ZnO through decomposition of Zn(OH)<sub>2</sub> at various growth temperatures using CBD method. *Optical Materials*, 2015, **46**, P. 292–298.
- [36] Ki-Woong Chae, Qifeng Zhang, Jeong Seog Kim, Yoon-Ha Jeong, Guozhong Cao. Low-temperature solution growth of ZnO nanotube arrays. *Beilstein journal of nanotechnology*, 2010, **1**, P. 128–134.
- [37] Williamson G., Hall W. X-ray line broadening from filed aluminium and wolfram. *Acta Metallurgica*, 1953, **1**, P. 22–31.
- [38] Polyakov E.V., Maksimova M.A., Kuznetsova Y.V., Buldakova L.Y. Colloidal-chemical mechanism of growth of Zn(OH)<sub>2</sub>-ZnO layers in the glass-ammonia solution interface Zn(II). OOO “GeLime”, Proceeding of All-Russian Conference ”Solid State Chemistry and Functional Materials-2022, XIV Symposium on Functional Materials. Ekaterinburg, 2022, P. 278–280. (in Russian)
- [39] Balzar D. *Modeling of x-ray diffraction line broadening with the voigt function: applications to high-*tc* superconductors*. Colorado, National Institute of Standards and Technology, 1993, 87 p, NISTIR 3998.
- [40] Thanh N.T.K. Maclean N. Mahiddine S. Mechanisms of Nucleation and Growth of Nanoparticles in Solution. *Chemical Reviews*, 2014, **114**, P. 7610–7630.
- [41] Cheng J.J., Nicaise S.M., Berggren K.K., Gradečak S. Dimensional tailoring of hydrothermally-grown zinc oxide nanowire arrays. *Nano Letters*, 2016, **16**(1), P. 753–759.
- [42] Lining Yang, Jing Wang, Lan Xiang. Hydrothermal synthesis of ZnO whiskers from e-Zn(OH)<sub>2</sub> in NaOH/Na<sub>2</sub>SO<sub>4</sub> solution. *Particuology*, 2015, **19**, P. 113–117.

- [43] Farhat O.F., Halim M.M., Abdullah M.J., Ali M.K.M., Allam N.K. Morphological and structural characterization of single-crystal ZnO nanorod arrays on flexible and non-flexible substrates. *Beilstein journal of nanotechnology*, 2015, **6**, P. 720–725.
- [44] Koao L.F., Dejene F.B., Swart H.C. Properties of flower-like ZnO nanostructures synthesized using the chemical bath deposition. *Materials Science in Semiconductor Processing*, 2014, **27**, P. 33–34.
- [45] Mamedova M.T. Kinetics and thermodynamics of  $Zn^{2+}$  ion sorption on the Na-form of catio-exchanger KB-4p-2. *Actual Problems of the Humanities and Natural Sciences*, 2012, 1. (in Russian)
- [46] Acharyya D., Bhattacharyya P. An efficient BTX sensor based on ZnO nanoflowers grown by CBD method. *Solid-State Electronics*, 2015, **106**, P. 18–26.
- [47] Lausecker C., Salem B., Baillin X., Consonni V. Modeling the elongation of nanowires grown by chemical bath deposition using a predictive approach. *Journal of Physical Chemistry C*, 2019, **123**, P. 29476–29483.

---

*Submitted 17 January 2024; revised 21 April 2024, 20 May 2024, 26 June 2024; accepted 28 June 2024*

*Information about the authors:*

*Maria A. Maksimova* – ISSC UB RAS, 91, Pervomaiskaya str., 620108, Ekaterinburg, Russia; ORCID 0009-0004-2807-2222; msalimova1993@gmail.com

*Evgeny V. Polyakov* – ISSC UB RAS, 91, Pervomaiskaya str., 620108, Ekaterinburg, Russia; ORCID 0000-0001-7432-994X; polyakov@ihim.uran.ru

*Ilya V. Volkov* – ISSC UB RAS, 91, Pervomaiskaya str., 620108, Ekaterinburg, Russia; ORCID 0000-0001-8009-952X

*Aleksandr P. Tyutyunnik* – ISSC UB RAS, 91, Pervomaiskaya str., 620108, Ekaterinburg, Russia; ORCID 0000-0002-6394-4514

*Alexey A. Ioshin* – ISSC UB RAS, 91, Pervomaiskaya str., 620108, Ekaterinburg, Russia; ORCID 0009-0008-4679-1836; aaioshin@yandex.ru

*Conflict of interest:* the authors declare no conflict of interest.

## Composite sorbent based on $\text{Fe}_3\text{O}_4$ with $\text{Fe}(\text{N}_2\text{H}_4)_x\text{Cl}_y$ for the removal of Chromium(VI) from wastewater

Denis P. Ordinartsev<sup>1,a</sup>, Nadezhda V. Pechishcheva<sup>1,2,b</sup>, Svetlana Kh. Estemirova<sup>1,c</sup>,  
Angelina V. Kim<sup>1,2,d</sup>, Evgenii V. Sterkhov<sup>1,e</sup>, Sofia A. Petrova<sup>1,f</sup>, Galina A. Shilenko<sup>2,g</sup>

<sup>1</sup>Institute of Metallurgy of the Ural Branch of the Russian Academy of Sciences, Yekaterinburg, Russia

<sup>2</sup>Ural Federal University named after the First President of Russia B. N. Yeltsin, Yekaterinburg, Russia

<sup>a</sup>denis\_ordinartsev@mail.ru, <sup>b</sup>pechischeva@gmail.com, <sup>c</sup>esveta100@mail.ru,

<sup>d</sup>kim-angelina.95@mail.ru, <sup>e</sup>ev.sterhov@mail.ru, <sup>f</sup>danaus@mail.ru, <sup>g</sup>g\_shilenko@mail.ru

Corresponding author: Denis P. Ordinartsev, denis\_ordinartsev@mail.ru

**ABSTRACT** The paper presents a methodology for the synthesis of iron complex with hydrazine hydrate  $\text{Fe}(\text{N}_2\text{H}_4)_x\text{Cl}_y$ . The  $\text{Fe}(\text{N}_2\text{H}_4)_x\text{Cl}_y$  complex was investigated by X-ray phase analysis and scanning electron microscopy. Upon hydrolysis, the  $\text{Fe}(\text{N}_2\text{H}_4)_x\text{Cl}_y$  complex forms a composite sorbent, which is  $\text{Fe}_3\text{O}_4$  in a shell of  $\text{Fe}(\text{N}_2\text{H}_4)_x\text{Cl}_y$  complex. The composite sorbent can be used to treat wastewater from Cr(VI) ions and is effective in the pH range of 2 to 12. Based on the adsorption and electrokinetic potential data, a conclusion about the nature of the terminal groups of the adsorbent was made, a scheme of the structure of its electrical double layer and the adsorption mechanism were proposed. Depending on the conditions, Cr(VI) can be adsorbed on the composite sorbent or reduced to Cr(III). The efficiency of the composite sorbent in the removal of Cr(VI) ions was tested on a sample of real wastewater.

**KEYWORDS** Iron complex with hydrazine, magnetite sol, chromium adsorption, heavy metals, adsorption isotherms.

**ACKNOWLEDGEMENTS** The work was carried out according to the state assignment of IMET UB RAS using equipment of Collaborative usage centre “Ural-M” and with the support of the Ministry of Science and Higher Education of the Russian Federation (Ural Federal University Program of Development within the Priority-2030 Program), project No. 122080100074-1.

**FOR CITATION** Ordinartsev D.P., Pechishcheva N.V., Estemirova S.Kh., Kim A.V., Sterkhov E.V., Petrova S.A., Shilenko G.A. Composite sorbent based on  $\text{Fe}_3\text{O}_4$  with  $\text{Fe}(\text{N}_2\text{H}_4)_x\text{Cl}_y$  for the removal of Chromium(VI) from wastewater. *Nanosystems: Phys. Chem. Math.*, 2024, **15** (4), 510–519.

### 1. Introduction

The deterioration of drinking water quality is a global world problem that research groups around the world are working on [1–3]. There are many tasks to purify water from ecotoxicants of artificial and natural origin [4–6]. Technologies such as adsorption purification [7–9], membrane purification [10–12] and reagent purification [13–15] are widely used.

Among the ecotoxicants of artificial origin, Cr(VI) compounds occupy a special place. Cr(VI) has a low maximum permissible concentration (MPC) value in drinking water of  $0.05 \text{ mg}\cdot\text{L}^{-1}$  [16], so a high degree of wastewater is required. The topic of extraction of chromium compounds from wastewater is wide presented, many adsorbents have been developed [5, 17–19]. Reagent technologies [20, 21] are most often used for treatment of electroplating effluents from the main amount of chromium. The main approach is to reduce Cr(VI) to less hazardous Cr(III) compounds (MPC in drinking water –  $0.5 \text{ mg}\cdot\text{L}^{-1}$  [16]) and its further precipitation in the form of sludge. For Cr(VI) reduction, Fe(II) salts are mainly used, for example, rather cheap divalent iron sulfate [20].

Adsorption methods are one of the most promising for additional treatment, removal of residual concentrations of Cr(VI) from wastewater [22]. Adsorptive water treatment can be regenerative (i.e., with extraction of the substance from the adsorbent and its utilization) and destructive, in which the substances extracted from wastewater are stored in landfills or destroyed together with the adsorbent. The efficiency of adsorptive treatment reaches 80 – 95 % and depends on the chemical nature of the adsorbent [23].

Active carbons [24, 25], synthetic [26] and magnetic sorbents [27] are used as sorbents. Mineral sorbents include: clays, gels [26, 28], oxide hydrates [29], nanoactivated complexes of natural zeolite and diatomite [30]. Composite sorbents are a rather new type of adsorption materials. Modified montmorillonites are examples of composite sorbents [31, 32]. Modified and stabilized null-valent iron sols have been widely investigated [33]. This type of adsorbents can be categorized as destructive because after adsorption, the adsorbent binds firmly to the adsorbate, forming interaction products and, as a rule, is not regenerated. Due to this interaction, a high degree of water purification from ecotoxicants

can be achieved. Surface-modified sols of highly dispersed particles can also be referred to composite sorbents [34–36]. Also composite sorbents based on magnetite [37] or nanoparticles of magnetite are often used for Cr(VI) adsorption [38].

Methods for the preparation of magnetite nanoparticles are fairly well studied [39–41], however, methods for the preparation of composite sorbents using magnetite particles are constantly evolving, and each new composite usually requires a new synthesis method.

The present work describes a method for the extraction of chromium (VI) compounds using hydrazine and iron complexes. This type of compound was first described in 1908 by Franz and von Mayer [42] and the formula  $Fe[N_2H_4]_2Cl_2$  was determined. In further studies of these compounds [43], it was found that the amount of hydrazine and chlorine can be different and described compounds  $Fe[N_2H_4]_2Cl_4$  in which hydrazine is in the protonated form. The present work describes a simplified version of the synthesis of a compound of hydrazine with iron with the approximate formula  $Fe(N_2H_4)_xCl_y$ , which is a precursor for the synthesis of a composite sorbent. The presented composite sorbent is effective for Cr(VI) removal from wastewater and allows to obtain chromium-iron concentrate of regular composition.

The aim of the work is to synthesize  $Fe(N_2H_4)_xCl_y$  complex, to synthesize a sol of  $Fe_3O_4$  particles in the shell from  $Fe(N_2H_4)_xCl_y$  complex, to apply the obtained sol for the extraction of Cr(VI) compounds from aqueous solutions.

## 2. Experimental part

### 2.1. Synthesis of composite sorbent

The first step of the synthesis was to obtain the compound  $Fe_x(N_2H_4)_yCl_z$ . For this purpose, 6.19 g of iron (II) chloride (p.a., “LenReaktiv”) was first stirred with 25 mL of distilled water on a top-drive stirrer IKA RW 20 digital (IKA-Werke, Germany) at a speed of 600 rpm until complete dissolution. Then 25 mL of ethyl alcohol (95 wt%, “Khimproduktsiya”) and 2 mL of 10 % hydrochloric acid solution (puriss. spec., “Vekton”). In a separate beaker a hydrazine hydrate solution was prepared by taking 50 mL of distilled water and adding 3.62 g of hydrazine hydrate (puriss. spec., imp. “Vekton”). Then at 600 rpm stirring was dosed hydrazine hydrate solution into ferric chloride solution for 45 minutes, after completion of dosing was stirred for another 15 minutes. The reaction produced a light green precipitate, which turned light orange in air with time. The precipitate was filtered off, washed with three portions of ethyl alcohol and dried at 75 °C for 1 hour in air atmosphere.

To obtain the composite sorbent, hydrolysis was carried out. For this purpose, 1 g of  $Fe[N_2H_4]_2Cl_2$  compound was mixed with 14 mL of distilled water, stirred for 5 minutes until the formation of a dark gray precipitate. The mixture was kept for 48 hours at a temperature of 15 – 25 °C. A composite sorbent sol with an iron concentration of 2 wt% was obtained. If necessary, it is possible to centrifuge or magnetically separate the solution and precipitate and obtain the composite sorbent in powder form, but as a sol the sorbent is more convenient to dispense in adsorption studies.

### 2.2. Characterization of the material

The morphology and chemical composition of the  $Fe[N_2H_4]_2Cl_2$  precipitate surface were investigated by scanning electron microscopy (SEM) using a Carl Zeiss EVO 40 microscope (Carl Zeiss AG, Germany) with an accelerating voltage of 20 kV on a V-shaped tungsten cathode. Tablets were prepared by pressing, after which the investigated surface was ground using abrasive materials. The final surface treatment was performed using silicon carbide-based sanding paper with a grain size of ~2 microns. The elemental composition of the surface was determined by energy dispersive X-ray spectroscopy (EDS) using an INCA X-Act energy dispersive X-ray analyzer with an active detector area of 10 mm<sup>2</sup> (Oxford Instruments plc, UK). Statistics were typed for one minute (lifetime 85 – 90 %) for each of five different points in different compositional contrast areas.

The phase composition of the sample was determined by powder X-ray diffraction. The images were taken at room temperature (298 K) on a D8 ADVANCE diffractometer (Bruker, Germany) (Cu-K $\alpha$  radiation, 30 kV, 40 mA, position-sensitive detector VENTEC-1,  $\beta$ -filter). The data were recorded over an angle range of 10 – 80 °C with a step of 0.021 °C in  $2\theta$  and a point exposure equal to 1135 s. The phase composition and crystal structure of the sample were determined from X-ray diffraction data using the DIFFRAC.EVA V5.1 software package (Bruker AXS (2019), Bruker AXS GmbH, Germany) and the International Center for Diffraction Data ICDD PDF4 Release (2020) database [44]. Structure refinement was carried out by full-profile analysis using the TOPAS program [45]. The structure of  $Mn(N_2H_4)Cl_2$  [sp. gr. 12,  $a = 9.08(1)$  Å;  $b = 8.01(1)$  Å;  $c = 4.29(1)$  Å,  $\beta = 105.5(1)$ ,  $Z = 2$ ; PDF 04-016-1449] was taken as an initial model.

The electrokinetic potential of the composite sorbent was determined by a DelsaNanoC analyzer (Beckman Coulter, USA) in the range of pH values from 2 to 12. The determination is based on the measurement of electrophoretic mobility of particles using the Doppler effect. Depending on the nature of the particles and the dispersion medium, the zeta potential ( $\zeta$ ) is calculated from the electrophoretic mobility ( $\mu$ ) using either the Smoluchowski or Hückel equation. In order to choose the right equation, the Henry function  $f(k\alpha)$  is calculated independently and values between 1 and 1.5 are obtained [39]. The Smoluchowski equation (1) was chosen to calculate the electrokinetic potential because the value of  $f(k\alpha)$  is 1.43, which is closer to 1.5.

$$\zeta = \frac{\eta U_0}{E \varepsilon \varepsilon_0}, \quad (1)$$

where  $\eta$  is the viscosity of the medium, cSt;  $U_0$  is the linear velocity of the dispersed phase particles  $\text{cm}\cdot\text{s}^{-1}$ ;  $\varepsilon$  is the relative dielectric permittivity of the medium;  $\varepsilon_0$  is the electric constant;  $E$  is the electric field strength.

X-ray diffraction analysis of the precipitate formed during chromium extraction at optimum pH was performed on a XRD 7000 diffractometer (Shimadzu, Japan) with  $\text{Cu-K}\alpha$  radiation in continuous scanning mode at a speed of  $1^\circ/\text{min}$  in the range of angles  $2\theta = 20 - 100^\circ$ . The phase analysis was performed using the international ICDD PDF-2 file system with built-in modules of automatic phase search and semi-quantitative analysis by the corundum number method.

The particle size of the composite sorbent was determined by dynamic light scattering on a Zetasizer Nano S90 (Malvern, UK), laser radiation source with a maximum of 632.8 nm. The sol was diluted 100 times with glycerol, measurements were performed at  $20^\circ\text{C}$  taking into account the solvent properties (viscosity 1412  $\text{mPa}\cdot\text{s}$ , refractive index 1.474), and the number of replicates was 3.

### 2.3. Adsorption study

To obtain the dependence of Cr(VI) adsorption on pH, model solutions containing  $50\text{ mg}\cdot\text{L}^{-1}$  of chromium were prepared by diluting the initial solution of potassium dichromate  $1\text{ mg}\cdot\text{L}^{-1}$  (1.4145 g (p.a., "Reakhim") per 500 mL of distilled water):

- (1) pH 1.0 – 2.5 with sulfuric acid solution (puriss., "UfaKhimProekt");
- (2) pH 3.5 – 6.3 by acetate buffer solution (1 M of NaOH (p.a., "UfaKhimProekt") and 1 M of  $\text{CH}_3\text{COOH}$  (puriss., "Nevinnomyssky Azot"));
- (3) pH 7.0 by NaOH solution with addition of 1 M of  $\text{NaNO}_3$  (puriss., "UfaKhimProekt");
- (4) pH 8.0 – 10.0 by ammonia buffer solution (1 M of  $\text{NH}_4\text{OH}$  (p.a., "Sigma Tec") and 1 M of  $\text{NH}_4\text{Cl}$  (puriss., "Vekton"));
- (5) pH 12.0 with 1 M of NaOH solution.

The pH was monitored using an I-160 MI ionometer (Izmeritel'naya Tekhnika, Russia).

In adsorption study, 2.5 mL of composite sorbent was added to 20 mL of Cr(VI) solution with a certain pH value, stirred for 2 hours on a rotary mixer RM-1L (SIA "ELMI", Latvia). Then the solution and sorbent were separated by filtration using a paper filter "Blue Ribbon" ("Melior XXI").

The residual chromium concentration in the filtrate was measured by inductively coupled plasma atomic emission spectrometry (ICP-AES) on a SpectroBlue spectrometer (Spectro Analytical Instruments, Germany). The degree of chromium sorption ( $R$ , %) was calculated as the ratio of the difference between the initial ( $C_0$ ,  $\text{mg}\cdot\text{dm}^{-3}$ ) and equilibrium ( $C_e$ ,  $\text{mg}\cdot\text{dm}^{-3}$ ) concentrations of chromium in solution to the initial concentration:

$$R = \frac{C_0 - C_e}{C_0} \cdot 100\% \quad (2)$$

The amount of adsorbed chromium per 1 g of sorbent (equilibrium sorption capacity) –  $q$  ( $\text{mg}\cdot\text{g}^{-1}$ ), was calculated by the formula:

$$q = \frac{(C_0 - C_e) \cdot V}{m} \cdot 1000, \quad (3)$$

where  $V$  is the volume of solution,  $\text{dm}^3$ ;  $m$  is the mass of sorbent, g.

To study the influence of temperature on the adsorption process, adsorption isotherms (dependences  $q = f(C_e)$ ) were obtained at temperatures of 293 K, 313 K and 333 K.

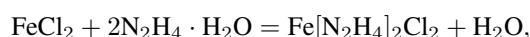
### 2.4. Removal of chromium from a real wastewater sample

As a real chromium-containing sample of wastewater, a water sample of JSC "Russian Chromium 1915" was taken before the stage of reagent treatment – a solution with chromium concentration of  $350\text{ mg}\cdot\text{L}^{-1}$  and  $\text{pH} = 11.5$ . Wastewater was filtered. 1 mL of 5 % sol of composite sorbent was added to 20 mL of filtrate, and stirred for 15 minutes. Sorbent was separated by centrifuge OPn-8 ("TNK"Dastan", Kyrgyz Republic) for 20 min at a speed of 7000 rpm. In the filtrate, the content of total chromium was determined by ICP-AES method. In addition, we performed an experiment comparing the efficiency of chromium removal by composite sorbent with chromium removal by treatment with iron (II) sulfate. For this purpose, wastewater was filtered, 0.0993 g  $\text{FeSO}_4\cdot 7\text{H}_2\text{O}$  (p.a., "JSC Reakhim") was added to 20 mL of filtrate, and stirred for 15 minutes. The solution and precipitate were separated by centrifugation. Chromium content was determined in the filtrate. Similarly, the experiment was performed for  $\text{pH} = 5.4$ , adding a few drops of concentrated sulfuric acid to the wastewater. The experimental conditions were similar to those described above. The only difference was that 2 mL of sol or 0.1986 g  $\text{FeSO}_4\cdot 7\text{H}_2\text{O}$  was added. The content of hexavalent chromium in the wastewater after adsorption was determined by spectrophotometric test with 1,5-diphenylcarbazide (p.a., sole proprietor S.A. Smirnova doing business as "InterKhim") [46].

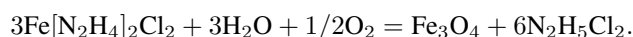
### 3. Results and discussion

#### 3.1. Synthesis of iron complex with hydrazine hydrate

During the interaction between iron (II) chloride and hydrazine hydrate, the following chemical reaction took place:



and as a result  $Fe[N_2H_4]_2Cl_2$  complex was formed, which was then filtered and washed with several portions of ethyl alcohol. The X-ray diffraction of the complex (Fig. 1a) confirms that there is a single phase. When the solid/water ratio is increased up to 1:14, the dissolution of  $Fe[N_2H_4]_2Cl_2$  complex increases, and its hydrolysis occurs, which in the presence of air oxygen leads to the formation of magnetite phase, the surface of which is completed by particles of  $Fe[N_2H_4]_2Cl_2$  complex:



Thus, particles of composite sorbent with the ratio of magnetite/iron complex phases 1:3 are formed, which is confirmed by X-ray studies (Fig. 1b). The system comes to a state of equilibrium and there is no further transformation of phases with increasing exposure time, and this means that there are factors preventing hydrolysis, the main of which is the formation of an electrical double layer (EDL). The synthesis scheme (Fig. 1c) shows the sequence of interactions prior to the formation of EDL.

It is worth noting that in this variant of synthesis, the main stabilization of the sol occurs due to the high value of the electrokinetic potential. A rather atypical picture is observed for the dependence of the electrokinetic potential on the pH of the medium (Fig. 2a). The high positive charge of the surface is maintained up to pH 9, and after that the surface sharply changes the sign of the charge and becomes negative, which indicates the rearrangement of the structure and the formation of a new type of sol. The value of the electrokinetic potential indicates high mobility of sol particles, and in this case the electrostatic stability factor plays a key role. The sign of the electrokinetic potential up to pH 9 suggest the structure of two-phase particles: the outer layer consists of hydrazine complex, and the inner layer contains magnetite. The high positive electrokinetic potential of the surface is due to complex iron ions or protonated hydrazine ions.

Protonating in acidic medium, hydrazine acquires a positive charge, which is compensated by chloride ion. Thus, it can be considered that the composite sorbent is a sol of  $Fe_3O_4@Fe(N_2H_4)_xCl_y$  particles. An important characteristic of the composite sorbent is the particle size, because it is the particle size that is associated with the stability of the sol, the specific surface area of the particles and the sorption characteristics. A rather narrow particle size distribution with a maximum of 30.7 nm (Fig. 2b), obtained by dynamic light scattering, indirectly indicates the formation of particles with a "core/shell" structure and that the process comes to equilibrium and no further particle enlargement occurs.

The absence of larger sized agglomerates is also noteworthy, although the particles have their own magnetic moment, and no additional dispersion by ultrasound or high speed agitation was performed prior to particle size measurement.

#### 3.2. Microscopic studies

The results of scanning electron microscopy examination of the sample of iron complex with hydrazine hydrate (Fig. 3) show that the sample is homogeneous and crystalline. The surface of the sample appears inhomogeneous under magnification, primarily due to topological contrast caused by grinding.

Light inclusions on the gray background should be attributed to compositional contrast. Its appearance is due to the fact that the chemical composition locally deviates from the ideal  $Fe:Cl:N=1:2:4$  ratio (Fig. 3a). The elemental maps show that the distribution of iron and chlorine in the sample surface is generally homogeneous, but there are regions with fluctuations in chemical composition. Using X-ray energy dispersive point analysis, it is shown that the iron content varies between 11.47 – 16.29 at%, chlorine 24.63 – 35.00 at% and nitrogen 48.71 – 63.89 at% in different regions. Thus, iron excess and deficiency regions of  $Fe(N_2H_4)_{1.7}Cl_{1.8}$  and  $Fe(N_2H_4)_{2.8}Cl_{2.1}$  are observed, respectively. That is, the exact formula of the compound has not yet been established, so in general we use the record of the compound –  $Fe(N_2H_4)_xCl_y$ .

#### 3.3. Investigation of chromium adsorption by the composite sorbent sol

Studies of chromium adsorption from Cr(VI) solution depending on pH of the medium (Fig. 4) showed the efficiency of the composite sorbent in the pH range from 2 to 12. The dependence of the degree of chromium adsorption on the pH of the medium shows that in a wide range of pH almost all chromium (about 99.9 %) is adsorbed, which proves the efficiency of the sorbent.

Decrease in adsorption at  $pH < 2$  is most likely due to the decrease in the electrokinetic potential of the composite sorbent and its dissolution.

To reveal the nature of the interaction of the composite sorbent with Cr(VI) ions, the dependence of adsorption on temperature was investigated (Fig. 5a).

At 293 K, the isotherm comes to saturation and probably monolayer adsorption occurs. The maximum capacity of the sorbent according to the graph is  $385 \text{ mg} \cdot \text{g}^{-1}$ . At temperatures above 313 K, the isotherm acquires an S-shaped form, which indicates either multilayer adsorption or the occurrence of chemical interactions in parallel with adsorption

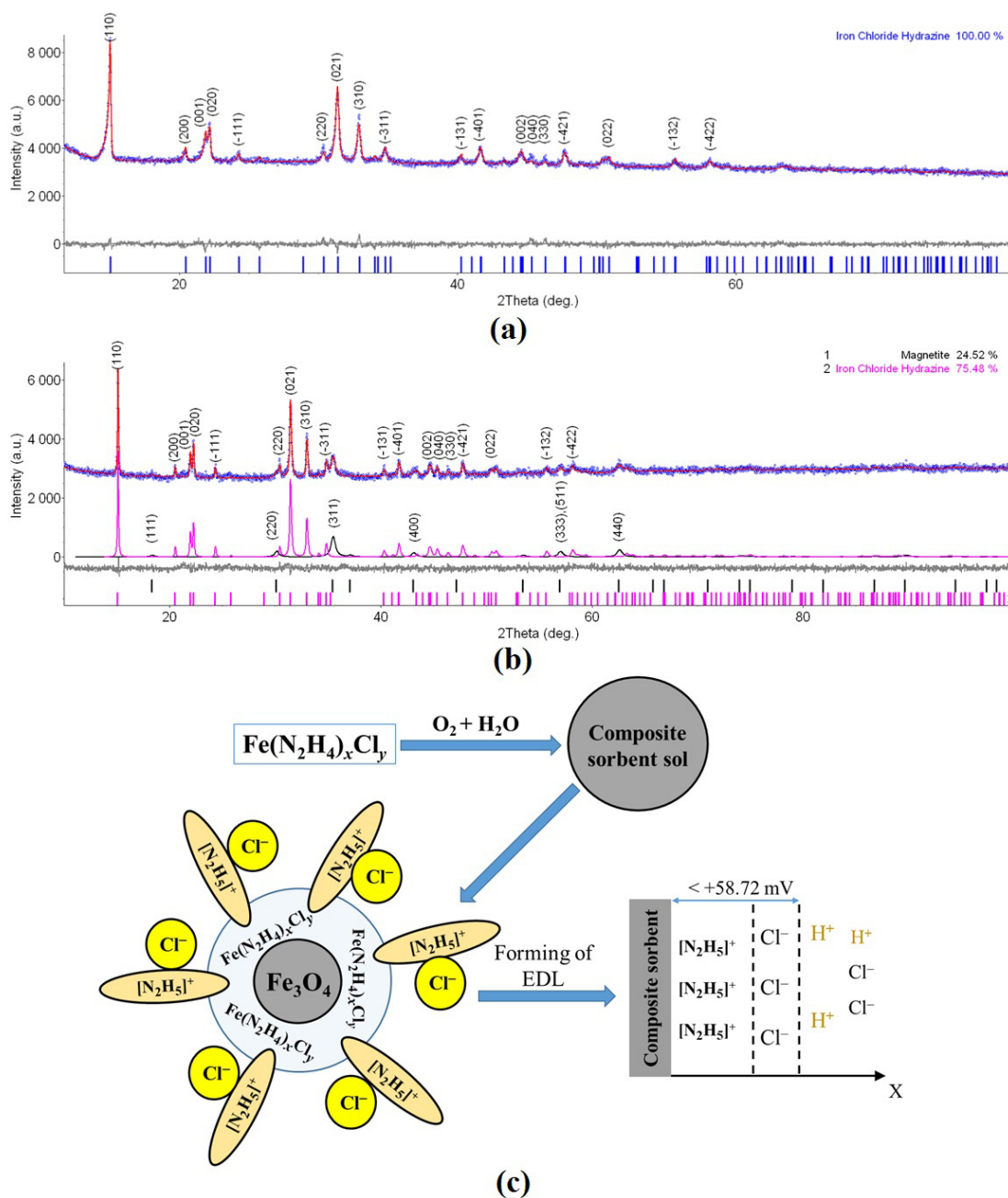


FIG. 1. Validation of the composite sorbent and synthesis scheme. XRD patterns of (a) Fe[N<sub>2</sub>H<sub>4</sub>]<sub>2</sub>Cl<sub>2</sub> complex and (b) Fe<sub>3</sub>O<sub>4</sub>@Fe(N<sub>2</sub>H<sub>4</sub>)<sub>x</sub>Cl<sub>z</sub> sample (@ is designation of the particle “core/shell”, to the left of the symbol phase – core, to the right – shell). Experimental (blue dots) and calculated (red curve) diffractograms, and difference curve (gray) of the sample. Vertical dashes correspond to Bragg reflections of the compounds. Scheme of formation and structure of EDL of the sol at pH values < 9 (c)

interactions. The ultimate capacity of the composite sorbent in this case cannot be calculated from the linear dependence (Fig. 5a), but it can be assumed that it will exceed 500 mg·g<sup>-1</sup>.

By plotting the linear dependence in Langmuir coordinates (Fig. 5b), it can be seen that at 293 K, the dependence has a linear form, but as the temperature increases, the dependence deviates from linear (the correlation coefficient decreases), which indicates multilayer adsorption or chemical interaction. That is, it is possible to assume the occurrence of at least three variants of reactions:

- (1)  $\text{HCrO}_4^- + \text{N}_2\text{H}_4 + 3\text{H}^+ = \text{Cr}^{3+} + \text{N}_2 + 4\text{H}_2\text{O}$  (redox reaction with N<sub>2</sub>H<sub>4</sub> as the reducing agent);
- (2)  $\text{HCrO}_4^- + \text{composite sorbent} + 7\text{H}^+ = \text{Cr}^{3+} + \text{Fe}^{3+} + 4\text{H}_2\text{O}$  (redox reaction with Fe<sup>2+</sup>);
- (3)  $\text{N}_2\text{H}_5^{5+} + \text{HCrO}_4^- = \text{N}_2\text{H}_5\text{HCrO}_4$  (ion exchange interaction).

Adsorption at 293 K is satisfactorily described by the Langmuir model, which means that monolayer adsorption occurs at this temperature, and this corresponds to the ion-exchange interaction (variant 3). At temperatures 313 and

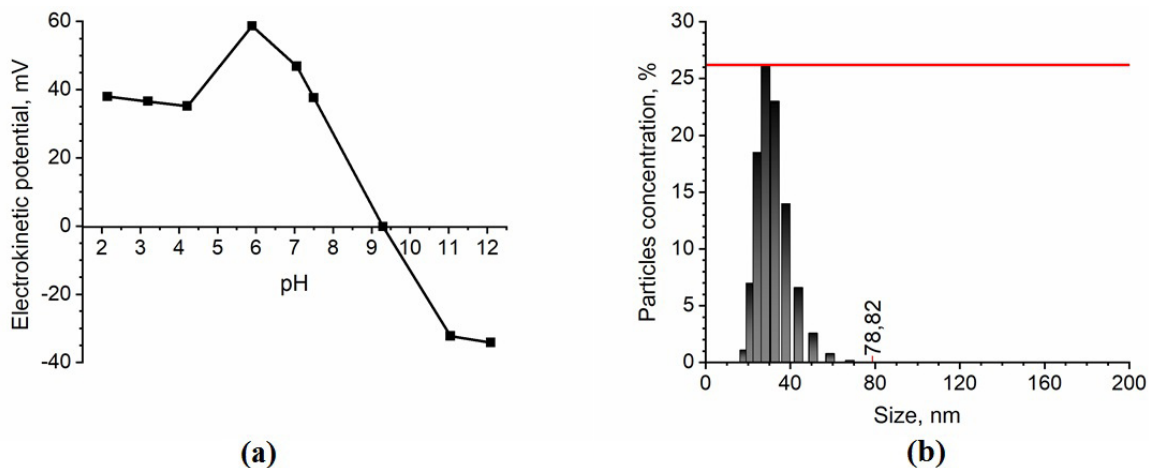


FIG. 2. Characteristics of the composite sorbent sol: dependence of the electrokinetic potential on the pH of the medium for the sol  $Fe_3O_4@Fe(N_2H_4)_xCl_y$  (a), dependence of the size (diameter) of the composite sorbent particles on the concentration by dynamic light scattering (b)

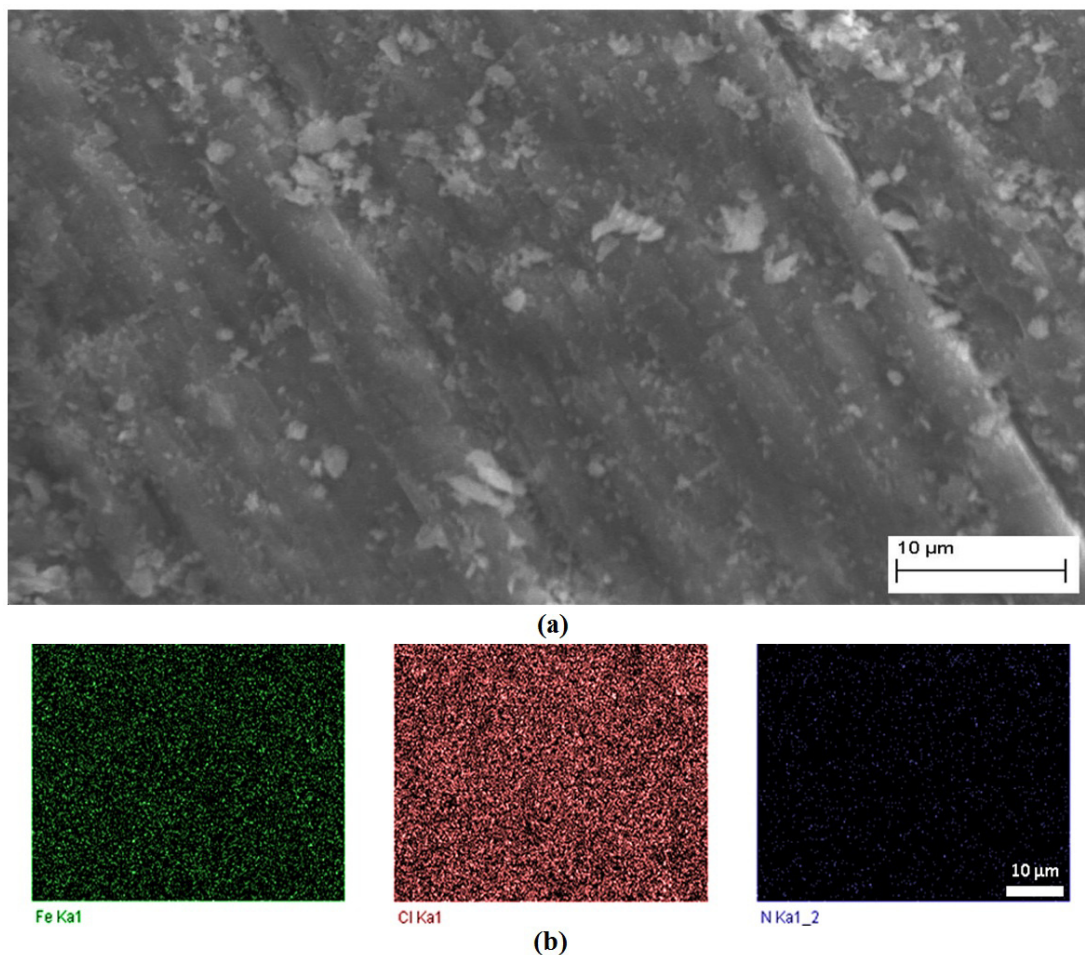


FIG. 3. Image of the  $Fe(N_2H_4)_xCl_y$  tablet surface in secondary electrons (a) and element distribution maps (b)

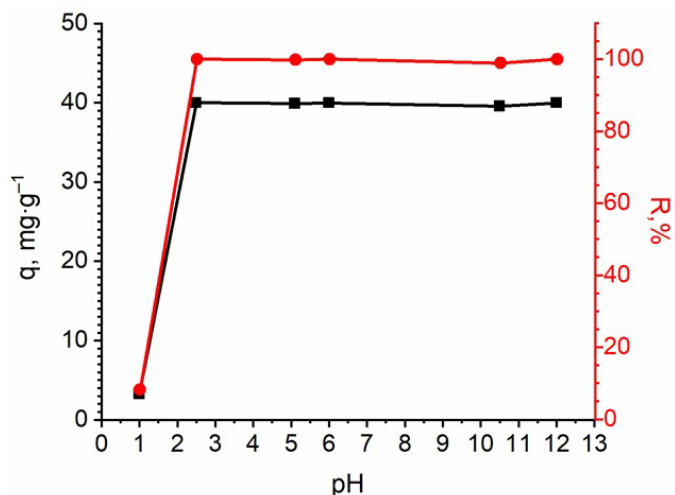


FIG. 4. Dependence of chromium adsorption on pH on Fe-sol (left axis, black color), of chromium adsorption degree on composite sorbent, % on pH (right axis, red color). Initial concentration of Cr(VI)  $50 \text{ mg}\cdot\text{L}^{-1}$ , adsorption time 2 h, temperature 293 K

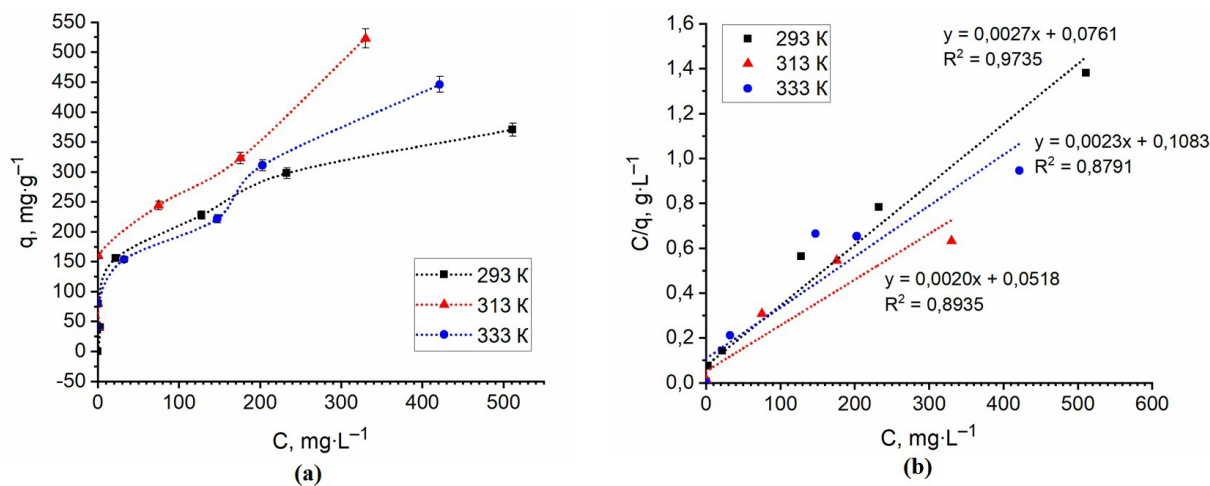


FIG. 5. Adsorption isotherms of Cr(VI) on composite sorbent (a); linear dependence of  $C - C_e/q$  for composite sorbent (b); pH = 5.0, acetate buffer, stirring 2 hours

333 K (Fig. 5a) we observe S-shaped adsorption isotherms, which is characteristic of polymolecular adsorption on non-porous sorbents, which may indirectly indicate the occurrence of chemisorption, i.e., in this case, variants 1 and 2 take place.

### 3.4. Purification of a real water sample from chromium (VI)

Adsorption of chromium (VI) from waste water of JSC “Russian Chromium 1915” before the stage of reagent treatment was carried out at temperature 290 K and pH = 5.4. The initial concentration of chromium in this water was  $350 \text{ mg}\cdot\text{L}^{-1}$ . After treatment with composite sorbent sol according to the procedure described in the experimental part, we determined the content of total chromium by ICP-AES method in supernatant, it amounted to  $0.087 \text{ mg}\cdot\text{L}^{-1}$ , which is less than MPC for trivalent chromium in drinking water. Hexavalent chromium was not detected in the solution after sorption (according to the test with 1,5-diphenylcarbazide).

X-ray phase analysis of the sorbent after adsorption of chromium showed the presence of FeO(OH) phases with tetragonal and orthorhombic structure and  $\text{Fe}_{1.8}\text{Cr}_{1.2}\text{O}_4$  (Fig. 6).

When the composite sorbent interacts with Cr(VI), iron passes into iron metahydroxide, and Cr(VI) – into Cr(III), while forming a solid solution of substitution – in the compound  $\text{Fe}_{1.8}\text{Cr}_{1.2}\text{O}_4$  chromium replaces iron in its positions in the spinel structure.

For comparison, tests were carried out with the currently used reagent for water purification from chromium (VI) compounds – iron (II) sulfate [47], with the same molar concentration of iron as when using the composite sorbent sol.

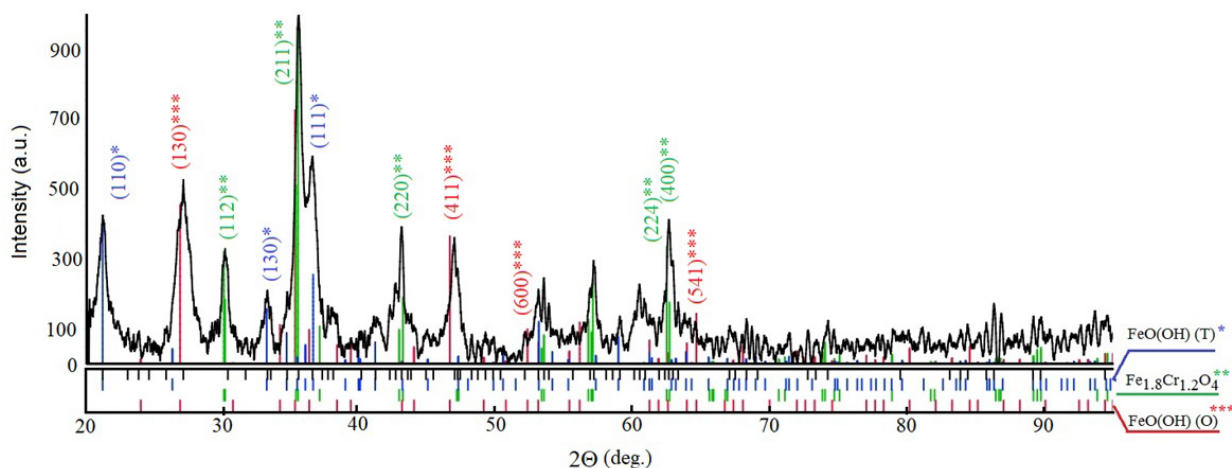


FIG. 6. XRD of the composite sorbent after Cr(VI) adsorption and results of X-ray phase analysis: the upper set of dashes is the dashed diagram of the sol after adsorption; the dashed diagrams below are in order from top to bottom: tetragonal FeO(OH),  $Fe_{1.8}Cr_{1.2}O_4$ , orthorhombic FeO(OH)

TABLE 1. Results of chromium removal from wastewater of JSC “Russian Chromium 1915” by two methods

Treatment	pH	$C_{Cr}$ after treatment, $mg \cdot L^{-1}$	R, %
$FeSO_4 \cdot 7H_2O$	5.4	225.6	35.5
	11	5.3	98.5
Composite sorbent	5.4	0.084	99.98
	11	26.4	92.5

According to the experimental data (Table 1), the composite sorbent sol is significantly superior to iron (II) sulfate in acidic medium and less effective in strongly alkaline medium.

In addition, in the acidic environment, it is possible to reach the MPC value for trivalent chromium. Also an important factor is that the product of chromium precipitation with composite sorbent is not contaminated with sulfur compounds, and all chromium passes into the trivalent state, forming a compound of regular composition  $Fe_{1.8}Cr_{1.2}O_4$ .

Thus, using the composite sorbent sol obtained by the proposed method it is possible to effectively remove Cr(VI) from the wastewater of metallurgical companies. Also we have to remember that hydrazine is toxic substance (MPC is  $0.01 \text{ mg} \cdot \text{L}^{-1}$ ) [16] and some quantity of hydrazine can penetrate to the aqua solution during working of sorbent. However, this is not a problem if we treat the effluent, as hydrazine readily decomposes into nitrogen and water when it interacts with oxygen [48], active chlorine or by the catalytic reaction in the presence of transition metals.

The proposed technological approach makes it possible to treat wastewater containing Cr(VI) to a residual concentration of  $0.084 \text{ mg} \cdot \text{L}^{-1}$  (with chromium remaining only in the form of Cr(III)), and to obtain a material of sufficiently regular composition, predominantly containing compounds of Cr(III) and iron. This material can be used for production of ferrochrome, chrome cast iron, metal flux or as a component in the production of ceramic products.

#### 4. Conclusions

The paper presents a method of synthesis of  $Fe(N_2H_4)_xCl_y$  complex where  $x = 1.7 - 2.8$ ,  $y = 1.8 - 2.1$  and subsequent formation of composite sorbent particles with a “core-shell” structure, in which the core is magnetite particles, and the shell is represented by  $Fe(N_2H_4)_xCl_y$  complex, which forms the positive charge of the surface. Such a composite sorbent allows the effective removal of Cr(VI) compounds from solutions in the pH range from 2 to 12. The  $Fe(N_2H_4)_xCl_y$  complex was certified by XRD, SEM and EDS methods. Based on the specificity of the interaction between the sorbent and Cr(VI) compounds, a scheme of the structure of its electrical double layer and adsorption mechanism is presented. Depending on the conditions, Cr(VI) can either adsorb on the surface of the highly dispersed sorbent or be reduced to Cr(III) by it. Purification of a sample of real wastewater by the obtained composite sorbent sol at room temperature in adsorption mode was carried out, it was shown that it allows to completely purify wastewater from Cr(VI) and from Cr(III) to concentrations below the MPC values in drinking water. At the same time, a high adsorption capacity of  $385 \text{ mg} \cdot \text{g}^{-1}$  and an adsorption degree of 99.9 % are achieved. The sludge after sorption can be used to obtain commercial products used in metallurgy as a substitute for ferrochrome. Comparison of wastewater treatment from chromium by composite

sorbent sol with the classical method of treatment using ferrous sulfate at different pH values of the medium showed that the sorbent  $\text{Fe}_3\text{O}_4 @ \text{Fe}(\text{N}_2\text{H}_4)_x \text{Cl}_y$  is effective in acidic environment, and allows to reach the MPC value, and ferrous sulfate is effective at pH = 11, but its use does not reach the MPC and sludge is obtained, not suitable for further use, because it is heavily contaminated with sulfur compounds.

## References

- [1] Trevett A.F., Carter R.C. Targeting appropriate interventions to minimize deterioration of drinking-water quality in developing countries. *J. Health Popul Nutr*, 2008, **26**(2), P. 125–138.
- [2] Danilov-Danilyan V.I. Global problem of fresh water deficit. *Age of globalization*, 2008, **1**, P. 45–56. (in Russian)
- [3] Lee E.J., Schwab K.J. Deficiencies in drinking water distribution systems in developing countries. *J. Water Health.*, 2005, **3**(2), P. 109–127.
- [4] Tikhomirova E.I., Plotnikova O.A., Atamanova O.V., Istrashkina M.V., Koshelev A.V., Podolsky A.L. The use of multicomponent adsorption filters in water purification systems and luminescent control of ecotoxicant content. *Theoretical and Applied Ecology*, 2019, **1**, P. 73–81.
- [5] Schwarzenbach R.P., Egli T., Hofstetter T.B., von Gunten U., Wehrli B. Global water pollution and human health. *Annual Review of Environment and Resources*, 2010, **35**(1), P. 109–136.
- [6] Chaturvedi A.D., Pal D., Penta S., Kumar A. Ecotoxic heavy metals transformation by bacteria and fungi in aquatic ecosystem. *World J. Microbiol. Biotechnol.*, 2015, **31**(10), P. 1595–1603.
- [7] Kalyukova E.N., Ivanskaya N.N. Adsorption properties of some natural sorbents towards chromium (III) cations. *Sorbtsionnye i Khromatograficheskie Protsestry*, 2011, **11**(4), P. 496–501. (in Russian)
- [8] Zhao Z.M., Wang Z.F., Cheng M.Y., Zhang Y.J. Effects of the combinations of 6 materials on the improvements in contaminant removals from surface water: purification mechanisms and adsorption kinetics. *IOP Conf. Ser.: Earth Environ. Sci.*, 2019, **398**(1), P. 012007.
- [9] Ambaye T.G., Vaccari M., van Hullebusch E.D., Amrane A., Rtimi S. Mechanisms and adsorption capacities of biochar for the removal of organic and inorganic pollutants from industrial wastewater. *Int. J. Environ. Sci. Technol.*, 2021, **18**(10), P. 3273–3294.
- [10] Huang Y.-C., Koseoglu S.S. Separation of heavy metals from industrial waste streams by membrane separation technology. *Waste Management*, 1993, **13**(5–7), P. 481–501.
- [11] Chandrashekar Nayak M., Isloor A.M., Inamuddin, Lakshmi B., Marwani H.M., Khan I. Polyphenylsulfone/multiwalled carbon nanotubes mixed ultrafiltration membranes: Fabrication, characterization and removal of heavy metals  $\text{Pb}^{2+}$ ,  $\text{Hg}^{2+}$ , and  $\text{Cd}^{2+}$  from aqueous solutions. *Arabian J. Chem.*, 2020, **13**(3), P. 4661–4672.
- [12] Qdais H.A., Moussa H. Removal of heavy metals from wastewater by membrane processes: a comparative study. *Desalination*, 2004, **164**(2), P. 105–110.
- [13] Pronina E.V., Akhmadullina F.Yu., Zakirov R.K., Pobedimskii D.G. Influence of the reagent pretreatment of wastewaters from chemical plants on the efficiency of their biological treatment. *Russ. J. Appl. Chem.*, 2009, **82**(1), P. 143–147.
- [14] Bolisetty S., Peydayesh M., Mezzenga R. Sustainable technologies for water purification from heavy metals: review and analysis. *Chem. Soc. Rev.*, 2019, **48**(2), P. 463–487.
- [15] Smart N.G., Carleson T.E., Elshani S., Wang Sh., Wai Ch.M. Extraction of toxic heavy metals using supercritical fluid carbon dioxide containing organophosphorus reagents. *Ind. Eng. Chem. Res.*, 1997, **36**(5), P. 1819–1826.
- [16] SanPiN 2.1.4.1074-01. Potable water. Hygienic requirements for the water quality of centralized drinking water supply systems. Quality control (supersedes SanPiN 2.1.4.559-96). (in Russian)
- [17] Rojas G., Silva J., Flores J.A., Rodriguez A., Ly M., Maldonado H. Adsorption of chromium onto cross-linked chitosan. *Separation and Purification Technology*, 2005, **44**(1), P. 31–36.
- [18] Recillas S., Colón J., Casals E., González E., Puentes V., Sánchez A., Font X. Chromium VI adsorption on cerium oxide nanoparticles and morphology changes during the process. *Journal of Hazardous Materials*, 2010, **184**(1–3), P. 425–431.
- [19] Álvarez-Ayuso E., García-Sánchez A., Querol X. Adsorption of Cr (VI) from synthetic solutions and electroplating wastewaters on amorphous aluminium oxide. *Journal of Hazardous Materials*, 2007, **142**(1–2), P. 191–198.
- [20] El-Shahawi M.S., Al-Saïdi H.M., Bashammakh A.S., Al-Sibaai A.A., Abdelfadeel M.A. Spectrofluorometric determination and chemical speciation of trace concentrations of chromium (III & VI) species in water using the ion pairing reagent tetraphenyl-phosphonium bromide. *Talanta*, 2011, **84**(1), P. 175–179.
- [21] Khalturina T.I., Bobrik A.G., Churbakova O.V. Reagent treatment of chromium-containing wastewater. *Proceedings of Irkutsk State Technical University*, 2014, **6**(89), P. 128–134. (in Russian)
- [22] Klimova O.V. Processes and apparatus design of wastewater treatment from chromium (VI) ions by carbon adsorbents: dis. – Ufa, 2016, 148 p. (in Russian)
- [23] Povarova L.V. Analysis of methods of oil-containing wastewater treatment. *Science. Engineering. Technology (polytechnical bulletin)*, 2018, **1**, P. 189–205. (in Russian)
- [24] Shaykimova A.K. New complex sorbents in the processes of additional treatment of chromium-containing wastewater. Proceedings of the “III Youth Environmental Forum”, Kemerovo, 06-08 October 2015, P. 84–84. (in Russian)
- [25] Nistratov A.V., Klushin V.N., Erofeeva V.B. Development of the process of chromium (VI) treatment of galvanic production wastewater by active carbon on a peat polymer basis. *Uspekhi v Khimii i Khimicheskoi Tekhnologii*, 2012, **26**(10 (139)), P. 94–98. (in Russian)
- [26] Ecology. Reference book. Adsorbents alumogel, 2021 (<https://ru-ecology.info/term/59686>). (in Russian)
- [27] Frolova L., Kharytonov M., Klimkina I., Kovrov O., Koveria A. Adsorption purification of waste water from chromium by ferrite manganese. *E3S Web of Conferences*, 2020, **168**, P. 00026.
- [28] Raouf M.E.A., Maysour N.E., Farag R.K., Abdul-Raheim A.R.M. Wastewater treatment methodologies, review article. *International Journal of Environment & Agricultural Science*, 2019, **3**(1), P. 18.
- [29] Stroganova Yu.I., Nagornov R.S., Lepilova A.M., Razgovorov P.B. Study of the surface state of aluminosilicate material during treatment with organic acids and alkali. Proceedings of the X All-Russian Scientific and Practical Conference “Technologies and equipment for the chemical, biotechnological and food industries”, Biysk, 24-26 May 2017, P. 304–307. (in Russian)
- [30] Malkin P. Wastewater treatment from heavy metal ions using nanoactivated complexes of natural zeolite and diatomite. *Nanotechnologies in Construction*, 2018, **10**(2), P. 21–41.
- [31] Keymirov M.A. Water purification of ions of heavy metals by montmorillonite modified with polyamine. *Journal of Water Chemistry and Technology*, 2018, **40**(6), P. 320–326.

- [32] Bhattacharyya K.G., Sen Gupta S. Influence of acid activation of kaolinite and montmorillonite on adsorptive removal of Cd (II) from water. *Ind. Eng. Chem. Res.*, 2007, **46**(11), P. 3734–3742.
- [33] Xiaomin N., Xiaobo S., Huangui Z., Dongen Z., Dandan Y., Qingbiao Z. Studies on the one-step preparation of iron nanoparticles in solution. *J. Cryst. Growth.*, 2005, **275**(3–4), P. 548–553.
- [34] Shapovalova O.E., Drozdov A.S., Bryushkova E.A., Morozov M.I., Vinogradov V.V. Room-temperature fabrication of magnetite-boehmite sol-gel composites for heavy metal ions removal. *Arabian J. Chem.*, 2020, **13**(1), P. 1933–1944.
- [35] Reddy D.H.K., Yun Y.-S. Spinel ferrite magnetic adsorbents: Alternative future materials for water purification? *Coord. Chem. Rev.*, 2016, **315**, P. 90–111.
- [36] Li X., Sotto A., Li J., Van der Bruggen B. Progress and perspectives for synthesis of sustainable antifouling composite membranes containing in situ generated nanoparticles. *Journal of Membrane Science*, 2017, **524**, P. 502–528.
- [37] Moges A., Nkambule T.T.I., Fito J. The application of GO- $Fe_3O_4$  nanocomposite for chromium adsorption from tannery industry wastewater. *J. Environ. Manage.*, 2022, **305**, P. 114369.
- [38] Rajput S., Pittman C.U., Jr., Mohan D. Magnetic magnetite ( $Fe_3O_4$ ) nanoparticle synthesis and applications for lead ( $Pb^{2+}$ ) and chromium ( $Cr^{6+}$ ) removal from water. *J. Colloid Interface Sci.*, 2016, **468**, P. 334–346.
- [39] Zhou Z.H., Wang J., Liu X., Chan H.S.O. Synthesis of  $Fe_3O_4$  nanoparticles from emulsions. *J. Mater. Chem.*, 2001, **11**(6), P. 1704–1709.
- [40] Iida H., Takayanagi K., Nakanishi T., Osaka T. Synthesis of  $Fe_3O_4$  nanoparticles with various sizes and magnetic properties by controlled hydrolysis. *J. Colloid Interface Sci.*, 2007, **314**(1), P. 274–280.
- [41] Ahmadi S., Chia C.-H., Zakaria S., Saeedfar K., Asim N. Synthesis of  $Fe_3O_4$  nanocrystals using hydrothermal approach. *J. Magn. Magn. Mater.*, 2012, **324**(24), P. 4147–4150.
- [42] Scoville A.N., Reiff W.M. Magnetic characterization of the linear chain polymer bis hydrazine ferrous chloride  $Fe(N_2H_4)_2Cl_2$ . *Inorg. Chim. Acta*, 1983, **68**, P. 57–61.
- [43] Kumar N.R.S., Nethaji M., Patil K.C. Preparation, characterization, spectral and thermal analyses of  $(N_2H_5)_2MCl_4 \cdot 2H_2O$  ( $M = Fe, Co, Ni$  and  $Cu$ ); crystal structure of the iron complex. *Polyhedron*, 1991, **10**(3), P. 365–371.
- [44] Gates-Rector S., Blanton T. The Powder Diffraction File: A Quality Materials Characterization Database. *Powder Diffr.*, 2019, **34**(4), P. 352–360.
- [45] Coelho A.A. TOPAS and TOPAS-Academic: an optimization program integrating computer algebra and crystallographic objects written in C++. *J. Appl. Cryst.*, 2018, **51**, P. 210–218.
- [46] Ordinartsev D.P., Pechishcheva N.V., Estemirova S.Kh., Kim A.V., Shunyayev K.Yu. Removal of Cr(VI) from wastewater by modified montmorillonite in combination with zero-valent iron. *Hydrometallurgy*, 2022, **208**, P. 105813.
- [47] Qin G., McGuire M.J., Blute N.K., Seidel C., Fong L. Hexavalent chromium removal by reduction with ferrous sulfate, coagulation, and filtration: A pilot-scale study. *Environ. Sci. Technol.*, 2005, **39**(16), P. 6321–6327.
- [48] Gaunt H., Wetton E.A.M. The reaction between hydrazine and oxygen in water. *J. Appl. Chem.*, 1966, **16**(6), P. 171–176.

---

Submitted 20 February 2024; revised 22 May 2024; accepted 19 June 2024

#### Information about the authors:

*Denis P. Ordinartsev* – Institute of Metallurgy of the Ural Branch of the Russian Academy of Sciences, 101, Amundsen street, Yekaterinburg, 620016, Russia; ORCID 0000-0002-4216-4770; denis\_ordinartsev@mail.ru

*Nadezhda V. Pechishcheva* – Institute of Metallurgy of the Ural Branch of the Russian Academy of Sciences, 101, Amundsen street, Yekaterinburg, 620016, Russia; Ural Federal University named after the First President of Russia B. N. Yeltsin, 19, Mira street, Yekaterinburg, 620002, Russia; ORCID 0000-0002-7281-1342; pechischeva@gmail.com

*Svetlana Kh. Estemirova* – Institute of Metallurgy of the Ural Branch of the Russian Academy of Sciences, 101, Amundsen street, Yekaterinburg, 620016, Russia; ORCID 0000-0001-7039-1420; esveta100@mail.ru

*Angelina V. Kim* – Institute of Metallurgy of the Ural Branch of the Russian Academy of Sciences, 101, Amundsen street, Yekaterinburg, 620016, Russia; Ural Federal University named after the First President of Russia B. N. Yeltsin, 19, Mira street, Yekaterinburg, 620002, Russia; ORCID 0000-0003-0610-1075; kim-angelina.95@mail.ru

*Evgenii V. Sterkhov* – Institute of Metallurgy of the Ural Branch of the Russian Academy of Sciences, 101, Amundsen street, Yekaterinburg, 620016, Russia; ORCID 0000-0002-4227-7740; ev.sterhov@mail.ru

*Sofia A. Petrova* – Institute of Metallurgy of the Ural Branch of the Russian Academy of Sciences, 101, Amundsen street, Yekaterinburg, 620016, Russia; ORCID 0000-0002-9796-5794; danaus@mail.ru

*Galina A. Shilenko* – Ural Federal University named after the First President of Russia B. N. Yeltsin, 19, Mira street, Yekaterinburg, 620002, Russia; ORCID 0000-0001-9856-4717; g-shilenko@mail.ru

*Conflict of interest:* the authors declare no conflict of interest.

## Phase formation of nanosized InGaZnO<sub>4</sub> obtained by the sol-gel method with different chelating agents

Gleb M. Zirnik<sup>1,2</sup>, Alexander S. Chernukha<sup>1,2,3</sup>, Daniil A. Uchaev<sup>3</sup>, Ibrohimi A. Solizoda<sup>1,2,4</sup>, Svetlana A. Gudkova<sup>1,2</sup>, Nadezhda S. Nekorysnova<sup>1</sup>, Denis A. Vinnik<sup>1,2,3</sup>

<sup>1</sup>Moscow Institute of Physics and Technology, Dolgoprudny, Russia

<sup>2</sup>St. Petersburg State University, St. Petersburg, Russia

<sup>3</sup>South Ural State University, Chelyabinsk, Russia

<sup>4</sup>Tajik National University, Dushanbe, Tajikistan

Corresponding author: Denis A. Vinnik, [vinnikda@susu.ru](mailto:vinnikda@susu.ru)

**ABSTRACT** The production of nano-sized semiconductor oxide materials, such as indium-gallium-zinc oxide (IGZO), will make it possible to use it for the transistors manufacture using printing methods. The sol-gel method is one of the widely known and used methods for producing nano-sized oxide materials. As is known, a chelating reagent (complexing agent) can influence both the synthesis process and the final phase composition. The results of sol-gel synthesis with various chelating reagents: citric acid, ethylene glycol, oxalic acid, urea, glycerol and sucrose are presented. The samples were studied by X-ray diffraction. It was found that ethylene glycol and glycerol as chelating reagents make it possible to obtain a homogeneous crystalline material at 900 °C with a YbFe<sub>2</sub>O<sub>4</sub>-type structure, R-3m (166) space group. Unit cell parameters and crystallite size (Halder-Wagner method) for InGaZnO<sub>4</sub> single-phase samples were calculated.

**KEYWORDS** indium-gallium-zinc oxide, In-Ga-Zn-O, IGZO, sol-gel method, complexing agent, chelating reagent, phase formation, nanomaterial

**ACKNOWLEDGEMENTS** This study represents an integration of two diverse projects supported by the Russian Science Foundation (No. 24-19-00468; conceptualization, comparative analysis of the chelating agents influence on the synthesis processes, as well as the synthesis and detailed characterization of samples IGZO-3, IGZO-4, IGZO-5, IGZO-6) and the Ministry of Science and Higher Education of the Russian Federation (Goszadaniye No. 075-03-2024-117, project No. FSMG-2024-0028; syntheses of IGZO-1 and IGZO-2 and its characterization).

**FOR CITATION** Zirnik G.M., Chernukha A.S., Uchaev D.A., Solizoda I.A., Gudkova S.A., Nekorysnova N.S., Vinnik D.A. Phase formation of nanosized InGaZnO<sub>4</sub> obtained by the sol-gel method with different chelating agents. *Nanosystems: Phys. Chem. Math.*, 2024, **15** (4), 520–529.

### 1. Introduction

Sol-gel technology makes it possible to obtain micro- and nanoparticles, including InGaZnO<sub>4</sub> material. Nanosized indium-gallium-zinc oxide (IGZO) production is extremely important, since it opens up the possibility of its use as an ink material for transistors printing [1–5].

Sol-gel technology is widely known. The most widely used technology, called the “Pechini method” or the “citrate gel” method, was patented by Maggio Pechini in 1967 [6]. Pechini proposed a method for titanates, zirconates, niobates of lead and alkaline earth metals obtaining. The method used a chelate reagent solution (citric acid in ethylene glycol) and the required oxide of metal, by evaporating the solvent, a transparent “gel” (the “resin” in original) was obtained, which was then heated to temperatures of 575 – 730 °C to obtain the final product. This synthesis method began to be successfully used to obtain other oxide materials later [7].

The literature contains a significant number of terms that essentially describe the same process, for example, “sol-gel method” [8], “sol-gel auto-combustion method” [9], “solution combustion synthesis” [10], “self-propagation combustion method” [11], “...mediated sol-gel combustion method” [12] (there is no common terminology). These terms often describe the same process in which desired metal nitrates react with organic complexing agents (which are also organic “fuels”) in an aqueous solution, after which a gel is formed. After this, the resulting material is slowly heated to the auto-combustion stage, during which nitrates act as the organic components oxidizers. The material obtained as an auto-combustion stage result described as a xerogel in the literature. The xerogel is ground and heated to remove the formed carbon to obtain the final material (with the required crystallinity).

When producing oxide materials by the sol-gel method, one chelating reagent is often used; two or more reagents are used less often. Also, the choice of a specific chelating reagent always remains unfounded. However, works that present

the study of several chelating reagents under the conditions of “sol-gel” synthesis have been found [13–15], but these studies are scarce and we have not found the preparation of IGZO with various chelating reagents in the sol-gel process in the literature.

The purpose of this work is to search for suitable complexing agents to obtain homogeneous  $\text{InGaZnO}_4$  samples at a minimum temperature (to obtain IGZO nanoparticles).

## 2. Methodology of experimental research

The synthesis of  $\text{InGaZnO}_4$  by sol-gel method was carried out according to the method below. Indium(III) nitrate 4.5-hydrate  $\text{In}(\text{NO}_3)_3 \cdot 4.5\text{H}_2\text{O}$ , gallium(III) nitrate nonahydrate  $\text{Ga}(\text{NO}_3)_3 \cdot 9\text{H}_2\text{O}$ , zinc(II) nitrate hexahydrate  $\text{Zn}(\text{NO}_3)_2 \cdot 6\text{H}_2\text{O}$ , citric acid, ethylene glycol, glycerol, urea, sucrose and oxalic acid was used for synthesis. All components were chemically pure. All metal nitrates used in the synthesis were preliminarily gravimetrically calcined at  $800^\circ\text{C}$  for 12 hours. A correction was introduced into the nitrate samples according to gravimetric data. Reagents were weighed on a Scientech SA 80 analytical balance with an accuracy of 0.1 mg. Stirring, heating, and evaporation of solutions were carried out on a magnetic stirrer with heating Stegler HS Pro-DT. Further heating of the samples was carried out in a Nabertherm L9/12/P330 muffle furnace with a programmable temperature controller.

The masses of metal nitrates were calculated to achieve a molar ratio of  $\text{In}^{3+}:\text{Ga}^{3+}:\text{Zn}^{2+} = 1:1:1$  in the product (the error in taking a sample of nitrates in all cases was no more than  $\pm 0.001$  g). The mass of salts was calculated to obtain 2.00 g of  $\text{InGaZnO}_4$ . The molar ratio of metal ions to complexing agent was chosen as  $\text{Me}^{x+}/\text{complexing agent} = 1:3$ . Weighed amounts of salts and complexing agent were separately dissolved in distilled water with stirring. After this, an aqueous solution of a complexing agent was added to the aqueous solution of nitrates and it was evaporated with intense stirring to a viscous gel. Next, the material was placed in a muffle furnace and subjected to heat treatment to remove residual water and initiate an auto-combustion reaction according to the following heating program: (i) heating up to  $100^\circ\text{C}$  for 1 hour and holding at this temperature for 2 hours; (ii) heating up to  $150^\circ\text{C}$  for 1 hour and holding at this temperature for 2 hours, (iii) heating up to  $200^\circ\text{C}$  for 1 hour and holding at this temperature for 2 hours, (iv) cooling the samples in air and grinding to the powder, (v) heating up to  $500^\circ\text{C}$  for 90 minutes and holding at this temperature for 6 hours, (vi) cooling samples in air, if necessary, taking part of the sample obtained at  $500^\circ\text{C}$  for 6 hours and sintering at  $700$ ,  $900$  or  $1000^\circ\text{C}$  for 12 hours, cooling the samples in air. Each of the syntheses was assigned a corresponding code: IGZO-1 for citric acid, IGZO-2 for ethylene glycol, IGZO-3 for oxalic acid, IGZO-4 for urea, IGZO-5 for glycerol and IGZO-6 for sucrose.

X-Ray diffraction (XRD) studies were carried out on a Rigaku Ultima IV powder X-ray diffractometer ( $\text{CuK}\alpha$ , 40 kV, 30 mA;  $\lambda = 0.15406$  nm, energy-dispersive semiconductor detector Rigaku D/teX Ultra) at a recording speed of  $5^\circ/\text{min}$ . Before studies, the samples were ground in an agate mortar to the fine powder. Qualitative analysis was carried out using the STOE Win XPow software package. Lattice parameters refinement and crystallite size determination was carried out in the Rigaku PDXL software package by WPPF (whole-powder-pattern fitting) method. To refine the unit cell parameters of IGZO single-phase samples, diffraction patterns were recorded at  $2^\circ/\text{min}$  speed. The crystal structure of  $\text{InGaZnO}_4$  was visualized using the VESTA software package [16]. Scanning electron microscopy (SEM) was carried out on a Jeol JSM 7001F scanning electron microscope (accelerating voltage = 20 kV, a conductive gold layer was deposited on the substrate by magnetron sputtering). Transmission electron microscopy (TEM) was carried out on a high-resolution transmission microscope JEOL JEM-2600 at a 160 kV accelerating voltage.

## 3. Results and discussion

Structurally,  $\text{InGaZnO}_4$  corresponds to the  $\text{YbFe}_2\text{O}_4$  compound of the rhombohedral system with R-3m (166) space group [17]. The prototype contains di- and trivalent iron, which is conveniently represented by the formula  $\text{Yb}^{3+}\text{Fe}^{3+}\text{Fe}^{2+}\text{O}_4$ . In  $\text{InGaZnO}_4$  structure, indium occupies ytterbium sites, gallium occupies  $\text{Fe}^{3+}$  sites, and zinc occupies  $\text{Fe}^{2+}$  sites [18]. In the structure of  $\text{InGaZnO}_4$ , layers can be distinguished. In a separate layer, indium atoms are located in a distorted  $\text{InO}_6$  octahedron, and zinc and gallium atoms are in a separate layer in the center of the  $\text{MO}_5$  trigonal bipyramid, where M is Zn or Ga (Fig. 1). Note that the distribution of gallium and zinc in one layer is not distinguishable by X-ray diffraction; for this reason, it is shown in Fig. 1 in the structural model, the positions of gallium and zinc were assumed to be equally probable. The diffraction pattern calculated for  $\text{InGaZnO}_4$  based on literature data [19] is in good agreement with experiment (Fig. 2).

Diffraction patterns of the obtained  $\text{InGaZnO}_4$  samples are presented in Figs. 3 – 8. It can be seen that in all cases, except for the IGZO-3 sample, the reflections of the main phase correspond to  $\text{InGaZnO}_4$  [17]. The obtained diffraction patterns were analyzed for the presence of possible impurity phases in the material, such as  $\text{In}_2\text{O}_3$  with a bixbyite structure [20],  $\text{Ga}_2\text{O}_3$  of various modifications, ZnO, as well as binary compounds ( $\text{In-Ga-O}$ ,  $\text{In-Zn-O}$ ,  $\text{Zn-Ga-O}$ , for example  $\text{ZnGa}_2\text{O}_4$  [21]) and ternary ( $\text{In-Ga-Zn-O}$ ) oxide systems.

The numbers in brackets correspond to the Miller indices of the corresponding plane on the Fig. 7. It should be noted that for most samples there is an overlap of the most intense reflections of  $\text{InGaZnO}_4$  and  $\text{In}_2\text{O}_3$ . Thus, for  $\text{InGaZnO}_4$  and  $\text{In}_2\text{O}_3$ , the main reflections have Miller indices of 009 and 104, located in the diffraction pattern at  $30.8$  and  $31.0^\circ 2\theta$ ,

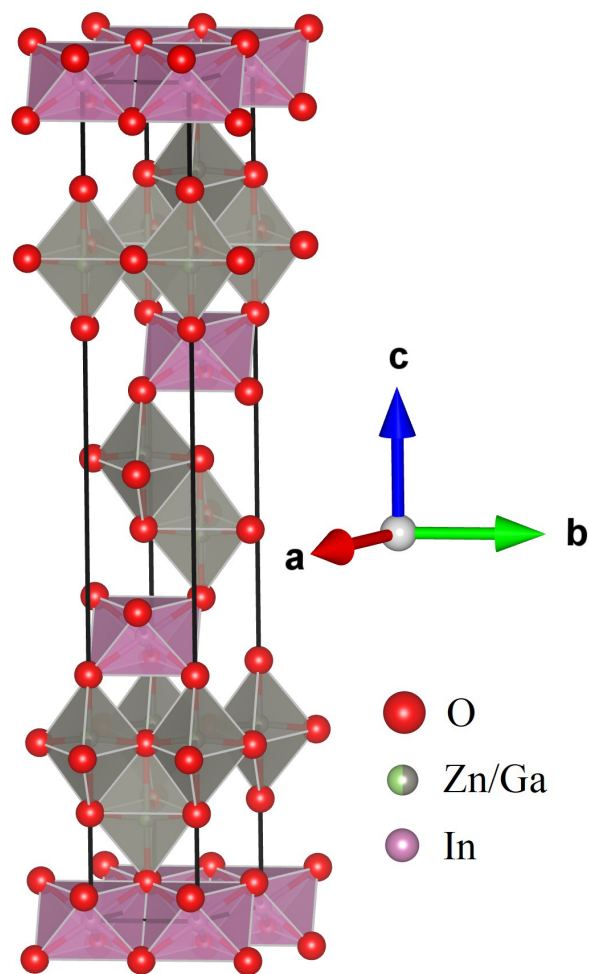


FIG. 1. Structural model of the unit cell of  $\text{InGaZnO}_4$  consisting of  $\text{InO}_6$  octahedra and  $\text{MO}_5$  trigonal bipyramids, where M is Zn or Ga

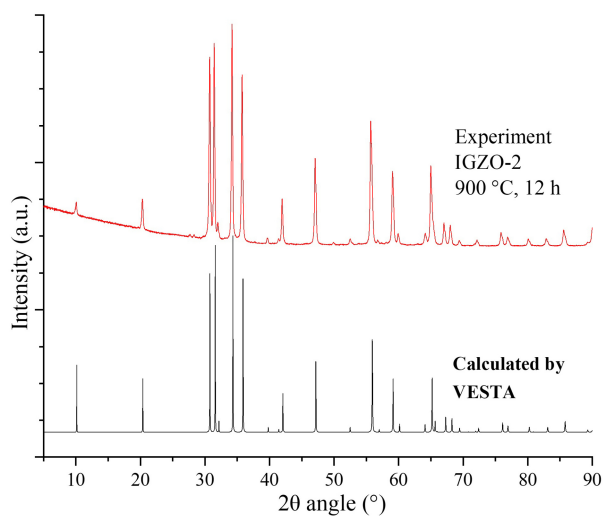


FIG. 2. Comparison of experimental and calculated diffraction patterns of  $\text{InGaZnO}_4$ . The calculation was performed in the VESTA software package based on data [19]

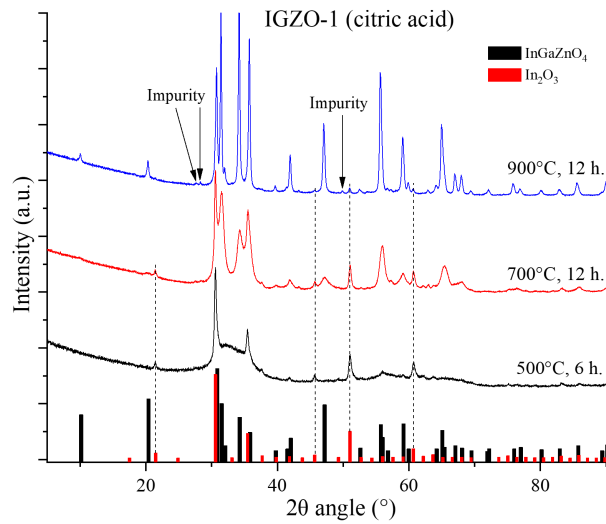


FIG. 3. XRD pattern of IGZO-1 prepared at 500, 700 and 900 °C. Black lines –  $\text{InGaZnO}_4$  [17], red line –  $\text{In}_2\text{O}_3$  [20]

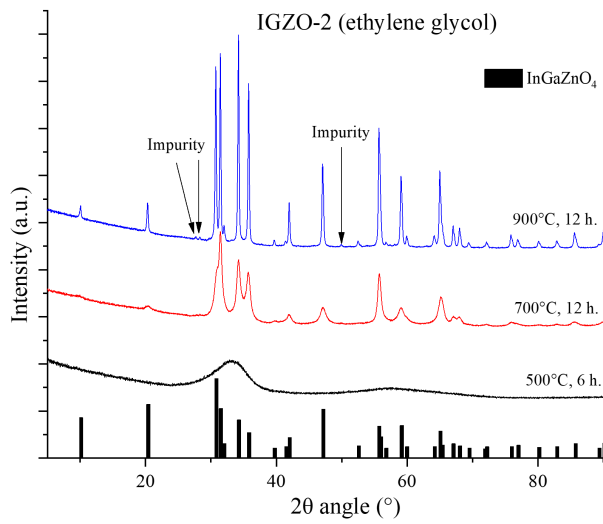


FIG. 4. XRD pattern of IGZO-2 prepared at 500, 700 and 900 °C. Black lines –  $\text{InGaZnO}_4$  [17]

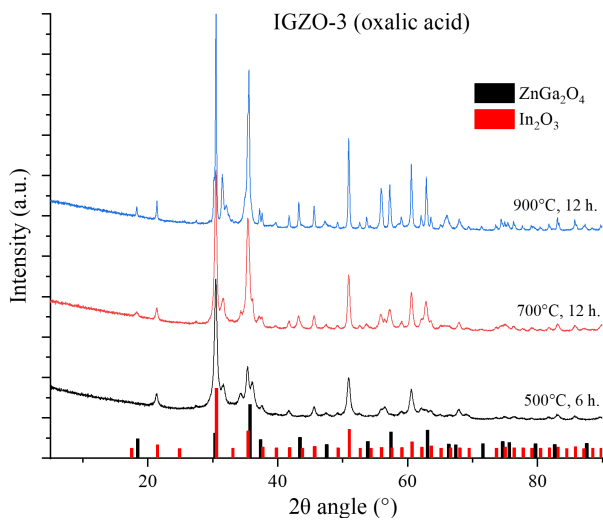


FIG. 5. XRD pattern of IGZO-3 prepared at 500, 700 and 900 °C. Black lines –  $\text{ZnGa}_2\text{O}_4$  [21], red lines –  $\text{In}_2\text{O}_3$  [20]

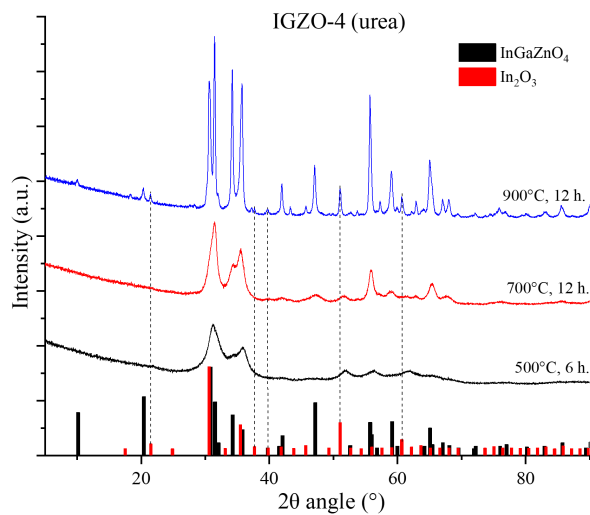


FIG. 6. XRD pattern of IGZO-4 prepared at 500, 700 and 900 °C. Black lines – InGaZnO<sub>4</sub> [17], red line – In<sub>2</sub>O<sub>3</sub> [20]

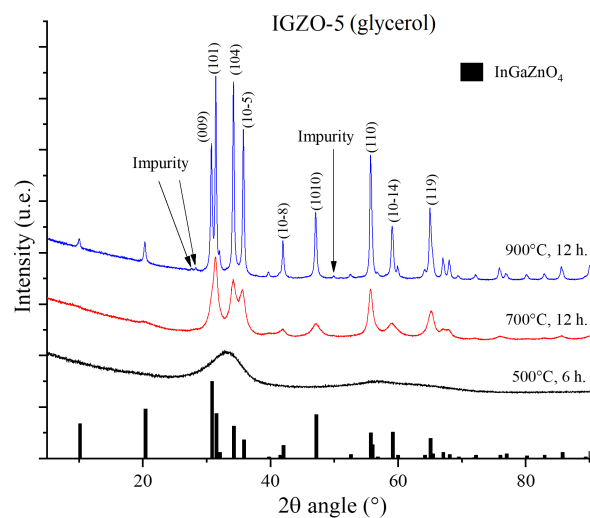


FIG. 7. XRD pattern of the IGZO-5 sample obtained at temperatures of 500, 700 and 900 °C. Black lines – InGaZnO<sub>4</sub> [17]

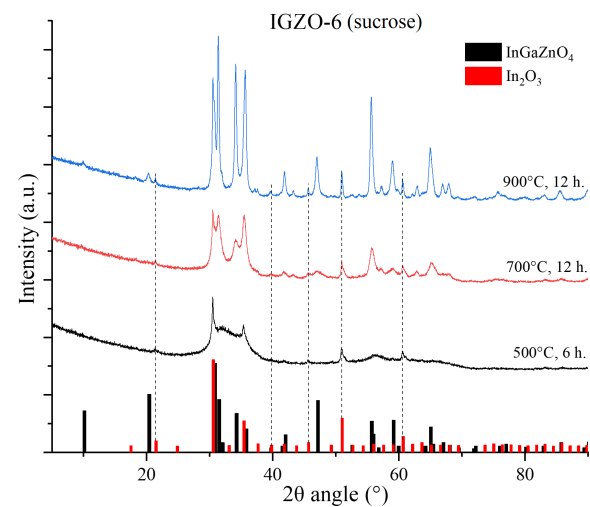


FIG. 8. XRD pattern of the IGZO-6, prepared at 500, 700 and 900 °C. Black lines – InGaZnO<sub>4</sub> [17], red lines – In<sub>2</sub>O<sub>3</sub> [20]

respectively. Therefore, to detect  $\text{In}_2\text{O}_3$  impurities in the composition of samples, use a less intense reflection, recorded at about  $51.0^\circ 2\theta$  and corresponding to reflection from the (440) plane.

First consider the XRD results of non-single-phase samples. XRD patterns of IGZO-4 and IGZO-6 follow that they are a mixture of  $\text{InGaZnO}_4$  and  $\text{In}_2\text{O}_3$ . Note that reflections corresponding to  $\text{In}_2\text{O}_3$  appear in the IGZO-4 sample obtained at  $500^\circ\text{C}$ , while the IGZO-6 sample at this temperature is still amorphous and does not contain crystalline phases. An increase in the sintering temperature causes an increase in the crystallinity of both the  $\text{InGaZnO}_4$  and  $\text{In}_2\text{O}_3$  phases. This can be seen from the decrease in the width of the reflections of these phases. In this case, the formation of a single-phase sample does not occur even at a temperature of  $900^\circ\text{C}$ .

IGZO-3 at  $500^\circ\text{C}$  is also non-single-phase sample. The main phases are solid solutions based on  $\text{In}_2\text{O}_3$  [20] and  $\text{ZnGa}_2\text{O}_4$  [21]. When the sintering temperature increases to  $900^\circ\text{C}$ , reflections corresponding to the  $\text{InGaZnO}_4$  phase appear, but its amount in the composition of this sample is minimal. Apparently, when using oxalic acid, individual metal oxalates are formed, for example:  $\text{Zn}(\text{C}_2\text{O}_4)$ ,  $\text{Ga}_2(\text{C}_2\text{O}_4)_3$  and  $\text{In}_2(\text{C}_2\text{O}_4)_3$ . Thus, when a solution of oxalic acid was introduced into a solution of metal nitrates, a white precipitate immediately formed, while other solutions remained transparent.

Samples IGZO-1, IGZO-2 and IGZO-5 are closest to the single-phase state. IGZO-1 sample obtained at  $500^\circ\text{C}$  is a mixture of an amorphous material with crystalline indium oxide  $\text{In}_2\text{O}_3$  (Fig. 3). However, as the temperature increases, the intensity of the  $\text{In}_2\text{O}_3$  reflections decreases and for the sample obtained at  $900^\circ\text{C}$ , their intensity becomes extremely low.

The IGZO-2 sample obtained with ethylene glycol at  $500^\circ\text{C}$  is amorphous; at  $700^\circ\text{C}$  – slightly crystallized. At these temperatures, no foreign phases were detected, however, the sample obtained at  $900^\circ\text{C}$  contains foreign reflections at  $27.7$ ,  $28.3$  and  $49.9^\circ 2\theta$ , which could not be identified (Fig. 4). The same reflections appear in the diffraction patterns of IGZO-1 and IGZO-5 obtained at  $900^\circ\text{C}$ .

In order to achieve homogenization at higher temperatures, samples IGZO-1, IGZO-2 and IGZO-5 were additionally kept at a temperature of  $1000^\circ\text{C}$  for 12 hours. The XRD pattern of samples are presented in Figs. 9 – 11.

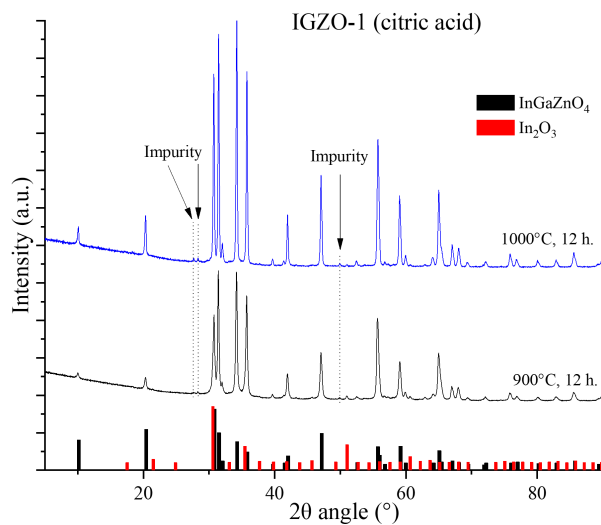
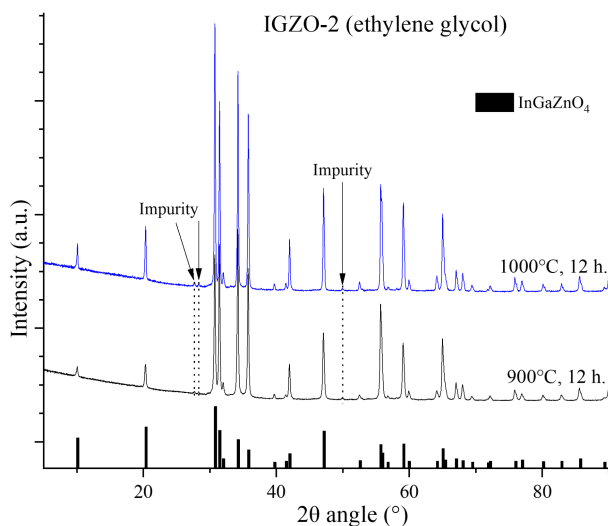
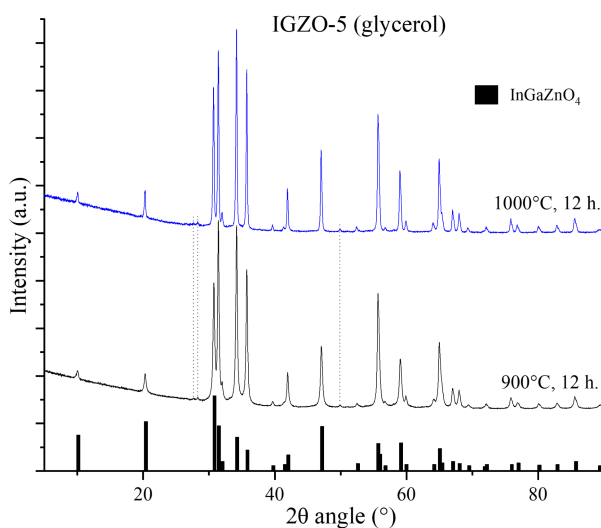


FIG. 9. XRD pattern of IGZO-1 prepared at  $1000^\circ\text{C}$ . Black lines –  $\text{InGaZnO}_4$  [17], red line –  $\text{In}_2\text{O}_3$  [20]

As can be seen from the obtained XRD pattern (Figs. 9 – 11), for all samples, with increasing processing temperature, their crystallinity increases. Thus, the half-width of the reflection of the main phase of the IGZO-2 sample, located at about  $34.2^\circ 2\theta$ , decreases when heated from 700 to 900 and  $1000^\circ\text{C}$ , respectively, from 0.63 to 0.21 and further to  $0.17^\circ 2\theta$ . For IGZO-1 and IGZO-5 samples, the decrease in the half-width of the reflection around  $34.2^\circ 2\theta$  occurs in a similar way. Calcination at higher temperatures is not advisable, since this will cause growth and sintering of particles [22, 23], which will negatively affect the possibility of using this oxide material for the further production of nanopowders.

For IGZO-2 and IGZO-5 samples obtained at 700 and  $900^\circ\text{C}$  and containing the least amount of impurities, the cell parameters and crystallite size were calculated (Tables 1 and 2). For the  $\text{InGaZnO}_4$  material obtained at  $1450^\circ\text{C}$  for 24 hours [17], the cell parameters are slightly smaller ( $a = 3.295 \text{ \AA}$ ,  $c = 26.07 \text{ \AA}$ ) than at 700 and  $900^\circ\text{C}$ , but in general they coincide well with them. The crystallite size was calculated using the Halder-Wagner method [24] using the six most intense reflections (Fig. 12).

Figure 13 shows SEM and TEM micrographs of the IGZO-5 sample obtained at  $500^\circ\text{C}$  for 6 hours. Both photographs clearly show that the material is an agglomerate of nanoparticles. SEM microphotography suggests that the size of most particles present in the cluster is less than 100 nm, but their exact size is difficult to determine. As can be seen from the TEM micrograph, the material actually consists of a large accumulation of particles, most of which have a size of about

FIG. 10. XRD pattern of IGZO-2 prepared at 1000 °C. Black lines – InGaZnO<sub>4</sub> [17]FIG. 11. XRD pattern of IGZO-5 prepared at 1000 °C. Black lines – InGaZnO<sub>4</sub> [17]TABLE 1. Unit cell parameters of homogeneous InGaZnO<sub>4</sub> samples

No.	Sample	Unit cell parameters					
		<i>a</i> , Å	<i>c</i> , Å	<i>a</i> , Å	<i>c</i> , Å	<i>a</i> , Å	<i>c</i> , Å
Sintering temperature		700 °C		900 °C		1000 °C	
1	IGZO-1	3.300(3)	26.17(3)	3.298(2)	26.11(2)	3.295(2)	26.13(2)
2	IGZO-2	3.307(3)	26.15(3)	3.296(2)	26.11(2)	3.295(2)	26.11(2)
3	IGZO-5	3.317(5)	26.11(4)	3.297(3)	26.11(2)	3.297(2)	26.14 (2)

TABLE 2. Crystallite sizes of homogeneous InGaZnO<sub>4</sub> samples

No.	Sintering temperature	700 °C	900 °C	1000 °C	
1	Crystallite size (Å)	IGZO-1	68 ± 9	221 ± 30	466 ± 59
2		IGZO-2	50 ± 8	439 ± 68	579 ± 124
3		IGZO-5	54 ± 6	242 ± 32	406 ± 56

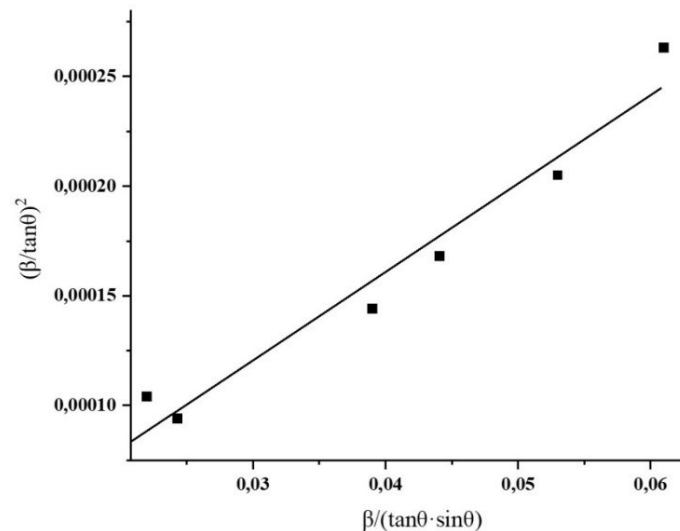


FIG. 12. Illustration for calculating crystallite size using the Halder–Wagner method for IGZO-5 obtained at 1000 °C

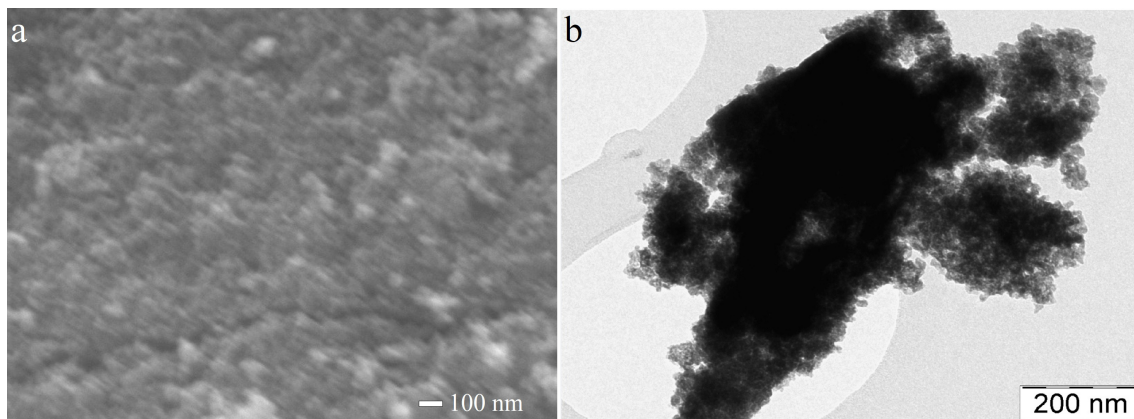


FIG. 13. SEM- (a) and TEM-image (b) of IGZO-5 prepared at 500 °C for 6 hours

20 – 30 nm, but there are areas where the particle size is much smaller. At the same time, it is worth saying that the material does not have a specific morphology. It was shown that indium gallium zinc oxide nanoparticles were obtained.

#### 4. Conclusions

It has been shown that the use of various complexing agents in the sol-gel method affects the phase composition of the product in the In–Ga–Zn–O system. The best complexing agents for producing  $\text{InGaZnO}_4$  by the sol-gel method are ethylene glycol and glycerol. The samples obtained using ethylene glycol and glycerol have an amorphous structure at 500 °C and a high degree of crystallinity at 700 – 900 °C. The use of citric acid as a complexing agent is relatively successful, but temperatures above 1000 °C are required to completely homogenize the sample. This casts doubt on the use of this complexing agent for the production of  $\text{InGaZnO}_4$  ternary oxide nanoparticles. The use of urea and sucrose results in indium gallium zinc oxide contaminated with indium oxide phase. The use of oxalic acid results in the formation of a three-phase product. The samples have a crystallite size in the nano-region at temperatures of 500 – 700 °C, that was confirmed and demonstrated for IGZO-5 (500 °C, 6 h) sample by SEM and TEM method.

## References

- [1] Kim G.H., Kim H.S., Shin H.S., Ahn B.D., Kim K.H., Kim H.J. Inkjet-printed InGaZnO thin film transistor. *Thin Solid Films*, 2009, **517** (14), P. 4007–4010.
- [2] Wang Y., Sun X.W., Goh G.K.L., Demir H.V., Yu H.Y. Influence of Channel Layer Thickness on the Electrical Performances of Inkjet-Printed In-Ga-Zn Oxide Thin-Film Transistors. *IEEE Trans. Electron Devices*, 2011, **58** (2), P. 480–485.
- [3] Lee Y.G., Choi W.-S. Electrohydrodynamic Jet-Printed Zinc-Tin Oxide TFTs and Their Bias Stability. *ACS Appl. Mater. Interfaces*, 2014, **6** (14), P. 11167–11172.
- [4] Jeong S., Lee J.-Y., Lee S.S., Oh S.-W., Lee H.H., Seo Y.-H., Ryu B.-H., Choi Y. Chemically improved high performance printed indium gallium zinc oxide thin-film transistors. *J. Mater. Chem.*, 2011, **21** (43), P. 17066–17070.
- [5] Fukuda N., Watanabe Y., Uemura S., Yoshida Y., Nakamura T., Ushijima H. In-Ga-Zn oxide nanoparticles acting as an oxide semiconductor material synthesized via a coprecipitation-based method. *J. Mater. Chem. C*, 2014, **2** (13), P. 2448–2454.
- [6] Pechini M.P. Method of Preparing Lead and Alkaline Earth Titanates and Niobates and Coating Method Using the Same to Form a Capacitor. US Patent 3330697, 1967.
- [7] Chernukha A.S., Zvereva A.A., Zirnik G.M., Pashnin D.R., Mustafina K.E., Belyaev I.E., Dyukova O.V., Artyukova M.V., Malev E.V., Zhivulin V.E., Mosunova T.V., Vinnik D.A. Synthesis of Barium Hexaferrite by the Self-combustion Method. *Bull. South Ural State Univ. Ser. "Chemistry"*, 2021, **13** (3), P. 40–48.
- [8] Kumar R., Kumar H., Singh R.R., Barman P.B. Variation in magnetic and structural properties of Co-doped Ni-Zn ferrite nanoparticles: a different aspect. *J. Sol-Gel Sci. Technol.*, 2016, **78** (3), P. 566–575.
- [9] Bhagwat V.R., Humbe A.V., More S.D., Jadhav K.M. Sol-gel auto combustion synthesis and characterizations of cobalt ferrite nanoparticles: Different fuels approach. *Mater. Sci. Eng. B*, 2019, **248**, 114388.
- [10] Khort A., Hedberg J., Mei N., Romanovski V., Blomberg E., Odnevall I. Corrosion and transformation of solution combustion synthesized Co, Ni and CoNi nanoparticles in synthetic freshwater with and without natural organic matter. *Sci. Rep.*, 2021, **11** (1), 7860.
- [11] Oladoja N.A., Anthony E.T., Olojede I.A., Saliu T.D., Bello G.A. Self-propagation combustion method for the synthesis of solar active Nano Ferrite for Cr(VI) reduction in aqua system. *J. Photochem. Photobiol. A Chem.*, 2018, **353**, P. 229–239.
- [12] Yadav R.S., Kuřitka I., Vilcakova J., Machovsky M., Skoda D., Urbánek P., Masař M., Jurča M., Urbánek M., Kalina L., Havlica J. NiFe<sub>2</sub>O<sub>4</sub> Nanoparticles Synthesized by Dextrin from Corn-Mediated Sol-Gel Combustion Method and Its Polypropylene Nanocomposites Engineered with Reduced Graphene Oxide for the Reduction of Electromagnetic Pollution. *ACS Omega*, 2019, **4** (26), P. 22069–22081.
- [13] Wahba M.A., Yakout S.M., Youssef A.M., Sharmoukh W., Elsayed A.M., Khalil M.Sh. Chelating Agents Assisted Rapid Synthesis of High Purity BiFeO<sub>3</sub>: Remarkable Optical, Electrical, and Magnetic Characteristics. *J. Supercond. Nov. Magn.*, 2022, **35** (12), P. 3689–3704.
- [14] Katelnikovas A., Barkauskas J., Ivanauskas F., Beganskiene A., Kareiva A. Aqueous sol-gel synthesis route for the preparation of YAG: Evaluation of sol-gel process by mathematical regression model. *J. Sol-Gel Sci. Technol.*, 2007, **41**, P. 193–201.
- [15] Yu L., Sun A. Influence of different complexing agents on structural, morphological, and magnetic properties of Mg-Co ferrites synthesized by sol-gel auto-combustion method. *J. Mater. Sci. Mater. Electron.*, 2021, **32** (8), P. 10549–10563.
- [16] Momma K., Izumi F. VESTA 3 for three-dimensional visualization of crystal, volumetric and morphology data. *J. Appl. Crystallogr.*, 2011, **44** (6), P. 1272–1276.
- [17] Kimizuka N., Mohri T. Spinel, YbFe<sub>2</sub>O<sub>4</sub>, and Yb<sub>2</sub>Fe<sub>3</sub>O<sub>7</sub> types of structures for compounds in the In<sub>2</sub>O<sub>3</sub> and Sc<sub>2</sub>O<sub>3</sub>–A<sub>2</sub>O<sub>3</sub>–BO systems [A: Fe, Ga, or Al; B: Mg, Mn, Fe, Ni, Cu, or Zn] at temperatures over 1000 °C. *J. Solid State Chem.*, 1985, **60** (3), P. 382–384.
- [18] Nespolo M., Sato A., Osawa T., Ohashi H. Synthesis, crystal structure and charge distribution of InGaZnO<sub>4</sub>. X-ray diffraction study of 20 kb single crystal and 50 kb twin by reticular merohedry. *Cryst. Res. Technol.* 2000, **35**(2), P. 151–165.
- [19] Xu C., Jiang P., Cong R., Yang T. Structure investigation of InGaZn<sub>1-x</sub>Cu<sub>x</sub>O<sub>4</sub> (x = 0–1) and magnetic property of InGaCuO<sub>4</sub>. *J. Solid State Chem.*, 2019, **274**, P. 303–307.
- [20] Mohamed S.H. Transparent conductive gallium-doped indium oxide nanowires for optoelectronic applications. *J. Korean Phys. Soc.*, 2013, **62** (6), P. 902–905.
- [21] Yang J., Sun X., Yang W., Zhu M., Shi J. The Improvement of Coralline-Like ZnGa<sub>2</sub>O<sub>4</sub> by Cocatalysts for the Photocatalytic Degradation of Rhodamine B. *Catalysts*, 2020, **10** (2), 221.
- [22] Zhivulin V.E., Trofimov E.A., Zaitseva O.V., Sherstyuk D.P., Cherkasova N.A., Taskaev S.V., Vinnik D.A., Alekhina Y.A., Perov N.S., Naidu K.C.B., Elsaedy H.I., Khandaker M.U., Tishkevich D.I., Zubar T.I., Trukhanov A.V., Trukhanov S.V. Preparation, phase stability, and magnetization behavior of high entropy hexaferrites. *iScience*, 2023, **26** (7), 107077.
- [23] Vinnik D.A., Sherstyuk D.P., Zhivulin V.E., Zhivulin D.E., Starikov A.Yu., Gudkova S.A., Zherebtsov D.A., Pankratov D.A., Alekhina Yu.A., Perov N.S., Trukhanov S.V., Trukhanova E.L., Trukhanov A.V. Impact of the Zn–Co content on structural and magnetic characteristics of the Ni spinel ferrites. *Ceram. Int.*, 2022, **48** (13), P. 18124–18133.
- [24] Nath D., Singh F., Das R. X-ray diffraction analysis by Williamson-Hall, Halder-Wagner and size-strain plot methods of CdSe nanoparticles – a comparative study. *Mater. Chem. Phys.*, 2020, **239**, 122021.

---

Submitted 7 June 2024; accepted 8 August 2024

### Information about the authors:

**Gleb M. Zirnik** – Moscow Institute of Physics and Technology, Laboratory of Semiconductor Oxide Materials, Institutsky lane, 9, Dolgoprudny, 141701, Russia; St. Petersburg State University, Institute of Chemistry, Universitetskaya emb., 7–9, 199034, St. Petersburg, Russia; ORCID 0009-0008-4546-1368; glebanaz@mail.ru

**Alexander S. Chernukha** – Moscow Institute of Physics and Technology, Laboratory of Semiconductor Oxide Materials, Institutsky lane, 9, Dolgoprudny, 141701, Russia; St. Petersburg State University, Institute of Chemistry, Universitetskaya emb., 7–9, 199034, St. Petersburg, Russia; ORCID 0000-0002-7117-7132; chernukha.as@mipt.ru;

**Daniil A. Uchaev** – South Ural State University, Scientific and Educational Center “Nanotechnologies”, Lenin Av., 76, Chelyabinsk, 454080, Russia; ORCID 0000-0002-8623-4769; uchaevda@susu.ac.ru

*Ibrohimi A. Solizoda* – Moscow Institute of Physics and Technology, Laboratory of Semiconductor Oxide Materials, Institutsky lane, 9, Dolgoprudny, 141701, Russia; St. Petersburg State University, Institute of Chemistry, Universitetskaya emb., 7–9, 199034, St. Petersburg, Russia; Tajik National University, Rudaki Av., 17, Dushanbe, 734025, Tajikistan; ORCID 0000-0001-6973-4633 ; solizoda.ia@mipt.ru

*Svetlana A. Gudkova* – Moscow Institute of Physics and Technology, Laboratory of Semiconductor Oxide Materials, Institutsky lane, 9, Dolgoprudny, 141701, Russia; St. Petersburg State University, Institute of Chemistry, Universitetskaya emb., 7–9, 199034, St. Petersburg, Russia, ORCID 0000-0002-3028-947X; svetlanagudkova@yandex.ru

*Nadezhda S. Nekorysnova* – South Ural State University, Scientific and Educational Center “Nanotechnologies”, Lenin Av., 76, Chelyabinsk, 454080, Russia; ORCID 0009-0002-1921-7915; nadin5004@mail.ru

*Denis A. Vinnik* – Moscow Institute of Physics and Technology, Laboratory of Semiconductor Oxide Materials, Institutsky lane, 9, Dolgoprudny, 141701, Russia; St. Petersburg State University, Institute of Chemistry, Universitetskaya emb., 7–9, 199034, St. Petersburg, Russia; South Ural State University, Scientific and Educational Center “Nanotechnologies”, Lenin Av., 76, Chelyabinsk, 454080, Russia; ORCID 0000-0002-5190-9834; vinnik.da@mipt.ru

*Conflict of interest:* the authors declare no conflict of interest.

## Formation of ultra- and nanodispersed “core-shell” structures $Ti_{0.8}Mo_{0.2}C_{0.5}N_{0.5}$ –Ni–Mo in the process of plasma-chemical synthesis of a mechanical mixture of titanium carbonitride with metallic nickel and molybdenum

Yuliya A. Avdeeva, Irina V. Luzhkova, Aidar M. Murzakaev, Alexey N. Ermakov

<sup>1</sup>Institute of Solid State Chemistry, Ural Branch, Russian Academy of Sciences, Ekaterinburg, Russia

<sup>2</sup>Institute of Electrophysics, Ural Branch, Russian Academy of Sciences, Ekaterinburg, Russia

<sup>a</sup>y-avdeeva@list.ru, <sup>b</sup>key703@yandex.ru, <sup>c</sup>aidar@iep.uran.ru, <sup>d</sup>ermakovihim@yandex.ru

Corresponding author: Yuliya A. Avdeeva, y-avdeeva@list.ru

PACS 61.46.+w, 61.46.-w, 61.66.Fn

**ABSTRACT** Ultradisperse and nanocrystalline powder compositions were obtained in the process of plasma-chemical synthesis of a mechanical mixture of titanium carbonitride  $TiC_{0.5}N_{0.5}$  with metallic nickel and molybdenum in a low-temperature nitrogen plasma (4000 – 6000 °C), taking into account recondensation in a turbulent flow of nitrogen gas. It was established by X-ray diffraction that their phase composition is characterized by the presence of cubic compounds in the form of titanium-molybdenum carbonitride  $Ti_{0.8}Mo_{0.2}C_{0.5}N_{0.5}$ , metallic Ni and Mo. High-resolution transmission electron microscopy was used to visualize a “core-shell” structure in the nanocrystalline fraction, which includes such phases as  $Ti_{1-n}Mo_nC_xN_y$ , Ni, NiO,  $TiO_2$ ,  $MoC_{0.5}N_{0.5}$ .

The experimental data on measurements of the specific surface area by the BET method and the pycnometric density made it possible to determine the calculated values of the average particle sizes which were 365 and 56 nm for the fractions from the cyclone and the filter, respectively. The average particle size of the nanocrystalline component of the fraction from the cyclone, according to the results of direct measurements, was 22 nm. Based on the obtained experimental results, a model for the formation of  $Ti_{0.8}Mo_{0.2}C_{0.5}N_{0.5}$ –Ni–Mo “core-shell” structures has been developed, which is implemented under the conditions of a turbulent flow of nitrogen gas formed in a quenching chamber of a plasma chemical plant.

**KEYWORDS** Titanium carbonitride, nickel, molybdenum, plasma-chemical synthesis, X-ray phase analysis, high-resolution transmission electron microscopy.

**ACKNOWLEDGEMENTS** The work was carried out in accordance with the state assignment for the Institute of Solid State Chemistry of the Ural Branch of the Russian Academy of Sciences (theme No. 124020600024-5).

**FOR CITATION** Avdeeva Yu.A., Luzhkova I.V., Murzakaev A.M., Ermakov A.N. Formation of ultra- and nanodispersed “core-shell” structures  $Ti_{0.8}Mo_{0.2}C_{0.5}N_{0.5}$ –Ni–Mo in the process of plasma-chemical synthesis of a mechanical mixture of titanium carbonitride with metallic nickel and molybdenum. *Nanosystems: Phys. Chem. Math.*, 2024, **15** (4), 530–539.

### 1. Introduction

The nanocrystalline state of substances is of considerable interest for both scientific experiments [1, 2] and practical application in various branches of technology [3–5].

It is known that single-phase nanocrystalline powders were initially obtained using various synthesis methods [6]. Such products required exceptional storage conditions due to their high chemical activity and, accordingly, pyrophoricity. In this context, methods for the passivation of highly dispersed materials providing long-term storage of especially nanocrystalline powder media under normal conditions were actively developed. Technologies of forced acidification, storage under a layer of liquid reagent, encapsulation of highly dispersed products with organic aerosols [7], etc. were used as passivation techniques.

At the same time, along with the development and improvement of methods for producing ultra- and nanodisperse materials, their separation and separation according to dispersed composition, density and specific surface area, experiments were performed to reduce the content of contaminants in highly dispersed systems. Such impurities, as a rule, were the materials of individual units of the installations in which synthesis was carried out (reactor walls, quenching chambers, cathodes, etc.) [8].

A more significant issue in the method of obtaining ultra- and nanodisperse materials is the formation of multiphase compositions, in which various phase components may be presented simultaneously, including those that cannot coexist within the same system or cannot be obtained using traditional ceramic technologies by solid-phase and liquid-phase synthesis. For the formation of multicomponent ultradisperse or nanocrystalline powder compositions, quite suitable are

certain methods for obtaining highly dispersed media aimed at atomic decomposition of the initial synthesis components under extreme exposure conditions. Such synthesis methods include gas-phase synthesis, plasma-chemical synthesis in low-temperature plasma, electric explosion of a conductor in a controlled gas atmosphere, and laser evaporation of a target [9].

The issues of the formation of microcrystalline solid solutions, complexly substituted in the metal sublattice, based on refractory titanium carbide-nitride compounds have been extensively studied and continue to be studied by scientists in many countries [10]. In particular, the introduction of IV – VIA metal elements into the metal sublattice promotes the formation of metal-ceramic compositions, provided that metal binders with participation of solid solutions of the  $Ti_{1-n}Me_nC_xN_y$  type are introduced as binding phases [11]. For example, the introduction of metallic molybdenum into the  $TiC_xN_y$  – Ni system during liquid-phase sintering results in the formation of a metal-ceramic alloy, the refractory grains of which have a “core-shell” structure where titanium carbonitride  $TiC_xN_y$  acts as the core and  $Ti_{1-n}Mo_nC_xN_y$  acts as the shell [12]. The intergranular spaces are filled with a Ni-Mo binder. The presence of titanium-molybdenum carbonitride  $Ti_{1-n}Mo_nC_xN_y$  in the form of a shell allows using such metal-ceramic compositions as tool materials developed by a team of authors under the leadership of Academician G. P. Shveikin at the Institute of Chemistry of the USC of the USSR Academy of Sciences [13]. The resulting alloy has satisfactory physical and mechanical characteristics and is suitable for finishing steel during machining. Metal-ceramic compositions based on titanium carbonitride with nickel, alloyed with metallic vanadium [14] and zirconium [15], have similar properties.

The purpose of this study was to obtain an ultra- and nanodispersed charge powder – tungsten-free hard alloy, having a “core-shell” structure, where the refractory core is titanium-molybdenum carbonitride  $Ti_{1-n}Mo_nC_xN_y$ , coated with metal layers of Mo and Ni.

## 2. Methods

Plasma-chemical synthesis in a low-temperature (4000 – 6000 °C) nitrogen plasma was chosen as the main method for the synthesis of highly dispersed materials [16]. The main technological characteristic of the plasma-chemical installation is its power, 25 kW ( $I = 90$  A,  $U = 220$  V). The productivity of the installation is 200 g/h. Process gas consumption: vortex chamber – 20 m<sup>3</sup>/h for hardening unit – 20 m<sup>3</sup>/h, 6 m<sup>3</sup>/h – for transportation of processed powders and separation in classifier 1 – vortex-type cyclone and classifier 2 – bag-type filter.

The composition of the mechanical mixture for plasma-chemical synthesis included 74.0 wt. %  $TiC_{0.5}N_{0.5}$ , 19.5 wt. % Ni, 6.5 wt. % Mo.

All the processed highly dispersed powders were subjected to encapsulation to reduce the chemical activity and, accordingly, pyrophoricity, which allows their long-term storage and safe use.

The resulting ultra- and nanodispersed powders based on titanium-molybdenum carbonitride  $Ti_{1-n}Mo_nC_xN_y$ , coated with layers of metallic Mo and Ni, were studied by X-ray diffraction methods (automatic X-ray diffractometer SHIMADZU XRD-7000,  $CuK_{\alpha}$  radiation,  $2\theta = 5 - 100^\circ$ , shooting step 0.030) and high-resolution transmission electron microscopy (JEOL JEM 2100 LaB<sub>6</sub> cathode). The research results were processed using the ICDD and ICSD database files and WinXPOW and PowderCell 2.3 software. The results of electron microscopy studies were processed in the Digital Micrograph 7.0 software. The density of all the obtained ultra- and nanodispersed compositions was determined using a pycnometer (AccuPyc II 1340 V1.09).

Additionally, in accordance with BET methods, the specific surface area of all the obtained fractions was determined (specific surface area analyzer Gemini VII 2390 V1.03). Taken together, using formula (1) [17], based on density and specific surface data, estimated values of the average particle sizes were calculated, provided that their shape is spherical.

$$d_{av} = \frac{6}{S_{sp}\rho}, \quad (1)$$

where  $d_{av}$  is the average particle diameter,  $S_{sp}$  is the specific surface area,  $\rho$  is the density.

## 3. Results and discussion

Metal ceramics based on titanium carbonitrides  $TiC_xN_y$  with various metal binders [18–20], sintered from microcrystalline powder compositions according to mechanisms [21], have satisfactory mechanical characteristics. In this case, the use of plasma-chemical ultra- and nanodisperse powders, where all the phase components of tungsten-free hard alloys charge regulated by [22] are present within one particle with a “core-shell” structure, will improve the strength-plastic characteristics of instrumental metal ceramics.

Since the processes of evaporation and especially recondensation occurring in low-temperature nitrogen plasma in accordance with [23] can be characterized as “quasi-equilibrium”, the physicochemical features of crystallization can be described under equilibrium thermodynamics conditions. In this work, it is proposed to introduce a metal, which is Mo, in the process of plasma-chemical synthesis in a low-temperature nitrogen plasma of a mechanical mixture  $TiC_{0.5}N_{0.5}$ -Mo-Ni, composed according to the formulation [22]. It is assumed that the introduction of molybdenum into the metallic sublattice of titanium occurs at the cooling stage in the quenching chamber at a rate of  $10^5$  °C/s, which can be expressed

by a decrease in the unit cell parameter of the  $TiC_xN_y$  carbonitride phase. It is also assumed that during the crystallization process, metallic Mo and Ni present in the initial charge are deposited in the form of individual layers.

The data of X-ray studies (Fig. 1) of the ultrafine fraction from classifier 1 – vortex-type cyclone (Table 1 No. 1) and the nanocrystalline fraction from classifier 2 – bag-type filter (Table 1 No. 2) show that both compositions have in their composition the phases of cubic (NaCl type) titanium carbonitride  $TiC_xN_y$  (sp. gr. Fm-3m), whose unit cell parameters differ significantly from the composition  $TiC_{0.5}N_{0.5}$ , as well as cubic Mo (sp. gr. Im-3m) and cubic Ni (sp. gr. Fm-3m). The nanocrystalline fraction from the bag-type filter, in addition to the above phases, contains nickel oxide NiO (sp. gr. Fm-3m). Besides, it should be noted that both fractions contain tetragonal titanium oxide  $TiO_2$  (sp. gr.  $P4_2/mnm$ ) in the form of stable rutile modification. The appearance of oxide phases in oxygen-free highly dispersed systems is due to forced acidification of recondensed powders in separation units (vortex-type cyclone and fabric filter) to reduce their pyrophoricity.

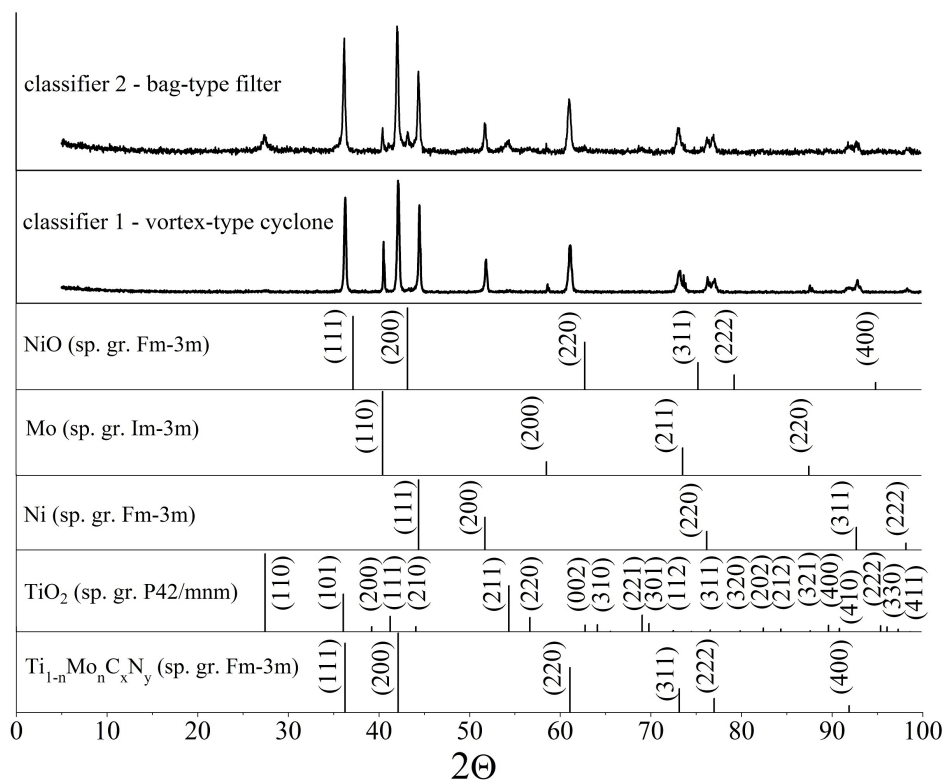


FIG. 1. Results of X-ray phase analysis of highly dispersed powders with a “core-shell” structure of the tungsten-free hard alloy charge based on titanium-molybdenum carbonitride  $Ti_{1-n}Mo_nC_xN_y$  with the participation of Ni and Mo formed during plasma-chemical synthesis in a low-temperature nitrogen plasma

Electron microscopic studies (HRTEM) of the nanocrystalline component of a sample of the processed mechanical mixture  $TiC_{0.5}N_{0.5} - Mo - Ni$  from classifier 2 – bag-type filter confirm the presence of a “core-shell” structure based on refractory cores of titanium-molybdenum carbonitride  $Ti_{1-n}Mo_nC_xN_y$ , coated with metal layers of cubic molybdenum and nickel (Fig. 2a).

Figure 2b illustrates the total particle size distribution histogram obtained on the basis of direct measurements in MEASURER software (developed at the Institute of Solid State Chemistry, Ural Branch, Russian Academy of Sciences), which shows that the average particle size is  $22.0 \pm 0.5$  nm.

A detailed study of nanocrystalline particle is presented in Fig. 3. In particular, in section 1 (Fig. 3b) of the image, interplanar distances of 0.29 nm and 0.26 nm were determined based on the results of the fast Fourier transform, which belong to the (001) and (100) reflections of molybdenum carbonitride  $TiC_{0.5}N_{0.5}$  of the hexagonal modification (sp. gr. R-6m2). In section 2 (Fig. 3c), the presence of a cubic NiO phase (sp. gr. Fm-3m) was detected, the unit cell parameter of which corresponded to 0.42 nm.

The presence of localized detected phases can be explained by the fact that in the process of plasma-chemical synthesis, along with the formation of titanium carbonitrides doped with molybdenum, the molybdenum carbonitride  $MoC_{0.5}N_{0.5}$  is formed simultaneously, in good agreement with data [24]. The presence of NiO can be regulated by acidification of the surface of the nanopowder composition as a result of the slow flow of air into the chamber where the bag-type filter is located.

TABLE 1. Phase composition, density and average particle size (estimated by calculation) of ultrafine and nanocrystalline powders of  $Ti_{1-n}Mo_nC_xN_y - Ni - Mo$  after plasma-chemical synthesis in a low-temperature nitrogen plasma

No.	Fraction	Phase composition ( $\pm 2$ wt%), $a, b, c$ ( $\pm 0.0001$ Å)	$S_{sp}, m^2/g$	$\rho, g/cm^3$	$d_{av}, \mu m$
1	cyclone	Mo (Im-3m), (4 %), $a = 3.1482$ ; Ni (Fm-3m), (19 %), $a = 3.5276$ ; $Ti_{1-n}Mo_nC_xN_y$ (Fm-3m), (76. %), $a = 4.2883$ ; $TiO_2$ (P4 <sub>2</sub> /mnm) (1 %), $a = 4.5838, c = 2.9551$ ;	2.9	5.660	0.365
2	filter	Mo (Im-3m), (1 %), $a = 3.1474$ ; Ni (Fm-3m), (14 %), $a = 3.5272$ ; $Ti_{1-n}Mo_nC_xN_y$ (Fm-3m), (64 %), $a = 4.2873$ ; $TiO_2$ (P4 <sub>2</sub> /mnm)(15 %), $a = 4.5880, c = 2.9632$ ; NiO (Fm-3m), (6 %), $a = 4.1802$ ;	20.9	5.133	0.056

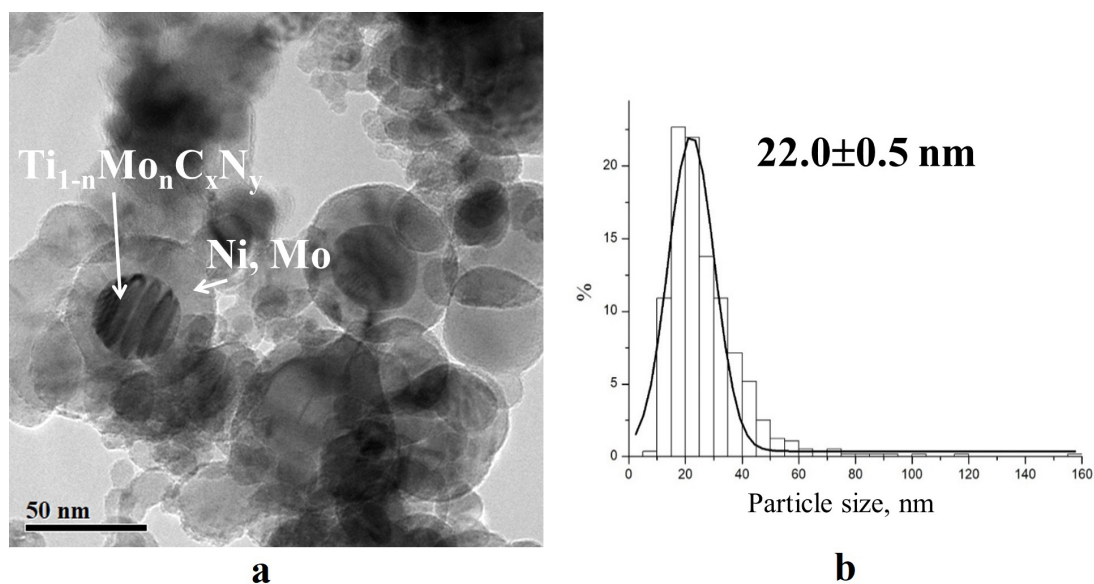


FIG. 2. HRTEM (a) of the nanocrystalline fraction of the processed mechanical mixture  $TiC_{0.5}N_{0.5} - Mo - Ni$  from classifier 2 – bag-type filter and particle size distribution histogram (b)

Similarly, using the fast Fourier transform, interplanar distances of 0.25 nm and 0.34 nm corresponding to the (101) and (110) planes of  $TiO_2$  (rutile) were determined on the surface of nanocrystalline particles of the  $Ti_{1-n}Mo_nC_xN_y - Ni - Mo$  alloy charge, as shown in Fig. 4a,b.

Figure 5 shows the results of transmission electron microscopy of a single particle having a faceted shape (Fig. 5a). Based on the results of measurement of interplanar distances, it was established that the particle under study is covered with a layer of hexagonal modification C. The fast Fourier transform of the selected area (Fig. 5b,c) illustrates the presence of titanium-molybdenum carbonitride  $Ti_{1-n}Mo_nC_xN_y$ , which corresponds to an interplanar distance of 0.21 nm (200).

The results of electron diffraction studies of a polycrystalline sample (Fig. 6, Table 2) illustrate the presence of  $TiO_2$  (sp. gr. P4<sub>2</sub>/mnm) in the form of rutile, as well as cubic  $Ti_{1-n}Mo_nC_xN_y$ , NiO, Ni (sp. gr. Fm-3m).

Summarizing all the information received about the presence and localization of various phase components included in the composition of ultra- and nanodispersed compositions obtained as a result of recondensation of the mechanical mixture  $TiC_{0.5}N_{0.5} - Mo - Ni$ , it is possible to formulate the chemical mechanism of the formation of nanocrystalline particles with a “core-shell” structure (Fig. 7). The mechanism should take into account the boiling and crystallization temperatures of all phase components detected by X-ray diffraction (Table 1). At the same time, the  $\Delta G(T)$  dependences [24] should be taken into account to justify the absence of some compounds that could be formed in highly dispersed powder materials.

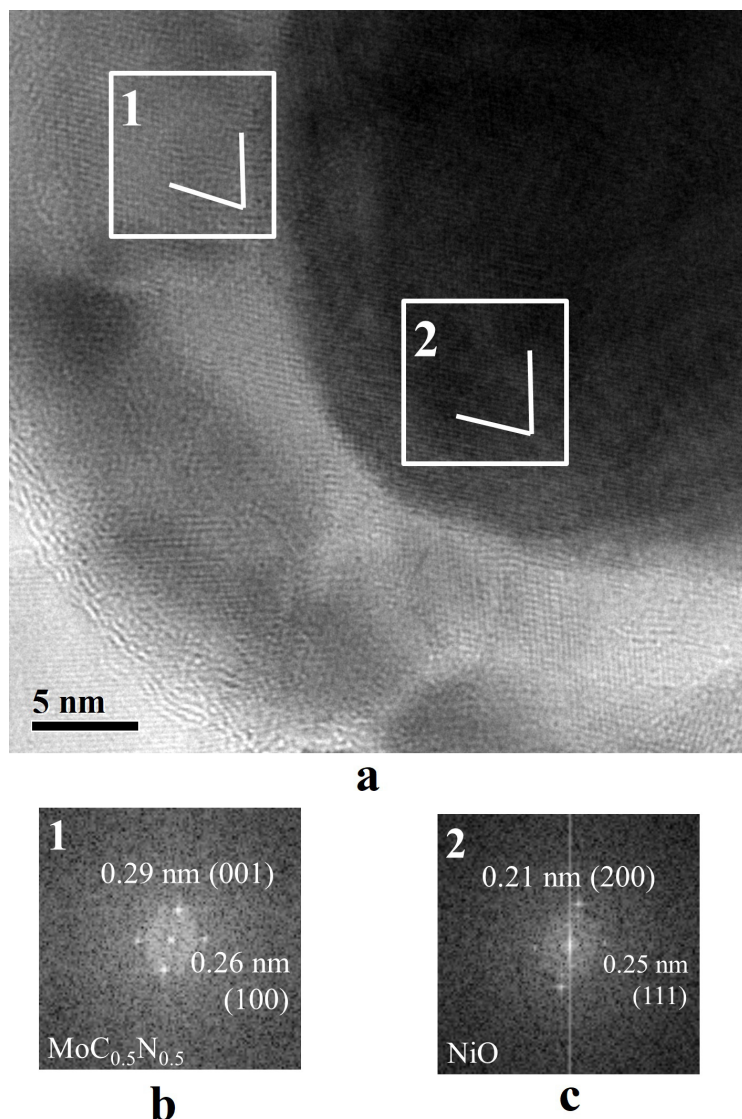
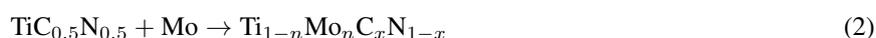


FIG. 3. Electron microscopic image of a nanocrystalline particle with a “core-shell” structure (a) of the  $Ti_{1-n}Mo_nC_xN_y - Ni - Mo$  tungsten-free hard alloy charge, taking into account the fast Fourier transform processing of various image sections containing  $MoC_{0.5}N_{0.5}$  (section 1) (b) and  $NiO$  (section 2) (c)

Modeling of the “core-shell” structure organization processes is based on the assumption that the space of the quenching chamber can be divided by temperature barriers along the axis of rotation of the tangential flow of nitrogen gas, provided technologically in the processes of recondensation of ultra- and nanodisperse particles in the quenching chamber of the plasmatron. A temperature of  $4000\text{ }^\circ\text{C}$  can be taken as an indicator of the first temperature barrier. At this temperature, the titanium carbide-nitride phases are in a gaseous state, because the crystallization temperature of titanium carbide  $TiC$  is  $3300\text{ }^\circ\text{C}$ , metallic  $Mo$  is in a similar state, and  $Ni$  is in the gaseous state. Upon reaching the second temperature barrier, characterized by the crystallization range of  $TiC$  and  $TiN$ , corresponding to  $3300 - 2913\text{ }^\circ\text{C}$  [25–27], crystallization of titanium carbonitride occurs by the “gas – solid” scheme, in accordance with works [28–31]. In the metal sublattice, a redistribution of positions between titanium and molybdenum ions takes place, taking into account the fact that its completeness is preserved according to reaction (2),



Gaseous nickel cannot react under these conditions due to its low affinity for carbon and nitrogen, which limits the formation of its carbide-nitride compounds compared to other metals located in the plasmatron chamber. The third temperature barrier corresponds to the crystallization temperature of  $Mo$ ,  $2623\text{ }^\circ\text{C}$ . A little earlier, at a temperature of  $2732\text{ }^\circ\text{C}$ , nickel passes to a liquid state and can react with  $Mo$ , forming intermetallic compounds, which were detected by electron microscopic studies. Regarding the interaction of  $Mo$  with gas components, it should be noted that due to the redistribution of carbon and nitrogen over the complete non-metallic sublattice, only gaseous  $N_2$ , used as a coolant gas,

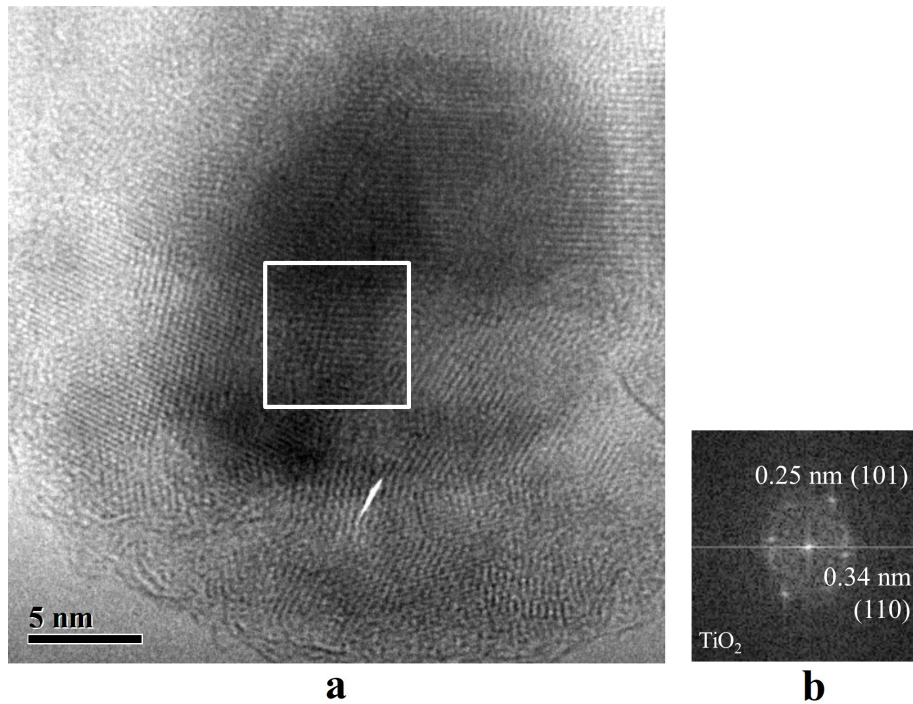


FIG. 4. Electron microscopic image of a nanocrystalline particle (a) of the  $Ti_{1-n}Mo_nC_xN_y - Ni - Mo$  alloy charge and FFT transformation of a section of the particle (b)

TABLE 2. Results of decoding of the electron diffraction pattern (Fig. 6)

Ring number	$d$ , nm	$hkl$ , compound
1	0.32	(110) $TiO_2$ ( $P4_2/mnm$ )
2	0.24	(101) $TiO_2$ ( $P4_2/mnm$ ) (111) $Ti_{1-n}Mo_nC_xN_y$ ( $Fm-3m$ )
3	0.21	(111) $TiO_2$ ( $P4_2/mnm$ ) (200) $Ti_{1-n}Mo_nC_xN_y$ ( $Fm-3m$ )
	0.20	(200) $NiO$ ( $Fm-3m$ ) (111) $Ni$ ( $Fm-3m$ )
4	0.16	(220) $Ti_{1-n}Mo_nC_xN_y$ ( $Fm-3m$ ) (211) $TiO_2$ ( $P4_2/mnm$ )
5	0.13	(311) $Ti_{1-n}Mo_nC_xN_y$ ( $Fm-3m$ ) (301) $TiO_2$ ( $P4_2/mnm$ )

can participate in the reaction with liquid-phase Mo. However, in accordance with [24], the affinity of molybdenum for nitrogen is very low and, accordingly, molybdenum nitride cannot be formed under these conditions. Thus, Mo crystallizes in its individual form while maintaining a cubic lattice (sp. gr.  $Im-3m$ ). The last temperature barrier is the crystallization temperature of liquid Ni, which corresponds to 1455 °C. Overcoming this temperature, metallic nickel crystallizes in the cubic modification (sp. gr.  $Fm-3m$ ) completely covering the surface of ultrafine and nanocrystalline particles.

The presented chemical mechanism of the formation of nanocrystalline particles of the  $Ti_{1-n}Mo_nC_xN_y - Ni - Mo$  tungsten-free hard alloy charge is in good agreement with the data of previously published works [32–36], describing the results of X-ray and electron microscopic studies, which were used as a basis to formulate the regularities of the organization of nanocrystalline particles with a “core-shell” structure of the composition  $Ti-C-Mo-Co$ ,  $Ti-N-Mo-Co$  as a result of plasma-chemical synthesis in a low-temperature nitrogen plasma of mechanical mixtures containing titanium carbides and nitrides, metallic Mo and Co. The formation of nanocrystalline  $TiN-Ni$  particles with a “core-shell” structure

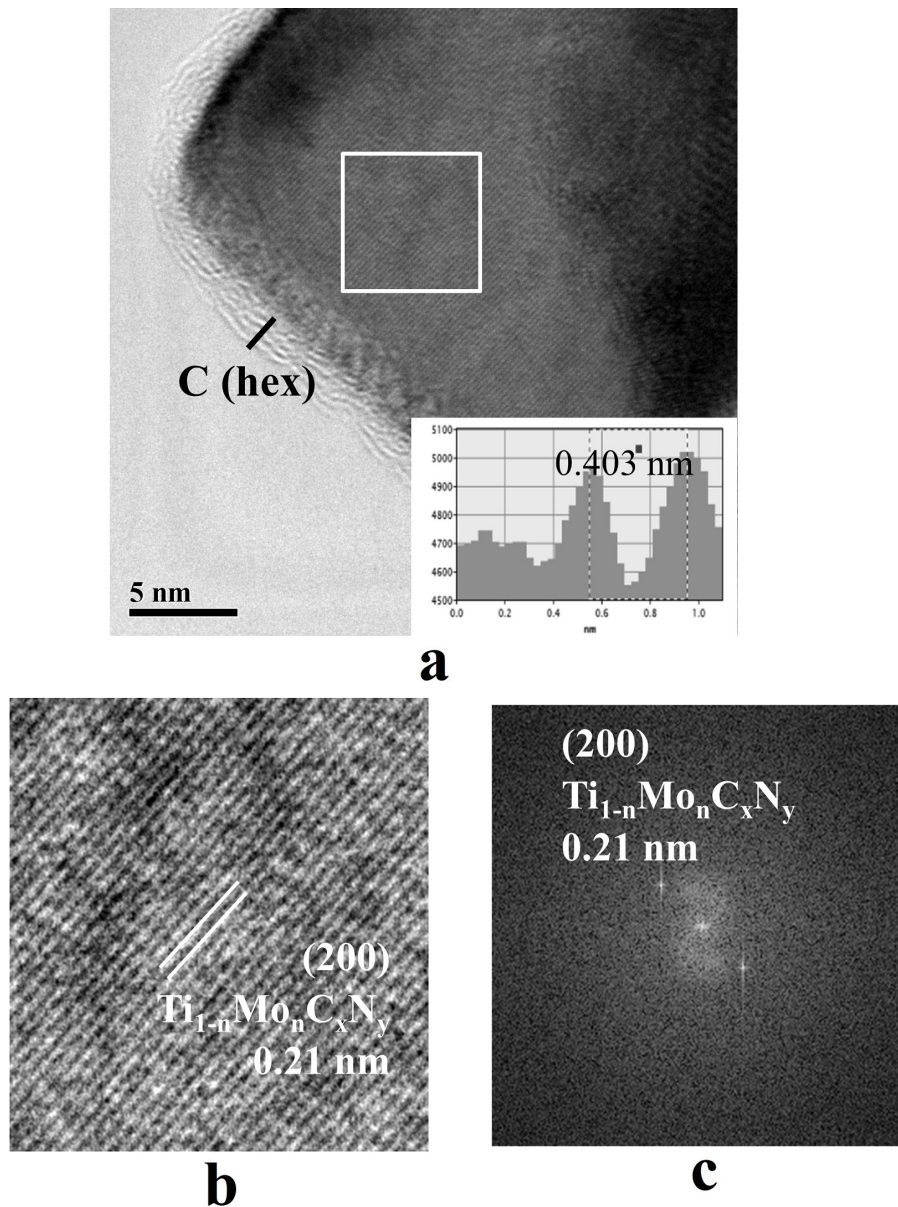


FIG. 5. Electron microscopic image (HRTEM) of (a) a nanocrystalline particle with a “core-shell” structure of the composition  $Ti_{1-n}Mo_nC_xN_y - Ni - Mo$  coated with carbon, enlarged image (b) and its fast Fourier transform results (c)

as a result of plasma recondensation (4000 – 6000 °C) of TiNi titanium nickelide powder in a turbulent flow of nitrogen gas was considered in works [37, 38].

#### 4. Conclusion

In the process of plasma-chemical synthesis in a low-temperature nitrogen plasma according to the plasma recondensation scheme, two highly dispersed fractions of the  $Ti_{1-n}Mo_nC_xN_y - Ni - Mo$  tungsten-free hard alloy charge were obtained from a mechanical mixture of titanium carbonitride, nickel and molybdenum, which were certified by helium pycnometry and BET. The calculated values of the average particle sizes were 365 and 56 nm for the cyclone and filter fractions, respectively.

Based on the X-ray diffraction results, it was established that the plasma-chemical powder compositions contain cubic phases of titanium-molybdenum carbonitride  $Ti_{1-n}Mo_nC_xN_y$ , metallic Mo and Ni.  $TiO_2$  and NiO formed as a result of forced acidification of the obtained highly dispersed powder compositions in the separation units of the plasma chemical plant are presented as additional phases.



The nanocrystalline component of the filter fraction was additionally investigated by high-resolution transmission electron microscopy; its average particle size according to direct measurements was 22 nm. The particles of the nanocrystalline component of the fraction from the filter represent a “core-shell” structure, in which the carbonitride  $Ti_{1-n}Mo_nC_xN_y$  acts as the core, and metallic Mo and Ni act as individual surface layers.

Based on the obtained experimental results, a chemical mechanism for the organization of a “core-shell” structure under the conditions of a turbulent flow of nitrogen gas with a cooling rate of  $10^5$  °C/s has been formulated for nanocrystalline particles of the tungsten-free hard alloy charge containing titanium-molybdenum carbonitride  $Ti_{1-n}Mo_nC_xN_y$  coated with metal layers of Mo and Co.

## References

- [1] Liu C., Lu W., Weng G.J., Li J. A cooperative nano-grain rotation and grain-boundary migration mechanism for enhanced dislocation emission and tensile ductility in nanocrystalline materials. *Materials Science and Engineering: A*, 2019, **756**, P. 284–290.
- [2] Lavrenko V.A., Podchernyaeva I.A., Shchur D.V., Zolotareno An.D., Zolotareno Al.D. Features of physical and chemical adsorption during interaction of polycrystalline and nanocrystalline materials with gases. *Powder Metallurgy and Metal Ceramics*, 2018, **56**, P. 504–511.
- [3] Prusty D., Pathak A., Mukherjee M., Mukherjee B., Chowdhury A. TEM and XPS studies on the faceted nanocrystals of  $Ce_{0.8}Zr_{0.2}O_2$ . *Materials Characterization*, 2015, **100**, P. 31–35.
- [4] Chaturvedi A., Yaqub R., Baker I. Microstructure and magnetic properties of bulk nanocrystalline MnAl. *Metals*, 2014, **4**(1), P. 20–27.
- [5] Guivar J., Martinez A., Anaya A., Valladares L., Félix L., Dominguez A. Structural and magnetic properties of monophasic maghemite ( $\gamma$ -Fe<sub>2</sub>O<sub>3</sub>) nanocrystalline powder. *Advances in Nanoparticles*, 2014, **3**(3), P. 49326.
- [6] Andrievsky R.A. Preparation and properties of nanocrystalline refractory compounds. *Uspekhi khimii*, 1994, **63**(5), P. 431–448. (In Russ.)
- [7] Morokhov I.D., Trusov L.I., Chizhik S.P. *Ultrafine metallic media*. Atomizdat, Moscow, 1977, 264 p. (In Russ.)
- [8] Gusev A.I. *Nanomaterials, nanostructures, nanotechnologies*. 2nd ed., rev. Fizmatlit, Moscow, 2007, 414 p. (In Russ.)
- [9] Gusev A.I. *Nanocrystalline materials: methods of preparation and properties*. UrO RAN, Ekaterinburg, 1998, 199 p. (In Russ.)
- [10] Panov V.S., Chuvilin A.M. *Technology and properties of hard alloys and products made from them*. Textbook for universities. MISIS, Moscow, 2001, 428 p. (In Russ.)
- [11] Fedorenko V.V. Interaction of titanium carbide, nitride and carbonitride with nickel-based melts. Dissertation for the degree of candidate of chemical sciences. Sverdlovsk, 1981, 141 p.
- [12] Zhilyaev V.A., Patrakov E.I., Shveikin G.P. Current status and potential for development of W-free hard alloys. Proc. 2nd Int. Conf. Science Hard Mater. A Hilger Ltd, Bristol, Boston, 1986, P. 1063–1073.
- [13] Method for manufacturing hard alloys based on titanium carbonitride. A.s. 424659 USSR MPK B22F 3/12, C22C 29/00. Mitrofanov B.V., Shveikin G.P., Lyubimov V.D., Zainulin Yu.G., Alyamovsky S.I.; patent holder IH UC AS SSR, No. 1766386.
- [14] Askarova L.K., Shchupachev E.V., Ermakov A.N., Grigorov I.G., Zainulin Yu.G. Effects of vanadium and niobium on the phase composition of titanium-carbonitride-base cermets with titanium–nickel binder. *Inorganic Materials*, 2001, **37**, P. 157–160.
- [15] Askarova L.Kh., Grigorov I.G., Fedorenko V.V., Zainulin Yu.G. Liquid-phase interaction in  $TiC_{0.5}N_{0.5}$ –TiNi–Ti–Zr and  $TiC_{0.5}N_{0.5}$ –TiNi–Ti–Zr alloys. *Metally*, 1998, **5**, P. 16–19. (In Russ.)
- [16] Storozhenko P.A., Guseinov Sh.L., Malashin S.I. Nanodispersed Powders: Synthesis Methods and Practical Applications. *Nanotechnologies in Russia*, 2009, **4**, P. 262–274.
- [17] Sadovnikov S.I., Gusev A.I. Effect of particle size and specific surface area on the determination of the density of nanocrystalline silver sulfide Ag<sub>2</sub>S powders. *Physics of the Solid State*, 2018, **60**, P. 877–881.
- [18] Kisly P.S., Bondaruk N.I., Borovikova M.S., Zaverukha O.V., Kozina G.K., Kryl Ya.A., Kuzenkova M.A., Kushtalova I.P., Prikhodko L.I., Watchman B.D. Cermets. *Naukova Dumka*, Kyiv, 1985, 272 p. (In Russ.)
- [19] Shveikin G.P., Alyamovsky S.I., Zainulin Yu.G., Gusev A.I., Gubanov V.A., Kurmaev E.Z. *Compounds of variable composition and their solid solutions*. UC USSR Academy of Sciences, Sverdlovsk, 1984, 292 p. (In Russ.)
- [20] Ormont B.F. *Compounds of variable composition*. Khimiya, Leningrad, 1969, 520 p. (In Russ.)
- [21] *Cermets*. Edited by J.R. Tinklepaugh and W.B. Crandall. Reinhold Publishing Corp., New York, 1960, 239 p.
- [22] Hard sintered tungsten-free alloys. GOST 26530-85. USSR State Committee for Standards. Publishing house of standards, Moscow, 1985, 7 p. (In Russ.)
- [23] Rykalin N.N. *Plasma processes in metallurgy and technology of inorganic materials*. Nauka, Moscow, 1973, 243 p.
- [24] Barin I. *Thermochemical Data of Pure Substances*. Third Edition. VCH, Weinheim, New York, Basel, Cambridge, Tokyo, 1995, 2003 p.
- [25] Krzhizhanovskiy R.E., Stern Z.Yu. *Thermophysical properties of non-metallic materials (carbides)*. Directory. Energiya, Leningrad, 1976, 120 p. (In Russ.)
- [26] Kosolapova T.Ya. *Handbook of high temperature compounds: properties, production, applications*. CRC Press, New York, Washington, Philadelphia, London, 1990, 958 p.
- [27] Knunyants I.L. *Chemical encyclopedia: in 5 volumes*. V. 3. Sovetskaya entsiklopediya, Moscow, 1992, 639 p. (In Russ.)
- [28] Knunyants I.L. *Chemical encyclopedia: in 5 volumes*. V. 2. Sovetskaya entsiklopediya, Moscow, 1990, 671 p. (In Russ.)
- [29] Gusev A.I., Rempel A.A. *Nonstoichiometry, disorder and order in solids*. NISO UrO RAN, Ekaterinburg, 2001, 579 p. (In Russ.)
- [30] Samokhin A.V., Polyakov S., Astashov A.G., Tsvetkov Yu.V. Simulation of the process of synthesis of nanopowders in a plasma reactor jet type. I. Statement of the problem and model validation. *Fizika i khimiya obrabotki materialov*, 2013, **6**, P. 40–46. (In Russ.)
- [31] Samokhin A.V., Polyakov S., Astashov A.G., Tsvetkov Yu.V. Simulation of the process of nanopowder synthesis in a jet-type plasma reactor. II. Nanoparticles formation. *Inorganic Materials: Applied Research*, 2014, **5**(3), P. 224–229.
- [32] Avdeeva Yu.A., Luzhkova I.V., Ermakov A.N., Samigullina R.F., Vovkotrub E.G., Dobrinsky E.K., Zainulin Yu.G. Thermal properties of ultra- and nanodispersed core-shell structures of Ti(Mo)C and Ti(Mo)C-Co obtained during plasma-chemical synthesis by plasma recondensation scheme. *Metallurgical and Materials Transactions B*, 2020, **51**, P. 1048–1059.
- [33] Avdeeva Yu.A., Luzhkova I.V., Ermakov A.N. Formation of titanium-cobalt nitride  $Ti_{0.7}Co_{0.3}N$  under plasma-chemical synthesis conditions in a low-temperature nitrogen plasma. *Nanosystems: Physics, Chemistry, Mathematics*, 2021, **12**(5), P. 641–649.
- [34] Avdeeva Yu.A., Luzhkova I.V., Ermakov A.N. Composition and structure of “core-shell” nanocrystalline particles based on titanium-molybdenum carbides obtained under the conditions of plasma-chemical synthesis. *Powder Metallurgy and Functional Coatings*, 2022, **2**, P. 4–12. (In Russ.)
- [35] Avdeeva Yu.A., Luzhkova I.V., Ermakov A.N. Plasmachemical synthesis of TiC–Mo–Co nanoparticles with a core-shell structure in a low-temperature nitrogen plasma. *Russian Metallurgy*, 2022, **2022**(9), P. 977–984.

- [36] Avdeeva Yu.A., Luzhkova I.V., Murzakaev A.M., Ermakov A.N. Plasma-chemical synthesis of nanocrystalline “core-shell” structures TiN–Mo–Co. *Nanosystems: Physics, Chemistry, Mathematics*. 2023, **14**(1), P. 132–141.
- [37] Ermakov A.N., Luzhkova I.V., Avdeeva Yu.A., Murzakaev A.M., Zainulin Yu.G., Dobrinsky E.K. Formation of complex titanium-nickel nitride  $Ti_{0.7}Ni_{0.3}N$  in the “core-shell” structure of TiN–Ni. *International Journal of Refractory Metals and Hard Materials*, 2019, **84**, P. 104996.
- [38] Avdeeva Yu.A., Luzhkova I.V., Ermakov A.N. Mechanism of formation of nanocrystalline particles with core-shell structure based on titanium oxynitrides with nickel in the process of plasma-chemical synthesis of TiNi in a low-temperature nitrogen plasma. *Nanosystems: Physics, Chemistry, Mathematics*, 2022, **13**(2), P. 212–219.

---

Submitted 26 December 2023; revised 19 June 2024; accepted 28 June 2024

*Information about the authors:*

*Yuliya A. Avdeeva* – Institute of Solid State Chemistry, Ural Branch, Russian Academy of Sciences Pervomaiskaya Street, 91, Ekaterinburg, 620990, Russia; ORCID 0000-0002-1470-0476; y-avdeeva@list.ru

*Irina V. Luzhkova* – Institute of Solid State Chemistry, Ural Branch, Russian Academy of Sciences Pervomaiskaya Street, 91, Ekaterinburg, 620990, Russia; ORCID 0000-0001-9123-5371; key703@yandex.ru

*Aidar M. Murzakaev* – Institute of Electrophysics, Ural Branch, Russian Academy of Sciences, Amundsen Street, 106, Ekaterinburg, 620216, Russia; ORCID 0000-0003-4440-427X; aidar@iep.uran.ru

*Alexey N. Ermakov* – Institute of Solid State Chemistry, Ural Branch, Russian Academy of Sciences Pervomaiskaya Street, 91, Ekaterinburg, 620990, Russia; ORCID 0000-0002-2746-5292; ermakovihim@yandex.ru

*Conflict of interest:* the authors declare no conflict of interest.

## Study of photocatalytic activity in two light ranges of Sr<sub>2</sub>Mn<sub>0.4</sub>Ti<sub>0.6</sub>O<sub>4</sub> oxide with the K<sub>2</sub>NiF<sub>4</sub>-type structure

Tatyana I. Chupakhina<sup>1,a</sup>, Olga I. Gyrdasova<sup>1,b</sup>, Anastasya M. Uporova<sup>1</sup>, Larisa Y. Buldakova<sup>1</sup>, Mikhail Y. Yanchenko<sup>1</sup>, Dzhavid V. Mamedov<sup>2</sup>, Yulia A. Deeva<sup>1</sup>, Inna V. Baklanova<sup>1</sup>

<sup>1</sup>Institute of Solid State Chemistry UB RAS, Ekaterinburg, Russia

<sup>2</sup>Zavoisky Physical-Technical Institute, FRC Kazan Scientific Center of RAS, Kazan, Russia

<sup>a</sup>chupakhina@yandex.ru, <sup>b</sup>gyrdasova@ihim.uran.ru

Corresponding author: Tatyana I. Chupakhina, chupakhina@yandex.ru

PACS 82.65.+r

**ABSTRACT** The photocatalytic properties of single-phase sample Sr<sub>2</sub>Mn<sub>0.4</sub>Ti<sub>0.6</sub>O<sub>4</sub> is studied as a representative of a series of Sr<sub>2</sub>Mn<sub>x</sub>Ti<sub>1-x</sub>O<sub>4</sub> solid solutions ( $x = 0.05, 0.15, 0.25, 0.4$ ) obtained by the SHS. The sample annealed at 1200 °C is characterized by a uniform distribution of Sr, Ti and Mn in the oxidation degree (4+) inside the aggregates, the average size of which does not exceed 1 μm. According to UV-Vis-NIR spectroscopy data, a narrowing of the band gap of Sr<sub>2</sub>TiO<sub>4</sub> from 3.16 to 1.8 eV is observed when it is doped with 40 mol% of manganese. This is due to the high photoactivity of Sr<sub>2</sub>Mn<sub>0.4</sub>Ti<sub>0.6</sub>O<sub>4</sub> in the HQ oxidation reaction in UV and blue light.

**KEYWORDS** nanostructured strontium titanate, Raddlesden–Popper structures, oxidative photocatalysis

**ACKNOWLEDGEMENTS** The work was supported by RCF, project No. 24-23-20123. The UV-Vis-NIR spectrum was recorded on equipment of the Center for Joint Use “Spectroscopy and Analysis of Organic Compounds” at the Postovsky Institute of Organic Synthesis, UB RAS.

**FOR CITATION** Chupakhina T.I., Gyrdasova O.I., Uporova A.M., Buldakova L.Y., Yanchenko M.Y., Mamedov D.V., Deeva Y.A., Baklanova I.V. Study of photocatalytic activity in two light ranges of Sr<sub>2</sub>Mn<sub>0.4</sub>Ti<sub>0.6</sub>O<sub>4</sub> oxide with the K<sub>2</sub>NiF<sub>4</sub>-type structure. *Nanosystems: Phys. Chem. Math.*, 2024, **15** (4), 540–547.

### 1. Introduction

The complex oxide Sr<sub>2</sub>TiO<sub>4</sub> with layered Raddlesden–Popper structure (A<sub>n+1</sub>B<sub>n</sub>O<sub>3n+1</sub>,  $n = 1$ , structural type K<sub>2</sub>NiF<sub>4</sub>) have high dielectric constant and low dielectric loss angle tangent. Strontium titanates are wide-gap semiconductors which are used in various fields of electronic engineering: electro-optical devices, multilayer capacitors and thermistors [1]. Sr<sub>2</sub>TiO<sub>4</sub>-based compounds find practical application in photosystems [2, 3] as photocatalysts in the process of H<sub>2</sub> evolution from H<sub>2</sub>O [4] or oxidation of toxic organic compounds to carbon dioxide and water [5]. Phenol derivatives are life-threatening pollutants of water resources. Titanium dioxide as a photocatalyst in the form of anatase/rutile structural mixture is traditionally used to decompose benzene-containing pollutants [6] and 1,4-dihydroxybenzene (hydroquinone) (60 %) *n*-benzoquinone and catechol are the main intermediates during phenol photooxidation by TiO<sub>2</sub> catalyst [7]. The hydroquinone oxidation reaction may be considered as a model process for photooxidation reaction of phenolic compounds. The main problem of using TiO<sub>2</sub> in photostimulated processes for removal of toxic contaminants is its limited spectral range of operation (UV region).

Structural analogs of TiO<sub>2</sub> in the anatase phase are strontium titanates. The band gaps of Sr<sub>2</sub>TiO<sub>4</sub> and TiO<sub>2</sub> are comparable (~ 3.3 eV) [8]. Therefore, compounds based on Sr<sub>2</sub>TiO<sub>4</sub> can become an alternative to the known catalysts (Degussa). At the same time, crystalline Sr<sub>2</sub>TiO<sub>4</sub>, like TiO<sub>2</sub>, shows photoactivity only under irradiating by light with wavelength  $\lambda_{\max} = 253$  nm (UV range) [8].

There is extensive information on methods of surface activation of perovskite-like oxides with description of various synthesis technologies, creation of composite structures, and design of heterostructures [9–14]. The main way to expand the spectral working range of strontium titanates is doping with d-metals in position B, as well as increasing the working surface area [9–13]. It is known that doping with transition elements like Mn, leads to enhanced light absorption ability of strontium titanates due to the effective reduction of the band gap. Thus, doping of perovskite-like structure strontium titanate with 1 and 3 at.% Mn increases its photocatalytic activity in the decomposition of methylene blue, and the oxide with lower Mn content is more effective as a catalyst [13]. In contrast, [14] found that in SrTi<sub>1-x</sub>Mn<sub>x</sub>O<sub>3</sub> ( $x = 0.05 - 0.2$ ), the sample with  $x = 0.15$  was found to be a more efficient catalyst for the decomposition of methylene blue.

There is no information on the application of manganese-containing layered perovskites based on  $\text{Sr}_2\text{TiO}_4$  in photocatalysis. There are also no studies in the field of using doped strontium titanates with the structure of the first and second homologues of the Radlesden–Popper series as photocatalysts for the decomposition of phenolic compounds.

Thus, the goal was to synthesize  $\text{Sr}_2\text{Ti}_{1-x}\text{Mn}_x\text{O}_4$  ( $0.05 \leq x \leq 0.4$ ) solid solutions and investigate their activity in the photooxidation of 1,4-dihydroxybenzene (hydroquinone).

By changing the doping of  $\text{Sr}_2\text{TiO}_4$  and the conditions of its production, it is possible to extend its photosensitivity to the visible range of spectrum.

Practically significant properties of such materials (specific surface area, degree of defectivity, porosity, size, morphology and internal architecture of aggregates) are set by synthesis. The authors propose a comprehensive solution to these problems by precursor synthesis method. The technology of salt composites pyrolysis was used for preparation of complex oxides with various composition (method of self-propagating high-temperature synthesis, SHS) [15, 16].

In this work, complex oxide  $\text{Sr}_2\text{Mn}_{0.4}\text{Ti}_{0.6}\text{O}_4$  with  $\text{K}_2\text{NiF}_4$ -type structure was generated by SHS method. Its catalytic properties were studied in the photooxidation reaction with 1,4-dihydroxybenzene (hydroquinone, HQ) when the sample was exposed to radiation with wavelengths of  $\lambda_{\text{max}} = 253$  nm (UV range) and  $\lambda_{\text{max}} = 440 - 460$  nm (visible blue).

## 2. Experimental

Reagents used are as follows: strontium nitrate  $\text{Sr}(\text{NO}_3)_2$  (high purity), titanium tetraisopropoxide  $\text{Ti}(\text{i-OC}(\text{CH}_3)_2)_4$  ( $\rho = 0.963$  g/cm<sup>3</sup>) and manganese (II) nitrate  $\text{Mn}(\text{NO}_3)_2 \cdot 4\text{H}_2\text{O}$  (high purity).  $\text{C}_2\text{H}_5\text{OH}$  96 % and  $\text{HNO}_3$  (high purity) were used as solvents. As an organic reducing agent for the initiation of the fuel process in a mixture of nitrates,  $(\text{NH}_4)_2\text{C}_6\text{H}_6\text{O}_7$  (high purity) was used.  $\text{Sr}_2\text{Mn}_{0.4}\text{Ti}_{0.6}\text{O}_4$  was prepared by SHS method according to the procedure described in [16]. The final single-phase oxide  $\text{Sr}_2\text{Mn}_x\text{Ti}_{1-x}\text{O}_4$  was obtained by annealing the SHS product at a temperature of 1200 °C during 8 h.

X-ray powder diffraction (XRD-7000 diffractometer, Shimadzu, Japan) using  $\text{CuK}\alpha$  radiation in the  $2\theta$  range 5 to 80° with a step of 0.03° was employed. The morphological peculiarities were examined by the scanning electron microscopy method (SEM) on a Tescan Vega Compact microscope with an EDS X-max Oxford Instruments. To confirm the change in band gap, the UV-Vis-NIR spectrum in the wavelength range of 190 – 1400 nm ( $\text{BaSO}_4$  was used as the standard) of compound  $\text{Sr}_2\text{Mn}_{0.4}\text{Ti}_{0.6}\text{O}_4$  was recorded using Shimadzu UV-2600 (Japan) spectrophotometer.

HQ working solution was prepared immediately before the experiment. 1.0 cm<sup>3</sup> of the initial hydroquinone solution with the concentration of  $\text{C}(\text{C}_6\text{H}_4(\text{OH})_2) = 1 \cdot 10^{-2}$  mol/dm<sup>3</sup>, 1.5 cm<sup>3</sup> of 0.5 M  $\text{Na}_2\text{SO}_4$  solution were placed in 25.0 cm<sup>3</sup> measuring flasks and brought to the mark with distilled water. The concentration of the working solution of hydroquinone is  $4.0 - 10^{-4}$  mol/dm<sup>3</sup>. Before the work, a calibration graph was fixed in the range of HQ concentrations  $0.0 - 4.0 \cdot 10^{-4}$  mol/dm<sup>3</sup> by measuring the height of the anodic oxidation peak of HQ at 0 V. The solutions were transferred to a cell in which 50 mg of photocatalyst was previously added and exposed to radiation. UV irradiation of HQ solutions was carried out in quartz cells using a BUV-15 lamp ( $\lambda_{\text{max}} = 253$  nm). Oxidation under the blue lamp ( $\lambda_{\text{max}} = 440 - 460$  nm) was carried out in glass cells. The HQ content in the solution was controlled by voltammetry.

Voltammetric study of  $\text{Sr}_2\text{Mn}_{0.4}\text{Ti}_{0.6}\text{O}_4$  samples was carried out with use of an electroactive carbon paste electrode (CPE). It consisted of a mixture of a substance to study, spectrally pure graphite with particles' size of  $\leq 63$  μm, and a binder (Vaseline oil), taken in a 1 : 9 : 3 weight ratio and had the working area of 0.07 cm<sup>2</sup>. The reference electrode was a saturated silver-silver chloride electrode. The voltammograms were recorded in two polarization modes of CPE, in 0.5 M  $\text{Na}_2\text{SO}_4$ . Redox processes on the surface of the samples were investigated as follows. The reduction processes were fixed from +0.6 to -1.6 V, the oxidation processes were recorded from -1400 to +600 V. All measurements were realized by PU-1 polarograph at scan rate 30 mV/s.

## 3. Results and discussion

In the studied system of solid solutions  $\text{Sr}_2\text{Mn}_x\text{Ti}_{1-x}\text{O}_4$  ( $T = 1200$  °C;  $x = 0.05, 0.15, 0.25, 0.4$ ) according to XRD data, only the composition  $\text{Sr}_2\text{Mn}_{0.4}\text{Ti}_{0.6}\text{O}_4$  is single phase (Fig. 1). The other samples contain SrO and  $\text{TiO}_2$  as impurity phases.

In [14], during the preparation of Mn-doping  $\text{SrTiO}_3$ , it was noted the presence of similar impurity phases, which was attributed by the authors to the formation of strontium carbonate. However, these impurities disappear at the highest possible Mn concentration, indicating that doping promotes the complete reaction. The absence of the MnO peak in the diffractograms means that it takes place the successful introduction of Mn into the lattice of  $\text{SrTiO}_3$  [14]. In addition, the authors suggested the different valence state of manganese during the decomposition of the carboxylate complex, especially noticeable at small amounts of dopant [17, 18].

For further study, we have chosen a single-phase sample of  $\text{Sr}_2\text{Mn}_{0.4}\text{Ti}_{0.6}\text{O}_4$ . The diffractogram of the sample  $\text{Sr}_2\text{Mn}_{0.4}\text{Ti}_{0.6}\text{O}_4$ , indexed in space group I4/mmm (No. 139) is presented in Fig. 1b. Crystallochemical characteristics of  $\text{Sr}_2\text{TiO}_4$  and  $\text{Sr}_2\text{Mn}_{0.4}\text{Ti}_{0.6}\text{O}_4$  are summarized in Table 1.

The decrease of the cell parameters with decreasing the unit cell volume of doped strontium titanate  $\text{Sr}_2\text{Mn}_{0.4}\text{Ti}_{0.6}\text{O}_4$  confirms the incorporation of the smaller  $\text{Mn}^{4+}$  ion (0.53 Å) into the octahedral positions occupied by the larger  $\text{Ti}^{4+}$  ion

TABLE 1. The crystallochemical parameters of  $\text{Sr}_2\text{TiO}_4$  and  $\text{Sr}_2\text{Mn}_{0.4}\text{Ti}_{0.6}\text{O}_4$  (space group I4/mmm, Sr (4e, 0; 0; z), Ti/Mn (2a, 0; 0; 0), O1 (4e, 0; 0.5; 0), O2 (4c, 0; 0; z))

	$\text{Sr}_2\text{TiO}_4$	$\text{Sr}_2\text{Mn}_{0.4}\text{Ti}_{0.6}\text{O}_4$
Cell parameters		
$a, \text{Å}$	3.883(4)	3.846(1)
$c, \text{Å}$	12.588(2)	12.562(5)
$V, \text{Å}^3$	189.894(3)	185.882(1)
Atom parameters		
Sr		
$z, \text{Å}$	0.354(7)	0.354(1)
O1		
Occupancy	0.979(5)	1.02(4)
O2		
$z, \text{Å}$	0.159(1)	0.160(1)
Occupancy	1.078(5)	1.01(4)
$B_{\text{iso}}, \text{Å}^2$		
Sr	0.317(2)	0.766(9)
Mn	—	0.616(2)
Ti	0.334(5)	0.616(2)
O1	0.546(1)	1.074(4)
O2	0.548(2)	1.433(4)
Selected bond lengths (Å)		
Ti/Mn – O1 ( $\times 4$ )	1.941(2)	1.923(1)
Ti/Mn – O2 ( $\times 2$ )	2.003(5)	2.018(8)
Sr – O1 ( $\times 4$ )	2.673(7)	2.653(7)
Sr – O2a ( $\times 4$ )	2.751(3)	2.726(5)
Sr – O2b ( $\times 4$ )	2.454(5)	2.434(3)
R-factors		
$R_{\text{wp}}, \%$	16.4	8.14
$R_{\text{exp}}, \%$	11.6	10.13
$R_p, \%$	10.6	5.79
$R_f$	3.83	3.82
$\chi^2$	1.99	0.72

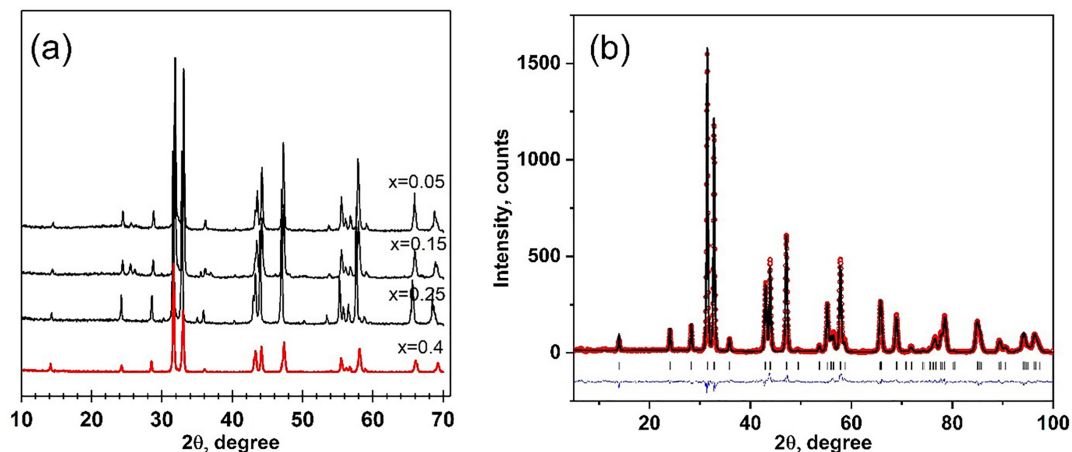


FIG. 1. (a) Diffractograms of  $\text{Sr}_2\text{Mn}_x\text{Ti}_{1-x}\text{O}_4$  ( $x = 0.05, 0.15, 0.25, 0.4$ ); (b) Experimental ('o'), theoretical (black line) and difference (blue line) diffractograms of  $\text{Sr}_2\text{Mn}_{0.4}\text{Ti}_{0.6}\text{O}_4$ , ('|') are Miller indices

(0.605 Å) [19]. According to SEM data, the pyrolysis product of the reaction mass  $\text{Sr}_2\text{Mn}_{0.4}\text{Ti}_{0.6}\text{O}_4$  consists of nanoscale particles (Fig. 2a).

After annealing in the indicated temperature range, agglomeration of crystallites up to 1 nm is observed. The results of EDAX study confirm the chemical composition of the compound. The uniform distribution of elements in the agglomerates is confirmed by EDS-mapping (Fig. 2b).

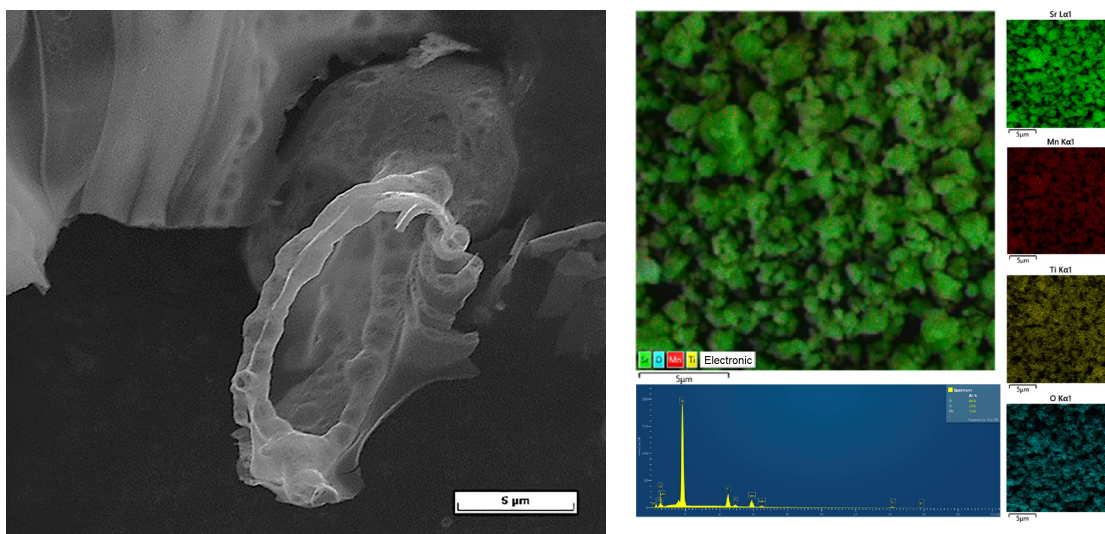


FIG. 2. SEM image of SHS-synthesis product (a) and EDS-mapping of  $\text{Sr}_2\text{Mn}_{0.4}\text{Ti}_{0.6}\text{O}_4$ , calcined at 1200 °C (b)

To establish the effect of the manganese dopant on the optical characteristics of  $\text{Sr}_2\text{TiO}_4$ , the optical absorption spectrum in the UV, visible and near-IR ranges was studied (Fig. 3a).

The absorption band at 459 nm is attributed to the  ${}^4\text{A}_{2g} \rightarrow {}^4\text{T}_{2g}$  transition of the  $\text{Mn}^{4+}$  ion, and the shoulder near 300 nm is most likely associated with the  ${}^4\text{A}_{2g} \rightarrow {}^4\text{T}_{1g}$  transition of the  $\text{Mn}^{4+}$  ion (Fig. 3a). The determination of the band gap is performed by the way of approximation of the absorption edge using the Tauc relation:  $(\alpha h\nu)^2 = A(h\nu - E_g)$ , where  $\alpha$  is the absorption coefficient,  $h\nu$  is the photon energy,  $E_g$  is the band gap,  $A$  is an independent constant. According to this equation, the optical band gap can be obtained by the extrapolation of the linear part of the  $(\alpha h\nu)^2 = f(h\nu)$  to the intersection with the abscissa axis (Fig. 3b). The band gap for  $\text{Sr}_2\text{Mn}_{0.4}\text{Ti}_{0.6}\text{O}_4$  is 1.8 eV.

To clarify the valence state of Mn in  $\text{Sr}_2\text{Mn}_{0.4}\text{Ti}_{0.6}\text{O}_4$ , EPR spectra and voltammetry (VA) data of the sample were investigated. To this date, there is no discussion about the nature and properties of  $\text{Mn}^{4+}$  centers in the STO crystal. It is generally accepted that tetravalent manganese ions isovalently replace the octahedrally coordinated position of titanium in the crystal. In this case, the ground state of  $\text{Mn}^{4+}$  ions is the orbital singlet  ${}^4\text{A}_2$ , i.e., the outer electron shell is characterized by a highly symmetric distribution  $d$  of electron density [17, 18]. In other words,  $\text{Mn}^{4+}$  ions should not

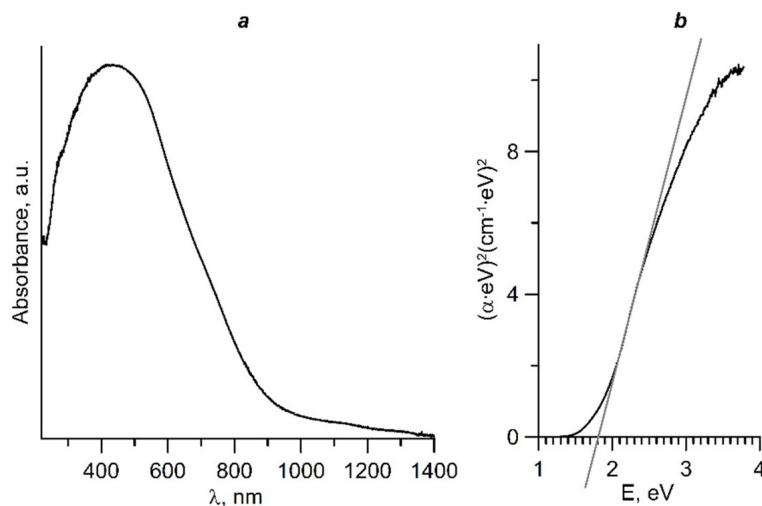


FIG. 3. (a) UV-Vis-NIR spectra of  $\text{Sr}_2\text{Mn}_{0.4}\text{Ti}_{0.6}\text{O}_4$ ; (b) band gap  $E_g$  estimation using Tauc plot method

introduce a perturbation into the crystal lattice that would lead to a decrease in the symmetry of the center. Therefore, the structure of the EPR spectrum should reflect the symmetry of the crystal field.

Figure 4a shows the EPR spectrum of  $\text{Sr}_2\text{Mn}_{0.4}\text{Ti}_{0.6}\text{O}_4$ . The EPR spectrum is symmetric, well described by the Lorentz function. The parameters of the Lorentz curve are resonance field  $H_{\text{res}} \approx 3379.9$  Oe, line width  $\Delta H \approx 173.2$  Oe, g-factor (having the value 1.99 which corresponds to the  $\text{Mn}^{4+}$  ion).

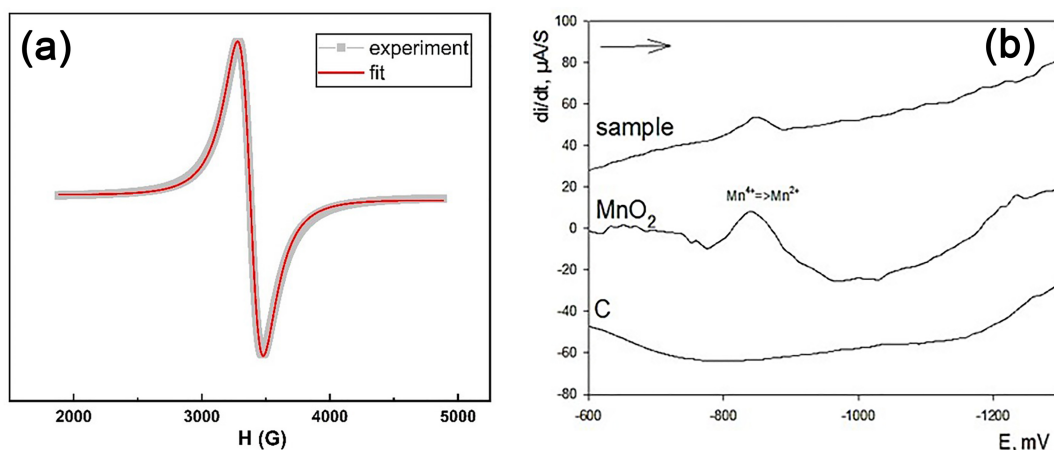


FIG. 4. (a) EPR spectra of  $\text{Sr}_2\text{Mn}_{0.4}\text{Ti}_{0.6}\text{O}_4$ ; (b) Voltammetric recovery curves of  $\text{Sr}_2\text{Mn}_{0.4}\text{Ti}_{0.6}\text{O}_4$ , carbon and  $\text{MnO}_2$ ; background electrolyte  $-0.5$  M  $\text{NH}_4\text{OH}$  and  $0.25$  M  $\text{Na}_2\text{SO}_4$

The value of g-factor is close to literature data for  $\text{Mn}^{4+}$  ions, both for highly concentrated and low concentrated compounds [20–23]. The absence of  $\text{Mn}^{4+}$  ion hyperfine structure in the EPR spectrum of  $\text{Sr}_2\text{Mn}_{0.4}\text{Ti}_{0.6}\text{O}_4$  may be due to exchange interactions between manganese ions.

Voltammetry data confirm the presence of  $\text{Mn}^{4+}$  (Fig. 4b). The VA behavior of Mn(IV) oxide was preliminarily studied. At cathodic wave of  $\text{MnO}_2$  at  $-850$  mV, one can see the reduction peak, that corresponds to the Mn(IV) reduction to Mn(II). A similar signal is recorded on voltammetry of  $\text{Sr}_2\text{Mn}_{0.4}\text{Ti}_{0.6}\text{O}_4$  (Fig. 4b). From the analysis of the obtained polarization curves, it can be concluded that manganese in the studied sample  $\text{Sr}_2\text{Mn}_{0.4}\text{Ti}_{0.6}\text{O}_4$  is initially in the form of  $\text{Mn}^{4+}$ .

According to UV-Vis-NIR spectroscopy data, the narrowing of the band gap of  $\text{Sr}_2\text{Mn}_{0.4}\text{Ti}_{0.6}\text{O}_4$  (1.8 eV) compared to  $\text{Sr}_2\text{TiO}_4$  (3.16 eV) indicates a significant shift of the photosensitivity of the compound to the visible range of the spectrum.

The photocatalytic activity of the samples was evaluated by the decomposition rate of the reference organic compound 1,4-dihydroxybenzene (hydroquinone, HQ). The sample was found to exhibit high photocatalytic activity in both light ranges (Fig. 5).

The stability of the catalyst performance was tested in three consecutive oxidation cycles for 6 hours (Fig. 5b). The photoefficiency of  $\text{Sr}_2\text{Mn}_{0.4}\text{Ti}_{0.6}\text{O}_4$  increases with increasing the number of cycles performed. Table 2 shows the values

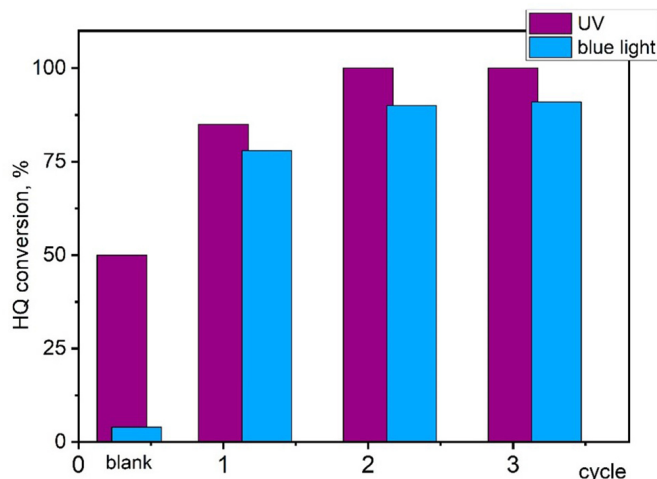


FIG. 5. Decrease in HQ concentration without catalyst (blank) and on  $\text{Sr}_2\text{Mn}_{0.4}\text{Ti}_{0.6}\text{O}_4$  as a function of irradiation type and cycling for 6 h

of the rate constants of the oxidation reaction of HQ under UV and visible light. Kinetic equations for the 1st order reaction were used. The main kinetic parameters of the investigated sample were compared with the commercial catalyst Degussa P25. The obtained data show that the photoefficiency of the catalyst  $\text{Sr}_2\text{Mn}_{0.4}\text{Ti}_{0.6}\text{O}_4$  exceeds Degussa P25 on average 4 times at UV stimulation (Table 2).

The increase in the rate of photooxidation and stabilization of photocatalytic properties of  $\text{Sr}_2\text{Mn}_{0.4}\text{Ti}_{0.6}\text{O}_4$  with increasing time of catalyst operation in HQ working solutions can be related to activation of its working surface during the first oxidation cycle. Therefore, to increase the efficiency of the catalyst before use, it should be pre-soaked for 4 – 6 hours in a working solution of hydroquinone. The approximate mechanism of photooxidation of organic substances on strontium titanates was discussed in a number of works [14–19]. Upon light stimulation of ZnO particles, photoinduced electrons migrate to the conduction band (CB), while photoinduced holes remain in the valence band (VB). The doping impurity cations (Mn) actively participate in the separation of the formed exciton  $e^-/h^+$  pair. In addition, manganese directly interacts with oxygen adsorbed on the surface of  $\text{Sr}_2\text{Ti}(\text{Mn})\text{O}_4$ . Other probable electron/hole trapping sites are charged oxygen vacancies ( $\text{VO}^+$ ,  $\text{VO}^{2+}$ ) [24]. As a result, various reactive oxygen species (ROS) such as hydroxyl and superoxide radicals ( $\bullet\text{HO}$  and  $\bullet\text{O}_2^-$ ), extremely active oxidizing agents, are formed in the reaction zone. These ROS subsequently participate in the oxidation of HQ.

High photoactivity of  $\text{Sr}_2\text{Mn}_{0.4}\text{Ti}_{0.6}\text{O}_4$  in HQ solutions indirectly indicates the formation of superoxide radical  $\bullet\text{O}_2^-$  on its working surface in the first place. In practice, the radical trap addition method is used to determine the type of

TABLE 2. Value of rate constants of HQ photooxidation reaction ( $k_s$ ) and HQ half-life ( $\tau$ ) in the presence of photocatalysts Degussa P25 and  $\text{Sr}_2\text{Mn}_{0.4}\text{Ti}_{0.6}\text{O}_4$

Catalyst	$\lambda_{\text{max}} = 253 \text{ nm}$				$\lambda_{\text{max}} = 440 - 460 \text{ nm}$		
	$k_s \cdot 10^5, \text{ s}^{-1}$ ( $n = 7, P = 0.95$ )*	$S \cdot 10^5$ **	$\varepsilon, \%$ ***	$\tau, \text{ h}$	$k_s \cdot 10^5, \text{ s}^{-1}$	$S \cdot 10^5$	$\tau, \text{ h}$
HQ blank.	1.34±0.12	0.11	8.9	14.4	0.15	0.03	132
Degussa P25	4.37±0.65	0.57	15.0	4.9	—	—	—
$\text{Sr}_2\text{Mn}_{0.4}\text{Ti}_{0.6}\text{O}_4$				$\text{Sr}_2\text{Mn}_{0.4}\text{Ti}_{0.6}\text{O}_4$			
1st cycle	10.70±7.22	5.20	6.7	1.8	7.18±2.34	1.32	2.7
2nd cycle	18.62±2.86	1.15	15.3	1.0	8.09±4.37	3.52	2.4
3rd cycle	18.90±2.90	5.21	6.8	1.0	7.72±2.67	2.16	2.5

\*Sample number  $n$  at confidence coefficient  $P$ ;

\*\*Standard deviation;

\*\*\*Relative error of the average value of  $k_s$ .

radicals. One of the most effective superoxide radical scavengers is the HQ derivative benzoquinone (BQ) [25]. According to our studies, the photoactivity of  $\text{Sr}_2\text{Ti}_{1-x}\text{Mn}_x\text{O}_4$  ( $\text{M} = \text{Mn}, \text{Cu}$ ) in the extended spectral range with respect to HQ oxidation exceeds essentially the known analogs [4–12]. Thus solid solutions  $\text{Ti}_{1-x}\text{Mn}_x\text{O}_{2-x}$  ( $0.003 \leq x \leq 0.016$ ) with spherical aggregate morphology degrade HQ by 100 % in 11 h of operation ( $\tau = 5.5$ ) in the UV and in 12 h ( $\tau = 6$ ) with 90 % yield in blue light [26]. The use of  $\text{Sr}_2\text{TiO}_4$ -based solid substitution solutions reduces the oxidation time of aromatic compounds: for comparison,  $\text{Sr}_2\text{Mn}_{0.4}\text{Ti}_{0.6}\text{O}_4$  decomposes HQ by 100 % in blue light in 5 h ( $\tau = 2.5$ ). This result makes  $\text{Sr}_2\text{Ti}_{1-x}\text{Mn}_x\text{O}_4$  promising targets for photooxidative catalysis in the visible light range.

#### 4. Conclusion

Mn-doped  $\text{Sr}_2\text{TiO}_4$  samples were prepared by SHS method with different concentrations of Mn: 5, 15, 25 and 40 mol%. XRD results indicate that the sample with maximum manganese concentration of  $\text{Sr}_2\text{Mn}_{0.4}\text{Ti}_{0.6}\text{O}_4$  is the single phase in this system. According to the results of voltammetry, EPR, UV-Vis-NIR spectroscopy, Mn in the compound appears in the oxidation degree (4+), and the forbidden band of  $\text{Sr}_2\text{Mn}_{0.4}\text{Ti}_{0.6}\text{O}_4$  narrows to 1.8 eV.

A study of the catalytic properties of  $\text{Sr}_2\text{Mn}_{0.4}\text{Ti}_{0.6}\text{O}_4$  in HQ solutions showed its photoefficiency in the UV and visible light ranges during 3 consecutive photooxidation cycles. Moreover, the photooxidation rate of HQ upon irradiation with blue light is as close as possible to that in the UV range. These results are unexpected for  $\text{Sr}_2\text{TiO}_4$  and require further investigation.

#### References

- [1] Liu B., Li L., Liu X.Q., et al.  $\text{Sr}_{n+1}\text{TiO}_{3n+1}$  ( $n = 1, 2$ ) microwave dielectric ceramics with medium dielectric constant and ultra-low dielectric loss. *J. of the American Ceramic Society*, 2017, **100** (2), P. 496–500.
- [2] Lu L.W., Lv M.L., Wang D., et al. Efficient photocatalytic hydrogen production over solid solutions  $\text{Sr}_{1-x}\text{Bi}_x\text{Ti}_{1-x}\text{Fe}_x\text{O}_3$  ( $0 \leq x \leq 0.5$ ). *Applied Catalysis B – Environmental*, 2017, **200**, P. 412–419.
- [3] Lu L.W., Lv M.L., Liu G., et al., Photocatalytic hydrogen production over solid solutions between  $\text{BiFeO}_3$  and  $\text{SrTiO}_3$ . *Applied Surface Science*, 2017, **391**, P. 535–541.
- [4] Sorkh-Kaman-Zadeh A., Dashtbozorg A. Facile chemical synthesis of nanosize structure of  $\text{Sr}_2\text{TiO}_4$  for degradation of toxic dyes from aqueous solution. *J. Molecular Liquids*, 2016, **223**, P. 921–926.
- [5] Chupakhina T.I., Eremina R.M., Gyrdasova O.I., et al. Perovskite-like  $\text{La}_x\text{Sr}_{2-x}\text{Ti}_{1-x/2}\text{Cu}_{x/2}\text{O}_4$  ( $x = 0.2, 0.3, 0.5$ ) oxides with the  $\text{K}_2\text{NiF}_4$ -type structure active in visible light range: new members of the photocatalyst family. *J. of the Korean Ceramic Society*, 2024, **61** (5).
- [6] Skvortsova L.N., Chukhlomina L.N., Gormakova N.A., et al. Investigation of B-N-Fe and Si-N-Fe catalysts ability to remove phenol compounds from water in presence of ozone and UV irradiation. *Vestnik Tomskogo Gosudarstvennogo Universiteta*, 2013, **370**, P. 190–193.
- [7] Sobczynski A., Duczmal L., Zmudzinski W., Phenol destruction by photocatalysis on  $\text{TiO}_2$ : an attempt to solve the reaction mechanism. *J. Molecular Catalysis A – Chemical*, 2004, **213** (2), P. 225–230.
- [8] Chen X.B., Shen S.H., Guo L.J., et al. Semiconductor-based Photocatalytic Hydrogen Generation. *Chemical Reviews*, 2010, **110** (11), P. 6503–6570.
- [9] Sun X.Q., Xie Y.H., Wu F.F., et al. Photocatalytic Hydrogen Production over Chromium Doped Layered Perovskite  $\text{Sr}_2\text{TiO}_4$ . *Inorganic Chemistry*, 2015, **54** (15), P. 7445–7453.
- [10] Sun X.Q., Xu X.X. Efficient photocatalytic hydrogen production over La/Rh co-doped Ruddlesden-Popper compound  $\text{Sr}_2\text{TiO}_4$ . *Applied Catalysis B – Environmental*, 2017, **210**, P. 149–159.
- [11] Sun X.Q., Mi Y.L., Jiao F., et al. Activating Layered Perovskite Compound  $\text{Sr}_2\text{TiO}_4$  via La/N Codoping for Visible Light Photocatalytic Water Splitting. *ACS Catalysis*, 2018, **8** (4), P. 3209–3221.
- [12] Yu J.X., Xu X.X. Fluorination over Cr doped layered perovskite  $\text{Sr}_2\text{TiO}_4$  for efficient photocatalytic hydrogen production under visible light illumination. *J. of Energy Chemistry*, 2020, **51**, P. 30–38.
- [13] Pany S., Nashim A., Parida K. Titanium-Based Mixed Metal Oxide Nanocomposites for Visible Light-Induced Photocatalysis. *Nanocomposites for Visible Light-Induced Photocatalysis*, 2017, P. 295–331.
- [14] Iriani Y., Afriani R., Sandi D.K., et al. Co-precipitation Synthesis and Photocatalytic Activity of Mn doped  $\text{SrTiO}_3$  for the Degradation of Methylene Blue Wastewater. *Evergreen Joint J. of Novel Carbon Resource Sciences & Green Asia Strategy*, 2022, **9** (4), P. 1039–1045.
- [15] Patial S., Hasija V., Raizada P., et al. Tunable photocatalytic activity of  $\text{SrTiO}_3$  for water splitting: Strategies and future scenario. *J. Environmental Chemical Engineering*, 2020, **8** (3), 103791.
- [16] Chupakhina T.I., Deeva Y.A., Melnikova N.V., et al. Synthesis, structure and dielectric properties of new oxide compounds  $\text{Ln}_{1-x}\text{Sr}_{1+x}\text{Cu}_{x/2}\text{Ti}_{1-x/2}\text{O}_4$  ( $\text{Ln} = \text{La}, \text{Pr}, \text{Nd}$ ) belonging to the structural type of  $\text{K}_2\text{NiF}_4$ . *Mendeleev Communications*, 2019, **29** (3), P. 349–351.
- [17] Thanh T.D., Phan T.L., Oanh L.M., et al. Influence of Mn doping on the crystal structure, and optical and magnetic properties of  $\text{SrTiO}_3$  compounds. *IEEE Trans. Magn.*, 2014, **201450**, P. 1–4.
- [18] Mansoor H., Harrigan W.L., Lehuta K.A., et al. Reversible Control of the Mn Oxidation State in  $\text{SrTiO}_3$  Bulk Powders. *Front. Chem.*, 2019, **7** (353), P. 1–8.
- [19] Shannon R.D., Prewitt C.T. Effective ionic radii in oxides and fluorides. *Acta Crystallogr. B*, 1969, **25** (5), P. 925–946.
- [20] Huber D.L. Linear temperature dependence of electron spin resonance linewidths in  $\text{La}_{0.7}\text{Ca}_{0.3}\text{MnO}_3$  and  $\text{YBaMn}_2\text{O}_6$ . 2013, arXiv:1309.6353.
- [21] Schaile S., et al. Korringa-like relaxation in the high-temperature phase of A-site ordered  $\text{YBaMn}_2\text{O}_6$ . *Physical Review B*, 2012, **85** (20), 205121.
- [22] Stoyanova R., Zhecheva E., Vassilev S.  $\text{Mn}^{4+}$  environment in layered  $\text{Li}[\text{Mg}_{0.5-x}\text{Ni}_x\text{Mn}_{0.5}]\text{O}_2$  oxides monitored by EPR spectroscopy. *J. Solid State Chemistry*, 2006, **179** (2), P. 378–388.
- [23] Li K., et al. Achieving efficient red-emitting  $\text{Sr}_2\text{Ca}_{1-\delta}\text{Ln}_\delta\text{WO}_6$ :  $\text{Mn}^{4+}$  ( $\text{Ln} = \text{La}, \text{Gd}, \text{Y}, \text{Lu}$ ,  $\delta = 0.10$ ) phosphors with extraordinary luminescence thermal stability for potential UV-LEDs application via facile ion substitution in luminescence-ignorable  $\text{Sr}_2\text{CaWO}_6$ :  $\text{Mn}^{4+}$ . *ACS Materials Letters*, 2020, **2** (7), P. 771–778.
- [24] Zheng W.C., Wu X.X. Studies of EPR g factors of the isoelectronic  $3d^3$  series  $\text{Cr}^{3+}$ ,  $\text{Mn}^{4+}$  and  $\text{Fe}^{5+}$  in  $\text{SrTiO}_3$  crystals. *J. of Physics and Chemistry of Solids*, 2005, **66** (10), P. 1701–1704.

- [25] Tan H., Zhao Z., Zhu W.B., et al. Oxygen vacancy enhanced photocatalytic activity of perovskite SrTiO<sub>3</sub>. *ACS Appl. Mater. Interfaces*, 2014, **6**, P. 19184–19190.
- [26] Wang Zh., Murugananthan M., Zhang Ya. Graphitic carbon nitride based photocatalysis for redox conversion of arsenic(III) and chromium(VI) in acid aqueous solution. *Applied Catalysis B – Environmental*, 2019, **248**, P. 349–356.
- [27] Baklanova I.V., Krasil'nikov V.N., Gyrdasova O.I., & Buldakova L.Y. Synthesis and optical and photocatalytic properties of manganese-doped titanium oxide with a three-dimensional architecture of particles. *Mendeleev Communications*, 2016, **26**, P. 335–337.

---

*Submitted 17 June 2024; revised 13 August 2024; accepted 14 August 2024*

*Information about the authors:*

*Tatyana I. Chupakhina* – Institute of Solid State Chemistry UB RAS, Pervomayskaya, 91, Ekaterinburg, 620990, Russia; ORCID 0000-0002-1317-3803; chupakhina@yandex.ru

*Olga I. Gyrdasova* – Institute of Solid State Chemistry UB RAS, Pervomayskaya, 91, Ekaterinburg, 620990, Russia; ORCID 0000-0002-0680-6094; gyrdasova@ihim.uran.ru

*Anastasya M. Uporova* – Institute of Solid State Chemistry UB RAS, Pervomayskaya, 91, Ekaterinburg, 620990, Russia; ORCID 0009-0006-1219-8909; nastyauporova99@gmail.com

*Larisa Y. Buldakova* – Institute of Solid State Chemistry UB RAS, Pervomayskaya, 91, Ekaterinburg, 620990, Russia; ORCID 0000-0003-3642-7121; buldakova@ihim.uran.ru

*Mikhail Y. Yanchenko* – Institute of Solid State Chemistry UB RAS, Pervomayskaya, 91, Ekaterinburg, 620990, Russia; ORCID 0000-0001-8306-906X; yanchenko@ihim.uran.ru

*Dzhavid V. Mamedov* – Zavoisky Physical-Technical Institute, FRC Kazan Scientific Center of RAS, Kazan, 420029, Russia; javi-m@yandex.ru

*Yulia A. Deeva* – Institute of Solid State Chemistry UB RAS, Pervomayskaya, 91, Ekaterinburg, 620990, Russia; ORCID 0000-0003-1207-7331; juliahik@mail.ru

*Inna V. Baklanova* – Institute of Solid State Chemistry UB RAS, Pervomayskaya, 91, Ekaterinburg, 620990, Russia; ORCID 0000-0002-5643-7004; inna.b@bk.ru

*Conflict of interest:* the authors declare no conflict of interest.

## The control of by-product formation rates in photocatalytic hydrogen evolution reaction from organic substances over Pt/g-C<sub>3</sub>N<sub>4</sub>

Ksenia O. Potapenko<sup>a</sup>, Egor E. Aydakov<sup>b</sup>, Evgeny Y. Gerasimov<sup>c</sup>, Ekaterina A. Kozlova<sup>d</sup>

Boreskov Institute of Catalysis, SB RAS, Novosibirsk, 630090, Russia

<sup>a</sup>potapenko@catalysis.ru, <sup>b</sup>e.ajdakov@g.nsu.ru, <sup>c</sup>gerasimov@catalysis.ru, <sup>d</sup>kozlova@catalysis.ru

Corresponding author: Ksenia O. Potapenko, potapenko@catalysis.ru

PACS 82.65.+r, 68.43.-h

**ABSTRACT** The results on the photocatalytic activity of 0 – 2 wt.% Pt/g-C<sub>3</sub>N<sub>4</sub> in the hydrogen evolution reaction under visible light (430 nm) are presented. Triethanolamine (TEOA), glycerol, glucose and cellulose were used as electron donor. During the reaction, not only the target product, hydrogen, but also by-products of the reaction in the gas phase, namely CO and CO<sub>2</sub>, were controlled. In order to study the chemical composition, microstructure and optical properties, the samples were investigated by XPS, TEM and diffuse reflection methods. The maximum hydrogen evolution rate obtained for 1 % Pt/g-C<sub>3</sub>N<sub>4</sub> from TEOA solution was 3.96 μmol·min<sup>-1</sup>, with a selectivity of 100 %. The use of glycerol and cellulose resulted in the production of syngas, and varying the platinum content allowed the selectivity of the process to vary (42.4 to 100 %). Glucose using led to the formation of a mixture of CO<sub>2</sub> and H<sub>2</sub> with a selectivity of 90 % or higher. In general, hydrogen-containing mixtures obtained using organic substrates can be further used in various applications.

**KEYWORDS** photocatalysis, hydrogen evolution, carbon nitride, triethanolamine, glycerol, cellulose, glucose, visible light

**ACKNOWLEDGEMENTS** This work was supported by the Ministry of Science and Higher Education of Russian Federation within the governmental order for Boreskov Institute of Catalysis (FWUR-2024-0033).

**FOR CITATION** Potapenko K.O., Aydakov E.E., Gerasimov E.Y., Kozlova E.A. The control of by-product formation rates in photocatalytic hydrogen evolution reaction from organic substances over Pt/g-C<sub>3</sub>N<sub>4</sub>. *Nanosystems: Phys. Chem. Math.*, 2024, **15** (4), 548–557.

### 1. Introduction

Currently, one third of the world's energy is produced by burning coal, with coal-fired power plants emitting large amounts of greenhouse gases into the atmosphere [1]. With the depletion of the world's fossil fuel reserves and global warming, the search for alternative energy sources is an urgent task today [2, 3]. Solar energy is sustainable, renewable and more environmentally friendly energy source than conventional energy sources as it has no negative impact on the environment [4]. In recent times, there has been a worldwide trend to convert the inexhaustible energy of solar irradiation into useful products, such as hydrogen in the process of photocatalytic hydrogen production using semiconductor catalysts [5, 6]. However, the realization of such a kinetically slow process requires the development of materials active under visible irradiation, since the spectral range of solar irradiation consists more of visible light [7].

The most common photocatalyst is titanium dioxide, as they are commercially available (e.g. Degussa P25) and non-toxic [8, 9]. However, the application area in photocatalytic reactions is limited to the UV range. Graphitic carbon nitride, an n-type semiconductor, is a new generation photocatalyst because it is nontoxic, thermally stable, chemically stable in both alkaline and acidic media, and its band structure is suitable for the process of photocatalytic hydrogen evolution [10, 11]. However, the activity of pristine g-C<sub>3</sub>N<sub>4</sub> in such a process is low due to the rapid recombination of electrons and holes [12]. Currently, several strategies have been proposed to increase the activity of graphitic carbon nitride, including doping with various heteroatoms [13, 14], deposition of co-catalysts [15–17], grinding of graphitic carbon nitride [18], surface engineering including nanosheet formation [19, 20], surface modification with acids [21], and so on. It is also interesting to modify the synthesis procedure, using different nitrogen-containing precursors, including combining them in different ratios [22]. For example, using a mixture of melamine and urea as precursors, a high surface area of g-C<sub>3</sub>N<sub>4</sub> can be achieved due to the formation of a supramolecular melamine-cyanuric acid complex during synthesis [22].

Platinum nanoparticles are known to increase photocatalytic activity. In this case, the formation of Schottky barrier between the metal (Pt, Au and Ag) and semiconductor (g-C<sub>3</sub>N<sub>4</sub>) is observed, which leads to an increase in photocatalytic activity due to an increase in the lifetime of electron-hole pairs [9]. Noble metal nanoparticles “capture” electrons in the conduction band of the semiconductor, which further reduce protons to form hydrogen. In addition, the work of electron

escape from vacuum for Pt in the metallic state is 5.40 eV, which is the highest value among noble metals [10]. Based on this, the choice of co-catalyst (Pt) for surface modification of graphitic carbon nitride was carried out.

When carrying out the photocatalytic process in solutions of organic compounds, an important task is to analyze all products in the gas phase, such as CO and CO<sub>2</sub>, which can be formed as a result of complete or partial oxidation of substrates. The composition of the resulting hydrogen-containing mixtures influences their further applications.

In this work, we have shown for the first time the complex influence of the mass fraction of platinum deposited on the surface of graphitic carbon nitride and the electron donor used on the activity and selectivity of photocatalytic hydrogen evolution under visible light irradiation (430 nm). Not only model substrates – triethanolamine, glycerol, but also components of plant biomass – glucose and cellulose – were used as electron donors. The novelty of the work consists in determining the correlation between the electron donor, the mass fraction of platinum Pt/g-C<sub>3</sub>N<sub>4</sub> and the selectivity of the photocatalytic hydrogen evolution reaction.

## 2. Materials and methods

### 2.1. Photocatalyst synthesis

A method to obtain graphitic carbon nitride is described in [22]. Briefly, the required amount of a mixture of melamine (Sigma-Aldrich, USA, 99 %) and urea (Acros Organics, USA, 99 %) in a mass ratio of 1:3 was placed in a crucible, then in a muffle oven with subsequent heating at a rate of 10 °C/min to 525 °C, held for 1 hour. The resulting powder was cooled to room temperature, grinded and used further.

The deposition of platinum particles was carried out by soft chemical reduction method. 500 mg of prepared g-C<sub>3</sub>N<sub>4</sub> was placed in a glass beaker, suspended in a small amount of distilled water, a solution of 0.1 M H<sub>2</sub>PtCl<sub>6</sub> (Reakhim, Russia, 98 %) was added dropwise and stirred for an hour. Then an excess of 0.1 M NaBH<sub>4</sub> solution was added and stirred for one hour. The precipitate was washed several times and then dried at 50 °C for 3 hours. The mass fraction of deposited platinum particles was varied during the synthesis. The catalysts were denoted by *x* % Pt/g-C<sub>3</sub>N<sub>4</sub>, where *x* = 0.1, 0.5, 1, 2.

### 2.2. Photocatalyst characterization

The photocatalysts were characterized by physicochemical methods of investigation, including X-ray photoelectron spectroscopy (XPS), transmission electron microscopy (TEM), diffuse reflectance electron spectroscopy (DRES) and UV-vis spectroscopy.

The chemical composition of the sample was investigated by X-ray photoelectron spectroscopy (XPS) on an electron spectrometer of SPECS SurfaceNanoAnalysisGmbH (Germany). The spectrometer was equipped with a PHOIBOS-150-MCD-9 hemispherical analyzer, XR-50 X-ray characteristic radiation source with double Al/Mg anode. Non-monochromatized radiation AlK $\alpha$  ( $h\nu = 1486.61$  eV) was used to record the spectra. The position of the peak corresponding to the carrier was used to account for the charging effect of the samples (Table 1). Relative concentrations of elements in the analysis zone were determined on the basis of integral intensities of the XPS peaks taking into account the photoionization cross section of the corresponding terms. For detailed analysis, decomposition of spectra into individual components was used [23]. Accordingly, after background subtraction using the Shirley method [24], the experimental curve was decomposed into a number of lines corresponding to the photoemission of electrons from atoms in different chemical environments. The data were processed using the CasaXPS program package [25]. The shape of the peaks was approximated by a symmetric function obtained by summation of the Gauss and Lorentz functions.

TABLE 1. Relative atomic concentrations of elements in the near-surface layer of the studied catalysts

Sample	[N]/[C]	[Pt]/[C]	%, Pt <sup>0</sup>	%, Pt <sup>2+</sup>	[O <sub>x</sub> ]/[C]	[Na]/[C]
<b>0.1 % Pt/g-C<sub>3</sub>N<sub>4</sub></b>	1.35	0.001	68	32	0.15	0.03
<b>0.5 % Pt/g-C<sub>3</sub>N<sub>4</sub></b>	1.33	0.004	83	17	0.18	0.03
<b>1 % Pt/g-C<sub>3</sub>N<sub>4</sub></b>	1.36	0.008	85	15	0.16	0.03
<b>2 % Pt/g-C<sub>3</sub>N<sub>4</sub></b>	1.33	0.008	82	18	0.20	0.03

\*[C] – carbon in the C–N=C carrier (288.1 eV);

\*\*[Carbon] – surface carbon of C=C (284.9 eV);

\*\*\*[O<sub>x</sub>] – surface oxygen-containing impurities.

The microstructure of the photocatalysts was studied by transmission electron microscopy (TEM) using a ThemisZ microscope (Thermo Fisher Scientific, USA) at an accelerating voltage of 200 kV.

The UV-vis diffuse reflectance spectra were obtained with the use of Shimadzu UV2501 PC (Shimadzu, Kyoto, Japan) spectrophotometer with an ISR-240A diffuse reflectance attachment in the wavelength range from 400 to 850 nm.

### 2.3. Photocatalytic experiments

The photocatalytic hydrogen evolution reaction was carried out in the reactor shown in Fig. 1. 50 mL of electron donor (10 vol.% triethanolamine (AO Base #1 Chemicals, h.), 0.4 M glycerol (AO Base #1 Chemicals, h.), 0.2 M  $\alpha$ -D(+)-glucose (Acros Organics, 98 %), 3 M  $\alpha$ -cellulose (Sigma)+ 0.1 M NaOH (Thermo Scientific, 98.5 %), and 25 mg of catalyst, which was pretreated in an ultrasonic bath for 10 minutes. The reactor was then purged with argon for 20 minutes. An LED with a wavelength of 430 nm was used as the light source. The gaseous reaction products including H<sub>2</sub>, CO, CO<sub>2</sub> were analyzed using a CHROMOS GC-1000 gas chromatograph equipped with a methanator and a thermal conductivity detector.

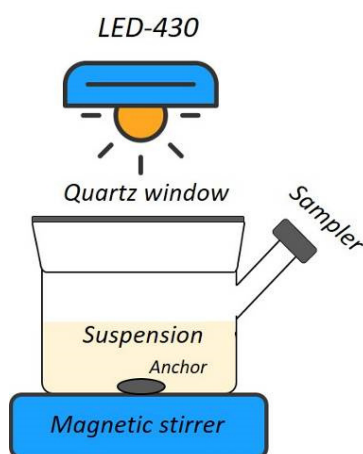


FIG. 1. Schematic representation of the reactor for photocatalytic hydrogen evolution reaction

In addition to the photocatalytic hydrogen evolution rate, the apparent quantum efficiency (AQE) was calculated using the formula

$$AQE = \frac{2W(H_2)}{N_f},$$

where  $W(H_2)$  is the hydrogen evolution rate, mol/min;  $N_f$  is the photon flux, mol/min.

## 3. Results and discussion

### 3.1. Photocatalyst characterization

All investigated catalysts were characterized by X-ray photoelectron spectroscopy. Peaks corresponding to Pt, N, C, Na, and O were detected in the XPS spectra of the catalysts. The relative concentrations (atomic ratios) of elements in the near-surface layer of the catalysts determined from the XPS data are presented in Table 1. The values of binding energies of  $C1s$ ,  $N1s$ ,  $Pt4f_{7/2}$  peaks are presented in Table 2. It is important to note that the peak in the  $C1s$  spectrum of carbon corresponding to the spectrum of the carrier ( $g-C_3N_4$ ) was chosen for calibration of the binding energy scale. At the same time, the obtained values of binding energy of the  $C1s$  carbon peak included in the carbon impurities on the catalyst surface lie in the range of 284.8 – 285.0 eV (Table 2), which confirms the correctness of the calibration.

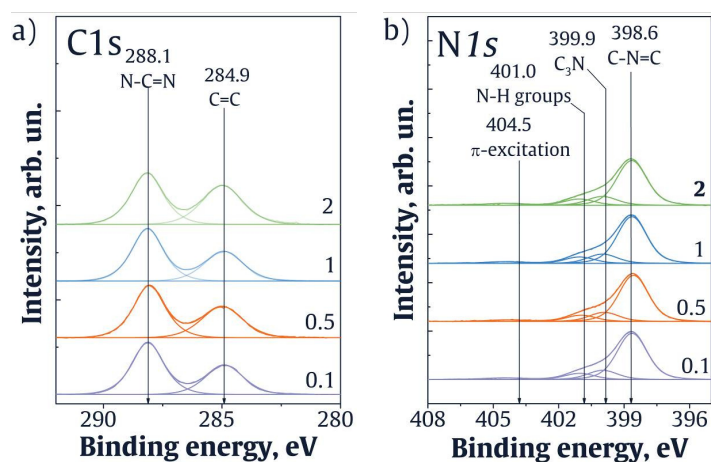
According to the data presented in Table 1, platinum in the investigated samples is represented by two forms: oxidized ( $Pt^{2+}$ ) and reduced ( $Pt^0$ ), and with the increase of its content in the samples, the fraction of metallic platinum increases and reaches 85 % for the sample 1 % Pt/ $g-C_3N_4$ .

Figure 2 shows the  $C1s$  and  $N1s$  spectra of the catalysts. The  $C1s$  spectrum is well described by two peaks with binding energies around 284.9 and 288.1 eV. The first peak is characteristic of carbon-containing impurities present on the surface of the catalysts. The second peak is characteristic of  $C1s$   $g-C_3N_4$  and corresponds to carbon forming bonds with nitrogen atoms in the  $g-C_3N_4$  structure [26, 27]. In the case of the  $N1s$  spectrum, 4 peaks with binding energies around 398.6, 399.9, 401.0, and 404.5 eV are observed. According to literature data, the first peak refers to nitrogen atoms forming a C–N=C bond, the second peak refers to form a bond with three carbon atoms N–(C)<sub>3</sub>, and the third peak refers to N–H terminal groups [26, 27]. The fourth peak corresponds to an excited  $\pi$ -bond.

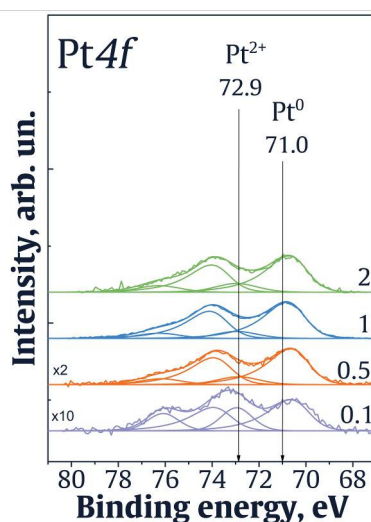
Figure 3 shows the  $Pt4f$  spectra of the studied catalysts. The  $4f$ -level of platinum is known to split into two sublevels  $Pt4f_{7/2}$  and  $Pt4f_{5/2}$  due to spin-orbit interaction, the spin-orbit splitting of which is 3.33 eV. In the literature, for massive

TABLE 2. Values of  $CI_s$ ,  $NI_s$  and  $Pt4f_{7/2}$  binding energies. The spectra are calibrated on the  $CI_s$  line (EeSv = 288.1 eV)

Sample	$CI_s$		$NI_s$				$Pt4f_{7/2}$	
	C=C, 284.9 eV	C-N=C, 288.1 eV	C-N=C, 398.6 eV	(C) <sub>3</sub> -N, 399.9 eV	N-H, 401.0 eV	$\pi$ , 404.5 eV	$Pt^0$ , 71.0 eV	$Pt^{2+}$ , 72.9 eV
0.1 % Pt/ g-C <sub>3</sub> N <sub>4</sub>	40	60	72	14	10	4	68	32
0.5 % Pt/ g-C <sub>3</sub> N <sub>4</sub>	42	58	73	14	10	3	83	17
1 % Pt/ g-C <sub>3</sub> N <sub>4</sub>	40	60	72	14	10	4	85	15
2 % Pt/ g-C <sub>3</sub> N <sub>4</sub>	47	53	72	14	10	4	82	18

FIG. 2.  $CI_s$  and  $NI_s$  spectra of the carrier. The  $NI_s$  spectrum is normalized by the integral intensity of the  $CI_s$  peak corresponding to the carrier spectrum (g-C<sub>3</sub>N<sub>4</sub>)

metallic platinum samples, the binding energy of  $Pt4f_{7/2}$  is 71.1 – 71.6 eV [28]. In turn, for massive PtO, PtO<sub>2</sub> and Pt(OH)<sub>4</sub>, the values of  $Pt4f_{7/2}$  binding energy lie in the range of 72.3 – 73.0, 74.0 – 74.1 and 74.2 – 74.4 eV [29–31]. In the case of the investigated catalysts, the  $Pt4f$  spectrum is approximated by two  $Pt4f_{7/2}$ - $Pt4f_{7/2}$  doublets with  $Pt4f_{7/2}$  binding energies around 70.8 – 71.0 and 72.8 – 72.9 eV, respectively. These doublets are related to platinum in the metallic state as well as to platinum in the oxidized state,  $Pt^{2+}$ .

FIG. 3.  $Pt4f$  spectra of the investigated catalysts. The spectra were normalized by the integral intensity of the  $CI_s$  peak corresponding to the spectrum of the g-C<sub>3</sub>N<sub>4</sub>

The microstructure of the photocatalysts was studied by transmission electron microscopy (TEM). For the 0.1 % Pt/g-C<sub>3</sub>N<sub>4</sub> catalyst, small single Pt particles of size  $2.1 \pm 0.9$  nm uniformly distributed on the surface of graphitic carbon nitride g-C<sub>3</sub>N<sub>4</sub> were observed. With the increase in platinum loading (0.5 – 2 %), agglomeration of Pt particles is observed. Thus, in the case of 0.5 % Pt/g-C<sub>3</sub>N<sub>4</sub> the size of agglomerates is about 12 nm, and for 2 % Pt/g-C<sub>3</sub>N<sub>4</sub> it is about 50 nm. It should be noted that according to the particle size distribution (Fig. 4), the average particle size does not practically change with increasing platinum loading. The agglomeration of platinum particles may be related to the supersaturation of the graphitic carbon nitride surface by the platinum precursor H<sub>2</sub>PtCl<sub>6</sub>. The literature indicates that when using the precursor Pt(IV), namely H<sub>2</sub>PtCl<sub>6</sub>, there is no formation of  $\pi$ -complexes with carbon-containing surface, and therefore leads to a high degree of agglomeration of platinum particles [32].

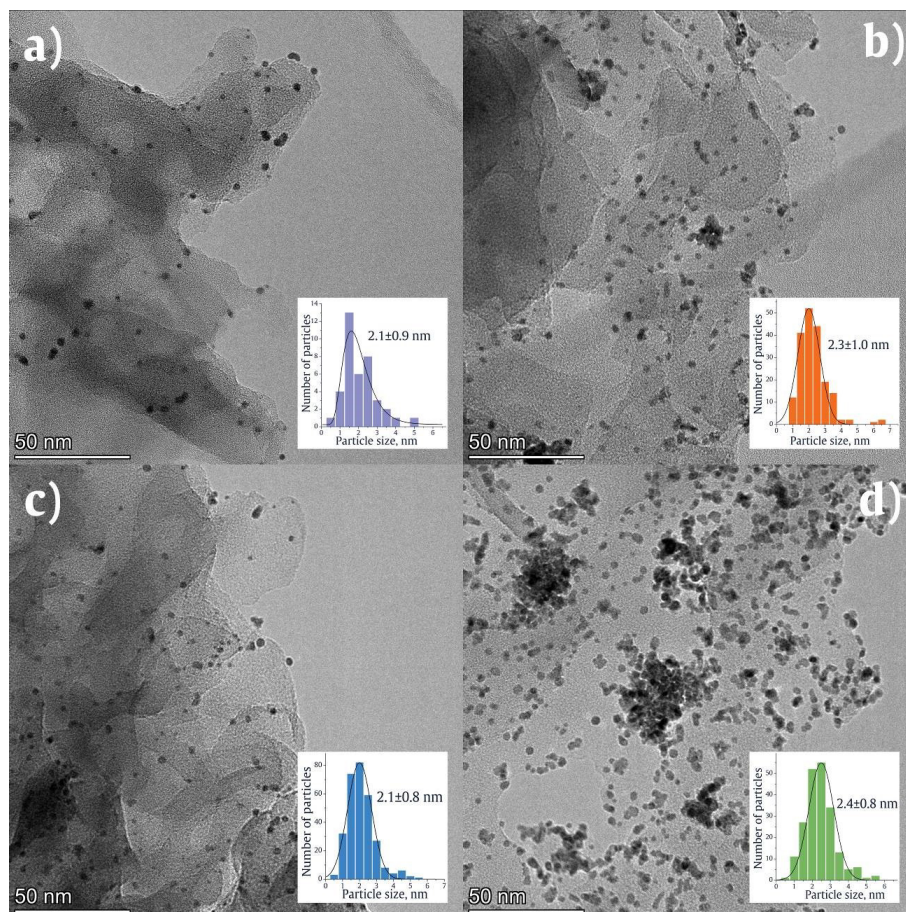


FIG. 4. SEM images and particle size distribution for 0.1 (a); 0.5 (b); 1 (c); 2 (d) % Pt/g-C<sub>3</sub>N<sub>4</sub> catalysts

The diffuse reflectance spectra for 0 – 2 % Pt/g-C<sub>3</sub>N<sub>4</sub> catalysts are shown in Fig. 5. Light absorption is shown to increase in the region of 450 – 800 nm when platinum particles are deposited on the surface of graphitic carbon nitride g-C<sub>3</sub>N<sub>4</sub>, which is due to the effect of surface plasmon resonance of Pt particles (Fig. 5a). The determined bandgap energies of all catalysts was carried out in Tauc coordinates (Fig. 5b) by extrapolating the dependence of  $(F(R) \cdot E)^{0.5}$  of  $E$ . For g-C<sub>3</sub>N<sub>4</sub>, 0.1 % Pt/g-C<sub>3</sub>N<sub>4</sub>, 0.5 % Pt/g-C<sub>3</sub>N<sub>4</sub>, 1 % Pt/g-C<sub>3</sub>N<sub>4</sub>, 2 % Pt/g-C<sub>3</sub>N<sub>4</sub>, the bandgap energies were 2.62, 2.69, 2.66, 2.63, 2.66 eV, respectively.

### 3.2. Photocatalytic activity

All synthesized Pt/g-C<sub>3</sub>N<sub>4</sub> catalysts were tested in the reaction of photocatalytic hydrogen evolution from aqueous solutions of electron donors: 10 vol.% triethanolamine, 0.4 M glycerol, 0.2 M  $\alpha$ -D(+)-glucose (glucose), 3 M  $\alpha$ -cellulose (cellulose) + 0.1 M NaOH. Summary on the rates of formation of photocatalytic reaction products for all catalysts from aqueous solutions of electron donors is presented in Table 3.

When studying the dependence of the hydrogen evolution rate on the platinum content on the surface of graphitic carbon nitride, a dome-shaped dependence was obtained in the case of using TEOA, glycerol and glucose as electron donors, as shown in Fig. 6. An increase in the platinum content (0.1 – 1 %) on the surface of graphitic carbon nitride g-C<sub>3</sub>N<sub>4</sub> leads to an increase in the number of adsorption centers for organic molecules [33, 34] and an increase in metal-semiconductor contacts, due to which the lifetime of photogenerated charges increases [35]. On the other hand, high metal concentration (2 %) hinders the light absorption and also limits the adsorption of organic electron donors. When

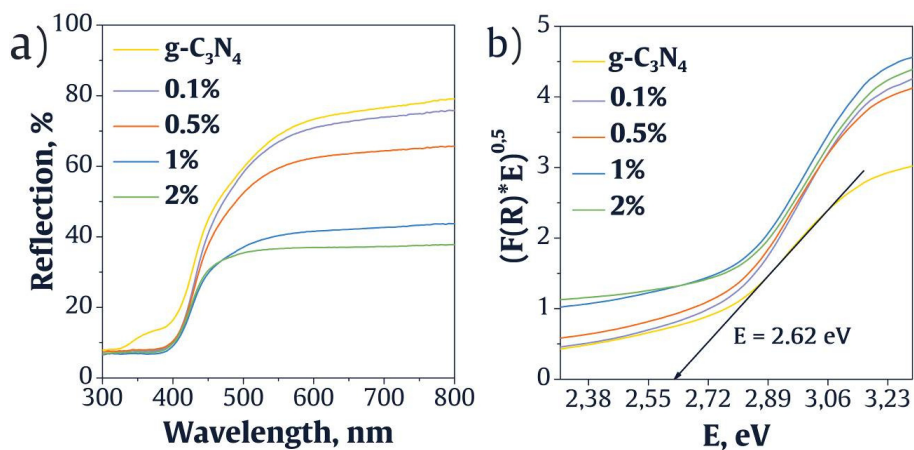


FIG. 5. Electronic diffuse reflectance spectra of UV-visible spectroscopy (a) and plot of the dependence of  $(F(R) \cdot E)^{0.5}$  on  $E$ (b)

TABLE 3. Summary table of the rates of formation of photocatalytic reaction products for 0 – 2 % Pt/g-C<sub>3</sub>N<sub>4</sub> catalysts from aqueous solutions of electron donors

Electron donor	$x$ % Pt/g-C <sub>3</sub> N <sub>4</sub>	W			AQE, %
		H <sub>2</sub> , $\mu\text{mol} \cdot \text{min}^{-1}$	CO, $\text{nmol} \cdot \text{min}^{-1}$	CO <sub>2</sub> , $\text{nmol} \cdot \text{min}^{-1}$	
TEOA	0.1	0.7	0	0	0.5
	0.5	1.9			1.2
	1	4.0			2.6
	2	2.8			1.8
Glycerol	0.1	0.1	1.4	0	<0.1
	0.5	0.2	2.2		0.1
	1	0.3	0.2		0.2
	2	0.1	0.4		<0.1
Glucose	0.1	0.06	0	0.4	<0.1
	0.5	0.03		3.6	<0.1
	1	0.2		15.2	0.1
	2	0.1		10.0	<0.1
Cellulose	0.1	0.0008	0.5	0	<0.1
	0.5	0.006	1.3		<0.1
	1	0.02	1.0		<0.1
	2	0.07	1.0		<0.1

the mass fraction of Pt increases, according to TEM images (Fig. 4), nanoparticles begin to aggregate, which is one of the possible reasons for the decrease in catalytic activity. According to the XPS results (Table 1), the highest proportion of metallic platinum, namely 85 %, is observed for the 1 % Pt/g-C<sub>3</sub>N<sub>4</sub> catalyst, which in turn is the most active in the process of hydrogen evolution for all the substrates used. Thus, the separation of photogenerated electrons and holes proceeds more efficiently with higher amounts of reduced platinum (Pt<sup>0</sup>). In general, the observed dependence is a combination of several factors: the platinum state (oxidized Pt<sup>2+</sup>, reduced Pt<sup>0</sup>) and its content on the surface of graphitic carbon nitride g-C<sub>3</sub>N<sub>4</sub>, as well as the distribution of platinum particles on the catalyst surface. The maximum rate of hydrogen evolution was observed from TEOA solution (10 vol.%) when 1 % Pt/g-C<sub>3</sub>N<sub>4</sub> was added and was 3.96  $\mu\text{mol}\cdot\text{min}^{-1}$ .

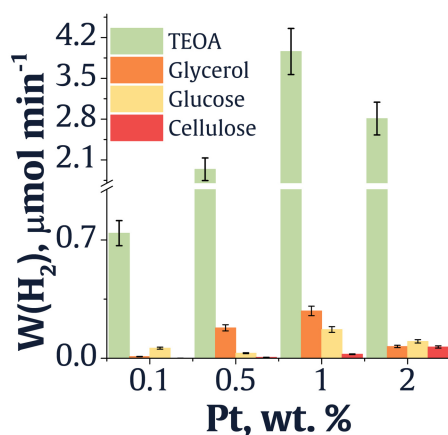


FIG. 6. Dependence of hydrogen evolution rate on Pt loading on g-C<sub>3</sub>N<sub>4</sub>. Experimental conditions:  $m(\text{catalyst}) = 25 \text{ mg}$ ,  $V(\text{suspension}) = 50 \text{ ml}$ ,  $\lambda = 430 \text{ nm}$ ,  $t(\text{reaction}) = 90 \text{ min}$ ,  $C(\text{TEOA}) = 10 \text{ vol.}\%$ ;  $C(\text{Glycerol}) = 0.4 \text{ M}$ ;  $C(\text{Glucose}) = 0.2 \text{ M}$ ;  $C(\text{Cellulose}) = 3 \text{ M}$

In addition to the identification of the target product, hydrogen, the presence of carbon monoxide and carbon dioxide in the gas phase was additionally analyzed. The formation of such products can occur in the process of complete or partial oxidation of organic substrates. The dependence of the product ratio on the mass fraction of platinum on the surface of graphitic carbon nitride using TEOA (Fig. 7a), glycerol (Fig. 7b), glucose (Fig. 7c), cellulose (Fig. 7d) as electron donors is presented in Fig. 7.

When the photocatalytic hydrogen evolution reaction is carried out from triethanolamine solution, the formation of pure hydrogen is observed. Impurity-free hydrogen can be used to power fuel cells, since proton exchange membranes inside fuel cells are known to undergo CO poisoning [36]. Probably, during photocatalytic transformations triethanolamine is oxidized to glyceraldehyde by photogenerated holes, while complete oxidation does not occur.

The use of glycerol and cellulose results in a mixture consisting of hydrogen and carbon monoxide. A general pattern is observed: the mass content of platinum on the surface of graphitic carbon nitride strongly influences the distribution of reaction products, and hence the selectivity for CO and H<sub>2</sub>. In particular, in cellulose solution at increasing of Pt loading mainly reaction product in gas phase is hydrogen, while for catalysts 0.1 % Pt/g-C<sub>3</sub>N<sub>4</sub> and 0.5 % Pt/g-C<sub>3</sub>N<sub>4</sub> the CO:H<sub>2</sub> ratio is 1:1.3 and 1:3.7, respectively. This result can be explained by the fact that Pt is a catalyst for hydrogenation, so with the increase of its loading the amount of CO decreases both in the case of the reaction in glycerol solution and in cellulose solution [37,38]. Hydrogenation of carbon monoxide to various reaction products (probably light hydrocarbons) takes place [38].

Varying the ratio of gases in the carbon monoxide:hydrogen mixture makes it possible to obtain products for the production of synthetic fuel (synfuel). Synthesis of synfuel is extremely important because such combustible liquids are used as motor fuel in internal combustion engines [39]. The combustion of synfuel proceeds without the formation of soot and NO<sub>x</sub>, etc [40]. Thus, for production of ethylene glycol and vinyl acetate synthesis gas is used in the ratio 1:1 (CO:H<sub>2</sub>), and for realization of steam conversion process the ratio 1:2,2 (CO:H<sub>2</sub>) is necessary [41].

As for the products of substrate oxidation in the liquid phase, according to literature data, in the case of glycerol, oxidation proceeds through the C–C bond, which ultimately leads to the formation of the main product C<sub>2</sub> in the liquid phase – glycolic acid [42]. This is explained by the fact that irradiation of the photocatalyst results in the formation of a large number of reactive oxygen species, which induce the conversion of the intermediate product, glyceraldehyde, into glycolic acid. The formation of glyceric acid and dihydroxyacetone is also observed [43]. When carrying out the photocatalytic reaction in a weakly alkaline cellulose solution, the mechanism of oxidation of the organic substrate is more complex, since such a process can proceed in several directions simultaneously. Thus, oxidation of primary alcohol groups (C<sub>6</sub>) with formation of aldehyde and then carboxyl groups; secondary alcohol groups (C<sub>2</sub> and C<sub>3</sub>) with formation of ketones and their subsequent oxidation to carboxyl groups is possible [44]. In general, glycerol and cellulose are resistant to oxidation by photogenerated holes, so complete oxidation of substrates does not occur.

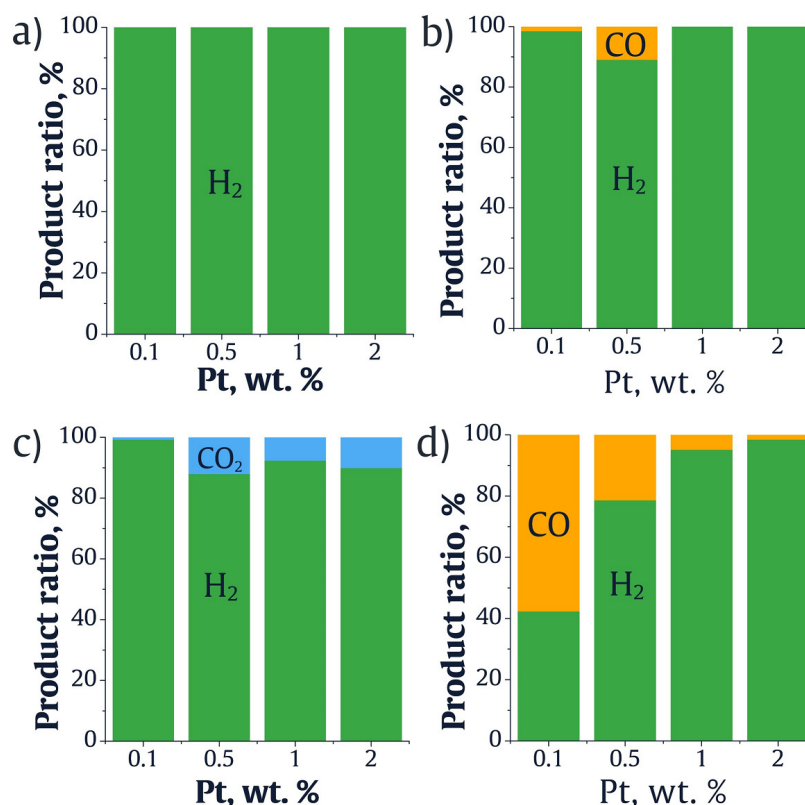


FIG. 7. Distribution of products in the gas phase as a function of platinum loading for the Pt/g-C<sub>3</sub>N<sub>4</sub> catalyst when the process is carried out in a solution of TEOA (a), glycerol (b), glucose (c), cellulose (d). Reaction conditions:  $m(\text{catalyst}) = 25 \text{ mg}$ ,  $V(\text{suspension}) = 50 \text{ mL}$ ,  $\lambda = 430 \text{ nm}$ ,  $t(\text{reaction}) = 90 \text{ min}$ ,  $C(\text{TEOA}) = 10 \text{ vol.}\%$ ;  $C(\text{Glycerol}) = 0.4 \text{ M}$ ;  $C(\text{Glucose}) = 0.2 \text{ M}$ ;  $C(\text{Cellulose}) = 3 \text{ M}$

Complete oxidation of glucose proceeds relatively easily even in anaerobic environment, so a mixture of CO<sub>2</sub> and H<sub>2</sub> was detected in gas phase analysis for all catalysts. The selectivity is almost independent of the amount of platinum deposited on the surface of g-C<sub>3</sub>N<sub>4</sub>. The mixture of gases obtained in this case can be converted into carbon monoxide, which, as previously mentioned, is a valuable product for organic synthesis. It is also possible to obtain methane by hydrogenation of CO<sub>2</sub>. From the thermodynamic point of view, the more favorable product of glucose oxidation in the liquid phase at high temperatures is lactic acid. On the contrary, lower temperatures are favorable for the production of formate [45]. The photocatalytic reactions presented in this work were carried out at room temperature, hence, the main oxidation product in the liquid phase is probably formic acid.

When comparing the results obtained with literature data (Table 4), it was found that the values of the rates of formation of photocatalytic reaction products exceed or are on par with already published data. It should be noted that there are very few papers devoted to photocatalytic hydrogen evolution with simultaneous detection of not only the target product – hydrogen, but also detection of reaction by-products, including CO and CO<sub>2</sub>. At the same time, there are no papers in which low-soluble biomass components, such as cellulose, are used as electron donors.

#### 4. Conclusion

In this work, a series of photocatalysts based on graphitic carbon nitride g-C<sub>3</sub>N<sub>4</sub> with subsequent surface modification with Pt particles (0 – 2 wt.%) were synthesized. The samples were tested in the reaction of photocatalytic hydrogen evolution under visible irradiation (430 nm) not only from model substrates, including triethanolamine, glycerol, but also from plant biomass components – glucose and cellulose. The dependence of catalyst activity on platinum content was a combination of several factors, namely: the state of platinum: Pt<sup>2+</sup>, Pt<sup>0</sup>, and the ratio of these forms; the distribution of platinum-containing particles on the catalyst surface: single particles or agglomerates. The maximum hydrogen evolution rate was observed when 1 %Pt/g-C<sub>3</sub>N<sub>4</sub> was added from triethanolamine solution and amounted to 9.6 mmol·g<sup>-1</sup>·h<sup>-1</sup> (AQE = 2.6 %). When studying the influence of Pt loading and the nature of electron donor on the selectivity of reaction product formation in the gas phase, it was found that using cellulose and glycerol, it is possible to obtain synthesis gas in different CO:H<sub>2</sub> ratios by varying the Pt loading. Carrying out the target reaction in TEOA solution resulted in the production of high-purity hydrogen. The formation of a mixture of CO<sub>2</sub> and H<sub>2</sub> occurred when glucose was used as an electron donor.

TABLE 4. Comparison of the obtained values of formation rates of reaction products, including H<sub>2</sub>, CO and CO<sub>2</sub>, of the synthesized sample with literature data

Catalyst	Light source	Electron donor	W(H <sub>2</sub> ), μmol·g <sup>-1</sup> ·h <sup>-1</sup>	W(CO), μmol·g <sup>-1</sup> ·h <sup>-1</sup>	W(CO <sub>2</sub> ), μmol·g <sup>-1</sup> ·h <sup>-1</sup>	Ref.
Cd <sub>0.8</sub> Zn <sub>0.2</sub> S/2 wt.% Au/gC <sub>3</sub> N <sub>4</sub>	Xe lamp λ > 420 nm	0.1 M glucose	123.21	8.1	38.2	[46]
0.5 wt.% Pt / TiO <sub>2</sub> /g-C <sub>3</sub> N <sub>4</sub>	LED λ = 450 nm	10 vol.% TEOA	5100	0	2100	[47]
		10 vol.% glycerol	860	0	2100	
1 wt.% Pt/g-C <sub>3</sub> N <sub>4</sub>	LED λ = 430 nm	10 vol.% TEOA	9600	0	0	This work
		0.4 M glycerol	720	0.5	0	
		0.2 M glucose	480	0	36.5	
		3 M cellulose	48	2.4	0	

## References

- Li J., Xin Y., Hu B., Zeng K., Wu Z., Fan S., Li Y., Chen Y., Wang S., Wang J., et al. Safety and Thermal Efficiency Performance Assessment of Solar Aided Coal-Fired Power Plant Based on Turbine Steam Double Reheat. *Energy*, 2021, **226**, 120277.
- Alola A.A., Olanipekun I.O., Shah M.I. Examining the Drivers of Alternative Energy in Leading Energy Sustainable Economies: The Trilemma of Energy Efficiency, Energy Intensity and Renewables Expenses. *Renew. Energy*, 2023, **202**, P. 1190–1197.
- Zlotin S.G., Egorova K.S., Ananikov V.P., Akulov A.A., Varaksin M.V., Chupakhin O.N., Charushin V.N., Bryliakov K.P., Averin A.D., Beletskaya I.P., et al. The Green Chemistry Paradigm in Modern Organic Synthesis. *Russ. Chem. Rev.*, 2023, **92**, RCR5104.
- Azam M.S., Bhattacharjee A., Hassan M., Rahaman M., Aziz S., Ali Shaikh M.A., Islam M.S. Performance Enhancement of Solar PV System Introducing Semi-Continuous Tracking Algorithm Based Solar Tracker. *Energy*, 2024, **289**, 129989.
- Xu F., Weng B. Photocatalytic Hydrogen Production: An Overview of New Advances in Structural Tuning Strategies. *J. Mater. Chem. A*, 2023, **11**, P. 4473–4486.
- Chu X., Sathish C.I., Yang J.H., Guan X., Zhang X., Qiao L., Domen K., Wang S., Vinu A., Yi J. Strategies for Improving the Photocatalytic Hydrogen Evolution Reaction of Carbon Nitride-Based Catalysts. *Small*, 2023, **19**, 2302875.
- Li T., Tsubaki N., Jin Z. S-Scheme Heterojunction in Photocatalytic Hydrogen Production. *J. Mater. Sci. Technol.*, 2024, **169**, P. 82–104.
- Dorosheva I.B., Volkhintsev A.S., Weinstein I.A., Rempel A.A. Induced Surface Photovoltage in TiO<sub>2</sub> Sol-Gel Nanoparticles. *Nanosystems: Phys. Chem. Math.*, 2023, **14**, P. 447–453.
- Kozlova E.A., Valeeva A.A., Sushnikova A.A., Zhurenok A.V., Rempel A.A. Photocatalytic Activity of Titanium Dioxide Produced by High-Energy Milling. *Nanosystems: Phys. Chem. Math.*, 2022, **13**, P. 632–639.
- Maeda K., Wang X., Nishihara Y., Lu D., Antonietti M., Domen K. Photocatalytic Activities of Graphitic Carbon Nitride Powder for Water Reduction and Oxidation under Visible Light. *J. Phys. Chem. C*, 2009, **113**, P. 4940–4947.
- Gao F., Xiao H., Yang J., Luan X., Fang D., Yang L., Zi J., Lian Z. Modulation of Electronic Density in Ultrathin G-C<sub>3</sub>N<sub>4</sub> for Enhanced Photocatalytic Hydrogen Evolution through an Efficient Hydrogen Spillover Pathway. *Appl. Catal. B Environ.*, 2024, **341**, 123334.
- Fu J., Yu J., Jiang C., Cheng B. G-C<sub>3</sub>N<sub>4</sub>-Based Heterostructured Photocatalysts. *Adv. Energy Mater.*, 2018, **8**, 1701503.
- Feng C., Tang L., Deng Y., Wang J., Liu Y., Ouyang X., Yang H., Yu J., Wang J. A Novel Sulfur-Assisted Annealing Method of g-C<sub>3</sub>N<sub>4</sub> Nanosheet Compensates for the Loss of Light Absorption with Further Promoted Charge Transfer for Photocatalytic Production of H<sub>2</sub> and H<sub>2</sub>O<sub>2</sub>. *Appl. Catal. B Environ.*, 2021, **281**, 119539.
- Zou J., Liao G., Jiang J., Xiong Z., Bai S., Wang H., Wu P., Zhang P., Li X. In-Situ Construction of Sulfur-Doped g-C<sub>3</sub>N<sub>4</sub>/Defective g-C<sub>3</sub>N<sub>4</sub> Isotype Step-Scheme Heterojunction for Boosting Photocatalytic H<sub>2</sub> Evolution. *Chinese J. Struct. Chem.*, 2022, **41**, P. 2201025–2201033.
- Zhang G., Lan Z.A., Wang X. Surface Engineering of Graphitic Carbon Nitride Polymers with Cocatalysts for Photocatalytic Overall Water Splitting. *Chem. Sci.*, 2017, **8**, P. 5261–5274.
- Rosman N.N., Yunus R.M., Shah N.R.A.M., Shah R.M., Arifin K., Minggu L.J., Ludin N.A. An Overview of Co-Catalysts on Metal Oxides for Photocatalytic Water Splitting. *Int. J. Energy Res.*, 2022, **46**, P. 11596–11619.
- Kharina S.N., Kurenkova A.Y., Saraev A.A., Gerasimov E.Y., Kozlova E.A. Copper-Modified g-C<sub>3</sub>N<sub>4</sub>/TiO<sub>2</sub> Nanostructured Photocatalysts for H<sub>2</sub> Evolution from Glucose Aqueous Solution. *Nanosystems: Phys. Chem. Math.*, 2024, **15**, P. 388–397.
- Chebanenko M.I., Lebedev L.A., Tenevich M.I., Stovpiaga E.Y., Popkov V.I. Planetary Grinding's Impact on the Structure and Photocatalytic Characteristics of Urea-Derived g-C<sub>3</sub>N<sub>4</sub> Nanocrystals. *Nanosystems: Phys. Chem. Math.*, 2023, **14**, P. 705–712.
- Huang D., Li Z., Zeng G., Zhou C., Xue W., Gong X., Yan X., Chen S., Wang W., Cheng M. Megamerger in Photocatalytic Field: 2D g-C<sub>3</sub>N<sub>4</sub> Nanosheets Serve as Support of 0D Nanomaterials for Improving Photocatalytic Performance. *Appl. Catal. B Environ.*, 2019, **240**, P. 153–173.
- Chen L., Maigbay M.A., Li M., Qiu X. Synthesis and Modification Strategies of G-C<sub>3</sub>N<sub>4</sub> Nanosheets for Photocatalytic Applications. *Adv. Powder Mater.*, 2024, **3**, 100150.
- Liu C., Jing L., He L., Luan Y., Li C. Phosphate-Modified Graphitic C<sub>3</sub>N<sub>4</sub> as Efficient Photocatalyst for Degrading Colorless Pollutants by Promoting O<sub>2</sub> Adsorption. *Chem. Commun.*, 2014, **50**, P. 1999–2001.
- Potapenko K.O., Cherepanova S.V., Kozlova E.A. A New Strategy for the Synthesis of Highly Active Catalysts Based on G-C<sub>3</sub>N<sub>4</sub> for Photocatalytic Production of Hydrogen under Visible Light. *Dokl. Phys. Chem.*, 2023, P. 1–9.

- [23] Scofield J.H. Hartree-Slater Subshell Photoionization Cross-Sections at 1254 and 1487 eV. *J. Electron Spectros. Relat. Phenomena*, 1976, **8**, P. 129–137.
- [24] Shirley D.A. High-Resolution X-Ray Photoemission Spectrum of the Valence Bands of Gold. *Phys. Rev. B*, 1972, **5**, 4709.
- [25] Fairley N. URL: [www.casaxps.com](http://www.casaxps.com).
- [26] Dong F., Zhao Z., Xiong T., Ni Z., Zhang W., Sun Y., Ho W.K. In Situ Construction of G-C<sub>3</sub>N<sub>4</sub>/g-C<sub>3</sub>N<sub>4</sub> Metal-Free Heterojunction for Enhanced Visible-Light Photocatalysis. *ACS Appl. Mater. Interfaces*, 2013, **5**, P. 11392–11401.
- [27] Liu H., Chen D., Wang Z., Jing H., Zhang R. Microwave-Assisted Molten-Salt Rapid Synthesis of Isotype Triazine/Heptazine Based g-C<sub>3</sub>N<sub>4</sub> Heterojunctions with Highly Enhanced Photocatalytic Hydrogen Evolution Performance. *Appl. Catal. B Environ.*, 2017, **203**, P. 300–313.
- [28] Tenney S.A., He W., Ratliff J.S., Mullins D.R., Chen D.A. Characterization of Pt-Au and Ni-Au Clusters on TiO<sub>2</sub>(110). *Top. Catal.*, 2011, **54**, P. 42–55.
- [29] Barr T.L. An ESCA Study of the Termination of the Passivation of Elemental Metals. *J. Phys. Chem.*, 1978, **82**, P. 1801–1810.
- [30] Bernsmeier D., Sachse R., Bernicke M., Schmack R., Kettemann F., Polte J., Kraehnert R. Outstanding Hydrogen Evolution Performance of Supported Pt Nanoparticles: Incorporation of Preformed Colloids into Mesoporous Carbon Films. *J. Catal.*, 2019, **369**, P. 181–189.
- [31] Golabiewska A., Lisowski W., Jarek M., Nowaczyk G., Zielińska-Jurek A., Zaleska A. Visible Light Photoactivity of TiO<sub>2</sub> Loaded with Monometallic (Au or Pt) and Bimetallic (Au/Pt) Nanoparticles. *Appl. Surf. Sci.*, 2014, **317**, P. 1131–1142.
- [32] Maillard F., Schreier S., Hanzlik M., Savinova E.R., Weinkauff S., Stimming U. Influence of Particle Agglomeration on the Catalytic Activity of Carbon-Supported Pt Nanoparticles in CO Monolayer Oxidation. *Phys. Chem. Chem. Phys.*, 2005, **7**, P. 385–393.
- [33] Vorontsov A.V., Stoyanova I.V., Kozlov D.V., Simagina V.I., Savinov E.N. Kinetics of the Photocatalytic Oxidation of Gaseous Acetone over Platinized Titanium Dioxide. *J. Catal.*, 2000, **189**, P. 360–369.
- [34] Lam S.W., Chiang K., Lim T.M., Amal R., Low G.K.C. The Effect of Platinum and Silver Deposits in the Photocatalytic Oxidation of Resorcinol. *Appl. Catal. B Environ.*, 2007, **72**, P. 363–372.
- [35] Kozlova E.A., Parmon V.N. Heterogeneous Semiconductor Photocatalysts for Hydrogen Production from Aqueous Solutions of Electron Donors. *Russ. Chem. Rev.*, 2017, **86**, P. 870–906.
- [36] Mazumder V., Lee Y., Sun S. Recent Development of Active Nanoparticle Catalysts for Fuel Cell Reactions. *Adv. Funct. Mater.*, 2010, **20**, P. 1224–1231.
- [37] Lordi V., Yao N., Wei J. Method for Supporting Platinum on Single-Walled Carbon Nanotubes for a Selective Hydrogenation Catalyst. *Chem. Mater.*, 2001, **13**, P. 733–737.
- [38] Emmanuel J. Comparative Activity of Platinum and Gold Nanoparticles Catalysts for Carbon Monoxide Oxidation. *Ethiop. J. Sci. Technol.*, 2022, **15**, P. 155–172.
- [39] Haynes C.A., Gonzalez R. Rethinking Biological Activation of Methane and Conversion to Liquid Fuels. *Nat. Chem. Biol.*, 2014, **10**, P. 331–339.
- [40] Sartipi S., Makkee M., Kapteijn F., Gascon J. Catalysis Engineering of Bifunctional Solids for the One-Step Synthesis of Liquid Fuels from Syngas: A Review. *Catal. Sci. Technol.*, 2014, **4**, P. 893–907.
- [41] Centi G., Perathoner S. Status and Gaps toward Fossil-Free Sustainable Chemical Production. *Green Chem.*, 2022, **24**, P. 7305–7331.
- [42] Ketchie W.C., Murayama M., Davis R.J. Selective Oxidation of Glycerol over Carbon-Supported AuPd Catalysts. *J. Catal.*, 2007, **250**, P. 264–273.
- [43] Limpachanangkul P., Liu L., Hunsom M., Piumsomboon P., Chalermssinsuwan B. Application of Bi<sub>2</sub>O<sub>3</sub>/TiO<sub>2</sub> Heterostructures on Glycerol Photocatalytic Oxidation to Chemicals. *Energy Reports*, 2022, **8**, P. 1076–1083.
- [44] Coseri S., Biliuta G., Simionescu B.C., Stana-Kleinschek K., Ribitsch V., Harabagiu V. Oxidized Cellulose—Survey of the Most Recent Achievements. *Carbohydr. Polym.*, 2013, **93**, P. 207–215.
- [45] Jin B., Yao G., Wang X., Ding K., Jin F. Photocatalytic Oxidation of Glucose into Formate on Nano TiO<sub>2</sub> Catalyst. *ACS Sustain. Chem. Eng.*, 2017, **5**, P. 6377–6381.
- [46] Zhao H., Ding X., Zhang B., Li Y., Wang C. Enhanced Photocatalytic Hydrogen Evolution along with Byproducts Suppressing over Z-Scheme Cd<sub>x</sub>Zn<sub>1-x</sub>S/Au/g-C<sub>3</sub>N<sub>4</sub> Photocatalysts under Visible Light. *Sci. Bull.*, 2017, **62**, P. 602–609.
- [47] Herrera-Beurnio M.C., López-Tenllado F.J., Hidalgo-Carrillo J., Martín-Gómez J., Estévez R., Urbano F.J., Marinas A. Glycerol Photoreforming for Photocatalytic Hydrogen Production on Binary and Ternary Pt-g-C<sub>3</sub>N<sub>4</sub>-TiO<sub>2</sub> Systems: A Comparative Study. *Catal. Today*, 2024, **430**, 114548.

---

*Submitted 6 June 2024, revised 8 August 2024, accepted 9 August 2024*

#### *Information about the authors:*

*Ksenia O. Potapenko* – Borekov Institute of Catalysis, SB RAS, Novosibirsk, 630090, Russia; ORCID 0000-0002-7868-3409; [potapenko@catalysis.ru](mailto:potapenko@catalysis.ru)

*Egor E. Aydakov* – Borekov Institute of Catalysis, SB RAS, Novosibirsk, 630090, Russia; ORCID 0000-0002-7730-7655; [e.ajdakov@g.nsu.ru](mailto:e.ajdakov@g.nsu.ru)

*Evgeny Y. Gerasimov* – Borekov Institute of Catalysis, SB RAS, Novosibirsk, 630090, Russia; ORCID 0000-0002-3230-3335; [gerasimov@catalysis.ru](mailto:gerasimov@catalysis.ru)

*Ekaterina A. Kozlova* – Borekov Institute of Catalysis, SB RAS, Novosibirsk, 630090, Russia; ORCID 0000-0001-8944-7666; [kozlova@catalysis.ru](mailto:kozlova@catalysis.ru)

*Conflict of interest:* the authors declare no conflict of interest.



# NANOSYSTEMS:

**PHYSICS, CHEMISTRY, MATHEMATICS**

## INFORMATION FOR AUTHORS

The journal publishes research articles and reviews, and also short scientific papers (letters) which are unpublished and have not been accepted for publication in other magazines. Articles should be submitted in English. All articles are reviewed, then if necessary come back to the author to completion.

The journal is indexed in Web of Science Core Collection (Emerging Sources Citation Index), Chemical Abstract Service of the American Chemical Society, Zentralblatt MATH and in Russian Scientific Citation Index.

### Author should submit the following materials:

1. Article file in English, containing article title, the initials and the surname of the authors, Institute (University), postal address, the electronic address, the summary, keywords, MSC or PACS index, article text, the list of references.
2. Files with illustrations, files with tables.
3. The covering letter in English containing the article information (article name, MSC or PACS index, keywords, the summary, the literature) and about all authors (the surname, names, the full name of places of work, the mailing address with the postal code, contact phone number with a city code, the electronic address).
4. The expert judgement on possibility of publication of the article in open press (for authors from Russia).

Authors can submit a paper and the corresponding files to the following addresses: nanojournal.ifmo@gmail.com, popov1955@gmail.com.

### Text requirements

Articles should be prepared with using of text editors MS Word or LaTeX (preferable). It is necessary to submit source file (LaTeX) and a pdf copy. In the name of files the English alphabet is used. The recommended size of short communications (letters) is 4-6 pages, research articles– 6-15 pages, reviews – 30 pages.

#### Recommendations for text in MS Word:

Formulas should be written using Math Type. Figures and tables with captions should be inserted in the text. Additionally, authors present separate files for all figures and Word files of tables.

**Recommendations for text in LaTeX:**

Please, use standard LaTeX without macros and additional style files. The list of references should be included in the main LaTeX file. Source LaTeX file of the paper with the corresponding pdf file and files of figures should be submitted.

References in the article text are given in square brackets. The list of references should be prepared in accordance with the following samples:

- [1] Surname N. *Book Title*. Nauka Publishing House, Saint Petersburg, 2000, 281 pp.
- [2] Surname N., Surname N. Paper title. *Journal Name*, 2010, 1 (5), P. 17-23.
- [3] Surname N., Surname N. Lecture title. In: Abstracts/Proceedings of the Conference, Place and Date, 2000, P. 17-23.
- [4] Surname N., Surname N. Paper title, 2000, URL: <http://books.ifmo.ru/ntv>.
- [5] Surname N., Surname N. Patent Name. Patent No. 11111, 2010, Bul. No. 33, 5 pp.
- [6] Surname N., Surname N. Thesis Title. Thesis for full doctor degree in math. and physics, Saint Petersburg, 2000, 105 pp.

**Requirements to illustrations**

Illustrations should be submitted as separate black-and-white files. Formats of files – jpeg, eps, tiff.



# **NANOSYSTEMS:**

**PHYSICS, CHEMISTRY, MATHEMATICS**

**Журнал зарегистрирован**

Федеральной службой по надзору в сфере связи, информационных технологий и массовых коммуникаций

(свидетельство ПИ № ФС 77 - 49048 от 22.03.2012 г.)

ISSN 2220-8054

**Учредитель:** федеральное государственное автономное образовательное учреждение высшего образования

«Национальный исследовательский университет ИТМО»

**Издатель:** федеральное государственное автономное образовательное учреждение высшего образования

«Национальный исследовательский университет ИТМО»

**Отпечатано в Учреждении «Университетские телекоммуникации»**

Адрес: 197101, Санкт-Петербург, Кронверкский пр., 49

**Подписка на журнал НФХМ**

На первое полугодие 2025 года подписка осуществляется через

ОАО «АРЗИ», подписной индекс Э57385